The Dissertation Committee for Kaustubh Shrivastava Certifies that this is the approved version of the following Dissertation:

Hydraulic Fracture Modeling in Naturally Fractured Reservoirs

Committee:

Mukul M. Sharma, Supervisor

Jon E. Olson

Kishore Mohanty

Maša Prodanović

Roger Bonnecaze

Hydraulic Fracture Modeling in Naturally Fractured Reservoirs

by

Kaustubh Shrivastava

Dissertation

Presented to the Faculty of the Graduate School of

The University of Texas at Austin

in Partial Fulfillment

of the Requirements

for the Degree of

Doctor of Philosophy

The University of Texas at Austin

December 2019

To my parents Purnima and Rakesh Shrivastava, for their endless love and support.

To my brother Maitray, for his guidance and encouragement.

Acknowledgments

I would like to express my sincere gratitude towards my advisor, Dr. Mukul Sharma, for his guidance and continuous support throughout my stay at UT Austin. I am very fortunate to have him as my advisor. He has been a constant source of inspiration and has played an important role in shaping my personal and professional life. I am thankful to my committee members, Dr. Jon Olson, Dr. Kishore Mohanty, Dr. Maša Prodanović, and Dr. Roger Bonnecaze, for the time they took to review my dissertation and for proving their valuable feedback.

During my stay at UT, I was very fortunate to have met some exceptional people, and I am grateful to have them in my life as my friends. I thank Ashish Kumar, Eva Vinegar, Prachi Mehta, Shashvat Doorwar, Donna Vakharia, Prasanna Iyer, Ajit Gopalakrishnan, Manoj Rao, and Gurpreet Singh as they have made this journey a memorable and enjoyable one. Special thanks to my close friend, Robin Singh, whom I have known for the past 11 years, and I find myself very lucky to have shared my academic journey at UT and my undergraduate school IIT KGP with him.

Many thanks to all my colleagues at Dr. Sharma's lab, Jongsoo Hwang, Ripudaman Manchanda, Yaniv Brick, Brendan Elliott, Shivam Agrawal, Javid Shiriyev, Murtadha Al Tammar, Sophie Yi, Peng Zhang, Deepen Gala and others for their advice and all the technical discussions.

I would like to thank the departmental staff at UT PGE for their help. I thank Frankie Hart, Glen Baum, Gary Miscoe, and Amy Stewart for their support during my stay at UT PGE. Special thanks to Jin Lee, as she was always there when I needed help.

Finally, I would like to thank my family. Without their support and patience, this work would not have been possible. I am grateful and indebted to their sacrifices and love.

Abstract

Hydraulic Fracture Modeling in Naturally Fractured Reservoirs

Kaustubh Shrivastava, Ph.D.

The University of Texas at Austin, 2019

Supervisor: Mukul M. Sharma

Hydraulic fracturing of horizontal wells is one of the key technological breakthroughs that has led to the shale revolution. Hydraulic fracturing models are used to engineer hydraulic fracture design and optimize production. Typically, hydraulic fracturing models treat hydraulic fractures as planar, bi-wing fractures. However, recent core-through investigations have suggested that during hydraulic fracturing in naturally fractured reservoirs, complex hydraulic fracture geometries can be created due to the interaction of the growing hydraulic fracture with natural fractures. This limits the application of planar fracture models for optimizing hydraulic fracturing design in naturally fractured reservoirs.

In this research, we present a novel three-dimensional displacement discontinuity method based hydraulic fracturing simulator that allows us to model hydraulic fracture growth in the presence of natural fractures along with proppant transport in an efficient manner. The model developed in this dissertation is used to investigate the interaction of a hydraulic fracture with natural fractures and study the transport of proppant in the resulting complex fracture networks. This investigation gives us novel insight into the influence of fracture geometry and stress interference on the final distribution of proppant in fracture

networks. Based on this investigation, suggestions are made to improve proppant transport in complex fracture networks.

In order to correctly capture the effect of natural fractures on fracture growth, knowledge about the distribution of natural fractures in the reservoir is imperative. Typically, little is known about the in-situ natural fracture distribution, as direct observation of the reservoir is not possible. A novel technique of synthetic coring is developed to create a discrete fracture network (DFN) from core data, and it is used to create a DFN based on the Hydraulic Fracturing Test Site #1 data. Hydraulic fracture propagation is modeled in the created DFN, and the results are compared with field observations.

As the reservoir may contain thousands of natural fractures, simulations in a realistic DFN can be computationally very expensive. In order to reduce the computational requirements of the simulator, we present a novel predictor step based on the local linearization method that provides a better initial guess for solving the fluid-solid interaction problem. This is shown to reduce computational time significantly.

A novel technique, Extended Adaptive Integral Method, to speed up the simulator is developed. The method uses an effective medium to represent the interaction between displacement discontinuity elements and reduces the order of complexity of solving the geomechanical system of equations from $O(N^2)$ to $O(N\log N)$. The novel formulation of this method is presented, and sensitivity studies are conducted to show the improvement in computational efficiency.

Table of Contents

List of Tables

List of Figures

Chapter 1: Introduction

1.1 BACKGROUND

Hydraulic fracturing of horizontal wells has made the economic recovery of hydrocarbons from ultra-low permeability shale reservoirs possible. In the past decade, the production of hydrocarbons from shale reservoirs in the United States has increased significantly. The development of novel technologies of horizontal drilling and hydraulic fracturing has played a vital role in this increase in the production and has made the US the largest oil producer in the world (see Figure 1.1) in 2018. US oil production has more than doubled in the last ten years (see Figure 1.2). This has made the US less dependent on foreign energy resources and has also made access to energy more affordable. According to the U.S. Energy Information Administration (EIA), about 6.5 million barrels of crude oil were produced per day from tight oil resources in the United States in 2018. This was equal to about 59% of total U.S. crude oil production in that year. It is predicted that the United States will export more energy than it imports by 2020 as increases in crude oil, natural gas, and natural gas plant liquids production will outpace the growth of the U.S. energy consumption.

In addition, in recent years several shale reservoirs have been found in other parts of the world. According to EIA, the world has around 418.0 billion barrels of technically recoverable tight oil and 7576.6 trillion cubic feet of wet shale gas (Figure 1.4)(U.S. Energy Information Administration, 2013). This huge resource, which has become economically accessible due to the development of hydraulic fracturing, ensures the availability of affordable energy for the foreseeable future.

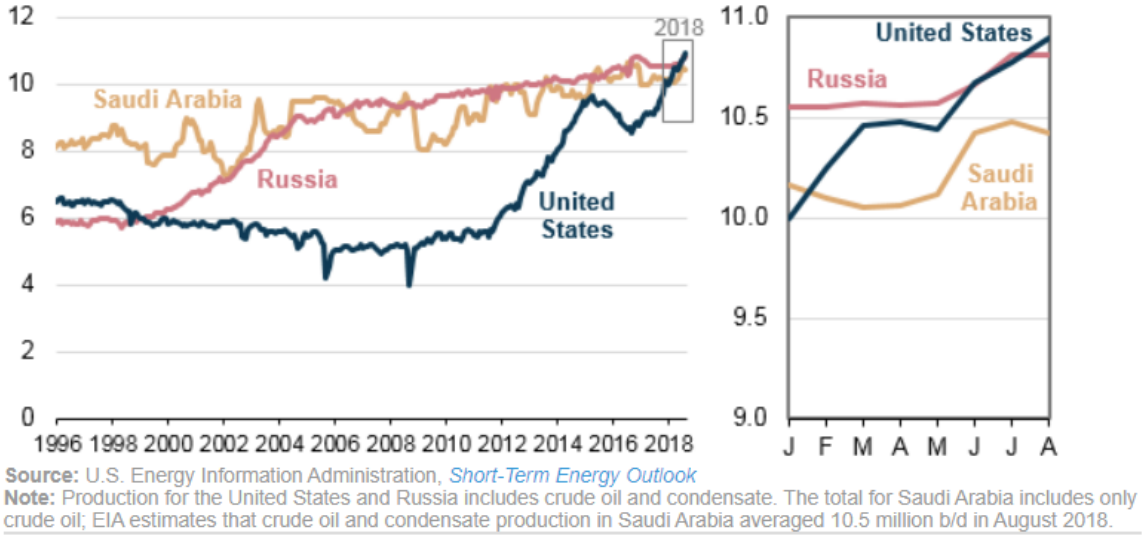

Source: U.S. Energy Information Administration, *Short-Term Energy Outlook*
Note: Production for the United States and Russia includes crude oil and condensate. The total for Saudi Arabia includes only crude oil; EIA estimates that crude oil and condensate production in Saudi Arabia averaged 10.5 million b/d in August 2018.

Figure 1.1: Monthly crude oil production (from Jan 1996 - Aug 2018) of the world's major oil-producing countries in millions of bbl per day (source: U.S. Energy Information Administration).

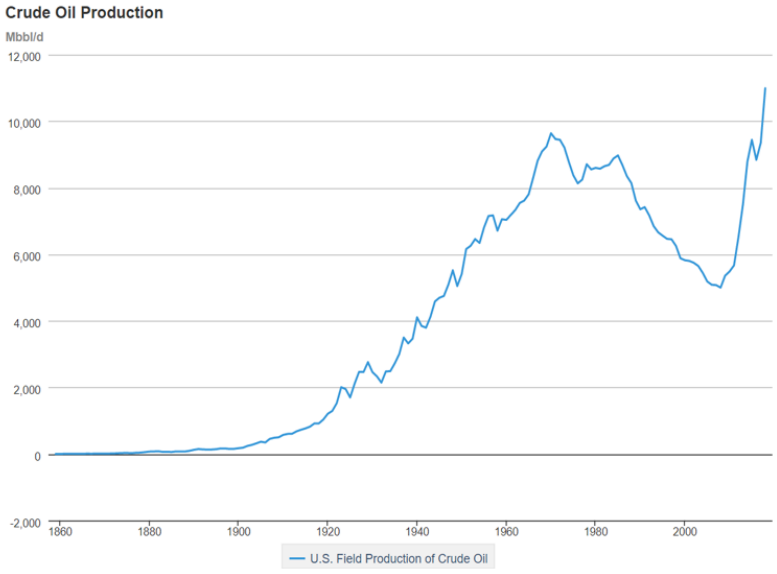

Figure 1.2: Crude oil production of the U.S. It can be observed that post-2010, oil production has dramatically increased (U.S. Energy Information Administration).

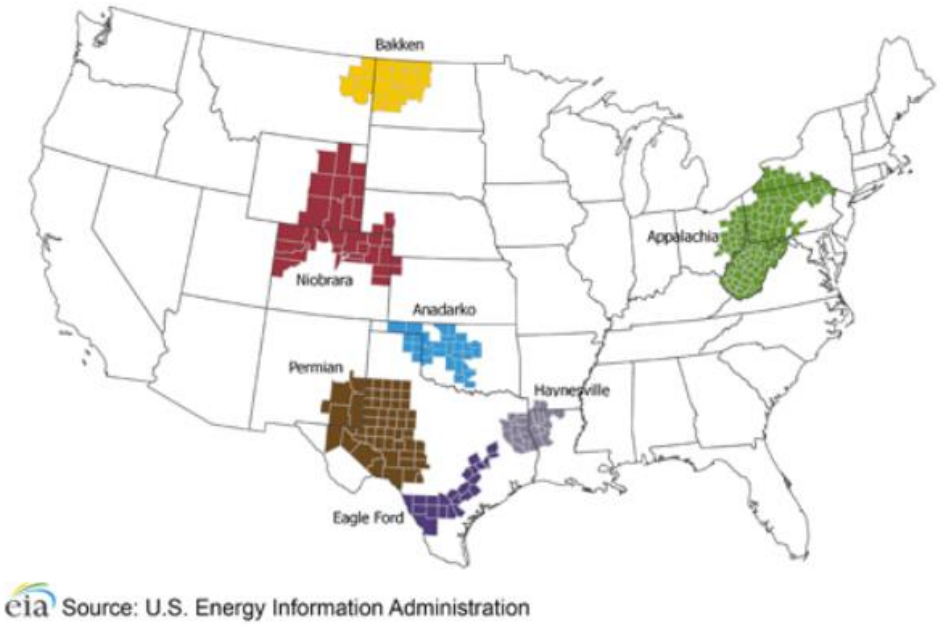

Figure 1.3: Shale plays in the United States (U.S. Energy Information Administration).

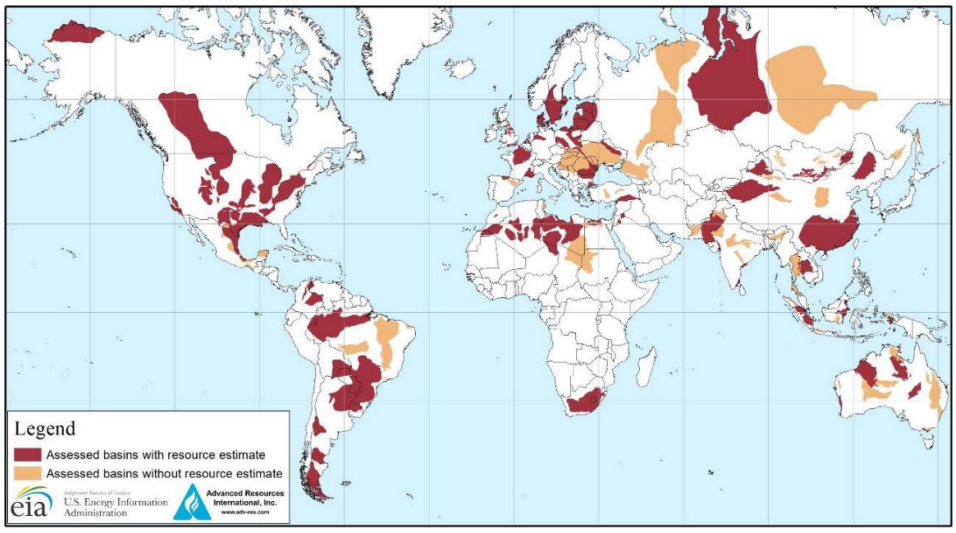

Figure 1.4: Map of shale resource distribution in the world (U.S. Energy Information Administration, 2013).

1.2 HYDRAULIC FRACTURING

Hydraulic fracturing is the primary method of increasing production from unconventional reservoirs. To enhance petroleum production, fracturing fluid is pumped into the perforations in the well at high enough rates to create fractures in the reservoir. The first fracturing treatment to increase the production was conducted in the Hugoton gas field in 1947 in a vertical well (Montgomery and Smith, 2010). In modern hydraulic fracturing treatments, hydraulic fracturing is performed on horizontal wells. This allows us to create multiple hydraulic fractures from the same horizontal wellbore in the pay zone (the region containing hydrocarbons) and increase the area of contact with the reservoir (see Figure 1.5).

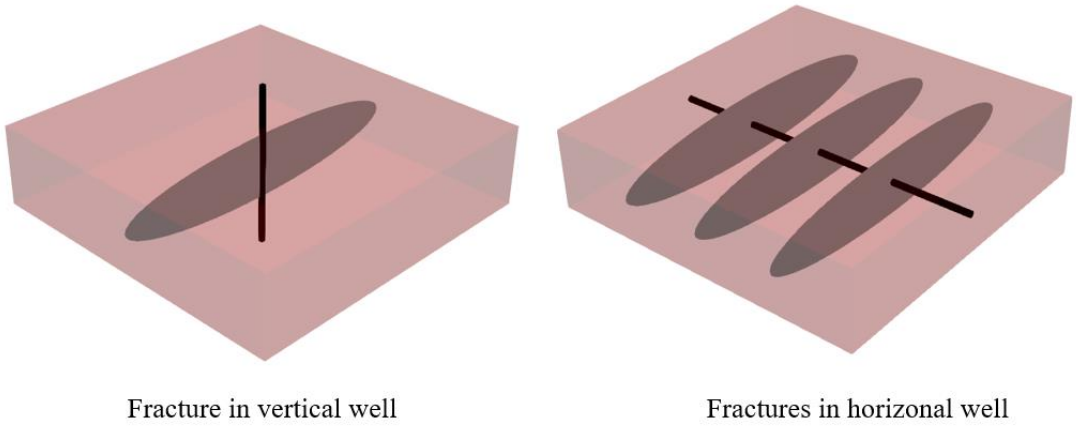

Figure 1.5: The figure shows the configuration of the fractures originating from a vertical well (on the left) and a horizontal well (on the right). A horizontal well allows more fractures to be created in the pay zone.

The pressure of the fracturing fluid acts on the surface of the created fractures against the in-situ stresses in the reservoir and opens the fractures. The opening of a fracture increases the stress concentration at its tip, which leads to its propagation. During fracturing, fractures open against the local minimum stress direction in the reservoir, as opening against minimum horizontal stress requires the least energy of all the possible directions.

Hydraulic fracturing in horizontal wells is performed in stages. Each stage in a hydraulic fracturing treatment is a section of the horizontal wellbore with a set of clusters along the length. A cluster represents a set of perforations that are created for the initiation of the fractures. In each cluster, the perforations are placed close to each other (typically all the perforations in a cluster are within a few feet along the wellbore). As the fracturing fluid is injected, the fluid flows through the perforations into the created fractures (see Figure 1.6 and Figure 1.7). During pumping, isolation of each stage is maintained in order to ensure that only the clusters of a single-stage take fluid at a time. This provides more control over the hydraulic fracturing process. This, however, forces the growth of multiple hydraulic fractures simultaneously (at least one fracture from each cluster). As multiple fractures grow simultaneously from a stage, they interact with each other (exert stresses on each other), and this can affect their growth.

At the start of the hydraulic fracturing process in each stage, a clean fracturing fluid (without any proppant), called “pad”, is injected. The purpose of this “pad” is to initiate the propagation of hydraulic fractures. This is followed by the injection of fracturing fluid along with proppant particles. The proppant particles, along with the fracturing fluid, travel in the created fractures. The proppant is added to the fracturing fluid to keep the created channels open even when the fracturing fluid has leaked off into the formation. These open

channels act as high conductivity pathways that allow the flow of hydrocarbons from the reservoir to the wellbore.

After the pumping of the fracturing fluid and proppant is completed, the stage is shut-in for the fluid to leak-off into the formation and the fracture closes on the injected proppant. The practice of relying on leak-off for fracture closure in horizontal wells in low permeability reservoirs provides excessive time for proppant settling, even for high viscosity fluids. This leads to the formation of a proppant bank at the bottom of the created fracture, significantly reducing the total area available for production. To counter the problem of poor proppant transport, the industry uses large amounts of water and proppant. The current popular practice of using low viscosity fluids (slick-water fracturing) results in very poor proppant transport characteristics. It can lead to a sub-optimal proppant distribution and result in lower well productivity. The low viscosity of slickwater not only causes ineffective lateral placement of proppant but also leads to concerns about the vertical coverage across the pay zone(s) and may also result in settling during pumping depending on the geometry of the created fracture.

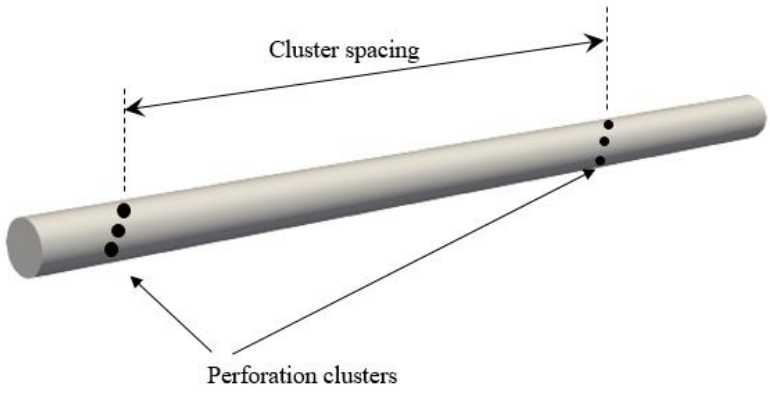

Figure 1.6: The figure shows two clusters from a hydraulic fracturing stage. Each cluster has a set of perforations, typically arranged in a helical pattern around the wellbore.

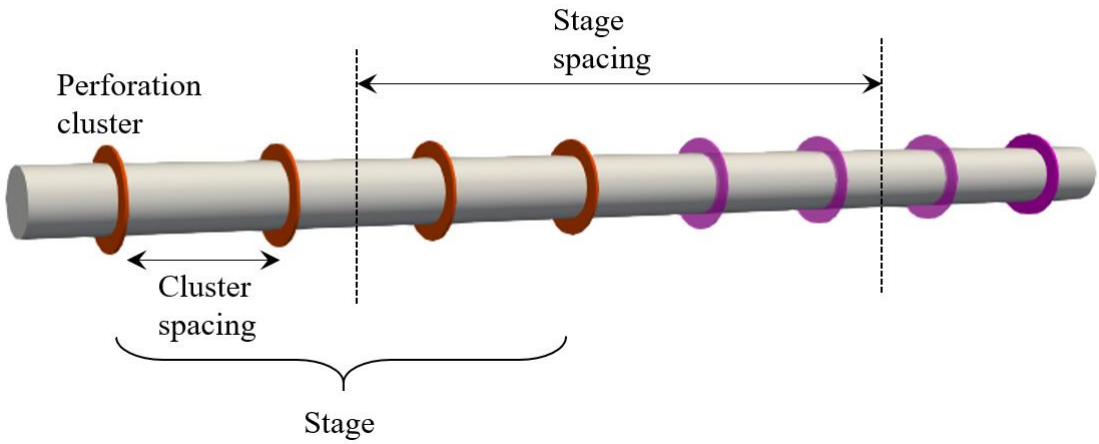

Figure 1.7: Description of stages in a horizontal wellbore. Each colored ring represents a perforation cluster. The same colored perforation clusters belong to a single stage. The distance between perforation clusters is called cluster spacing, and the distance between stage centers is called stage spacing.

As the creation of the hydraulic fracture and the distribution of proppant inside the fracture cannot be directly monitored or measured in the field, we primarily rely on modeling techniques for fracture design. Modeling fracture growth along with the transport of proppant is complex as several parameters affect the fracture growth and the distribution of proppant inside the fracture.

In addition, recent investigations have suggested that the interaction of hydraulic fracture with natural fractures can significantly alter the geometry of the created fracture. A natural fracture can intersect with the growing hydraulic fracture and provide a path of least resistance for its growth. The orientation of the natural fractures is a result of the history of the stress state in the reservoir and may not coincide with the current principal stress directions. Hence on the intersection with a natural fracture, the propagation direction of the hydraulic fracture may not coincide with maximum stress direction. Therefore, the interaction of a hydraulic fracture with natural fractures increases the complexity of the created fracture networks and creates convoluted pathways for the flow of proppant and fracturing fluid.

The hydraulic fracturing process in a naturally fractured reservoir with the transport of proppant is too intricate to model without numerical and computational techniques. This creates the need for a holistic model that can take all the critical factors into account and predict proppant distribution in multiple growing fractures in a computationally efficient manner.

In this work, we seek to improve hydraulic fracturing and proppant placement by developing a better understanding of the behavior of fracture growth in the presence of natural fractures using numerical techniques.

1.3 RESEARCH OBJECTIVES

The main objective of this thesis is to develop a hydraulic fracturing simulator that can model the interaction of growing hydraulic fractures with natural fractures and model the transport of proppant in fracture networks for field-scale problems in a computationally efficient manner. In addition, the work also focuses on understanding the effect of natural fractures on the propagation of a hydraulic fracture and transport of proppant. The overall objective can be achieved by addressing the following:

1. Develop a computationally efficient hydraulic fracturing simulator that can model the interaction of hydraulic fractures with natural fractures and transport of proppant.
2. Investigate the effect of natural fracture properties on the created fracture network geometry.
3. Investigate the parameters affecting the transport of proppant in complex fracture networks.
4. Develop techniques to generate discrete fracture networks based on field data.
5. Develop algorithms to speed up the hydraulic fracturing simulations to reduce the computational complexity of the problem.

1.4 LITERATURE REVIEW

This section provides a literature review of the scientific work related to hydraulic fracture modeling.

1.4.1 Fracture Models

In the past, many hydraulic fracturing models have been developed for understanding the growth of the fracture due to pressurized fluid injection (Barree, 1983;

Ativani et al., 1990; Adachi et al., 2007; Gu et al., 2008; Dahi-Taleghani and Olson, 2011; Weng et al., 2011; Gordeliy and Peirce, 2013; Wu and Olson, 2014, 2016; McClure et al., 2016). In hydraulic fracture simulators, three physical processes are modeled: 1) deformation of the surface of the fracture 2) flow of fracturing fluid and proppant inside the fracture 3) growth of the fracture (propagation). Typically, for simulating the deformation of the fracture surface, linear elasticity is used (Chen et al., 2009; Yao, 2012; Atkinson, 2015), although with better understanding of the effect of reservoir depletion on the fracture growth, poroelasticity based fracture models are getting developed (Boone and Ingraffea, 1990; Rahman and Rahman, 2013; Oterkus et al., 2017; Manchanda et al., 2019).

The first models developed for modeling hydraulic fracturing were analytical in nature and assumed a simplified fracture geometry. These models are generally employed for validation of more complicated models. There are two commonly used fracture models that assume simplified geometry of the fracture: 1) the Perkins and Kern (PKN) model (2) Khristianovic-Geertsma de Klerk (KGD) model. The Perkins and Kern (PKN) model assumes constant fracture height independent of fracture length (Perkins and Kern, 1961; Nordgren, 1972). PKN follows a plane strain assumption in the vertical plane. In the model, the fracture has an elliptical cross-section both in the horizontal and vertical directions and the fracture height is assumed to be much smaller than the fracture length. The PKN model includes energy loss from fluid flow and ignores energy losses due to fracture toughness. The PKN model is applicable when fracture length is much larger than the height of the fracture. Figure 1.8 shows a schematic of a fracture from a PKN model.

The KGD model assumes a constant fracture height which is much larger than the fracture length (Khristianovic and Zheltov, 1955). The model follows a plane strain assumption on the fracture plane and the width of the fracture is assumed to be constant

along the height of the fracture. Figure 1.9 shows a schematic of the fracture geometry from a KGD model.

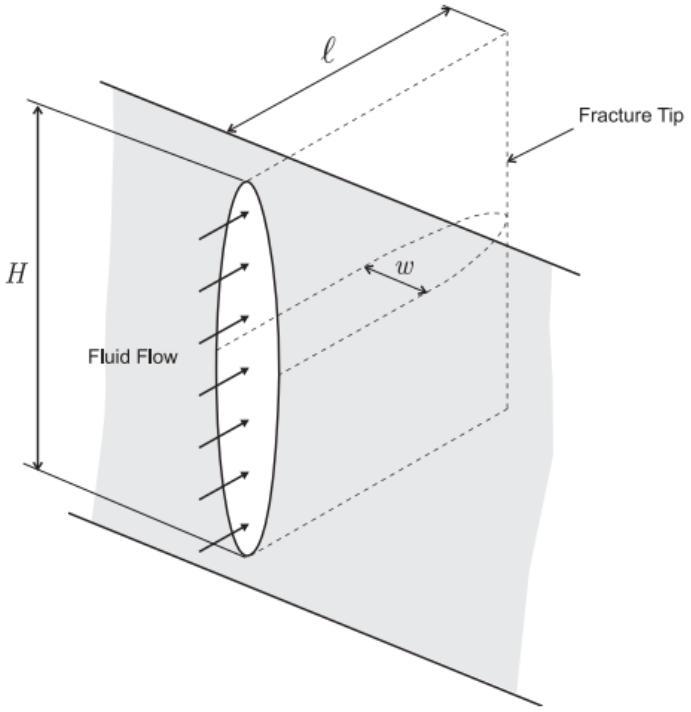

Figure 1.8: Schematic showing a fracture with PKN geometry (Adachi et al., 2007)

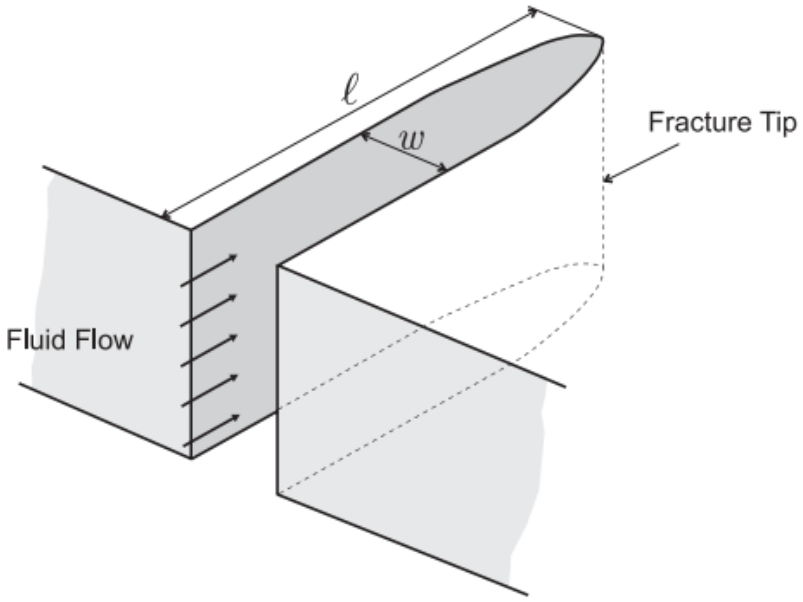

Figure 1.9: Schematic showing a fracture with KGD geometry (Adachi et al., 2007).

These simplified fracture models provide an efficient solution to the fracture growth problem. The assumptions made in these models make them unsuitable for simulating fractures with varying height and varying reservoir stresses. In order to model fractures with varying stresses and height, Pseudo-3D (P3D) models were developed (Settari and Cleary, 1986; Fung et al., 1987). The P3D models can be categorized into two different types: 1) the cell-based models in which the fracture is divided along the length into several cells and each cell follows PKN solution (Simonson et al., 1978; Fung et al., 1987; Bochkarev et al., 2016) (Figure 1.10); 2) lumped parameter models that assume that the fracture consists of two half-ellipses joined at their centers in the fracture direction (Economides and Nolte, 2000)(Figure 1.11). Lumped parameter models can simulate fractures with different lateral and vertical extent (Cleary et al., 1983).

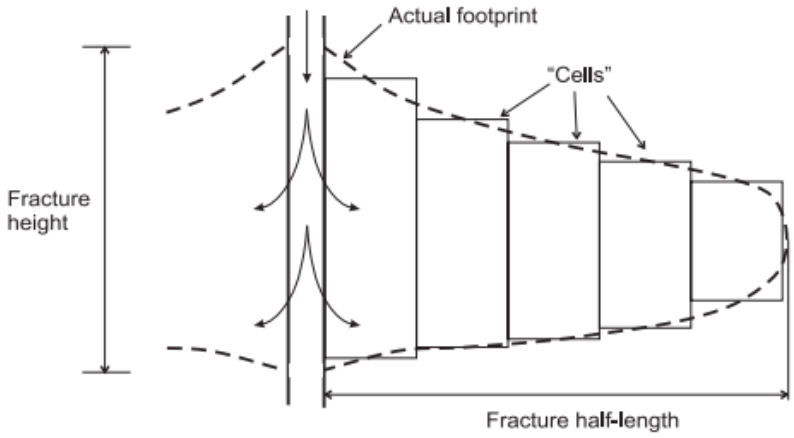

Figure 1.10: Schematic of cell-based pseudo-3D fracture geometry (Adachi et al., 2007)

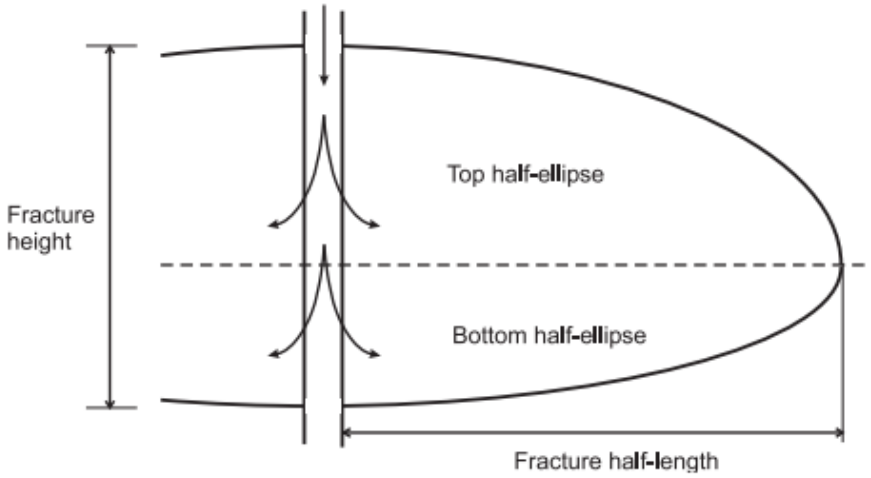

Figure 1.11: Schematic of fracture geometry based on lumped pseudo-3D models. The fracture is represented as two ellipses (Adachi et al., 2007).

In order to improve the accuracy of the fracture geometries resulting from heterogeneous properties of the reservoir, planar three-dimensional models (PL3D) were developed. These models assumed that the fractures can be represented by planar geometries. Although they are more accurate than the P3D models, they are still limited by the assumption that fractures are planar. These models worked well with vertical wells

where only a single fracture propagated during fracturing. In modern hydraulic fracturing process, multiple fractures propagate simultaneously during pumping from a single stage. In addition, recent core through investigations have found complex fracture geometries (multi-planar) are formed due to interaction of the hydraulic fractures and natural fractures (Raterman et al., 2017; Gale et al., 2018; Shrivastava et al., 2018a) which can influence the fracture geometry significantly and result in formation of non-planar complex geometries.

In order to simulate fully three-dimensional fractures, several attempts have been made (Lee, Cardiff, et al., 2015; Ouchi et al., 2015; Mcclure and Kang, 2017). The computational requirements of such coupled systems are substantial for running field-scale hydraulic fracture simulations. Most of these models are not designed to model naturally fractured reservoirs and the interaction of hydraulic fractures with natural fractures.

1.4.2 Interaction of Natural Fractures with Hydraulic Fractures

Naturally occurring fractures are present in most shale reservoirs (Gale et al., 2007; Gale et al., 2017). Several examples of complex microseismic patterns have been associated with hydraulic fracture stimulation and interpreted as a result of natural fracture reactivation (Fisher et al., 2004, 2005; Warpinski, 2009). It is believed that natural fractures play an important role in production from shale reservoirs as hydrocarbon production rate commonly exceeds the production rate expected from such ultra-low permeability shale reservoirs. These natural fractures can become conductive and increase the effective permeability of the reservoir (Dunphy and Campagna, 2011). In addition, they can interact with growing hydraulic fracture and result in the formation of complex networks.

In order to understand the interaction of hydraulic fractures with natural fractures several studies have been conducted (Warpinski and Teufel, 1987; Renshaw and Pollard, 1995; Gu and Weng, 2010; Bahorich et al., 2012; Olson et al., 2012; Taleghani and Olson,

2014; Wang et al., 2013, 2018; Lee, Olson, et al., 2015; Ouchi et. al., 2017; Al Tammar, 2018; Agarwal. et al., 2019). A hydraulic fracture on the intersection with natural fracture can get diverted, arrested or can bypass the natural fracture. This can increase the complexity of the created fracture and lead to the formation of a network of fractures. In order to predict the behavior of hydraulic fracture growth due to the interaction with a natural fracture, several criteria have been proposed. Blanton proposed a criterion for interactions between hydraulic fractures and pre-existing fractures for different approach angles and stress states. The criterion predicted whether the hydraulic fracture crosses or gets diverted along the natural fracture. The developed criterion was based on the assumption that if the pressure required to reinitiate the fracture on the other side of the natural fracture is greater than opening pressure of the natural fracture, then the natural fracture will open, otherwise the hydraulic fracture will cross the natural fracture. Renshaw and Pollard (1995) proposed a criterion to predict interaction of propagating fractures with frictional interfaces at orthogonal approaching angle based on Linear Elastic Fracture Mechanics (LEFM). The criterion was based on the stresses generated due to the fracture tip and predicted the diversion or crossing of fracture according to slippage of the frictional interface. If the interface slips, fracture gets diverted; otherwise it crosses the interface. Gu and Weng (Gu and Weng, 2010) extended the criterion for non-orthogonal intersection angles. Chuprakov et al. (2013) presented a new analytical crossing criterion that accounts for the effect of flow rate and fluid viscosity. Agrawal et al. (2019) using a peridynamics based model investigated the remote shear failure of natural fracture due to approaching hydraulic fracture and presented new criteria for predicting crossing, kinking, and branching of the hydraulic fracture. The crossing criteria typically treat the natural fracture as a frictional interface. Although, in some formations, natural fractures can be partially or fully cemented and filled with calcite or quartz minerals(Gale et al., 2007; Lander and

Laubach, 2014). For predicting hydraulic fracture interaction with cemented natural fracture, Taleghani and Olson (2009) proposed a new crossing criterion based on energy release rate. Ouchi et al. (2017) used a peridynamics based model to investigate fracture propagation in heterogeneous reservoirs with different types of heterogeneity (two-layer model, three-layer model, etc.). They showed that fracture turning along a layer is primarily controlled by the fracture toughness and principal stress direction for intact interfaces. They also investigated the effect of intersection angle, Young's modulus contrast, horizontal stress contrast on the turning, branching, and kinking behavior of the hydraulic fracture.

In addition to analytical and numerical investigations, several experimental studies have also been conducted to understand the effect of natural fracture of hydraulic fracture propagation. Wang et al. (2013) used semi-circular bending tests in synthetic hydrostone samples to assess the effects of pre-existing cemented fractures with different approach angles, cement strengths, and thickness on hydraulic fracture propagation. They found that the hydraulic fracture tends to cross the cemented fracture (strong or weak inclusions in the hydrostone) for a high approach angle and divert for low approach angle. Al Tammar (2018) investigated experimentally the behavior of a hydraulic fracture as it approaches a cemented natural fracture. They showed that hydraulic fractures tend to cross thick natural fractures filled with a softer material than the host rock and get diverted for harder materials.

The investigation of the interaction of hydraulic and natural fracture has also been conducted using numerical modeling using different numerical methods. The commonly used numerical methods for simulation of interaction between hydraulic fractures with natural fracture include Finite Element Method (Xu et al., 2019), Extended Finite Element Method(Taleghani and Olson, 2009; Shi et al., 2017), Boundary Element Method (Zhang and Jeffrey, 2006, 2008; Zhang et al., 2007; Kresse and Weng, 2013; Wu and Olson, 2015;

Xu et al., 2015; McClure et al., 2016), Peridynamics (Ouchi et. al, 2017; Agrawal et. al, 2019), and DEM (Yoon et al., 2014, 2015, 2016; Damjanac and Cundall, 2016). The most popular method among them to model hydraulic fracture at field scale is BEM as in the formulation it has fewer unknowns compared to other methods and is computationally less expensive.

In this work, we have used the Displacement Discontinuity Method, a special direct Boundary Element Method for developing a computationally efficient simulator for modeling hydraulic fracture growth in the presence of natural fractures and transport of proppant in the created fracture network.

1.4.3 Displacement Discontinuity Method

The solution of linear elasticity problems is of great interest in many engineering applications. It has played a principal role in the investigation of the hydraulic fracturing process in the oil and gas industry. Numerical methods for solving elasticity problems can be divided into two types: the domain methods and the boundary methods. Finite difference and finite element methods constitute the first type, and the boundary element methods (BEMs), such as the displacement discontinuity method, are the second type. In the case of BEMs, discretization is required only on the boundary of the domain and this reduces the dimension of the problem by one. Furthermore, the method is inherently more accurate than domain methods because the exploited analytical solution is valid throughout the domain. These qualities make BEMs more attractive especially for infinite, homogeneous elastic domains (Shou, 1993).

The displacement discontinuity method appears to be first used by Hackett (1959) to consider an excavation in a tabular ore deposit. He proposed that the distribution of stresses and displacements around a long thin excavation could be represented by the two-

dimensional elastic solution for a line crack in an infinite body. In 1976, Crouch employed Neuber-Papkovich potential functions corresponding to point dislocations and developed the two-dimensional displacement discontinuity method with the assumption that the stress at the center of a straight crack represents the average stress over the element. This generalized displacement discontinuity method expressed the stresses and displacements in an elastic solid in terms of normal and shear displacement discontinuities over a line segment. Crawford and Curran (1982) developed a higher-order DDM that improves the accuracy of the method by not assuming constant stress over the entire element. Shou (1993) extended Crouch's model to give a higher-order, fully three-dimensional displacement discontinuity method. Dong et al. (2001) proposed a quadratic displacement discontinuity method having collocation points inside each element and increased the accuracy of numerical implementation. Olson (2004) demonstrated that a pseudo-3D approach can give a reasonable level of accuracy for constant height fractures (no discretization in the fracture height direction). The drawback is the lack of information about the stress intensity factor at the top or bottom, which limits the method to constant height fractures. In 2012, Olson and Wu presented a model that incorporates fracture deformation using pseudo-3D DDM coupled with non-Newtonian fluid flow in the wellbore and fractures. Wu and Olson (2015a) developed a model that simulates complex fracture geometry in three dimensions with high computational efficiency by use of a simplified 3-D DDM method. In this approach, they ignore any stress component involving dip-slip shear in the formulation, thereby improving the efficiency of the computation. The major drawback of this technique is its simplification of considering only one element in the height direction. This can limit the model's usage in proppant transport applications as width profile information along the fracture height direction may not be available.

1.5 ORGANIZATION OF THE DISSERTATION

The dissertation is divided into seven chapters. Chapter 2 presents the formulation of the hydraulic fracturing model using a fully 3-D displacement discontinuity formulation and provides validation results from the model. Chapters 3 and 4 focus on the investigation of hydraulic fracture natural fracture interaction for field-scale cases. Chapter 5 presents a novel technique for generating a discrete fracture network that represents the in-situ natural fracture distribution based on field data. Chapter 6 discusses the Adaptive Integral Method, a novel mathematical technique developed to speed up the displacement discontinuity method.

In Chapter 2, our new fracture propagation model is described in detail. The formulation of the geomechanics using three-dimensional displacement discontinuity method, fluid mechanics and the proppant transport model using the finite difference method is presented. The coupling algorithm to get the solution of the pressure and width inside the created fracture network is discussed. In this chapter, we also present the methodology used to capture the interaction of hydraulic fractures and natural fractures. Two different kinds of interactions that are captured in the model are discussed. These interactions describe the cases when hydraulic fracture comes in direct contact with the natural fracture and when it does not directly intersect with the natural fracture. A novel technique, local linearization method, to reduce the number of iterations for reaching the solution is also presented. Finally, the validation of the model using PKN and Sneddon's solution is shown.

In Chapter 3, we focus on the interaction of hydraulic fractures and natural fractures for field-scale cases. The effect of natural fracture properties (natural fracture length, orientation, and height) on the geometry of the created fracture network is shown. The interaction of natural fractures with hydraulic fractures in three-dimension is discussed.

The objective of Chapter 4 is to investigate the transport of proppant in fracture networks. Two scenarios are discussed, transport of proppant for the interaction of hydraulic fracture with natural fracture and interaction of growing hydraulic fracture with a bedding plane. The effect of proppant size on the transport of proppant in fracture networks is also presented.

Chapter 5 discussed a novel technique of synthetic coring for generating discrete fracture networks based on core data. This investigation is based on the data from the Hydraulic Fracturing Test Site #1 project. First, we present the description of the core, based on visualization of the core data in three-dimensions. Later, the data is used to create a DFN using the synthetic coring technique. The developed simulator is used for creating a fracture network in the generated DFN, and the results obtained are compared with the field data.

Chapter 6 focuses on a novel technique, Extended Adaptive Integral Method, to speed up the simulations and reduce the computational complexity of the Displacement discontinuity method which arises from the dense nature of the created coefficient matrix. The formulation of the method for the three-dimensional DDM method is presented and its accuracy is verified. A sample case with 3000 fracture elements is simulated and the reduction in computation complexity is discussed.

Finally, Chapter 7 presents the conclusions of the research and provides recommendations for future research.

Chapter 2: Model Description and Verification

2.1 INTRODUCTION

Hydraulic fracturing is the primary method used for producing hydrocarbon from ultra-low permeability reservoirs economically. To optimize the hydraulic fracturing process, it is essential to understand the growth behavior of fractures and correctly estimate the geometry of created fractures. Numerical simulators are often used to estimate the geometry of created fractures based on the fracturing parameters (injection rate, injection volume, etc.) and reservoir properties. In simulators, the fracture geometry is typically assumed to be bi-wing and planar to reduce the computational effort typically required for solving field-scale problems.

Recently, several investigations have shown that hydraulic fracturing can result in the formation of fracture networks due to their interaction with natural fractures (Raterman et al., 2017; Gale et al., 2018). Hence, there is a need for a simulator that can handle the growth of hydraulic fractures in naturally fractured formations and can account for the complex geometry of the hydraulic fractures, as observed in the field. In this chapter, we present a hydraulic fracturing model and a simulator, Multi-Frac-NF, that can handle the interaction of hydraulic fractures with natural fractures and generate non-planar fractures in a computationally efficient manner. The objective of this chapter is to describe the governing equations associated with the problem and the algorithm used in the model to obtain the solution. At the end of this chapter, we present the validation of the model using two different validation example solutions.

2.2 MODEL DESCRIPTION

Hydraulic fracturing is a multi-physics process that involves solving the solid mechanics of fracture propagation in the reservoir and solving the fluid mechanics of the

fracturing fluid flowing inside the fracture in a coupled manner. The fracturing fluid exerts normal stresses on the surface of the fracture and leads to its opening. This opening, in turn, increases the permeability of the fracture and allows the fracturing fluid to flow. In order to model this fluid-solid interaction, two types of numerical methods are typically used: domain-type and boundary-type methods. These methods differ from each other in the way they solve the solid mechanics problem. The domain-type method solves the solid mechanics in the domain of the problem (examples of these methods are finite element/volume/difference methods). In the case of hydraulic fracture modeling, the domain of the problem is the reservoir; therefore, the entire reservoir needs to be discretized to obtain the solution. The boundary-type method (an example of this method is the Boundary Element Method, BEM) requires only the boundary of the domain (the surface of the created fracture) to be discretized. As the volume-to-surface ratio of crack problems is much larger than one, the number of discretized elements in the domain-type method is much higher than in the boundary-type method. Therefore, compared to the domain-type methods, less computational operations and memory are needed for boundary-type methods to obtain the same level of accuracy. In addition, for domain-type methods, it is difficult to mesh cracks with complex geometries where multiple fractures are intersecting and creating fracture networks. These reasons make boundary-type methods the preferred choice for solving field-scale hydraulic fracturing problems that include the interaction of hydraulic fractures with natural fractures (Kresse and Weng, 2013; Wu and Olson, 2015a; Mcclure and Kang, 2017).

In the model presented in this chapter, the geomechanics of the problem is solved using a displacement discontinuity method (DDM). DDM is a special type of Boundary Element Method designed for solving crack problems. The fluid mechanics for fluid flow in the fracture networks in the model is solved using the Finite Difference Method. As the

fracturing fluid is modeled inside the fracture network, only the volume of the fracture needs to be discretized. The two problems are solved in a coupled manner to get the distribution of fracture width and pressure in the fracture network. In addition, the model can capture the interaction of hydraulic fracture with natural fractures. This can result in the formation of fracture networks with multiple branches. The model allows these fracture branches to grow simultaneously, and their growth is based on the stress intensity factor at the fracture tips. The propagation direction of the fracture tips is determined using the maximum circumferential stress criterion and accounts for the interaction of the growing hydraulic fracture with all other fractures in the model. The model is developed with the purpose of simulating field-scale problems and understanding the behavior of fracture growth in naturally fractured formations. As field-scale problems can be computationally expensive, a novel technique called the local-linearization method that efficiently solves the coupled problem is also discussed.

The following subsections describe the formulation and solution of the geomechanics and fluid mechanics of the problem in detail.

2.2.1 Geomechanics

In the model, fractures are treated as a discontinuity in an infinite, isotropic, homogenous, and linear elastic medium. Each fracture is represented by two disconnected surfaces joined only at the tip of the fracture. As the two surfaces of the fracture are disconnected, they can have different displacements relative to each other.

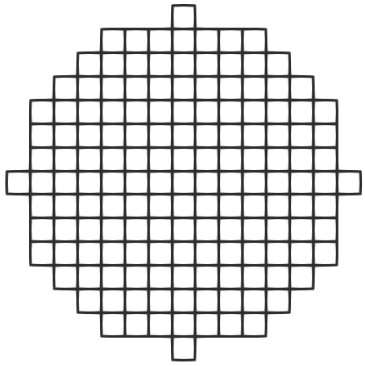

Figure 2.1: A discretized radial fracture in the model. Each small rectangle represents a discretized element in the model.

The relative displacement of one fracture surface to the other represents the opening and shearing of the fractures. This relative displacement results because of the stresses that are acting on the surface of the fracture. These stresses are due to the in-situ stresses in the reservoir, the fracturing fluid pressure acting on the surface of the fracture, and the stress shadow from nearby fractures. In the model, the displacement is solved using a fully three-dimensional displacement discontinuity method (DDM) (Crouch and Starfield, 1983; Shou, 1993). DDM is a special case of the direct boundary element method. The surface of the fracture in the model is discretized into two-dimensional rectangular grid elements of uniform size (see Figure 2.1). Each discretized element is composed of two surfaces S^+ and S^-, representing the two surfaces of the fracture. Each discretized fracture surface element is characterized by three displacement discontinuities, defined as the relative displacement of one fracture surface (S^+) to the other (S^-) along the local x, y, and z-direction with respect to the element (see Figure 2.2). In the model, it is assumed that the displacements and the tractions (stresses acting on the surface) are constant over each discretized element. The next subsection describes details of the DDM method.

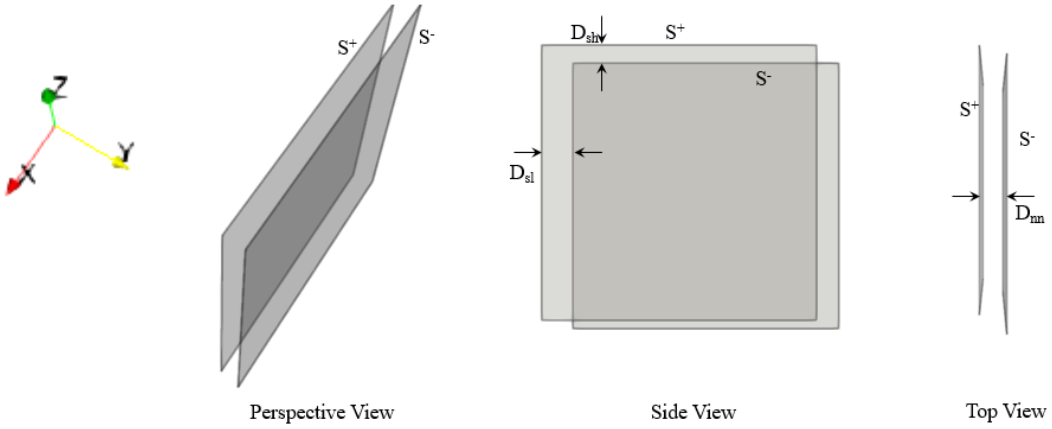

Figure 2.2: A single discretized fracture element with fracture surfaces S^+ and S^- shown at three different views. As shown, D_{sl}, D_{sh}, and D_{nn} are the relative displacement of one fracture surface to the other in local x-direction, y-direction, and z-direction respectively.

2.2.1.1 Displacement Discontinuity Method

The displacement discontinuity method gives the relationship between the displacement and boundary stresses based on Somigliana's formula (Shou, 1993):

$$u_j(\xi) = \int_S U_{ij}(\xi,\eta)t_i(\eta)dS(\eta) - \int_S T_{ij}(\xi,\eta)u_i(\eta)dS(\eta) \qquad (2.1a)$$

$$\sigma_{jk}(\xi) = \int_S D_{ijk}(\xi,\eta)t_i(\eta)dS(\eta) - \int_S E_{ijk}(\xi,\eta)u_i(\eta)dS(\eta) \qquad (2.1b)$$

where $u_j(\xi)$ and $\sigma_{jk}(\xi)$ are the displacement and stresses at point ξ. $t_i(\eta)$, and $u_i(\eta)$ are the traction and the displacement over the boundary surface of the region. $U_{ij}(\xi,\eta)$, $T_{ij}(\xi,\eta)$, $D_{ijk}(\xi,\eta)$, and $E_{ijk}(\xi,\eta)$ are tensor fields representing the influence coefficients that establish a relationship between the effect of a concentrated force at point η on traction and displacement at point ξ, and S is the surface of the region. As the solution of the problem is difficult to obtain analytically for fracture networks, the problem is solved

numerically. After discretization and using DDM, we get a linear relationship between the displacement discontinuities of all the discretized elements in the model and the stresses acting on them. The final form of the system of linear equations describing the relationship between all of the grid elements of the fracture surface is shown below:

$$\begin{bmatrix} A_{11} & . & A_{1,n-1} & A_{1,3n} \\ . & . & . & . \\ . & . & . & . \\ . & . & . & . \\ . & . & . & . \\ . & . & . & . \\ . & . & . & . \\ A_{3n-1,1} & . & . & A_{3n-1,3n} \\ A_{3n,1} & . & A_{3n,3n-1} & A_{3n,3n} \end{bmatrix} \begin{vmatrix} D_{x1} \\ . \\ D_{xn} \\ D_{y1} \\ . \\ D_{yn} \\ D_{z1} \\ . \\ D_{zn} \end{vmatrix} = \begin{vmatrix} \sigma_{x1} \\ . \\ \sigma_{xn} \\ \sigma_{y1} \\ . \\ \sigma_{yn} \\ \sigma_{z1} \\ . \\ \sigma_{zn} \end{vmatrix} \tag{2.2}$$

where A is the coefficient of the influence matrix, σ is the resultant stress acting on the surface of elements. D_x, D_y, and D_z are the displacement discontinuities in the x, y, and z directions, and n is the total number of elements in the model. In DDM, the influence coefficients are only a function of the location of the discretized elements. The methodology to get the influence matrix from the location of the discretized elements is described in detail in the appendix (see section 2.5.2) of this chapter. As every fracture element influences every other fracture element, the influence matrix is dense. Figure 2.3 shows the sparsity pattern of the DDM matrix for the sample case shown. As the matrix is dense, the number of operations needed for solving the system of equations follows $O(N^2)$ for iterative methods and $O(N^3)$ for direct inversion methods. Hence, for $O(N^2)$ time complexity algorithms, if the size of the problem doubles, the computational operations required to solve the problem quadruples. For DDM, the size of the matrix is smaller compared to Finite Element/Volume (FEM/FVM) based models for similar problems, as

the reservoir does not need to be discretized. Although the DDM matrix is a dense matrix (most of the elements of the matrix are non-zero), compared to FEM/FVM, it still requires less computational operations and memory to obtain the same level of accuracy (Wu, 2014).

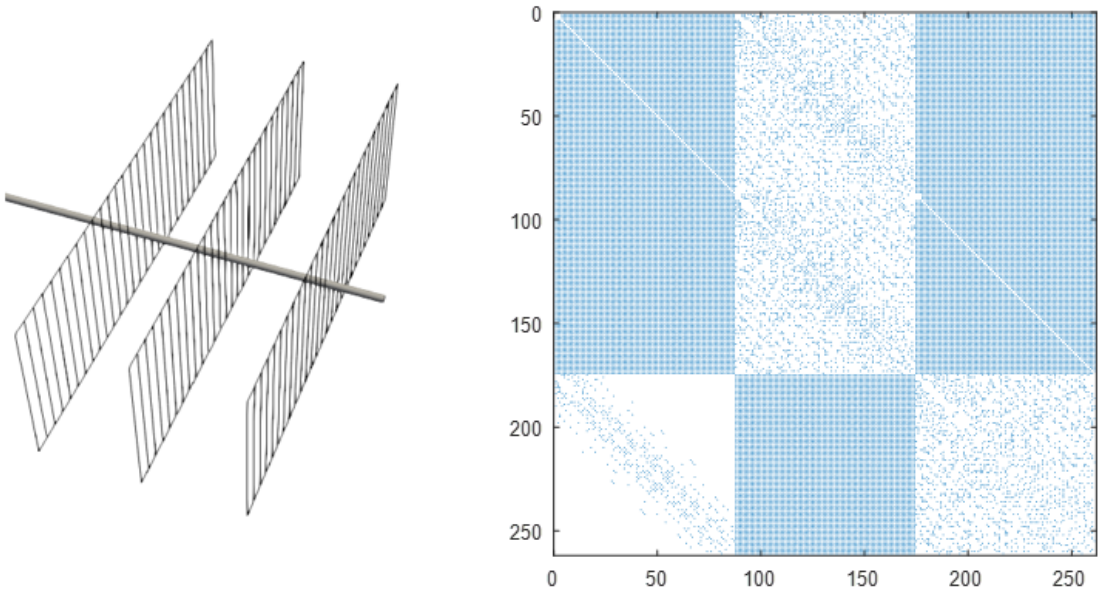

Figure 2.3: The figure on the right shows the sparsity pattern of the created matrix for the case shown on the left. Each pixel in the sparsity pattern, if colored, represents a non-zero element in the influence matrix. If the pixel is white, then it represents a zero value. The sparsity pattern is for a case where three planar fractures are propagating parallel to each other from a horizontal wellbore. Each fracture has 29 elements in this case.

In the model, all the fracture elements in the simulation, preexisting and propagating, are considered to be in a single domain, and hence the influence coefficients generated and used in the influence matrix account for all the fractures in the problem while defining the relationship between the displacement discontinuity and stresses. This allows the model to capture the effect of stress interference between all existing fracture elements

without any explicit effort. As the entire domain is solved at each iteration, the influence of the growth of the fracture from the current pumping stage on previous stages is also captured implicitly.

2.2.1.2 Fracture Propagation Criterion

In the model, the fracture propagates based on the Mode I stress intensity factor calculated at the fracture tips. If the mode I stress intensity at the fracture tip is greater than a critical stress intensity of the reservoir material, then the fracture is allowed to grow. The mode I stress intensity factor is determined from the normal displacement discontinuities of the crack tip using the following equation (Olson, 1991; Sheibani and Olson, 2013):

$$K_I = \frac{0.806 D_n E \sqrt{\pi}}{4(1-\nu^2)\sqrt{2a}} \tag{2.3}$$

where D_n and D_s are normal and shear displacement discontinuities at the tip, E is Young's modulus, ν is Poisson's ratio, and a is the half-length of the element. At each time step, K_I at all the four edges of the element is calculated for determining the direction of fracture growth (see Figure 2.4). Each discretized element has four possible directions for propagation in the model (top, bottom, front, and back) as the fracture plane can grow in four directions from a rectangular element based on the mode I stress intensity. If the element already has a neighboring element associated with any of its edges, those edges are not considered for fracture growth calculations. The relative location of elements in each fracture in the model is stored in a two-dimensional matrix. This allows the connectivity of elements in the fracture network to be efficiently stored and to avoid adding more than one element at the same location.

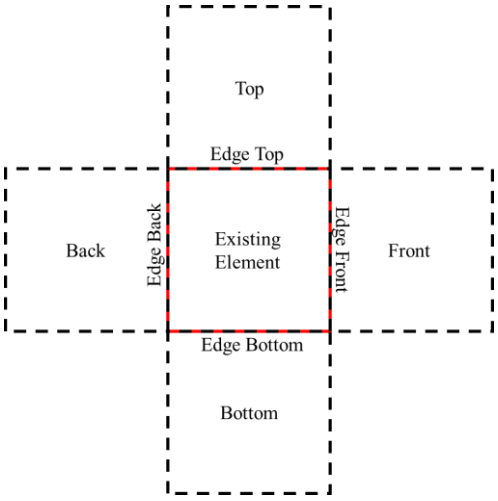

Figure 2.4: The neighboring elements of the tip element are stored in a two-dimensional matrix. The fracture tips can grow from the four edges in the corresponding direction.

2.2.1.3 Determination of Direction of Fracture Propagation

In the model, after determining the fracture propagation based on the stress intensity at the fracture tip, the direction of the fracture tip propagation is determined. Each tip of the fracture can propagate independently. The direction of propagation of the fracture tip is determined using the maximum circumferential stress criterion (Erdogan and Sih, 1963). According to the criterion, the fracture tip propagates in the direction perpendicular to the maximum tensile stress (see Figure 2.5). Hence the fracture grows along the maximum stress direction. The direction of propagation of the fracture is found from the solution of the following equation (Erdogan and Sih, 1963):

$$K_I sin\theta + K_{II}(3cos\theta - 1) = 0 \tag{2.4}$$

where K_I and K_{II} are the mode I and mode II intensity at the fracture tip, respectively, and θ is the direction of propagation of the fracture with respect to the original fracture direction.

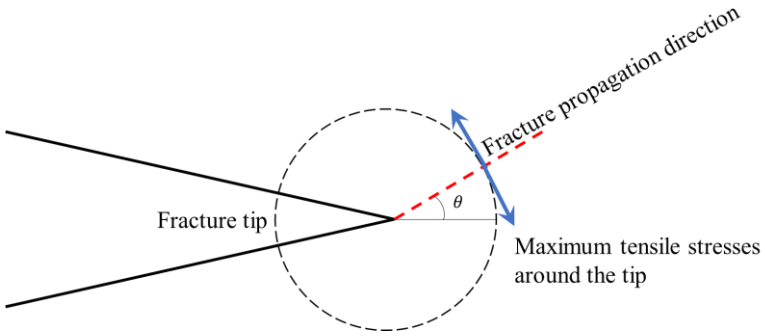

Figure 2.5: According to the maximum circumferential stress criterion, the fracture propagates (red line) perpendicular to the maximum tensile stress direction (blue arrows).

The mode II stress intensity factor is determined from the shear displacement discontinuities (D_{sh}) of the crack tip from the following equation (Sheibani and Olson, 2013):

$$K_{II} = \frac{0.806 D_{sh} E \sqrt{\pi}}{4(1-\nu^2)\sqrt{2a}} \tag{2.5}$$

where D_{sh} are the shear displacement discontinuities at the tip in the horizontal plane, E is Young's modulus, ν is Poisson's ratio, and a is the half-length of the element.

2.2.1.4 Three-Dimensional Non-Planar Fracture Growth

In the model, a hydraulic fracture with multiple DDM elements (discretized elements) along the height of the fracture is allowed to assume a non-planar geometry. As explained in the previous section, the fracture propagation direction during propagation is determined using the maximum circumferential stress criterion. Each fracture element along the height direction can experience different stresses and can have different turning angles according to the maximum circumferential stress criterion. This can result in branching of the fracture (see Figure 2.6) as the fracture is propagating. In order to avoid

this behavior, the model forces the tip of the trailing DDM elements to turn at an angle that is equal to the leading fracture element (see Figure 2.7). This allows us to simulate smooth turning of fractures with multiple elements along the height direction without fracture branching as is observed in the case shown in Figure 2.7.

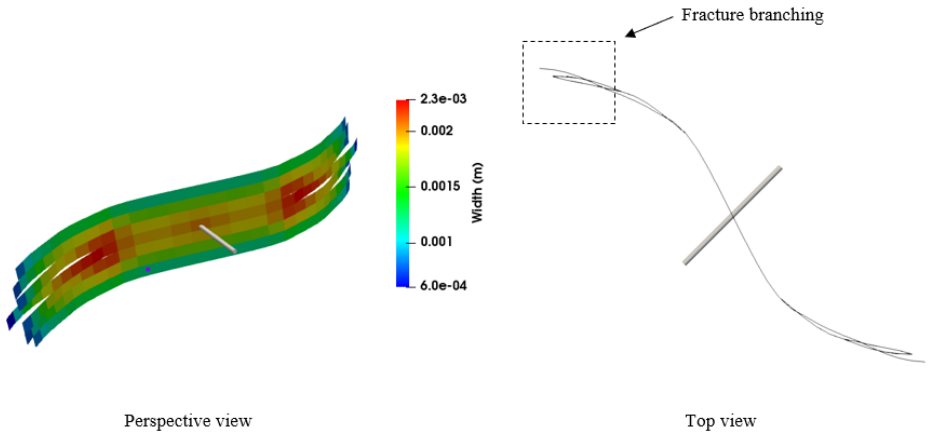

Figure 2.6: Figure showing branching of fracture due to turning of fracture tips at different angles along the height of the fracture.

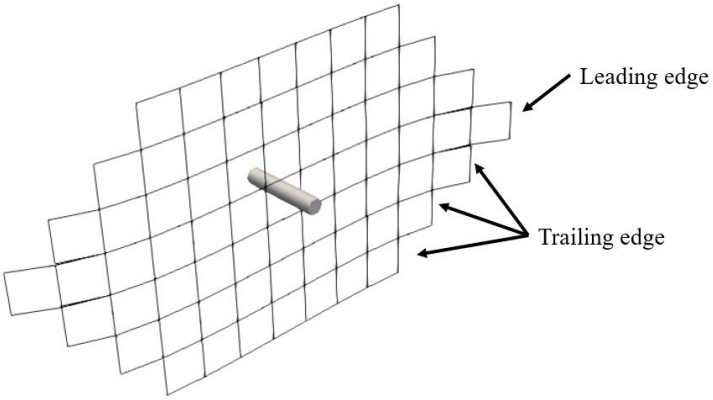

Figure 2.7: Figure showing leading and trailing elements of the fracture tip in a propagating fracture.

2.2.2 Modeling Fracture Containment

The simulator allows us to model contained fractures and captures the effect of stress and critical stress intensity variation and formation stress intensity variation. This is done by storing the distribution of the stresses and critical stress intensity factor in a two-dimensional matrix form. The matrix represents the properties of the plane of the fracture. This provides us the flexibility to have variations in these properties along both the height of the fracture and the length of the fracture. Each entry in the matrix represents the properties associated with one grid cell of the model. In the following figure, an example of contained fracture growth due to a high stress layer is shown.

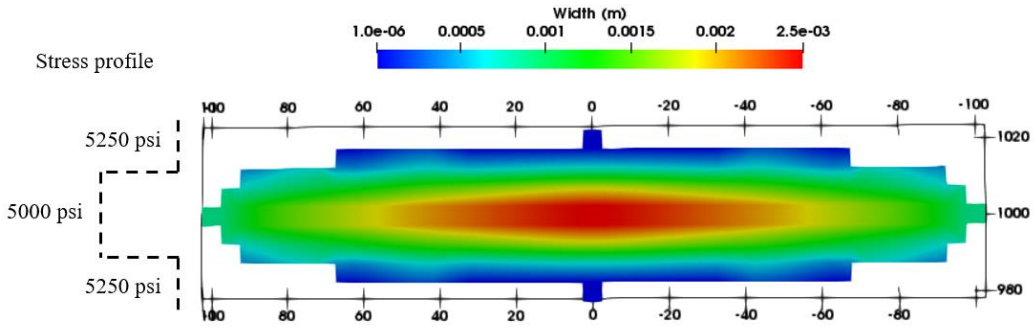

Figure 2.8: Figure shows the width profile of a contained fracture. High stress layer with a stress contrast of 250 psi is used both above and below the wellbore location to symmetrically contain the fracture.

It can be observed that the fracture has a smaller width in the high stress layers. This reduces the stress intensity at the fracture tip elements in the high stress layers and thus, the fracture preferably grows in the low stress layer.

2.2.3 Fluid Flow in Fracture Networks

In the model, the fluid flow inside the fracture is described using the Reynolds lubrication equation (Adachi et al., 2007; Yew and Weng, 2014). The governing equation

for flow respects conservation of mass and conservation of momentum and is given as follows:

$$\frac{\partial(\rho \mathrm{v})}{\partial \mathrm{t}} = \nabla \cdot \left(\frac{k\rho A}{\mu} \nabla P\right) - \dot{m}_{leakoff} + \dot{m}_{inj} \tag{2.6}$$

where ρ is the density of the slurry, v is the volume of the fracture, k is fracture permeability, A is cross-sectional area of flow, P is fluid pressure, μ is fluid viscosity, $\dot{m}_{leakoff}$ is the rate at which fluid leaks off into the formation, and $\dot{m}_{inj}$ is the fluid injection rate.

The fracture is considered to be completely filled with fluid. The fluid inside the fracture is assumed to be single-phase, slightly compressible, and isothermal. The discretized elements of the fractures are treated as thin rectangular slits of constant width with the permeability computed as follows:

$$k = \frac{w^2}{12} \tag{2.7}$$

where w is the width of the fracture element, and k is the fracture permeability.

2.2.4 Leak-off calculation

As the fracturing fluid pressure is higher than the reservoir pressure, the fracturing fluid leaks off into the formation. As the fracturing fluid moves into the pore space of the formation, it compresses the reservoir fluid. In addition, if the fracturing fluid contains suspended material which is larger in size compared to the pore size of the reservoir, a cake gets formed on the surface of the fracture that can resist the leak-off of the fluid.

The loss of fluid into the matrix from the fracture is calculated using Carter's leak-off equation (Howard and Fast, 1957). Carter's equation captures the resistance to fluid-loss by three mechanisms: 1) the resistance due to compression of the reservoir fluid, 2) the resistance due to flow of fluid inside the invaded zone as per Darcy's flow, and 3) the resistance of the flow of fluid due to filter-cake formation on the surface of the fracture due to deposition of suspended material from the fracturing fluid on the fracture surface in the form of a cake (see Figure 2.9). The simulator captures the effect of all three mechanisms for the calculation of leak-off volume. The relationship between the leak-off of the fracturing fluid and the resistance to flow due to these mechanisms is established using equation 2.8. The coefficients used in equation 2.8 associated with resistance related to the different mechanisms are found using equation 2.9, 2.10, and 2.11 (Howard and Fast,1970 ; Schechter, 1992):

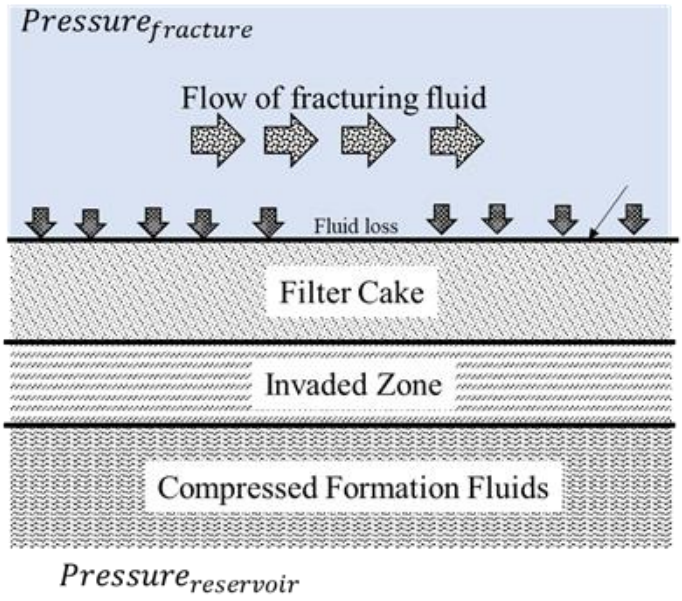

Figure 2.9: Fluid loss from a fracture into the reservoir (Schechter, 1992)

$$u_N\sqrt{t} == \frac{-\frac{1}{C_c} + \sqrt{\frac{1}{C_c^2} + \frac{4}{C_v^2} + \frac{4}{C_f}}}{2\left(\frac{1}{C_v^2} + \frac{1}{C_w^2}\right)} = C \tag{2.8}$$

$$C_c = \alpha_c \Delta P = \sqrt{\frac{\phi K_{fl} k}{\pi \mu_f}} \Delta P \tag{2.9}$$

$$C_v = \alpha_v \Delta P = \sqrt{\frac{\phi k}{2\mu_f}} (\Delta P)^{\frac{1}{2}} \tag{2.10}$$

$$C_w = \alpha_w \Delta P^{\frac{1}{2}} \tag{2.11}$$

where C_v is the viscous fluid-loss coefficient, C_c is the compressibility fluid-loss coefficient and C_w is the wall-building fluid-loss coefficient. u_N is the flux at the interface, and t is time. K_{fl} is the isothermal compressibility of the formation fluid, k is the formation permeability, μ_f is the viscosity of the formation fluid, ϕ is the porosity. ΔP is defined as the pressure difference between the fracturing fluid and the reservoir pressure. The reservoir pressure is known whereas the fracturing pressure is treated as an unknown in the simulator. In case the C_w is zero (no cake build-up scenario), the coefficient is removed from equation 2.8 while calculating C. Finally, the fluid leak-off flux rate is obtained using the following equation:

$$u_L = 2u_N = \frac{2C_l}{\sqrt{t - \tau(x)}} \tag{2.11}$$

where $\tau(x)$ is the time at which fracture element was created at location x, u_L is the flux rate.

2.2.5 Numerical Solution of Fluid Flow Inside Fracture Networks

In the simulator, equation 2.6 is solved using the finite difference method (FDM). The mesh created for the geomechanics solution is reused for the FDM, and the central difference scheme is used for discretization. Each element in the mesh can have 4 neighbors for planar fractures. In case the growing hydraulic fracture intersects with a natural fracture to create bi-furcation of the fracture tip, a new mesh is created for the natural fracture and stitched together with the growing hydraulic fracture mesh (see Figure 2.10). This is achieved by adding two additional neighbors to the intersecting elements. These two additional neighbors are accounted for while creating the FDM matrix to capture the exchange of fluid between the hydraulic fracture mesh and the natural fracture mesh. In the case when a growing hydraulic fracture intersects another existing hydraulic fracture the model stores this connection as a seventh neighbor and accounts for it during the generation of the FDM matrix.

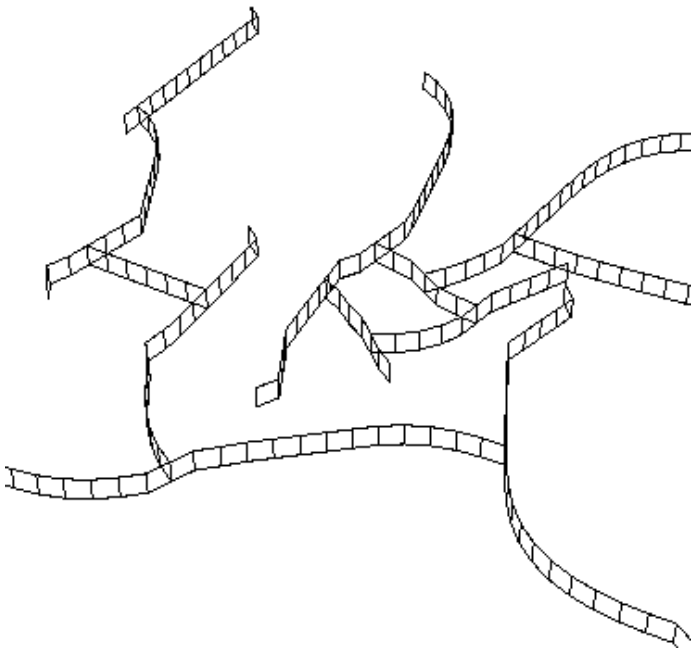

Figure 2.10: Multiple fluid flow meshes stitched together at their point of intersection to form a complex fracture network.

Each neighbor manifests as a non-diagonal entry in the fluid flow matrix solved for determining the pressure distribution inside the fracture. As the number of neighbors/intersections can not be determined in advance and results due to the interaction of the growing hydraulic fractures with natural fractures, the change in network connectivity is captured by creating the matrix on the fly. The simulator stores the relationship between neighbors in a list and uses the relationship to generate the matrix as per the created fracture network. Due to this unpredictability in the growth of the fracture the created fluid flow matrix is not strictly diagonal in natural, although it retains its sparsity. Figure 2.11 shows the sparsity pattern of the FDM matrix for the described case.

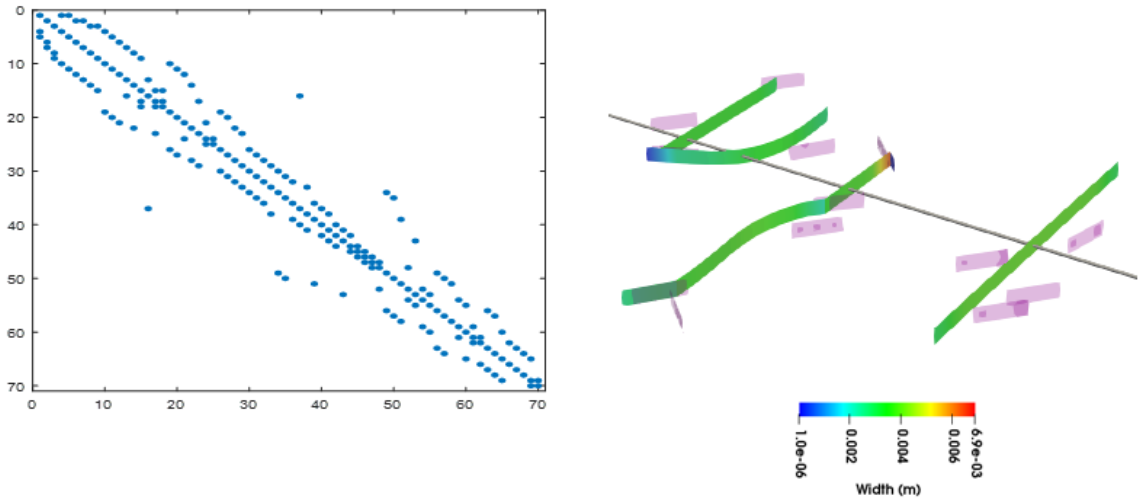

Figure 2.11: The sparsity pattern of the created fluid flow matrix is shown (left) along with the shape of the created fracture (right). Each blue colored pixel in the sparsity pattern shows a non-zero element, whereas the white pixels show zero values. It can be seen that the matrix is not strictly diagonal in nature and is influenced by the connectivity of the created fracture network. The colors on the right figure show the width of the fracture. The pink-colored elements are natural fractures. There are 70 discretized fracture elements in the simulation.

2.2.6 Proppant Transport

Our model can simulate proppant flow in fracture networks. The proppant particles are assumed to be in suspension in the fracturing fluid. The relative motion of the proppant particles with respect to the fluid is considered to be due to two reasons: 1) settling due to the difference in the densities of the fluid and the proppant and 2) retardation due to the slip of the proppant particles relative to the fluid.

The proppant distribution inside the fracture is governed by the scalar transport equation (Eq. 2.12). A no-flux boundary condition is used for the fluid and the proppant on the fracture surface. The following equation describes the transport of proppant in the model:

$$\frac{d(cw)}{dt} = \nabla.(vc) \tag{2.12}$$

where w is the fracture width, c is proppant concentration, and v is the proppant velocity.

The resultant velocity of the proppant particles is obtained by vectorial summation of the proppant velocity due to the motion of the base fluid (retardation), and the velocity due to settling.

The retardation factor of proppant particles is defined as follows:

$$\beta = \frac{\vec{v}_{proppant}}{\vec{v}_{fluid}}$$

where $\vec{v}_{proppant}$ is the velocity of the proppant particles and the $\vec{v}_{fluid}$ is the velocity of the fluid.

The retardation factor for proppant transport is determined using the correlation developed by Blyton et al. (2015) shown below:

$$\beta = 1 \qquad \frac{d}{w} < 0.4 \tag{2.13a}$$

$$\beta = -1.73\left(\frac{d}{w}\right)^3 + 2.45\left(\frac{d}{w}\right)^2 - 0.69\left(\frac{d}{w}\right) \qquad 0.4 \leq \frac{d}{w} \leq 0.95 \tag{2.13b}$$

$$\beta = -21.45\left(\frac{d}{w}\right) + 21.45 \qquad \frac{d}{w} \geq 0.95 \tag{2.13c}$$

where β is the retardation factor, d is the proppant diameter, and w is the width of the fracture.

The settling velocity of the proppant particles is calculated based on the correlations developed by Gadde et al. (2004). The settling velocity is a function of the Reynolds number of the flowing slurry, concentration of the proppant particles, and the width of the particles. The correlations used are as follows:

$$v_{settling} = U_{stokes} * f(Re) * f(c) * f(w) \tag{2.14a}$$

$$U_{stokes} = \frac{1}{18}\left(\rho_{sand} - \rho_{fluid}\right)\frac{d^2}{\mu}g \tag{2.14b}$$

where ρ_{sand} is the density of the proppant particles, ρ_{fluid} is the density of the fracturing fluid, d is the diameter of the proppant particles, μ is the viscosity of the fracturing slurry, and g is the acceleration due to gravity in consistent units. $v_{settling}$ is the settling velocity of the proppant particles and U_{stokes} is the Stokes settling velocity calculated as shown in equation 2.14b.

The functions $f(Re)$, $f(c)$, and $f(w)$ are given by the following equations:

$$f(Re) = 0.3736 * \frac{(\mu)^{.57}}{\rho_f^{0.29}\left(\rho_p - \rho_f\right)^{0.29} * d^{0.86}} \tag{2.14c}$$

$$f(c) = 1 - 4.8c + 8.8c^2 - 5.9c^3 \tag{2.14d}$$

$$f(w) = 1 - 1.563\left(\frac{d}{w}\right) + 0.563\left(\frac{d}{w}\right)^2 \tag{2.14e}$$

where c is the concentration of the proppant particles.

The mesh used for fluid flow is also used for solving the proppant transport equation. Hence the complex geometry of the created mesh is accounted for while solving proppant transport equation. A fully implicit finite difference method with an upwinding scheme is used to solve the proppant transport equation (Eq. 2.12). The upwinding scheme uses a solution sensitive finite difference stencil and takes into account the direction of the flow in creating the finite difference matrix. The scheme is used for convection dominant flow with suppressed diffusion effects. In addition, the CFL criterion is respected in the model, and the time steps used in the simulation are accordingly limited based on the criterion. The CFL condition is a necessary condition for convergence while numerically solving the proppant transport equation, which is a hyperbolic partial differential equation. According to the CFL criterion,

$$C = \frac{u\Delta t}{\Delta x} \leq 1 \tag{2.15}$$

where u is the velocity of the proppant particles, Δx is the size of the mesh used in the simulation and Δt is the timestep used in the simulation. C is called the Courant number.

The presence of the suspended solid particles (proppant) in the slurry changes its rheological behavior. This change in rheology can influence the geometry of the created fracture geometry. In order to capture the rheological behavior of the slurry correctly, the slurry is modeled as a Power-law fluid, and the effective viscosity of the fluid is given by the following relationship:

$$\mu_{eff} = K\left(\frac{du}{dy}\right)^{n-1} \tag{2.16}$$

where K is the flow consistency index, $\frac{du}{dy}$ is the shear rate or the velocity gradient perpendicular to the plane of shear, and n is the flow behavior index.

To accurately capture the effect of proppant particles on the rheology of the slurry, correlations developed by Shah (1993) are incorporated in the model. The correlations provide a relationship between the concentration of proppant particles and the rheological parameters of the slurry as follows:

$$n_s = n' e^{Bc} \tag{2.17a}$$

$$K_s = K' e^{Qc} \tag{2.17b}$$

where n_s is the dimensionless flow behavior index of slurry, K_s is the flow consistency index of slurry, n' is the dimensionless flow behavior of the clean fluid, K' is the flow consistency index of the clean fluid, B and Q are coefficients given by Shah (1993), and c is the volumetric concentration of proppant particles.

2.2.7 Natural Fracture Interaction

In the model, the natural fractures are defined as a collection of rectangular elements connected to each other. Each rectangular element can act as a location for a hydraulic fracture to intersect with the natural fracture. This provides the flexibility to create an intersection at any location on the natural fracture. Each natural fracture is allowed to have a different set of properties, thus allowing a realistic distribution of properties for the natural fracture population. Two different kinds of interactions of growing hydraulic fractures with a natural fracture are captured in the model: 1) the interaction with natural fractures when they come in direct contact with the growing hydraulic fracture, and 2) the interaction of hydraulic fractures with natural fractures not

in direct contact with the hydraulic fracture. The two types of interactions and the approaches to capture these interactions in the model are discussed in the following sections.

2.2.7.1 Interaction of Hydraulic Fractures with Intersecting Natural Fractures

Whenever a hydraulic fracture grows, a new DDM element is added to the network. As the new element is added, its intersection with natural fracture elements in its vicinity is checked. If a natural fracture intersects with the new hydraulic fracture element, the stresses at the boundary of the process zone on the natural fracture plane are calculated using equation 2.19 (Wu and Olson, 2014). The stresses are then transformed into the plane of the intersected natural fracture, and the Mohr-Coulomb criterion is applied to predict its slippage (see Figure 2.12):

$$\begin{Bmatrix}\sigma_{xx}\\ \sigma_{yy}\\ \tau_{xy}\end{Bmatrix} = \begin{Bmatrix}S_{Hmax}\\ S_{Hmin}\\ 0\end{Bmatrix} - \frac{K_I}{\sqrt{(2\pi r)}}\begin{Bmatrix} cos\left(\frac{\theta}{2}\right)\left[1 - sin\left(\frac{\theta}{2}\right)sin\left(\frac{3\theta}{2}\right)\right]\\ cos\left(\frac{\theta}{2}\right)\left[1 + sin\left(\frac{\theta}{2}\right)sin\left(\frac{3\theta}{2}\right)\right]\\ sin\left(\frac{\theta}{2}\right)cos\left(\frac{\theta}{2}\right)cos\left(\frac{3\theta}{2}\right)\end{Bmatrix} - \frac{K_{II}}{\sqrt{(2\pi r)}}\begin{Bmatrix} -sin\left(\frac{\theta}{2}\right)\left[2 + cos\left(\frac{\theta}{2}\right)cos\left(\frac{3\theta}{2}\right)\right]\\ sin\left(\frac{\theta}{2}\right)cos\left(\frac{\theta}{2}\right)cos\left(\frac{3\theta}{2}\right)]\\ cos\left(\frac{\theta}{2}\right)\left[1 - sin\left(\frac{\theta}{2}\right)sin\left(\frac{3\theta}{2}\right)\right]\end{Bmatrix} \quad (2.19)$$

where σ_{xx}, σ_{yy}, and τ_{xy} represents the normal stress in x-direction, normal stress in y-direction, and shear stress, respectively. K_I is the mode I stress intensity factor, K_{II} is the mode II stress, r is the distance from the tip of the fracture, θ is the angle from the tip of the fracture.

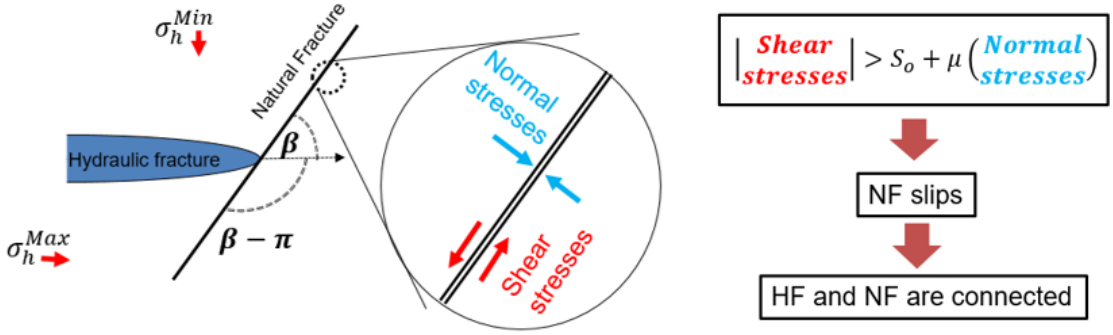

Figure 2.12: The process of natural fracture slip using the Mohr-Coulomb criterion and its connection to the fracture network

In the case of the natural fracture's failure, as the stress concentration cannot cross through the slipped natural fracture, it is assumed that the fracture tip is blunted and the failed natural fracture element is converted into a DDM element. Also, the fluid flow mesh of the natural fracture is stitched with the existing hydraulic fracture fluid mesh. Figure 2.13 shows the propagation of a hydraulic fracture in the presence of natural fractures.

In some cases, the natural fracture may not geometrically fall at the edge of the growing hydraulic fracture when they intersect. In such situations, a failed natural fracture element (DDM element on the natural fracture) may cross the growing hydraulic fracture DDM element. This situation can lead to instability as the calculated influence coefficients are singular in nature. This results in an ill-conditioned DDM influence matrix. In order to avoid such a situation, the natural fracture element is shifted to obtain a stable intersection with the existing hydraulic fracture element before it is included in the DDM matrix. The natural fracture DDM element is placed such that an edge to edge contact of the hydraulic fracture DDM element with the natural fracture DDM element is maintained. This results in higher stability for the model even for randomly distributed natural fractures locations.

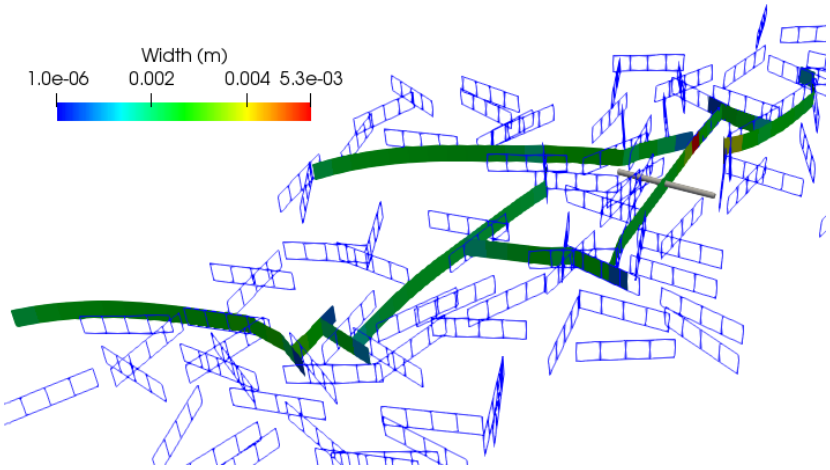

Figure 2.13: The figure shows the generated fracture network from a propagating fracture in a naturally fractured formation. The wire mesh elements depict pre-existing natural fractures.

2.2.7.2 Interaction of Hydraulic Fractures with non-Intersecting Natural Fractures

Growing hydraulic fractures can change the stresses in their vicinity. This change in stresses can lead to slippage (shear failure) of natural fractures. In order to capture the shear failure of the disconnected natural fractures, stresses are calculated on the natural fracture elements at each time step using DDM. In the model, the natural fractures are included as geometrical shapes at the start of the simulation. As the hydraulic fracture propagates, only the natural fractures in a critical radius are included in the simulation for carrying out stress calculations. As the system of equations is linear, the principle of superposition is used to get the total stress acting on the natural fracture plane. In order to do this, the DDM equations are transformed into a global coordinate system. Details about the calculation of stresses acting on a natural fracture are presented in the appendix of this chapter (see section 2.5.2). The calculated stresses are then used to predict the slippage of natural fractures using the Mohr-Coulomb criterion. In the case of slippage, a possible

microseismic event is registered and stored. These failed natural fractures are not treated as DDM elements, and their displacement discontinuities are not calculated using the DDM matrix. Each discretized element of the natural fracture can slip separately and hence the model is able to capture the partial failure of natural fractures. Figure 2.14 shows the microseismic events simulated for a radially growing fracture using the model.

In this work, an extension of the model has also been developed (see section 3.3) that accounts for the frictional forces acting on the slipped but hydraulically disconnected natural fractures. In the extended model, the slipped natural fractures are treated as DDM elements and their displacement discontinuity is accurately solved at each iteration. Although, this leads to a significant increase in the computational cost and the extended model is not recommended for use in large scale problems with thousands of natural fractures.

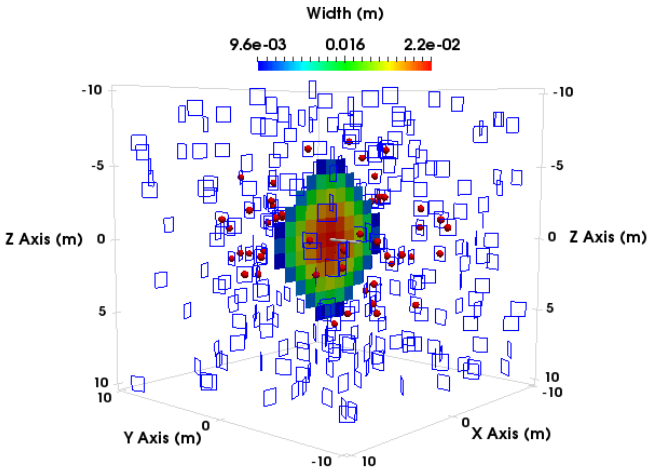

Figure 2.14: Microseismic signature due to shear failure of natural fracture elements in the vicinity of a radially growing fracture. The red dots represent registered microseismic events. The blue squares are natural fractures.

2.2.8 Convergence Scheme

In the previous section, the methodology to obtain the solution of geomechanics, fluid mechanics and proppant transport has been explained in detail. In this section, the overall solution algorithm is presented.

2.2.8.1 Solution Algorithm

Figure 2.15 shows the overall algorithm followed for each time step to get the final fracture geometry, the displacement discontinuity of fracture elements, and the stresses acting on the fracture network. As the fluid mechanics equation (Eq 2.13) is non-linear in the normal displacement discontinuity (width of the fracture) of the elements, iterative algorithms are used to find a solution.

The solution strategy used in the model consists of three loops that control the behavior of the model. The innermost loop is the convergence loop (shown in green color in Figure 2.15) that ensures that the solution of the coupled DDM and the fluid flow equations is converged within a specified tolerance (shown in Figure 2.15 with green color). The solution of the system of equations is achieved using the Picard iterative algorithm with relaxation. Both the fracturing fluid pressure (normal stresses) and the fracture width (normal displacement discontinuity) are relaxed in the method i.e. only a fraction of the new solution is used to update the current solution as shown in the following equation:

$$P_{i+1} = P_i(r) + P_{solution}(1 - r) \tag{2.20}$$

$$W_{i+1} = W_i(1 - r) + W_{solution}(1 - r) \tag{2.21}$$

where P and W represent the fracturing fluid pressure and fracture width, r is the relaxation factor, the subscript i represents the iteration number, and the subscript $solution$ represents the solution of the system of equations obtained using the Picard algorithm.

Once the solution is converged using the Picard method, the width of each element in the fracture network is checked for its magnitude. If any element has a negative value of the width, the solution is rejected, as a negative value of width is not physical. The problem is reinitialized to the last time step values and is relaxed (value of the relaxation factor is increased) and solved again to achieve a solution, if possible, with non-negative values. Hence, the model adaptively relaxes itself based on the iterative solutions obtained. Relaxation reduces the rate of convergence of the problem and increases the iterations required to reach the solution. In case a converged solution with a positive value of width is not obtained and the relaxation factor goes above a threshold value, the elements with negative width are treated as closed elements with a fixed zero width (or close to zero width). The DDM coefficients in the DDM influence matrix associated with the closed elements that affect the displacement discontinuity of other elements are set to zero. This allows us to include extra information about the closed nature of these elements into the solution mathematically. This ensures that the zero-width element does not influence the opening or shearing of other fracture elements in the simulation. The problem is reinitialized to the last time step values and solved again.

After a converged solution with a positive value of width at each element in the network is reached, the network is checked for propagation of each tip using the propagation criterion explained in Section 2.2.1.2. The algorithm goes into the propagation loop (shown in blue in Figure 2.15). If the propagation criterion is satisfied (see 2.2.1.2), an element is added to the tips that have sufficient stress intensity according to the propagation criterion. If at least one element is added to the fracture network, the geometry

of the problem changes. In this scenario, the values of the variables (width and pressure) in the problem are restored to the end of the previous time step, and it is solved again for the new geometry of the problem. The proppant transport equation is solved in each iteration after solving the fluid flow equation, as the velocity of the fluid inside the fracture is used to calculate the velocity of the proppant. The changes in the rheology of the fluid due to a change in the concentration of proppant particles are updated after solving the proppant transport equation (as described in section 2.2.6). This ensures a tight coupling and captures the effect of proppant transport on the fracture growth correctly.

As the fracture network grows, the natural fractures present in the simulation can come in direct contact with the growing fractures. In this scenario, the crossing criterion discussed in Section 2.2.7.1 is used to predict whether the hydraulic fracture crosses the natural fracture or intersects it. If any natural fracture intersects the growing hydraulic fracture, then the natural fracture's fluid mesh is stitched with the hydraulic fracture mesh. As this merging of meshes changes the geometry of the problem, in the case of an intersection of hydraulic fractures with natural fractures, the variables of the problem are restored to the values corresponding to the end of the previous time step, and the problem is solved again.

As the solution of the system of equations progresses, the hydraulic fracture network approaches a final geometry that no longer changes, and the stress intensity at all the fracture tips are below the critical stress intensity of the formation. The converged solution of this geometry is stored as the final result obtained for the current time step and the algorithm continues to solve the problem for the next time step. This loop is called the time step loop and is shown in red in Figure 2.15. This continues until the fracture fluid pumping is completed.

The described algorithm, while more efficient compared to FVM/FEM, still requires significant computational power to run stage-scale simulations. This is because of the non-linearity of the problem arising from the fluid flow inside the fracture. In the following section, a novel algorithm to reduce the computational time is presented. The proposed algorithm uses a predictor step that solves a linearized form of the fluid flow equation and displacement discontinuity equation together to find an initial guess of the solution. The predicted solution is then used as an initial guess in an iterative method to solve the coupled problem. Results from a simulated case are presented to show the effectiveness of the new algorithm on increasing computational efficiency.

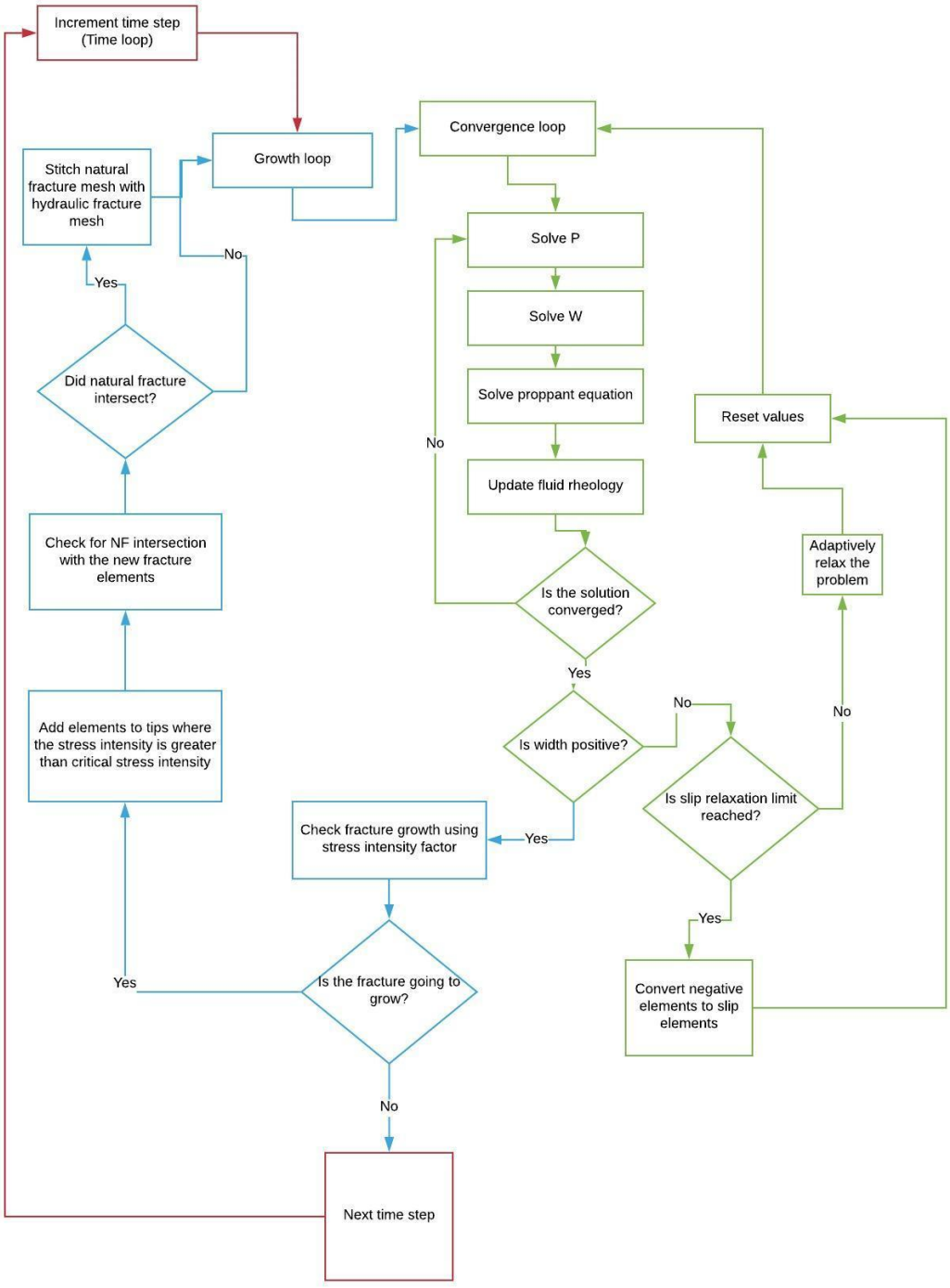

Figure 2.15: Algorithm used in the model to achieve a solution for each time step.

2.2.8.2 Local Linearization Method

The procedure described in the previous section to get a solution of the coupled DDM and fluid flow equations with changing fracture geometry can take several iterations, in some cases even thousands of iterations, before it converges to a final solution. Due to the fully populated nature of the coefficient matrix, these iterations require considerable time for achieving a solution. As this operation is repeated for each time step, the overall simulation (simulation of the full pumping period) can take up to several hours.

In order to reduce the number of iterations for each time step, we used an additional predictor step in the solution procedure (Figure 2.16). In the predictor step, the linearized form of the fluid flow equation is solved along with the displacement discontinuity equation using the direct substitution method to obtain an initial guess for the solution.

If the difference between the solutions of the system of equations between subsequent time steps is small, then the fluid flow equation can be linearized around the current solution using a Taylor series expansion. The steps required to get the linearized fluid flow equation is presented in an Appendix of this chapter (see section 2.5.1). Equation (2.19) gives the final form of the linearized equation:

$$\frac{d(\rho w_{k+1})}{dt} = \nabla \cdot \left(\frac{(3w_k^2 w_{k+1} - 2w_k^3)\rho}{12\mu} (\nabla \mathrm{P}_{\mathrm{k+1}}) \right) - \frac{\dot{m}_{leakoff}}{A_m} + \frac{\dot{m}_{inj}}{A_m} \tag{2.19}$$

where ρ is the density of the fracturing fluid, w is the width of the fracture, μ is the viscosity of the fluid, P is the pressure of the fracturing fluid, subscript k represents the previous time step known solution, $k+1$ represents the sought solution, $\dot{m}_{leakoff}$ is the leak-off mass rate, $\dot{m}_{inj}$ is the injection mass rate, A_m is the area of the mesh.

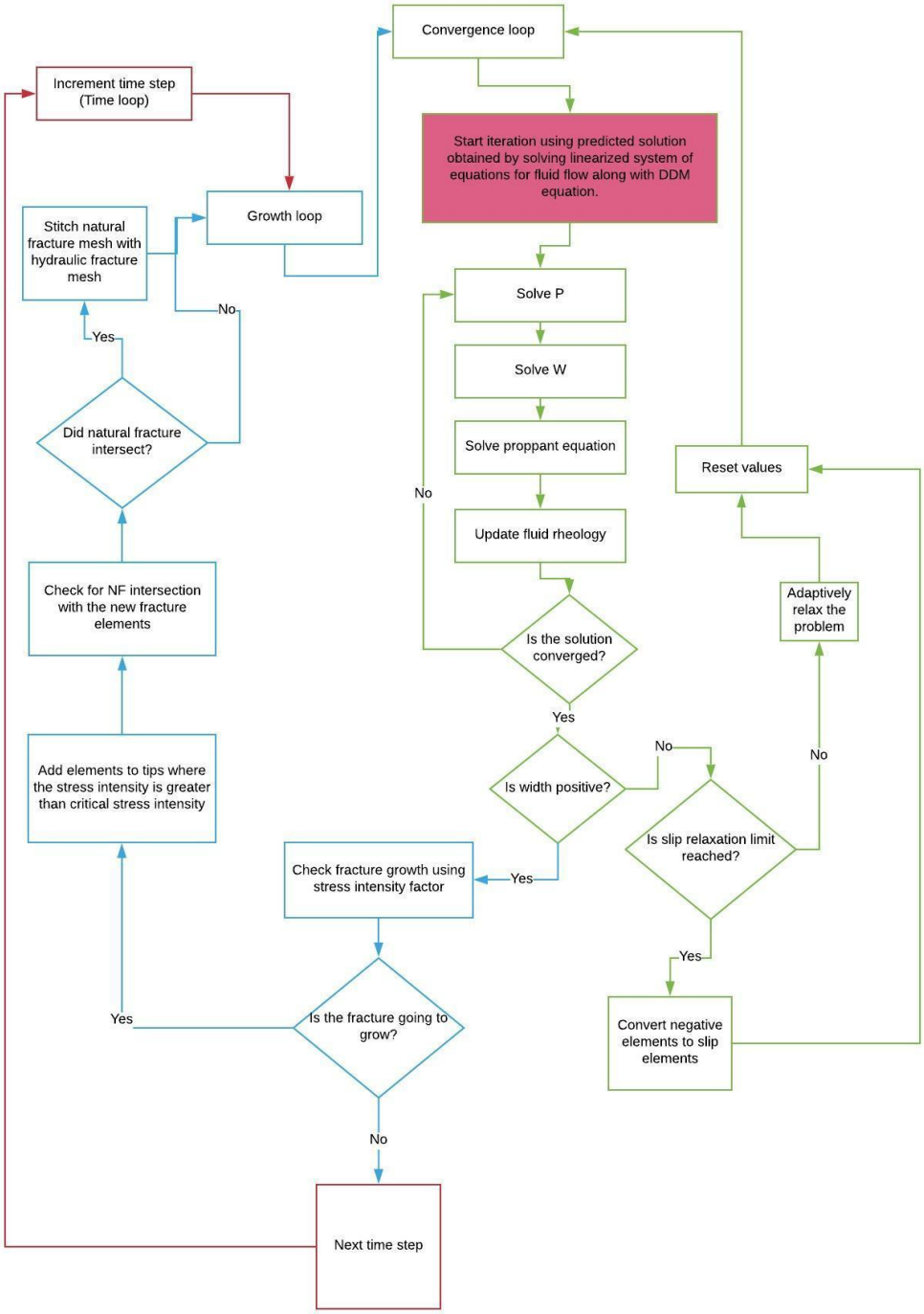

Figure 2.16: Algorithm of the iterative solution procedure with the “predictor” step. The change in the algorithm compared to the original algorithm is highlighted in pink.

The above equation is discretized using the finite difference method, and a linear formulation of the fluid flow equation is formed as shown below:

$$AP^{n+1} + Bw^{n+1} = C \tag{2.20}$$

where A, B, and C are constants.

This equation is solved simultaneously with the DDM equation to obtain the predicted solution. The predicted solution acts as an excellent starting point for the subsequent iterative procedure.

For comparing the effectiveness of the "predictor" algorithm, a simulation case is set up and compared against the previously discussed methodology. This section will focus on the effect of the predictor step on the rate of convergence and stability of the solution. The following parameters are used to setup the simulation case.

Property	**Value**	
Young's Modulus	2.50E+06	psi
Poisson's Ratio	0.25	
Minimum Horizontal Stress	5000	psi
Element Half Length	0.5	m
Injection Rate	1	bpm
Fluid Density	1000	kg/m^3
Fluid Viscosity	1	cP
Fluid Compressibility	2.20E+09	psi

Table 2.1: Input parameters for the simulated case

The fracture is allowed to grow radially in an infinite elastic medium. It is simulated as a vertical fracture originating from a horizontal wellbore. The grid element size is set at 1 meter in both length and height. Fracturing fluid is injected for 60 seconds, and the fracture grows up to a radius of 10 meters. Figure 2.17 shows the surface plot of the fracture depicting its final shape. In the simulated case, adaptive relaxation was not used in order to capture the effectiveness of the predictor step.

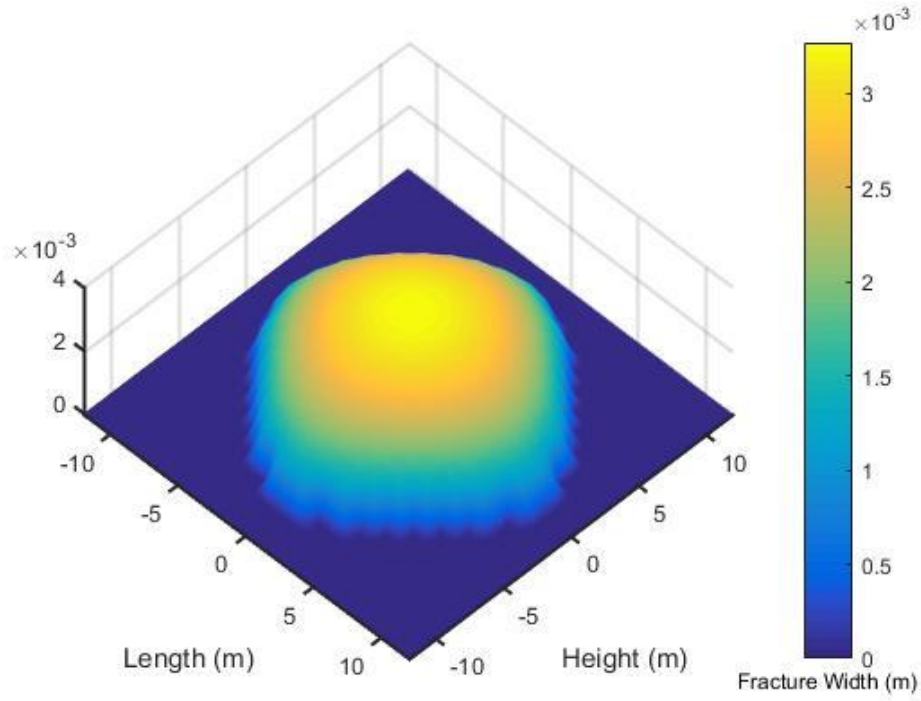

Figure 2.17: Width profile of the fracture at the end of injection

In Figure 2.18, the cumulative number of iterations required to achieve a converged solution as a function of the time step is shown. During the initial time steps of the simulation, the fracture grows rapidly, and the addition of elements to the fracture mesh is very frequent. Due to the finite size of the grid, the addition of each element can lead to a

significant change in the fracture volume especially when the fracture is small, in turn changing the solution significantly from the solution of the previous time step. Hence, there is little advantage of the algorithm during the early time period of the simulation. As the fracture grows, however, the frequency of addition of elements to the fracture starts to decrease, and we start to observe a reduction in the total number of iterations. A similar behavior is observed with the total simulation time as shown in Figure 2.19. As the number of elements in the DDM influence matrix grows by $9n^2$, where n is the number of elements, for large fractures, the addition of every element can increase the size of the solution matrix significantly. Hence, reducing iterations substantially reduces simulation time for larger fractures. This is seen in the quadratic behavior of the total simulation time required for obtaining a solution as a function of time step in Figure 2.19.

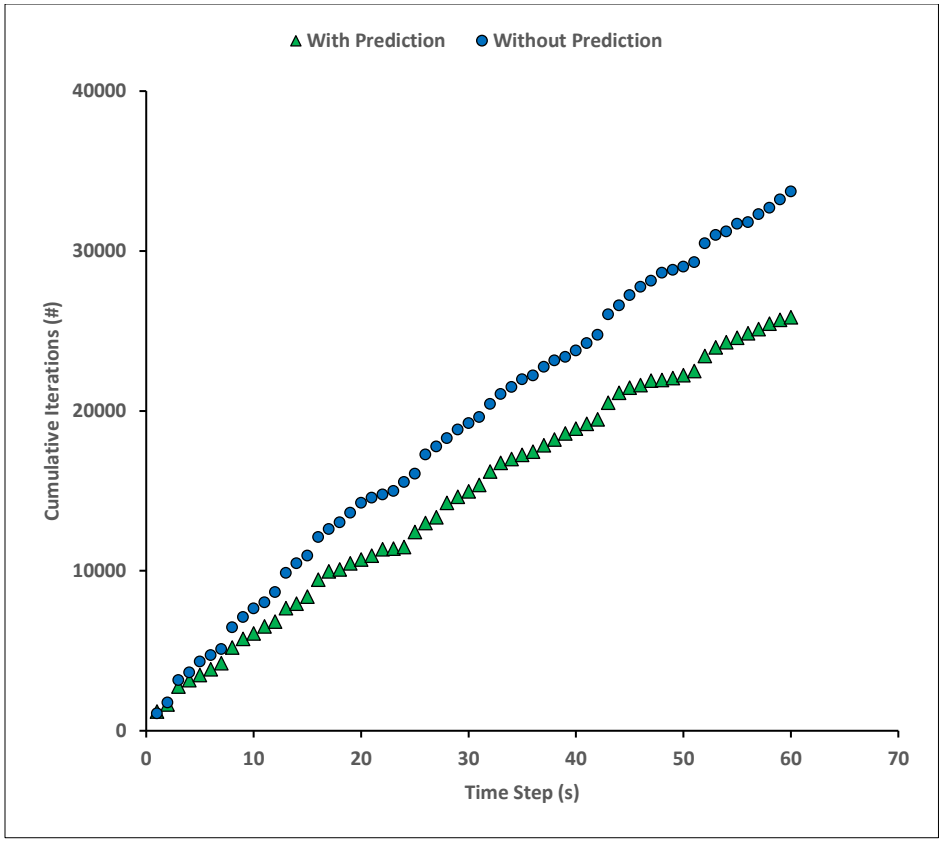

Figure 2.18: Effect of predictor step on the required number of cumulative iterations

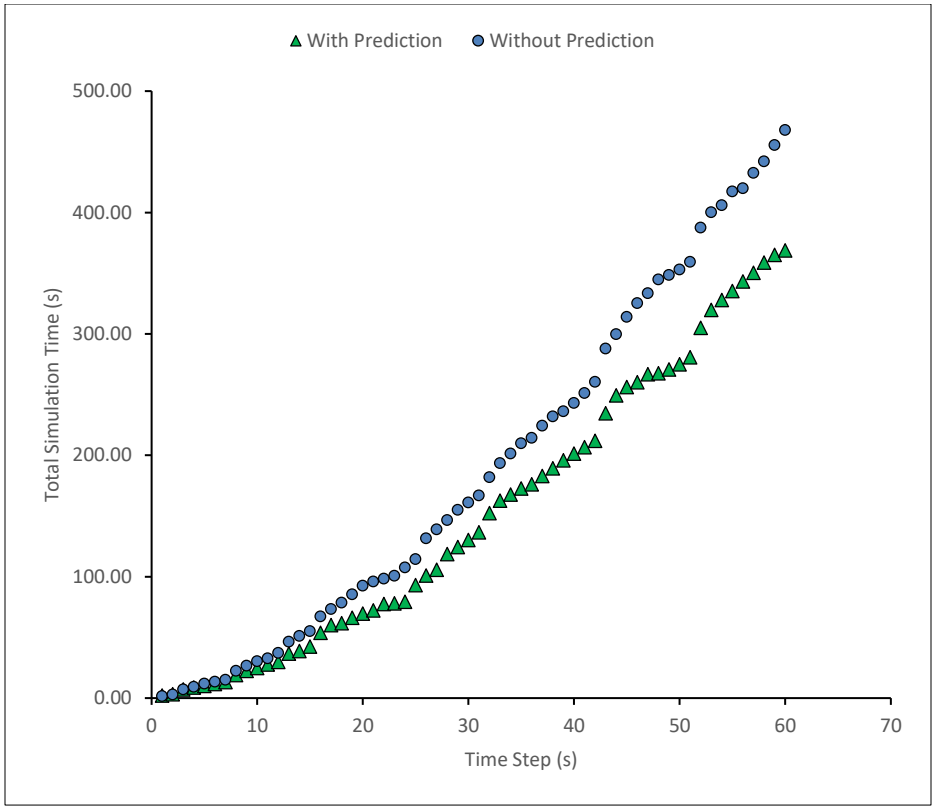

Figure 2.19: Effect of predictor step on the total simulation time required for the solution

The average percentage increase in the speed of convergence due to the new algorithm compared to the original iterative method is shown in Figure 2.20. The advantage in terms of average convergence speed when using the predictor step increases initially and then plateaus around 25 percent. When the speed increase for each time step is considered separately, an improvement of up to 93 percent is observed (Figure 2.21). It is also observed that in some time steps the speed decreases (up to 173% is observed in the investigated case).

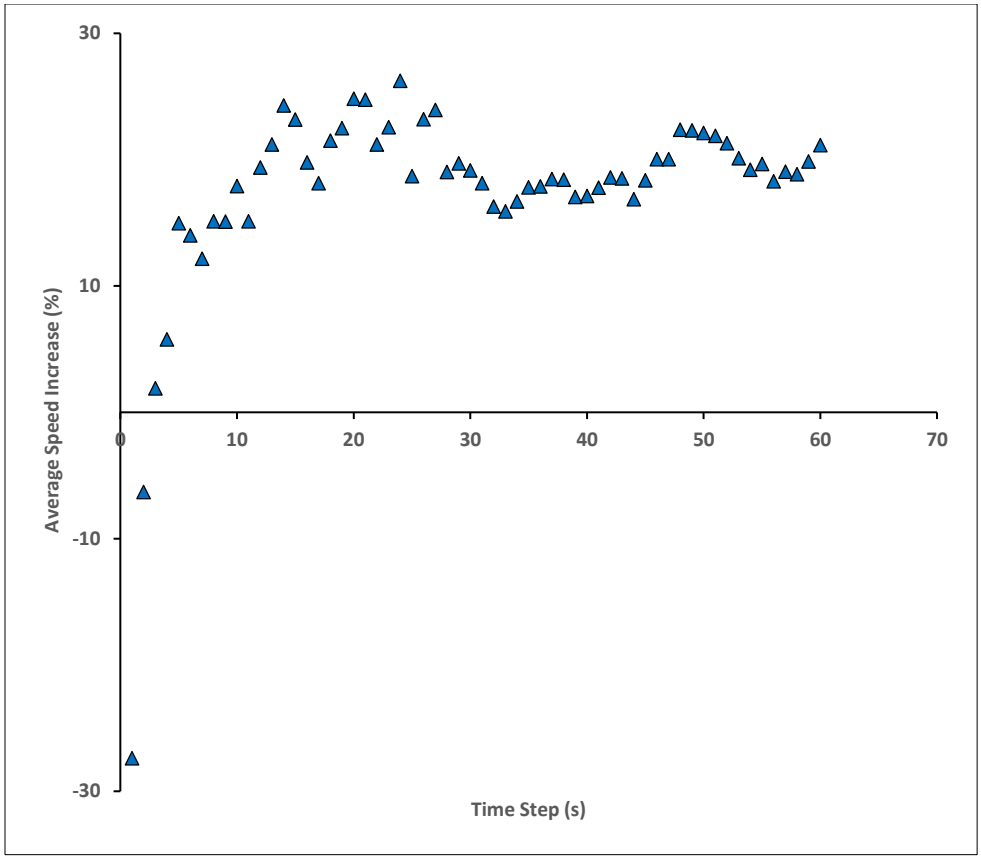

Figure 2.20: Percentage increase in the average simulation speed for the new algorithm compared to the original iterative method

This shows that the algorithm can result in a significant increase in performance if it is utilized in an appropriate case. As field case simulations have large fracture volumes and long pumping times, the use of this new algorithm can be very effective in improving the computational performance.

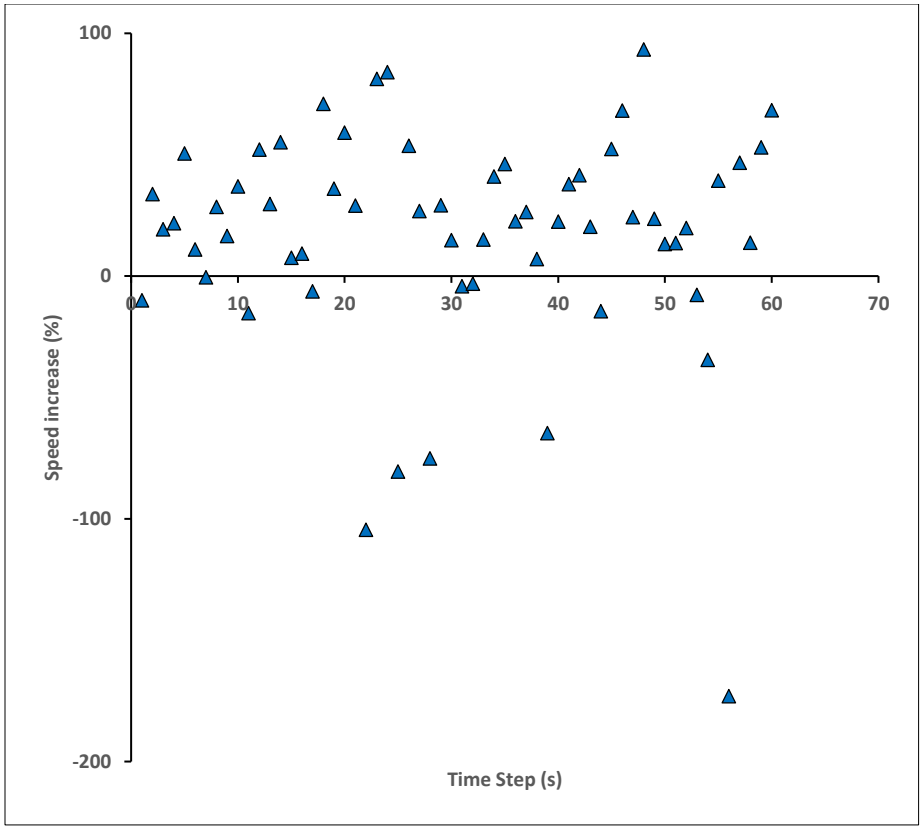

Figure 2.21: Percentage increase in the simulation speed for the new algorithm compared to the original iterative method

Figure 2.22 shows the effect of the predictor step on convergence. The graph shows the intermediate value of pressure during the iterative procedure in the wellbore between time steps 20 and 21. The new method results in a significant reduction in the fluctuation of the solution and increases stability. This allows the use of a larger relaxation factor in the iterative method without the increased risk of instability. Hence, the new algorithm not only reduces the number of iterations required for achieving the solution, but also allows the use of larger values of relaxation factors for faster convergence. Due to this, the

observed decrease in simulation time can be much higher than observed with the use of the new algorithm.

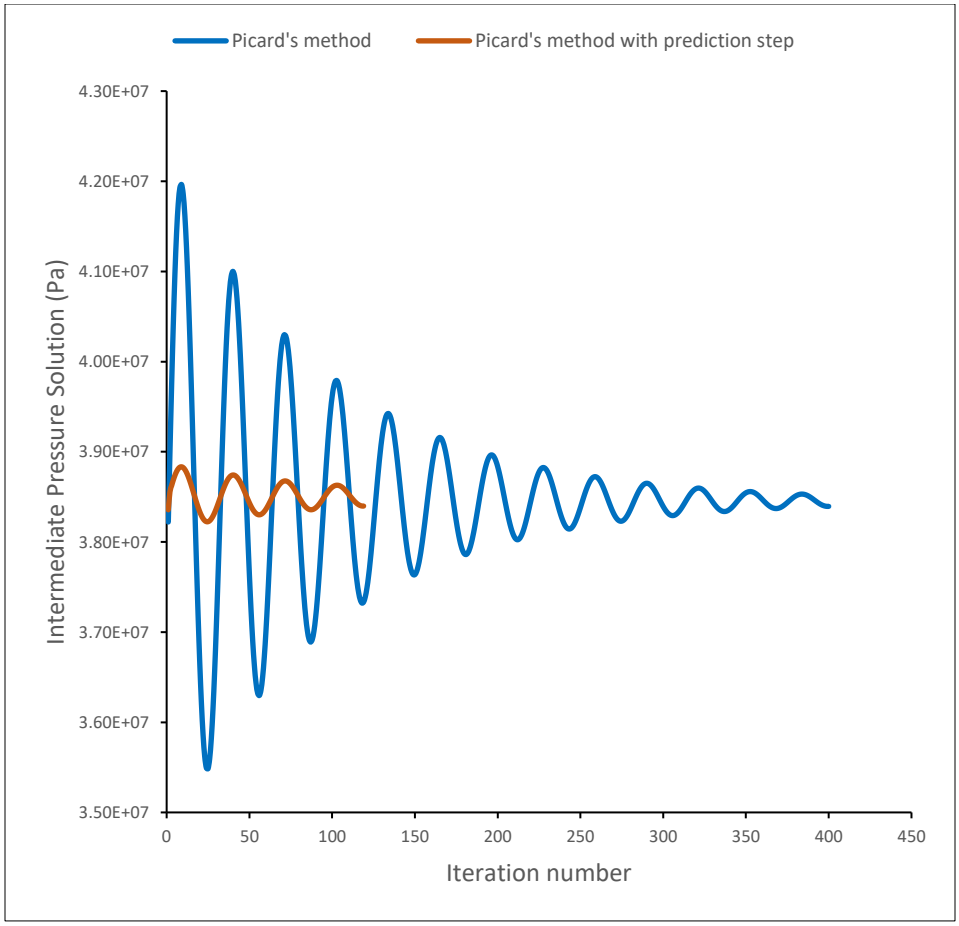

Figure 2.22: Comparison of oscillations in wellbore pressure during the iterative method

This section presents a new method for the solution of the fracture geomechanics and fluid flow interaction problem. In the simulated test case, we observed that the use of a predictor step can bring down the overall computation time required to model growing fractures using DDM on average by 25 percent. The new algorithm reduces the fluctuations in the solution during the iterative process which provides stability to the algorithm. This

allows the use of higher values of relaxation factors, leading to faster convergence. The method presented here provides a new approach to solve the coupled nonlinear system of equations-geomechanics and fluid flow-inside the fracture network.

2.3 VALIDATION

This section discusses two validation cases that have been used to evaluate the model.

2.3.1 Validation: Sneddon

This validation case compares the aperture obtained from the simulator with the aperture from Sneddon's equation for a static fracture at a constant pressure. The fracturing fluid is injected into the fracture and the fracture is allowed to propagate to a certain extent in the model. The injection of fracturing fluid is stopped and the model is solved for the next few time steps until the pressure inside the fracture is stabilized. In this state, the model is representing a shut-in condition in the field. The aperture of the fracture is extracted and compared with the aperture obtained from the Sneddon equation given as follows:

$$w(x) = \frac{2P_f x_f}{E'}\left(1 - \frac{x^2}{x_f^2}\right) \tag{2.21}$$

where x_f is the half-length of the fracture, P_f is the constant fracture pressure, E' is the plane strain Young's modulus, and x is the distance from the center of the fracture.

The following figure shows a comparison between the aperture obtained from the model and that from Sneddon's equation. It is observed that the solution follows a similar behavior as we get from the Sneddon equation, although there is a difference between the solutions, especially near the tip of the fracture. This is because the DDM element has a

single value of width for each element. Hence, near the tip, we observe that the width is equal to the width at the center of the tip element.

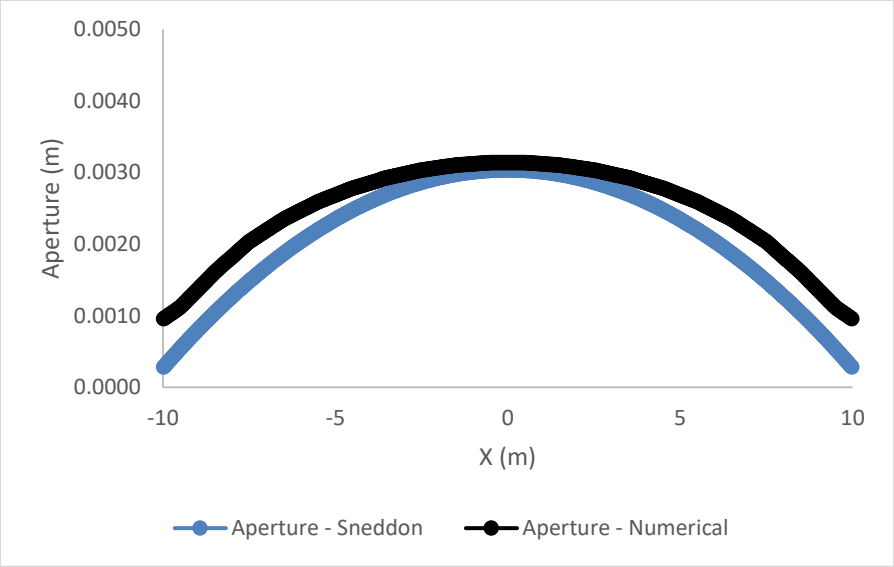

Figure 2.23: Comparison of the aperture of the simulated fracture with the Sneddon's analytical solution.

2.3.2 Validation: PKN Geometry

The PKN model describes the growth of a hydraulically driven fracture in a well-confined pay zone i.e. the stresses in the layers above and below the pay zone is sufficiently large to prevent height growth of the fracture. In the model, the fracture has a constant height and the model makes the plane strain assumption in the vertical plane. Hence, the fracture cross-section is elliptical in nature and the maximum width at any cross-section is proportional to the net pressure at the cross-section and is independent of width at any point of the fracture. Hence the fracture width is limited by the height of the fracture and is independent of the length of the fracture (see Figure 2.24). The geometry of the fracture and pressure at the injection point of the fracture are described by the following equations:

$$l_f = 0.524\left(\frac{E'q^3}{\mu_f h^4}\right)^{\frac{1}{5}} t^{\frac{4}{5}}$$

$$w_{max} = 3.04\left(\frac{\mu_f q^2}{E'h}\right)^{\frac{1}{5}} t^{\frac{1}{5}}$$

$$p_{net} = 1.52\left(\frac{E'^4 \mu_f q^2}{h^6}\right)^{\frac{1}{5}} t^{\frac{1}{5}}$$

where l_f is the half-length of the fracture, w_{max} is the width of the fracture at the wellbore, p_{net} is the pressure of the fracture at the wellbore, μ_f is the fluid viscosity, q is the injection rate, h is the height of the fracture,t is the time of injection, E' is the plane strain Young's modulus of the fracture. The units used in the above equation are SI.

The following parameters are used for the simulation:

Table 2.1: Properties used for PKN verification

Parameters	**Value**
Injection fluid viscosity	0.0005 cP
Injection Rate	0.05 m^3/sec
Young's Modulus	1.7235 x 10^{11} Pa
Poisson's Ratio	0.25
Height	10 m
Sh_{min}	34.47 MPa

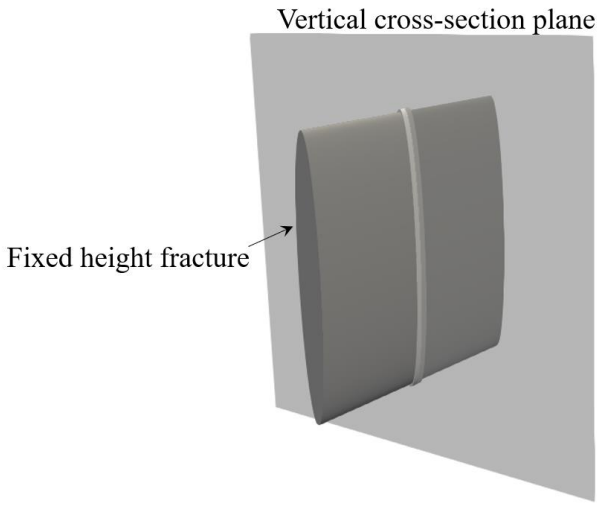

Figure 2.24: Vertical cross-section of the fracture. A plane strain assumption in the vertical plane is assumed in the PKN model. Hence, the geometry of the fracture of each vertical plane is independent of the rest of the fracture and is a function of only the height of the fracture.

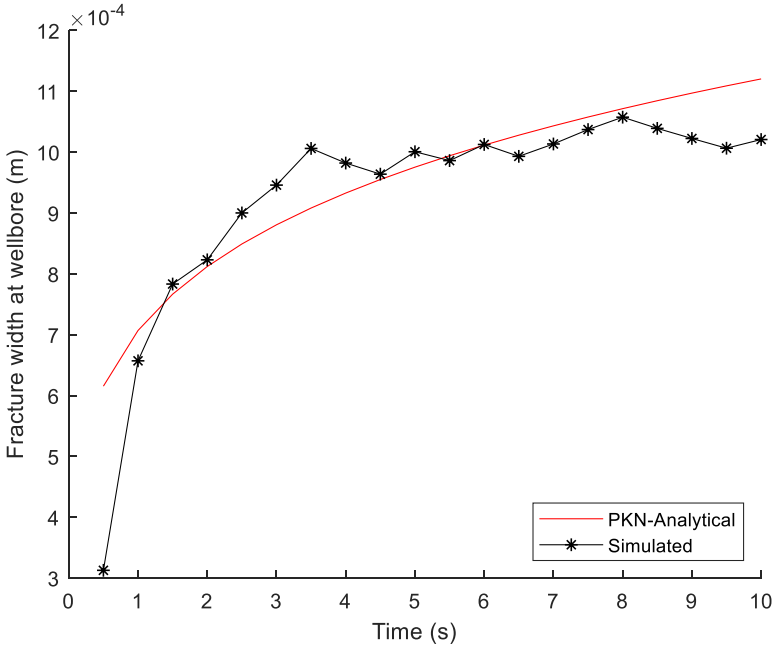

Figure 2.25: Comparison of the width of the fracture at the injection point simulated using our model with the width using the PKN model.

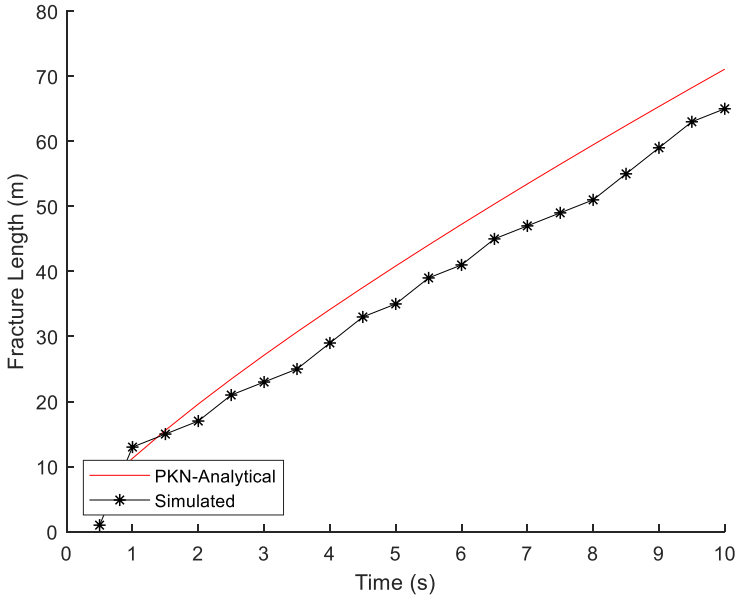

Figure 2.26: Comparison of the length of a simulated fracture simulated using our model with the length using the PKN model.

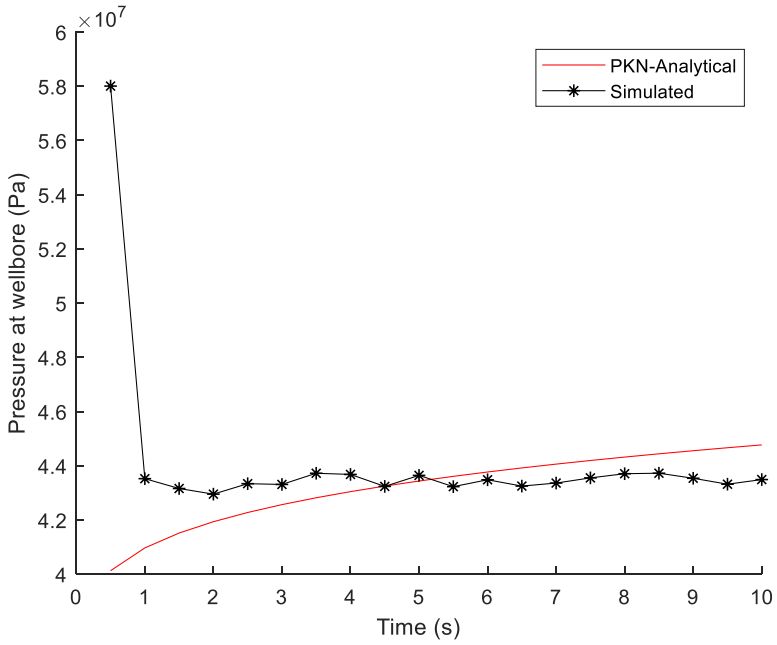

Figure 2.27: Comparison of the pressure at the injection point of a simulated fracture using our model with the pressure using the PKN model.

It is observed that the fracture length and the width compare well and follow a similar trend as is obtained from the PKN solution. The oscillations observed in the simulation results are due to the discrete growth of fractures in the simulation. This discrete behavior is because of the element size used in the simulation. In addition, the low compressibility of the fluid used in the simulation also contributes to the observed oscillations.

The pressure solution, although similar in value to that obtained from the PKN model, doesn't follow a similar trend. The pressure from the model decreases in the simulation at the start and then starts to increase, whereas the pressure in the PKN model increases as the fracture grows in length. This is because of the vertical plane strain assumption of the PKN model. As in the PKN model, the width of the fracture at a point is only a function of the local pressure, the increase in pressure is due to the viscous pressure

drop inside the fracture. By contrast, in the fully coupled simulator, the compliance of the fracture increases as the fracture becomes longer, and hence the pressure required at the wellbore to propagate the fracture decreases as the length of the fracture increases. In addition, in the simulator, the fracture starts to propagate with a radial geometry as the injection source is a point, whereas, in the PKN model, the injection is from a vertical well (line source). This can further increase the effect of the change of compliance on the pressure profile obtained from the simulator, especially at the start of the simulation. The overall pressure behavior from the developed simulator is a function of both the pressure drop inside the fracture and the compliance of the fracture.

2.4 CONCLUSION

In this chapter, we have discussed the formulation, solution, and verification of a DDM model to simulate the propagation of multiple fractures in the presence of natural fractures. The simulator is based on a coupled displacement discontinuity method (geomechanics) and finite difference method (fluid mechanics). The model allows us to model the propagation of fracture networks. The governing equations of geomechanics and fluid mechanics, fracture propagation criterion, propagation direction, the interaction of natural fracture and hydraulic fracture, leak-off, and proppant transport are presented. The solution algorithms used to solve the coupled fluid-solid interaction problem are also discussed.

We have also presented a new method for the solution of the fracture geomechanics and fluid flow problem. The computation of these problems requires a large number of iterations due to the non-linear nature of the coupled system. The new algorithm is implemented in a fully three-dimensional hydraulic fracturing model, and its advantages are investigated. We observed that the use of a predictor step brings down the overall

computation time required to model growing fractures using DDM up to 25 percent for the simulated case. An instantaneous speed increase up to 93 percent is also observed. The new algorithm reduces the fluctuations in the solution during the iterative process which provides stability to the algorithm. This can allow the use of higher values of relaxation factors, leading to faster convergence. The method presented here provides a new approach to solve the coupled non-linear system of equations of geomechanics and fluid flow inside the fracture.

2.5 APPENDIX

2.5.1 Local linearization method

Starting from equation 2.6

$$\frac{\partial(\rho \mathrm{v})}{\partial \mathrm{t}} = \nabla \cdot \left(\frac{k\rho A}{\mu}\nabla P\right) - \dot{m}_{leakoff} + \dot{m}_{inj} \qquad (A1.1)$$

$$\frac{\partial(\rho \mathrm{w})}{\partial \mathrm{t}} = \nabla \cdot \left(\frac{w^3\rho}{12\mu}\nabla P\right) - \frac{\dot{m}_{leakoff}}{A_m} + \frac{\dot{m}_{inj}}{A_m} \qquad (A1.2)$$

Using a Taylor series expansion, we can write for a function f(x) that is infinitely differentiable at a, the following power series:

$$f(x) = f(a) + \frac{f'(a)(x-a)}{1!} + \frac{f''(a)(x-a)^2}{2!} + \frac{f''(a)(x-a)^3}{3!} + \cdots \qquad (A1.3)$$

So,

$$w_{new}^3 = w_{old}^3 + \frac{3w_{old}^2(w_{new} - w_{old})}{1!} + \frac{6w_{old}(w_{new} - w_{old})^2}{2!} + \frac{6(w_{new} - w_{old})^3}{3!} \quad (A1.4)$$

or

$$w_{new}^3 = w_{old}^3 + \frac{3w_{old}^2(dw)}{1!} + \frac{6w_{old}(dw)^2}{2!} + \frac{6(dw)^3}{3!} \quad (A1.5)$$

Where $dw = w_{new} - w_{old}$

Neglecting $(dw)^2 and\ (dw)^3$, we can write

$$w_{new}^3 = w_{old}^3 + 3w_{old}^2(dw) \quad (A1.6)$$

$$w_{new}^3 = 3w_{old}^2 w_{new} - 2w_{old}^3 \quad (A1.7)$$

$$\frac{\partial(\rho w)}{\partial t} = \nabla \cdot \left(\frac{3w_{old}^2 w_{new} - 2w_{old}^3 \rho}{12\mu} \nabla P\right) - \frac{\dot{m}_{leakoff}}{A_m} + \frac{\dot{m}_{inj}}{A_m} \quad (A1.8)$$

$$\frac{\partial(\rho w^{k+1})}{\partial t} = \nabla \cdot \left(\frac{3w_{old}^2 w^{k+1}}{12\mu} \nabla P^k - \frac{2w^{3^k}\rho}{12\mu} \nabla P^{k+1}\right) - \frac{\dot{m}_{leakoff}}{A_m} + \frac{\dot{m}_{inj}}{A_m} \quad (A1.9)$$

2.5.2 Coefficients of Displacement Discontinuity Method

The analytical solution of stresses generated due to a single element of displacement discontinuity given by D_{x1}, D_{x2}, and D_{x3} acting at a point P in the local coordinate system at a location x_1, x_2, x_3 is given as follows (Rongved, 1957, Salamon, 1964):

$$\begin{pmatrix}\sigma_{11}\\ \sigma_{22}\\ \sigma_{33}\\ \sigma_{12}\\ \sigma_{13}\\ \sigma_{23}\end{pmatrix} = C * \begin{pmatrix} 2I_{13} - x_3I_{111} & 2\nu I_{23} - x_3I_{211} & I_{33} + (1-2\nu)I_{22} - x_3I_{311} \\ 2\nu I_{13} - x_3I_{122} & 2I_{23} - x_3I_{222} & I_{33} + (1-2\nu)I_{11} - x_3I_{322} \\ x_3I_{133} & x_3I_{233} & I_{33} - x_3I_{333} \\ (1-\nu)I_{23} - x_3I_{112} & (1-\nu)I_{13} - x_3I_{212} & -(1-2\nu\ )I_{12} - x_3I_{312} \\ I_{33} + \nu I_{22} - x_3I_{113} & -\nu I_{12} - x_3I_{213} & -x_3I_{313} \\ -\nu I_{21} - x_3I_{123} & I_{33} + \nu I_{11} - x_3I_{223} & -x_3I_{323} \end{pmatrix} \begin{pmatrix} D_{x1}\\ D_{x2}\\ D_{x3}\end{pmatrix} \quad (A2.1)$$

where σ represents the stress acting at point P in the local coordinate system, and C is given by the following equation:

$$C = \frac{G}{4\pi(1-\nu)} \quad (A2.2)$$

where G is the shear modulus, ν is the Poisson's ratio. I is the kernel analytical solution to the problem of a constant displacement over an arbitrarily oriented rectangular element in an infinite elastic medium solved given by the Green's function approach given as:

$$I(x_1, x_2, x_3) = \int_{-b}^{b}\int_{-a}^{a} \frac{1}{\sqrt{(x_1-\xi)^2 + (x_2-\xi_2)^2 + x_3^2}} d\xi_1 d\xi_2 \quad (A2.3)$$

The above equation can be integrated and the final form of the equation is presented below:

$$I(x_1, x_2, x_3) = [x_1' \ln(r + x_2') + x_2' \ln(r + x_1') - x_3\theta]|_{\xi_1=-a}^{\xi_1=a}|_{\xi_2=-b}^{\xi_2=b} \qquad (A2.4)$$

Where $x_1' = x_1 - \xi_1$, $x_2' = x_2 - \xi_2$, $\theta = \tan^{-1}\left(\frac{x_1' x_2'}{r x_3}\right)$

and $r = \sqrt{(x_1 - \xi_1)^2 + (x_2 - \xi_2)^2 + x_3^2}$

The derivatives used for calculating the stresses are defined as follows:

$$I_1 = \ln(r + x_2 - \xi_2) \qquad (A2.5)$$

$$I_2 = \ln(r + x_1 - \xi_1) \qquad (A2.6)$$

$$I_3 = -\tan^{-1}\left(\frac{(x_1 - \xi_1)(x_2 - \xi_2)}{x_3 r}\right) \qquad (A2.7)$$

$$I_{11} = \frac{x_1 - \xi_1}{r(r + x_2 - \xi_2)} \qquad (A2.8)$$

$$I_{22} = \frac{x_2 - \xi_2}{r(r + x_1 - \xi_1)} \qquad (A2.9)$$

$$I_{33} = \frac{(x_1 - \xi_1)(x_2 - \xi_2)(x_3^2 + r^2)}{r(x_3^2 + (x_1 - \xi_1)^2)(x_3^2 + (x_2 - \xi_2)^2)} \qquad (A2.10)$$

$$I_{12} = \frac{1}{r} \qquad (A2.11)$$

$$I_{13} = \frac{x_3}{r(r + x_2 - \xi_2)} \qquad (A2.12)$$

$$I_{23} = \frac{x_3}{r(r + x_1 - \xi_1)} \quad (A2.13)$$

$$I_{111} = -\frac{(r + x_2 - \xi_2)((x_1 - \xi_1)^2 - r^2) + (x_1 - \xi_1)^2 r}{r^3(r + x_2 - \xi_2)^2} \quad (A2.14)$$

$$I_{211} = -\frac{(x_1 - \xi_1)}{r^3} \quad (A2.15)$$

$$I_{311} = -\frac{(x_1 - \xi_1)x_3(2r + x_2 - \xi_2)}{r^3(r + x_2 - \xi_2)^2} \quad (A2.16)$$

$$I_{122} = -\frac{(x_2 - \xi_2)}{r^3} \quad (A2.17)$$

$$I_{222} = -\frac{(r + x_1 - \xi_1)((x_2 - \xi_2)^2 - r^2) + (x_2 - \xi_2)^2 r}{r^3(r + x_1 - \xi_1)^2} \quad (A2.18)$$

$$I_{322} = -\frac{(x_2 - \xi_2)x_3(2r + x_1 - \xi_1)}{r^3(r + x_1 - \xi_1)^2} \quad (A2.19)$$

$$I_{133} = -\frac{(r + x_2 - \xi_2)(x_3^2 - r^2) + x_3^2 r}{r^3(r + x_2 - \xi_2)^2} \quad (A2.20)$$

$$I_{233} = -\frac{(r + x_1 - 1)(x_3^2 - r^2) + x_3^2 r}{r^3(r + x_1 - \xi_1)^2} \quad (A2.21)$$

$$I_{333} = -x_3(x_1 - \xi_1)(x_2 - \xi_2)$$
$$\frac{(x_3^2 + (x_1 - \xi_1)^2)^2(x_3^2 + (x_2 - \xi_2)^2 + 2r^2) + (x_3^2 + (x_2 - \xi_2)^2)^2(x_3^2 + (x_1 - \xi_1)^2 + 2r^2)}{r^3(x_3^2 + (x_2 - \xi_2)^2)\text{^}2\,(x_3^2 + (x_1 - \xi_1)^2)^2} \quad (A2.22)$$

$$I_{123} = -\frac{x_3}{r^3} \qquad (A2.23)$$

The equations presented above are in the local coordinate system of the DDM element. In order to formulate the influence matrix, the equation is transformed from the local coordinate system to a global coordinate system. In addition, the relative distances between the elements are used in order to calculate the stresses acting on one element due to the opening of another. The equation is used to transform the relative distance between elements from a local coordinate system to a global coordinate system. The coordinate transformation for calculating the stresses generated due to displacement discontinuity of element B at location (X_B,Y_B,Z_B) at a point A at location (X_A,Y_A,Z_A) is shown using the following equation:

$$\begin{pmatrix} x_1 \\ x_2 \\ x_3 \end{pmatrix} = \begin{pmatrix} cos\beta cos\theta & sin\beta cos\theta & -sin\theta \\ cos\beta sin\theta & sin\beta sin\theta & cos\theta \\ -sin\beta & cos\beta & 0 \end{pmatrix} \begin{pmatrix} X_A - X_B \\ Y_A - Y_B \\ Z_A - Z_B \end{pmatrix} \qquad (A2.24)$$

where beta is the angle of the between x_1 and X, theta is the angle between x_2 and Z, where X, Y , and Z are unit vectors along the principal axes of the global coordinate system.

Now equation A2.1 can be simplified by writing the equation in the global coordinate system:

$$\begin{pmatrix} \sigma_{11} \\ \sigma_{22} \\ \sigma_{33} \\ \sigma_{12} \\ \sigma_{13} \\ \sigma_{23} \end{pmatrix} = [A] \begin{pmatrix} D_{x1} \\ D_{x2} \\ D_{x3} \end{pmatrix} \qquad (A2.25)$$

where A represents the influence coefficients in the global coordinate system. After converting the equations from a local to a global coordinate system, the principle of superposition is employed to generate the influence matrix. For example, stresses acting at point P due to the opening of N elements can be written as:

$$\begin{pmatrix} \sigma_{11} \\ \sigma_{22} \\ \sigma_{33} \\ \sigma_{12} \\ \sigma_{13} \\ \sigma_{23} \end{pmatrix}_p = \sum_{j=1}^{N} [A]_{i,j} \begin{pmatrix} D_{x1} \\ D_{x2} \\ D_{x3} \end{pmatrix}_j \qquad (A2.26)$$

The above equation is used in calculating the stresses acting on the natural fracture due to the growth of the hydraulic fracture. The stresses are then transformed on the plane of the natural fracture and the Mohr-Coulomb criterion is used to predict its failure. In order to get the relationship between the stresses and the displacement discontinuity of all the elements, the above equation is re-written in the following form:

$$\begin{pmatrix} \sigma_{sh} \\ \sigma_{sl} \\ \sigma_{nn} \end{pmatrix}_i = \sum_{j=1}^{N} [A]_{i,j} \begin{pmatrix} D_{sh} \\ D_{sl} \\ D_{nn} \end{pmatrix}_j \qquad (A2.27)$$

where, σ_{sh}, σ_{sl}, and σ_{nn} are the stresses acting on the surface of i^{th} element in the height direction (shear stress), length direction (shear stress), and width direction (normal stress), and D_{sh}, D_{sl}, and D_{nn} are the displacement discontinuities in the height, length, and the width direction of the element. Equations for all the elements are written and are rearranged in the following form:

$$\begin{bmatrix} A_{11} & . & A_{1,n-1} & A_{1,3n} \\ . & . & . & . \\ . & . & . & . \\ . & . & . & . \\ . & . & . & . \\ . & . & . & . \\ . & . & . & . \\ A_{3n-1,1} & . & . & A_{3n-1,3n} \\ A_{3n,1} & . & A_{3n,3n-1} & A_{3n,3n} \end{bmatrix} \begin{vmatrix} D_{x1} \\ . \\ D_{xn} \\ D_{y1} \\ . \\ D_{yn} \\ D_{z1} \\ . \\ D_{zn} \end{vmatrix} = \begin{vmatrix} \sigma_{x1} \\ . \\ \sigma_{xn} \\ \sigma_{y1} \\ . \\ \sigma_{yn} \\ \sigma_{z1} \\ . \\ \sigma_{zn} \end{vmatrix} \qquad (A2.28)$$

which gives the relationship between the stresses and displacement discontinuities for all the elements in the problem.

Chapter 3: Interaction of Hydraulic Fractures and Natural Fractures

In Chapter 2, a hydraulic fracturing simulator based on a fully three-dimensional displacement discontinuity method is presented that handles the interaction of natural fractures with a hydraulic fracture. Local linearization, a novel algorithm to solve the problem in a computationally efficient manner, is also discussed.

This chapter is dedicated to the application of this model to understand the effect of a hydraulic fracture's interaction with natural fractures on created fracture geometry. Three case studies have been presented that investigate the effect of natural fracture properties (natural fracture density, orientation, and height) on the growth of the hydraulic fracture network. The chapter also presents an extended model that is developed to correctly predict the shear failure of natural fractures as a hydraulic fracture approaches it. The extended model is used to investigate the interaction of a fracture and a natural fracture before the hydraulic fracture intersects the natural fracture. The stresses that the natural fracture experiences as the hydraulic fracture approaches it are discussed. The chapter also discusses the interaction of a hydraulic fracture and a natural fracture as the hydraulic fracture tip front (tip of a three-dimensional hydraulic fracture) crosses the natural fracture. This scenario is also simulated and the results are presented.

This chapter is adapted from papers "Shrivastava, Kaustubh, and Mukul M. Sharma. "Mechanisms for the formation of complex fracture networks in naturally fractured rocks." SPE Hydraulic Fracturing Technology Conference and Exhibition. Society of Petroleum Engineers, 2018, and Shrivastava, K., Agrawal, S., Kumar, A., Sharma, M.M., 2018. 3-D Interactions of Hydraulic Fractures with Natural Fractures, in: SPE International Hydraulic Fracturing Technology Conference and Exhibition. Society of Petroleum Engineers. In both the papers, Shrivastava designed and performed the research, developed and used the hydraulic fracturing model, and documented the results.

3.1 INTRODUCTION

With the advancement in our understanding of hydraulic fracturing, the importance of hydraulic fracture-natural fracture interaction to form complex fracture networks has become more evident. The evidence for the formation of fracture networks during fracturing has been found during mine-back experiments (Warpinski and Teufel, 1987; Jeffrey and Settari, 1995). These studies suggest the presence of multiple hydraulic fractures due to fracture propagation along planes of weakness such as bedding planes or natural fractures. In addition, microseismic monitoring (Maxwell et al., 2002) also supports the notion of numerous planes of weakness undergoing shear failure in the vicinity of the growing hydraulic fracture.

Several authors have investigated the interaction of hydraulic fractures with natural fractures. Renshaw and Pollard (1995) developed an analytical criterion for predicting growth or arrest of a hydraulic fracture during its orthogonal intersection with a frictional interface. This criterion was later extended by Gu and Weng (2010) for non-orthogonal angles of intersection. Wu and Olson (2014) modified the extended criterion to account for both modes I and II stress intensities at the fracture tip. Although these criteria provide useful insight into the process of fracture intersection with natural fractures, they need to be coupled with a numerical simulator to describe the complete process of fracture network growth.

Besides the analytical models discussed above, there are several numerical studies that have addressed different aspects of hydraulic fracture and natural fracture interaction. Chuprakov et al. (2011) investigated the elastic interaction of a pre-existing natural fracture with a hydraulic fracture and examined the effect of net pressure. Taleghani and Olson (2013) developed a crossing criterion for cemented natural fractures based on the energy release rate. These studies have examined the fracture interaction in two-dimensions to

keep the problem tractable. However, the interaction in three-dimensions can lead to different characteristics, such as a combination of crossing and fracture turning (Bahorich et al., 2012). Also, when a three-dimensional radial hydraulic fracture approaches a natural fracture, the fracture tip is a continuous elliptical front crossing the natural fracture rather than a point, unlike in the case of two-dimensional interactions. Thus, 2-D simulations, while simple and convenient, cannot capture the interaction between a natural fracture and a hydraulic fracture completely.

In the first part of the chapter, we present a study that investigates hydraulic fracture growth in the presence of thousands of pre-existing natural fractures using the model presented in Chapter 3. A systematic investigation of the effect of natural fracture density, orientation, and height is presented.

In the second part of the chapter, we have analyzed the stresses acting on a three-dimensional natural fracture generated due to a radially growing hydraulic fracture as it approaches and then crosses the natural fracture in a field-scale scenario. The compressive and tensile stresses acting on the natural fracture as the hydraulic fracture approaches have been presented and discussed. As the hydraulic fracture crosses the natural fracture, the stresses acting on the plane of the natural fracture due to the circumferential fracture tip of the radial hydraulic fracture are computed and presented. This investigation gives insight and presents the stresses generated due to the three-dimensional shape of fracture and its possible effects.

3.2 Effect of Natural Fracture Properties on Fracture Propagation

This section discusses cases run to understand the effect of natural fracture properties on the growth of the hydraulic fracture network.

3.2.1 Effect of Natural Fracture Density

Three simulation cases are run using our simulator to investigate the effect of natural fracture density (number of fractures per unit area of the reservoir) on the created fracture network complexity. The three cases have fracture densities of 500, 1,500, and 3,000 natural fractures per 10,000 square meters. A simulation region of 10,000 square meters is populated with a randomly generated natural fracture realization (natural fractures are placed at random locations in the simulation region). In the simulation, the natural fractures are of constant length of 2 m. At the start of the simulation the natural fractures are not treated as DDM elements but are converted into DDM elements on intersection with the growing hydraulic fracture. Each natural fracture has a different orientation, and the orientation distribution of natural fractures is shown in Figure 3.1 as a rose diagram. The rose diagram shows the frequency of natural fractures on a circular histogram where the orientation of the bins represents the orientation of the natural fractures used in the model. The 0^o-180^o orientation on the rose diagram represents the north(0^o)-south(180^o) direction in the simulation domain. The maximum horizontal stress is along the vertical direction.

It is assumed that the height of the natural fracture is the same as the height of the hydraulic fracture. The hydraulic fracture is simulated with only a single element in the height direction and the injection rate is normalized using the fracture height. Using only a single element along the fracture height can introduce error up to 50 percent in the obtained result (Wu, 2014), but can significantly reduce the computational requirement for large scale problem. In our simulation, we followed this approach as this allowed us to investigate the behavior of fracture growth in the presence of thousands of natural fractures with a reasonable simulation run time. Table 3.1 shows the parameters used for the simulation.

Table 3.1: Properties used in the simulator for the study.

Parameter	**Value**	**Units**
Young's Modulus	0.3	million psi
Poisson's Ratio	0.25	
Sh_{min}	2500	psi
Sh_{max}	2625	psi
Injection Rate	0.4	bbl / m / min
Run Time	10	minutes
Fluid Viscosity	1	cP
Reservoir Porosity	10	%
Reservoir Permeability	200	nD
Reservoir Pressure	2000	Psi

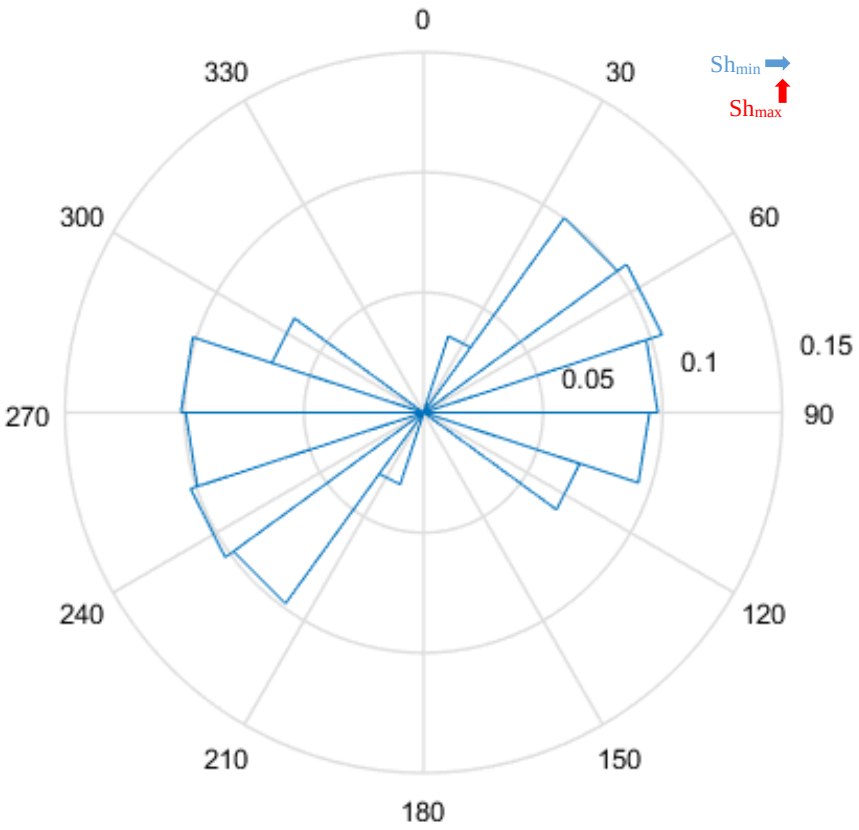

Figure 3.1: Rose diagram of the orientation of the natural fractures used in the simulation.

Figure 3.2, Figure 3.3, and Figure 3.4 show the growth of the fracture network for the three fracture densities. As the natural fracture density increases, the probability of the intersection of the propagating fracture tips with natural fractures increases. Upon intersection, the natural fracture redirects the growth of the hydraulic fracture along its orientation. Hence, for high natural fracture density, the propagation direction of the hydraulic fracture is dictated by the orientation of the natural fractures rather than the far-field stresses. This is also observed in the simulated cases where a higher fracture density resulted in fracture network growth towards the natural fracture direction, which is perpendicular to the Sh_{max} direction in the simulated cases (see Figure 3.4). In addition,

this behavior increased the complexity of the created fracture network in the simulated cases. Whereas for low natural fracture density (see Figure 3.2), the created fracture network grew predominantly towards the Sh_{max} direction.

The natural fracture density can change the aspect ratio of the created fracture network, and in turn, the drainage area of the fracture network. The dominant orientation of the natural fractures relative to the far-field stress directions should be accounted for during the selection of fracture spacing and well spacing while designing hydraulic fracturing treatments.

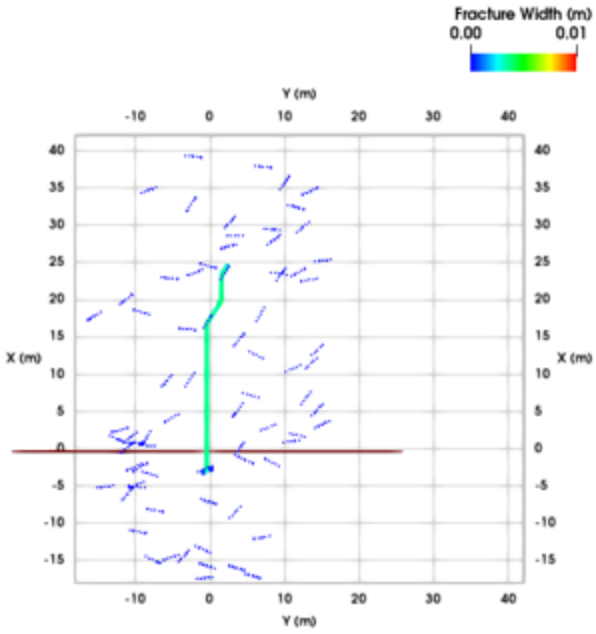

Figure 3-2A

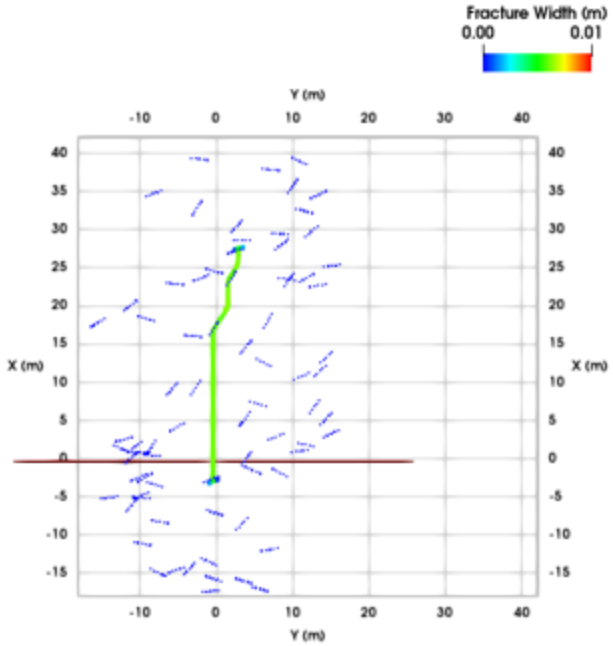

Figure 3-2B

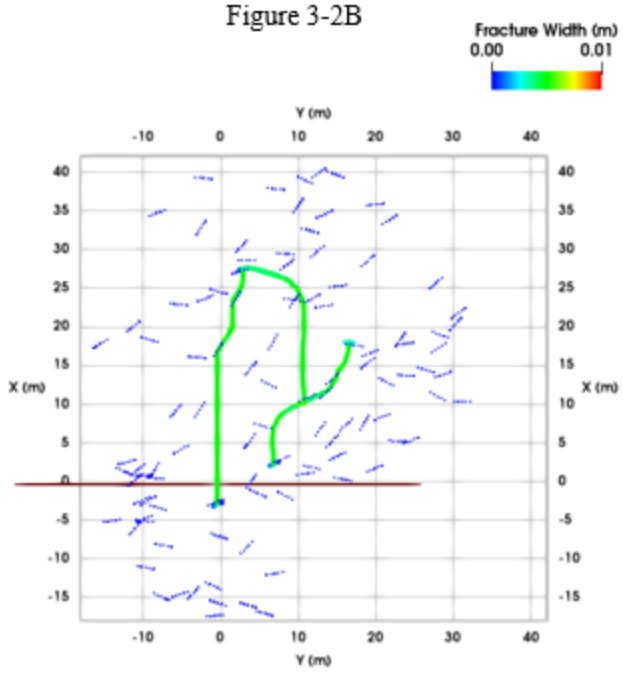

Figure 3-2C

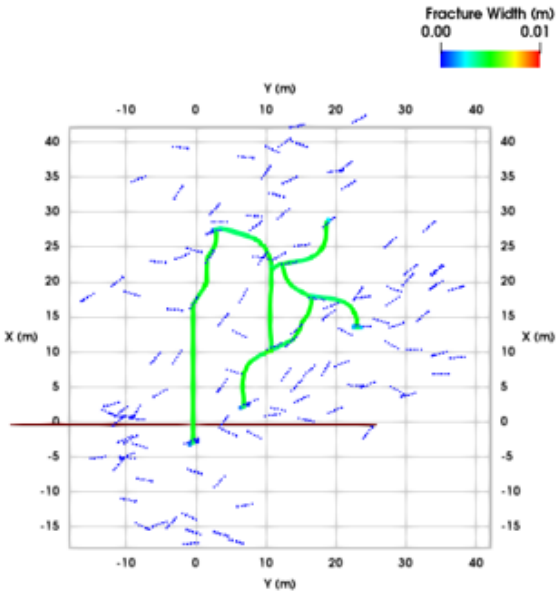

Figure 3-2D

Figure 3.2: Top view of the fracture network geometry and width (color bar) with natural fracture density of 500 natural fractures per 10,000 square meters. The blue lines show the natural fractures. Figure 3.2 A, B, C, and D show the geometry of the fracture at 150, 300, 450, and 600 seconds from the start of injection, respectively.

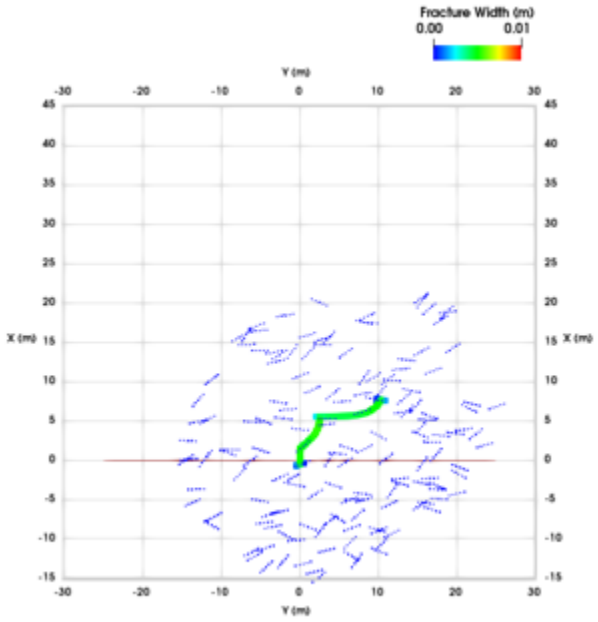

Figure 3-3A

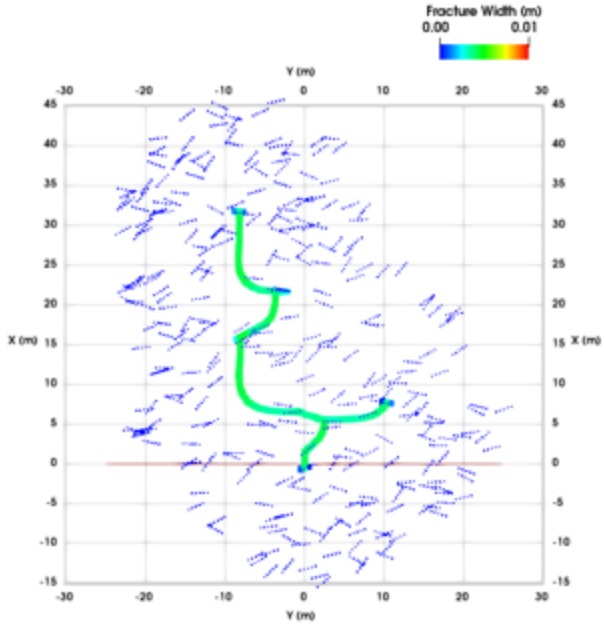

Figure 3-3B

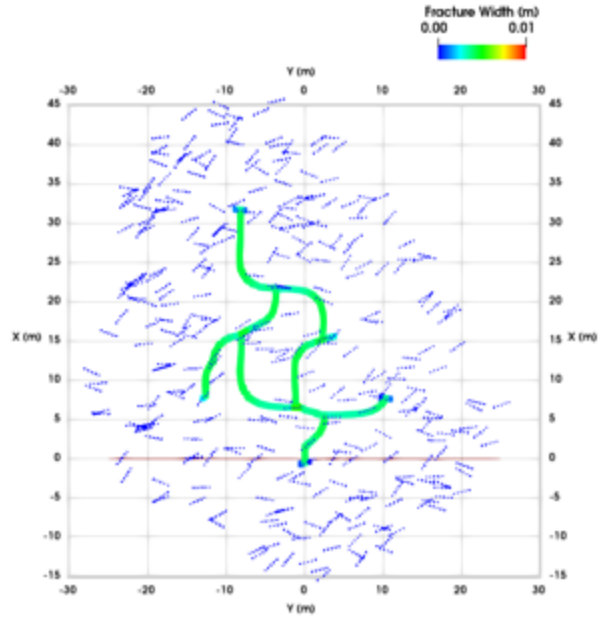

Figure 3-3C

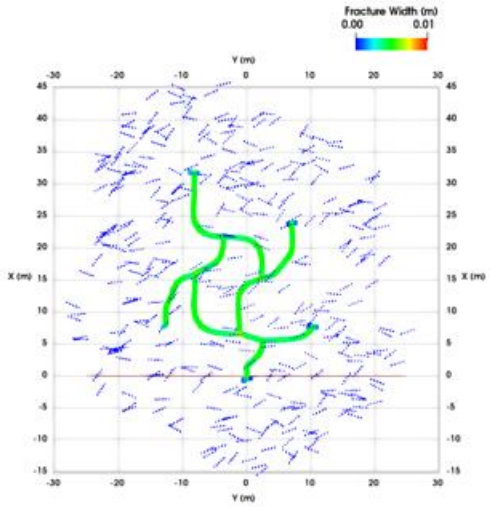

Figure 3-3D

Figure 3.3: Top view of the fracture network geometry and width with natural fracture density of 1500 natural fractures per 10000 square meters. The blue lines show the natural fractures. The figures 4-3 A, B, C, and D show the geometry of the fracture at 150, 300, 450, and 600 seconds from the start of injection, respectively.

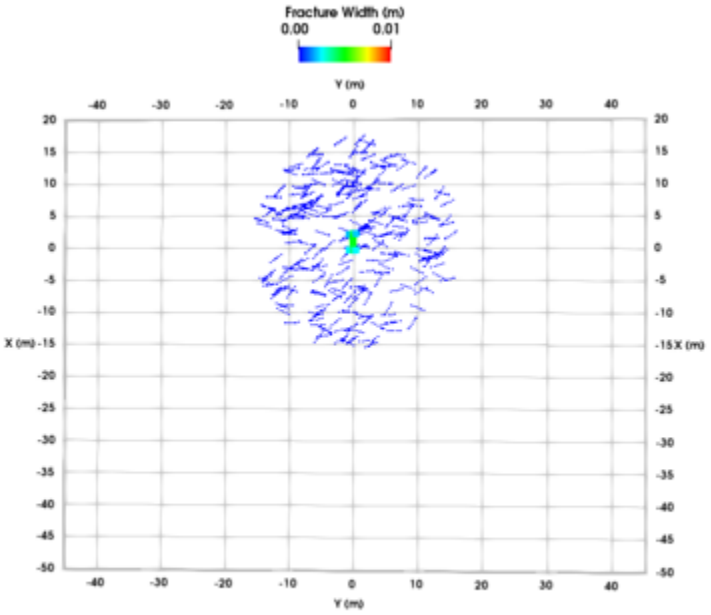

Figure 3-4A

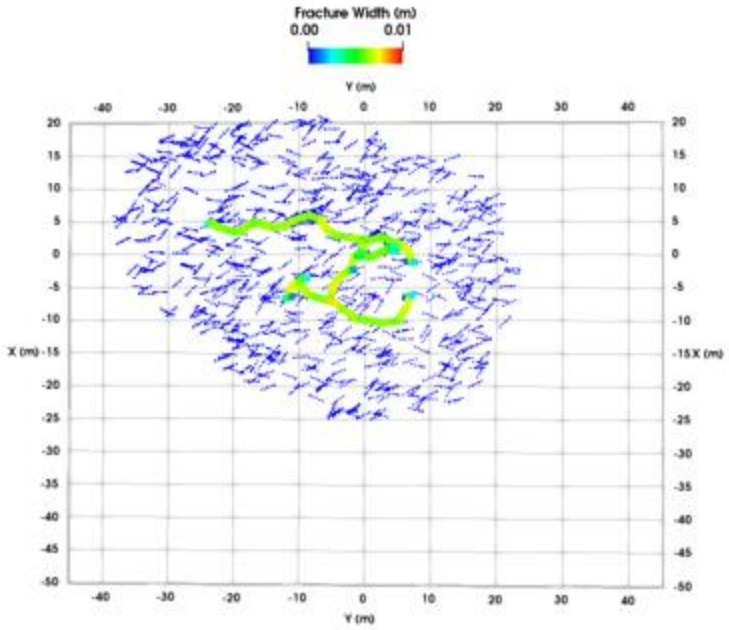

Figure 3-4B

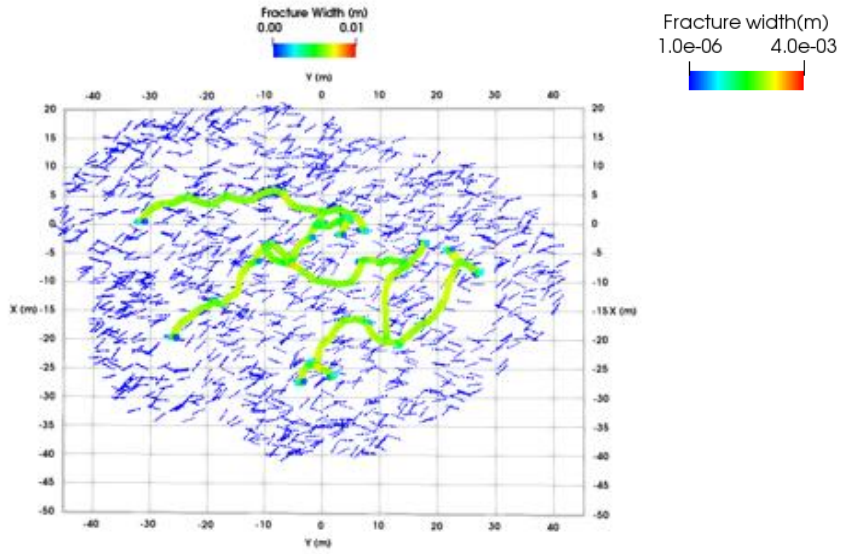

Figure 3-4C

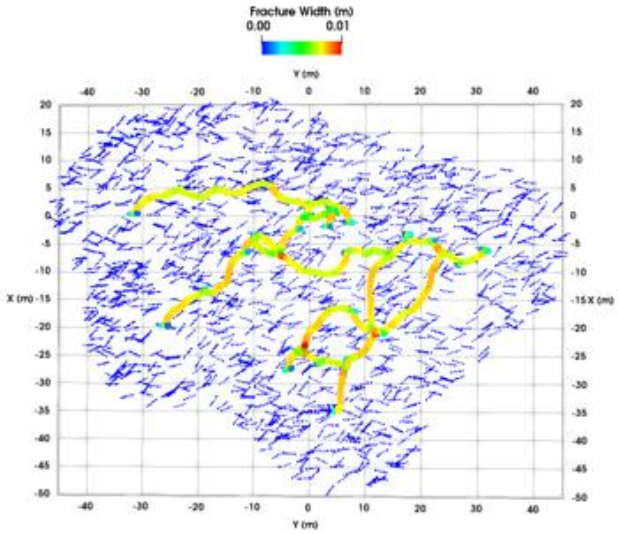

Figure 3-4D

Figure 3.4: Top view of the fracture network geometry and width with natural fracture density of 3000 natural fractures / 10000 square meters. The blue lines show the natural fractures. Figure 3.4 A, B, C, and D show the geometry of the fracture at 150, 300, 450, and at 600 seconds from the start of injection, respectively.

3.2.2 Effect of Natural Fracture Orientation

In this section, three cases are simulated to investigate the effect of the natural fracture orientation on fracture growth. For these cases, the orientation of natural fractures with respect to far-field stresses are chosen to be 30, 60, and 90 degrees. A natural fracture realization is generated that randomly distributes the natural fractures in the simulation domain. The location and length of the natural fractures are kept the same in all the three cases, and only the orientation is varied. The parameters used for the simulation are shown in Table 3.1.

Figure 3.5, Figure 3.6, and Figure 3.7 show the final geometry of the created hydraulically connected fracture network for the 30, 60, and 90 degrees cases, respectively. It is observed that the natural fracture orientation influences the propagation direction of the hydraulic fracture. The natural fracture, if intersected, acts as a path of least resistance

for fracture propagation and modifies the propagation direction. From the tip of the connected natural fracture, the fracture again starts to observe the influence of the far-field stresses and reorients itself to grow towards the Sh_{max} direction. Hence, if the natural fracture orientation is closer to the Sh_{max} direction, the generated fracture network will be very narrow and long (Figure 3.5) as can be seen for the 30-degree case. Whereas if the natural fracture orientation is perpendicular to the Sh_{max} direction, wider fracture networks with relatively smaller lengths will be generated (Figure 3.7) as can be observed for the 90-degree case.

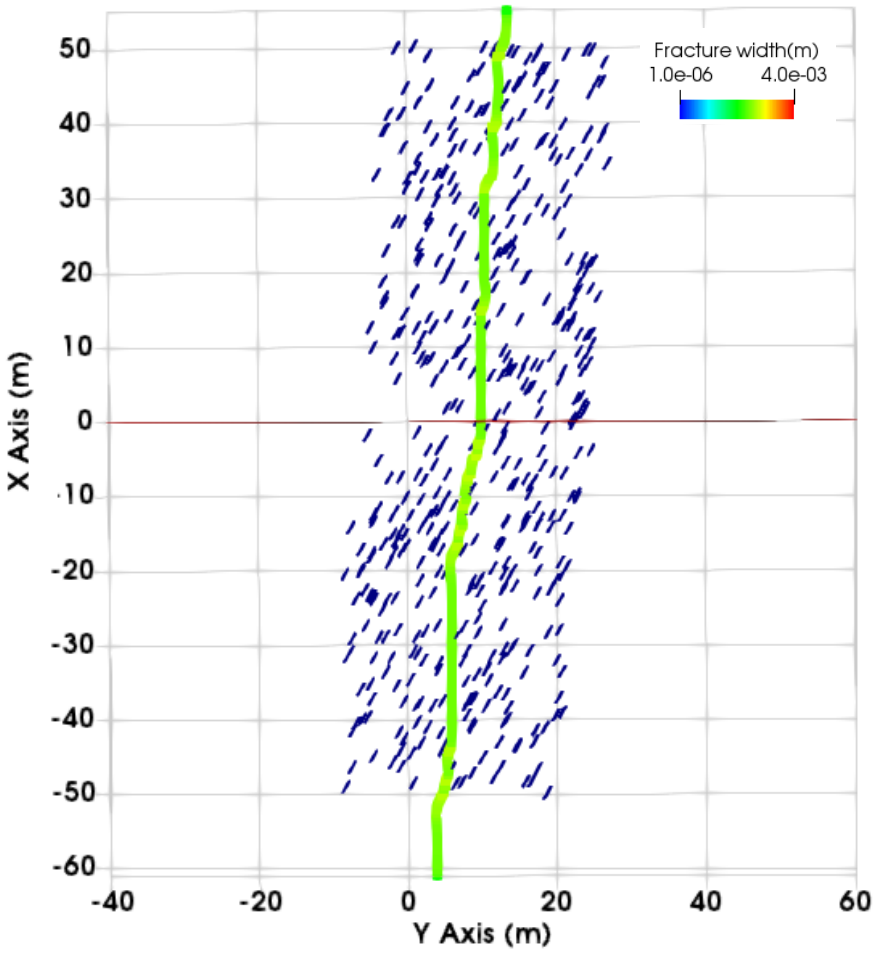

Figure 3.5: Top view of the fracture network geometry for orientation of natural fracture 30^{o} from the Sh_{max} direction. The blue lines show the natural fractures.

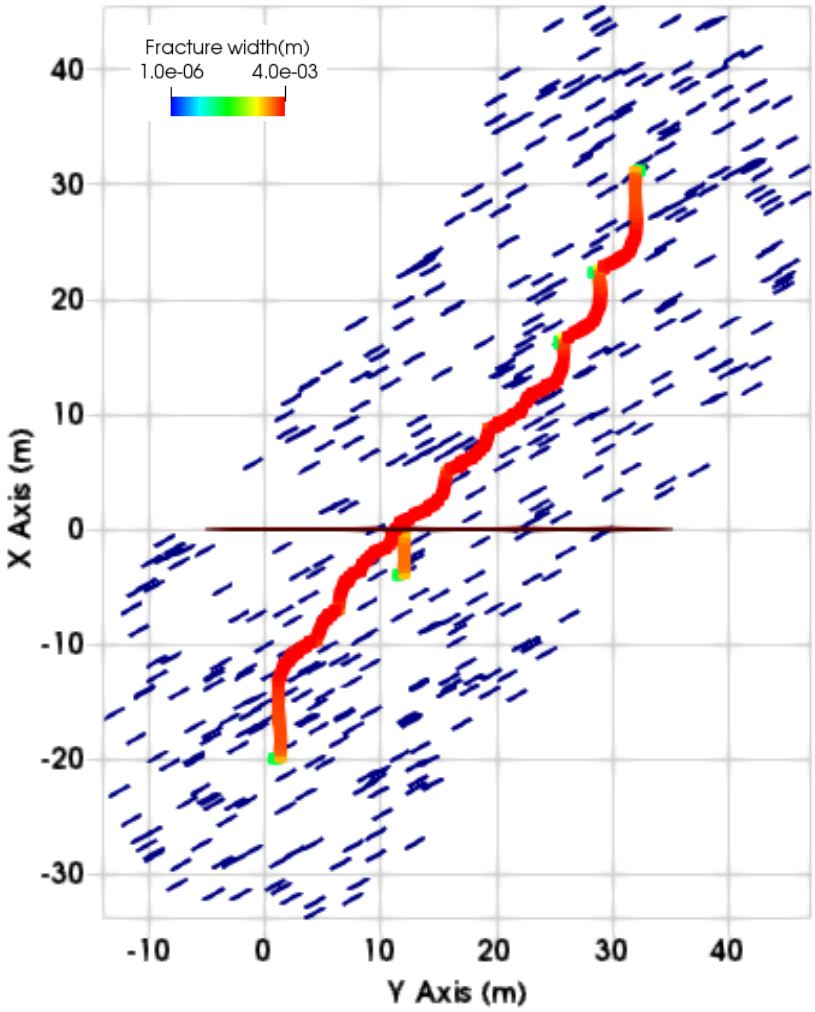

Figure 3.6: Top view of the fracture network geometry for orientation of natural fracture of 60^{o} from the Sh_{max} direction. The blue lines show the natural fractures.

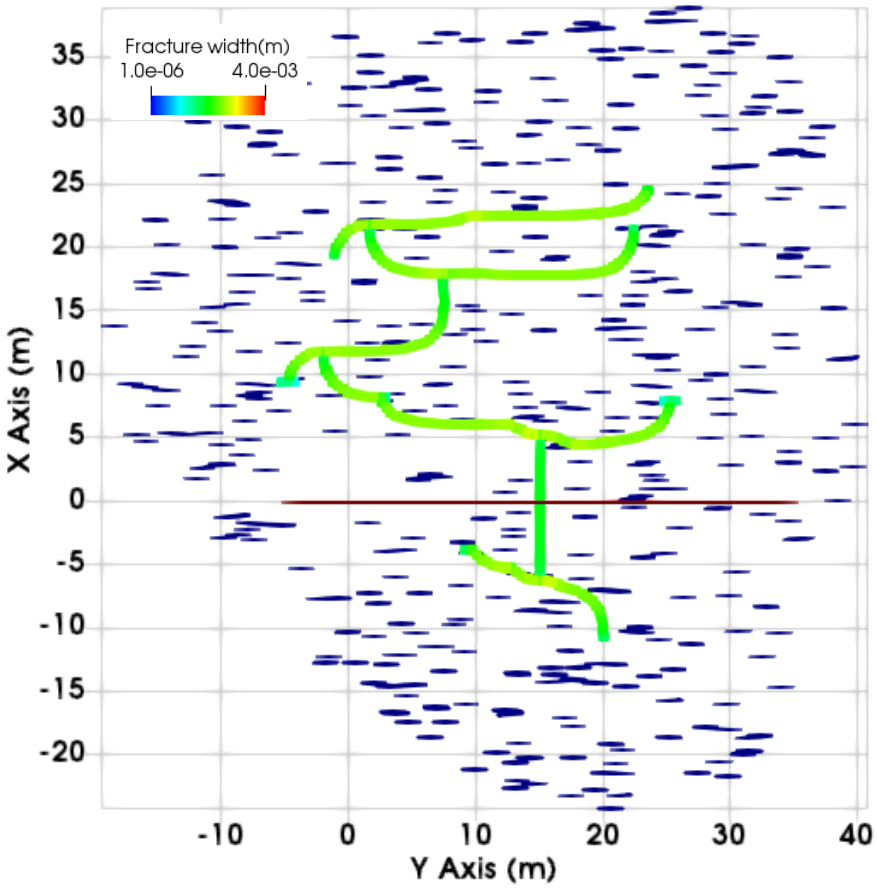

Figure 3.7: Top view of the fracture network geometry for natural fracture orientation 90º from the Sh_{max} direction. The blue lines show the natural fractures.

3.2.3 Effect of Fracture Height

In this section, the effect of the height of hydraulic fractures relative to natural fractures on fracture growth is investigated. Two simulation cases with different height of the hydraulic fracture relative to the natural fracture are set up. In Case 1, the height of the intersecting hydraulic fracture is smaller than the natural fracture, whereas in Case 2 the hydraulic fracture is allowed to grow and achieve a radius bigger than the natural fracture before the intersection. The parameters used in the simulation are tabulated in Table 3.1.

In Case 1, as the fluid is injected the hydraulic fracture starts to grow radially (see Figure 3.9). As the fracture grows, the element closest to the natural fracture intersects with it. Upon intersection, the natural fracture element slips, and in the model the slipped natural fracture's mesh is stitched to the hydraulic fracture mesh. The fracture propagates along the natural fracture, and the fracturing fluid flows into the natural fracture. The fracture propagates until the stress intensity at the fracture tip drops below the critical stress intensity. As the fluid flows into the natural fracture, the width of the natural fracture increases, and the natural fracture starts to exert stresses on the hydraulic fracture (see Figure 3.10). The increased stress reduces the width of the hydraulic fracture and pushes the fluid out of the hydraulic fracture. In addition, due to the reduced width of the hydraulic fracture the stress intensity on fracture tips reduces, and its growth stops. It is observed that the tips near the intersection on the hydraulic fracture has a lower width compared to the tips away from the intersection. As the size of the natural fracture is larger than the hydraulic fracture, on further injection of the fluid, the natural fracture grows, and the hydraulic fracture's width decreases (see Figure 3.11). Overall, in this case, the natural fracture growth dominates, and the hydraulic fracture's growth is hindered.

In Case 2, the hydraulic fracture achieves a much larger size before the intersection. Upon intersection, the natural fracture slips and gets connected to the growing hydraulic fracture network (see Figure 3.13 and Figure 3.14). Although, due to the higher stresses acting on the natural fracture plane, because of the larger hydraulic fracture, the natural fracture does not grow. On further pumping of the fracturing fluid, the hydraulic fracture keeps on growing.

A bias is observed in the growth of the hydraulic fracture. The tips of the hydraulic fracture furthest from the natural fracture grow more as the simulation progresses (see Figure 3.15). This is due to the opening of the natural fracture element. The opening exerts small stress on the hydraulic fracture tips and creates a bias for the hydraulic fracture to grow away from the natural fracture. In this case, the opening of a tall hydraulic fracture subdues the growth of the natural fracture.

Hence, in both the cases it is observed that a larger fracture suppresses the growth of a nearby smaller hydraulically connected fracture. This competition between fractures is expected in all the hydraulic fracture and natural fracture intersections during fracture growth.

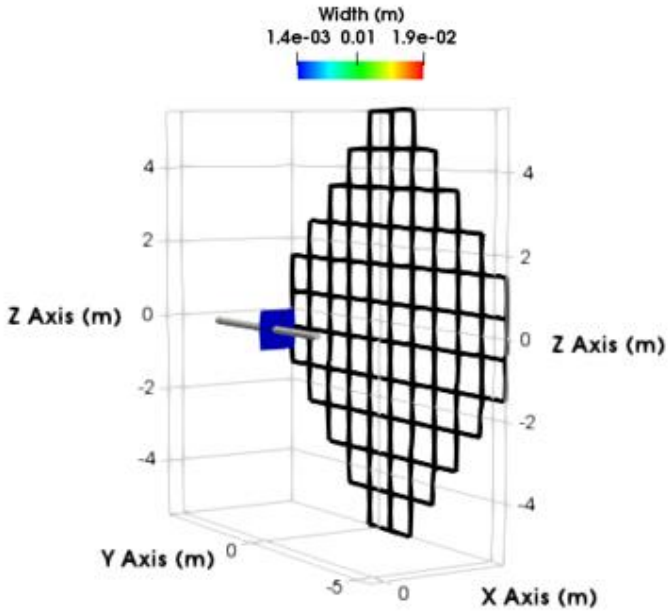

Figure 3.8: The fracture geometry at the start of pumping for the larger natural fracture case. The black squares show the shape of the natural fracture used in the simulation.

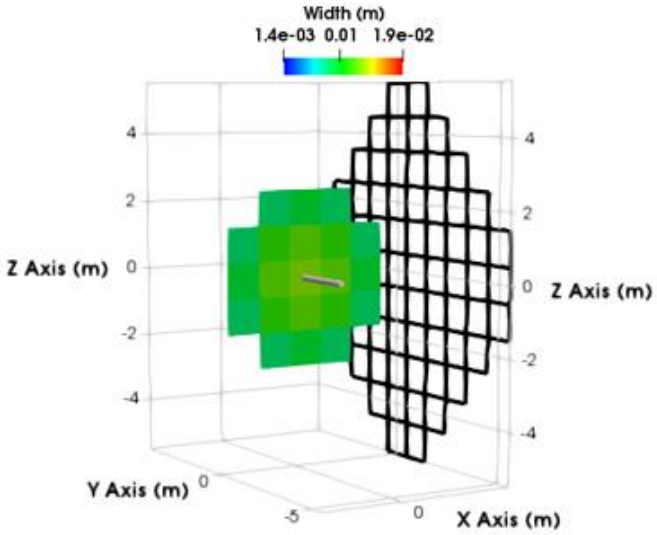

Figure 3.9: The geometry of the propagating hydraulic fracture just before the intersection with the natural fracture. In the next time step, the hydraulic fracture intersects with the natural fracture.

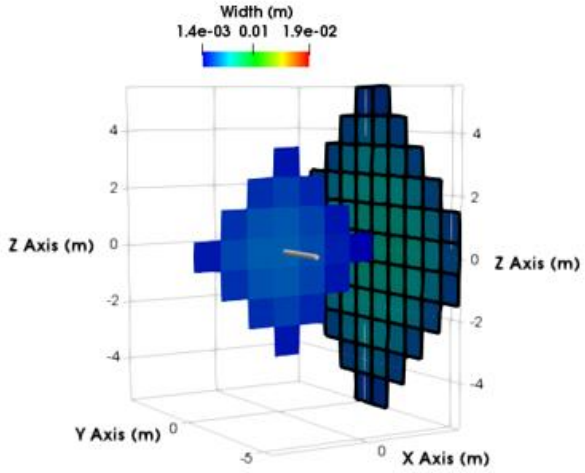

Figure 3.10: The width profile of the hydraulic fracture and natural fracture on intersection. The natural fracture has a higher width compared to the hydraulic fracture. It can be observed that upon intersection, the hydraulic fracture's width decreases as the fluid flows from the hydraulic fracture into the natural fracture.

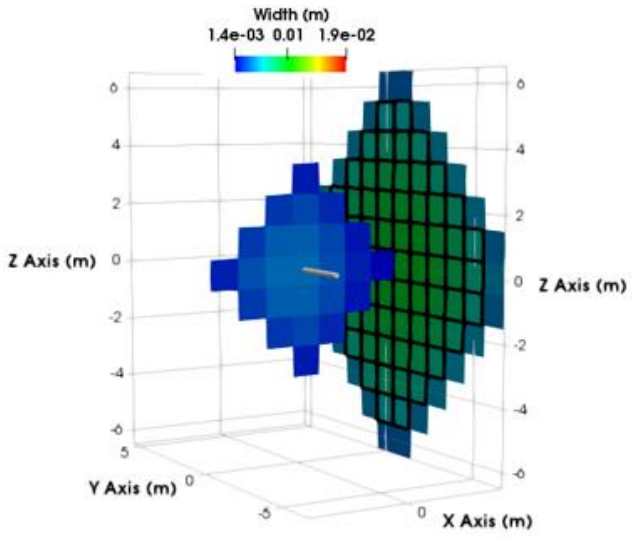

Figure 3.11: As the fluid is injected into the network after the intersection, it is observed that the natural fracture continues to propagate and increase in size. It can be observed that the elements of the hydraulic fracture closer to the natural fracture have a smaller width compared to the elements that are farther. This is because of the stress generated due to the opening of the natural fracture.

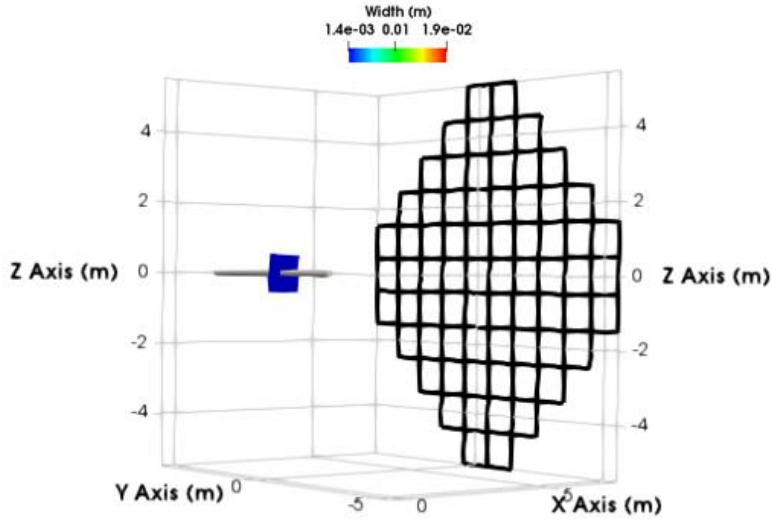

Figure 3.12: The fracture geometry at the start of pumping for the smaller natural fracture case. The black squares show the shape of the natural fracture used in the simulation.

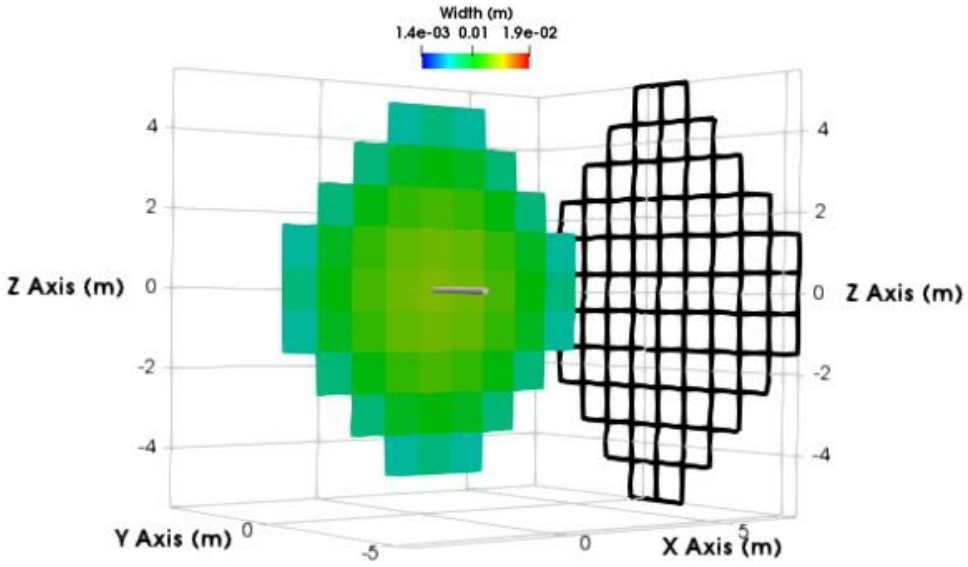

Figure 3.13: The radial shape of the hydraulic fracture and its width profile as it propagates towards the natural fracture.

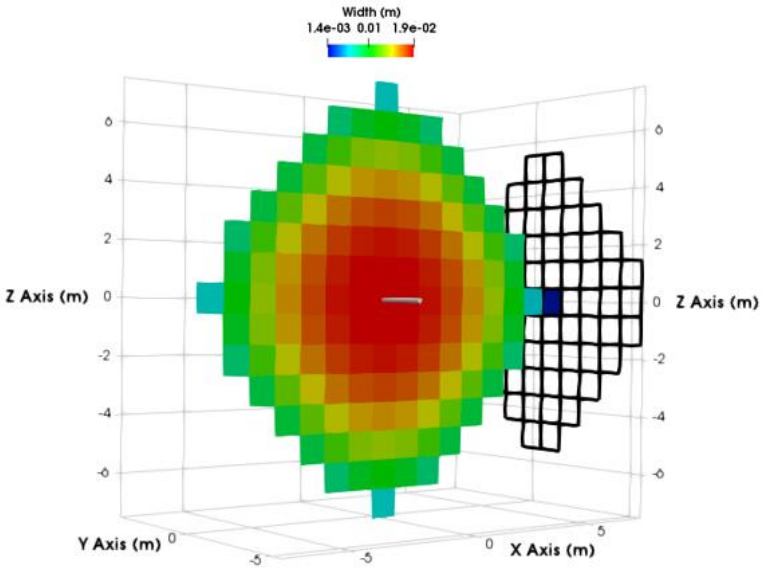

Figure 3.14: The snapshot of the simulation result (width of the fracture and the natural fracture) at the time when the hydraulic fracture intersects with the natural fracture.

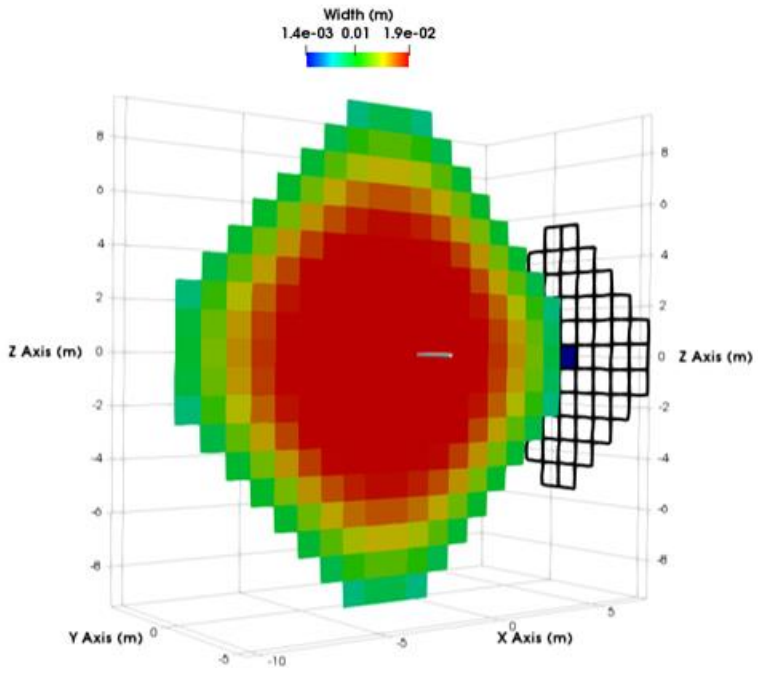

Figure 3.15: The figure shows the snapshot of the fracture width profile a few time steps after the intersection of the hydraulic fracture with the natural fracture. The tips of the hydraulic fracture are observed to propagate away from the natural fracture.

In the previous section, the interaction of hydraulic fractures with natural fractures is discussed. In these interactions, the natural fracture influences the geometry of the hydraulic fracture network when it comes in direct contact with the growing hydraulic fracture.

Growing hydraulic fractures can influence the stresses around natural fractures even before they come in direct contact with the natural fractures and this can lead to slippage of the natural fractures. The failed natural fractures, in turn, can alter the stresses further and affect the growth of the hydraulic fractures. The next section discusses the interaction of hydraulic fractures when they are not in direct contact with the natural fractures, and it will focus on the impact of natural fracture failure on the hydraulic fracture geometry. The algorithm described in Chapter 3 for hydraulic fracture-natural fracture interaction has been extended in this section, and two case studies are presented.

3.3 Extension of The Model

In the extended model, the slipped but hydraulically disconnected natural fractures are also included in the simulation. In case a hydraulically disconnected natural fracture element fails, that element's DDM coefficients are calculated and are included in the DDM (geomechanics) matrix (see section 2.2.1.1). The slipped natural fractures are assumed to be closed (approaching zero width). To capture the stresses generated from slipped but closed natural fractures in a computationally efficient manner, the coefficients of the displacement discontinuity matrix associated with the slipped natural fracture element are modified.

The coefficients of the DDM matrix associated with each element represents the effect of its opening and sliding on the stresses experienced on other elements. As the slipped and hydraulically disconnected natural fractures can only slide and cannot open

(due to the absence of high-pressure fracturing fluid in them), the coefficients representing the effect of their opening on the stresses acting on other elements are eliminated from the matrix. This elimination of the coefficients associated with opening direction displacement discontinuity helps in capturing additional information of the inability of the slipped elements to open in the system of equations mathematically. In addition, the frictional force acting on the slipped natural fractures is calculated explicitly. First, the modified DDM equation is solved along with fluid flow (inside hydraulic fracture) without frictional forces on the natural fractures, and the direction of the slip of natural fracture is calculated. This slip direction represents the tendency of the slipped natural fracture elements to move. The frictional forces are calculated and are applied in the opposite direction to this initial slip direction on all the failed natural fracture elements, as frictional forces will always resist the motion of the slipped elements, and the system is solved till the frictional forces acting on the slipped natural fractures converge to a given tolerance.

In the next section, the influence of a hydraulic fracture as it approaches the natural fracture is presented.

3.3.1 Stress Changes on a Natural Fracture due to an Approaching Hydraulic Fracture

A three-dimensional case is set up to understand the interaction between a hydraulic fracture and a natural fracture as the hydraulic fracture approaches the natural fracture (see Figure 3.16). In the simulation, the hydraulic fracture grows radially, and the stress changes on the natural fracture are computed and stored. The approach angle of the hydraulic fracture for the simulated case is set at 45 degrees (see Figure 3.16). The stresses acting on the natural fracture (on each element) are compared against the Mohr-Coulomb criterion to predict the failure of the natural fracture.

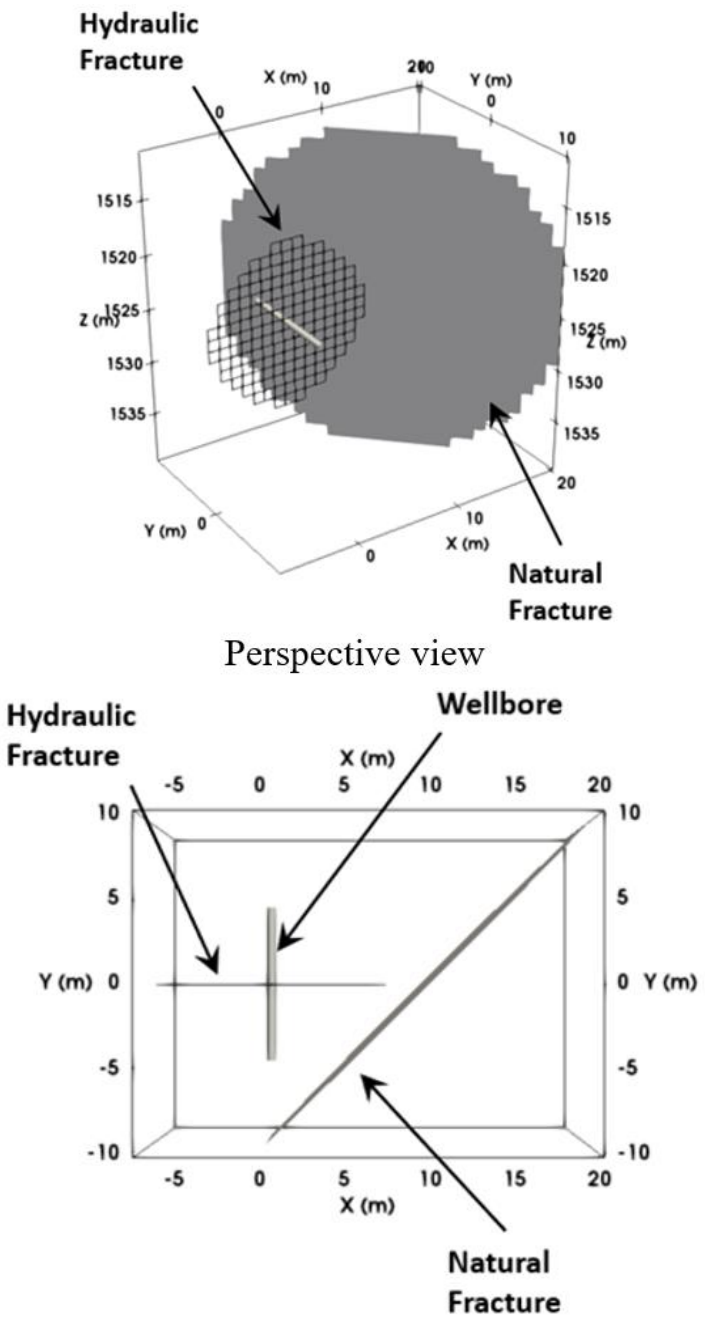

Figure 3.16: Geometry for pre-fracture intersection case.

Property	Value	Units
Youngs Modulus	2.5	million psi
Poisson's Ratio	0.25	
Sh_{min}	5000	psi
Sh_{max}	5200	psi
Reservoir Pressure	3800	psi
NF Cohesion	108.79	psi
NF Friction Coefficient	0.5	
Injection Rate	5	bbl/min
Run Time	60	s

Table 3.2: Parameters used in the simulation

3.3.1.1 Partial Failure of the Natural Fracture

It is observed that as the hydraulic fracture approaches the natural fracture, the natural fracture simultaneously experiences compressive and tensile stresses. The region of the natural fracture stress shadowed by the hydraulic fracture experiences compressive stresses due to the opening of the hydraulic fracture, whereas the region of the natural fracture in front of the hydraulic fracture experiences tensile stresses. Figure 3.17 and Figure 3.18 show the distribution of the stresses (normal and shear) acting on the natural fracture. In the figure, the stresses are acting on the plane of the natural fracture. Figure 3.19 shows a plot of the stress difference (δ_σ) on the plane of the natural fracture defined as follows

$$\delta_\sigma = \mu * \sigma_N + c - |\tau| \quad (3.1)$$

where μ is the coefficient of friction, σ_N is the normal stress acting on the plane of the natural fracture, c is the cohesion, and τ is the shear stress acting on the natural fracture. This quantity (stress difference) shows the likelihood of the natural fracture elements to fail. It can be observed from Figure 3.19 that the elements in front of the fracture tip are more likely to undergo shear failure, and the elements next to the hydraulic fracture are less likely to fail under shear. As a large natural fracture is likely to experience both compressive and tensile stresses, they may undergo partial failure.

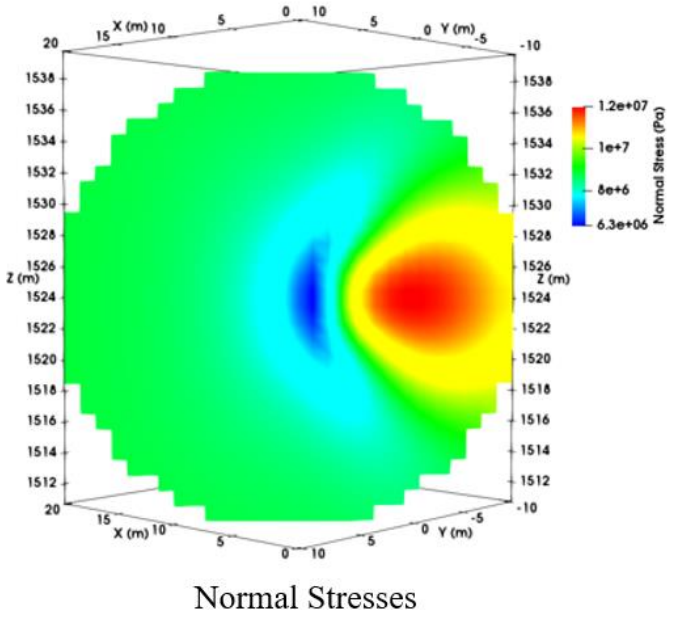

Figure 3.17: Normal stress acting on the plane of the natural fracture as the hydraulic fracture approaches.

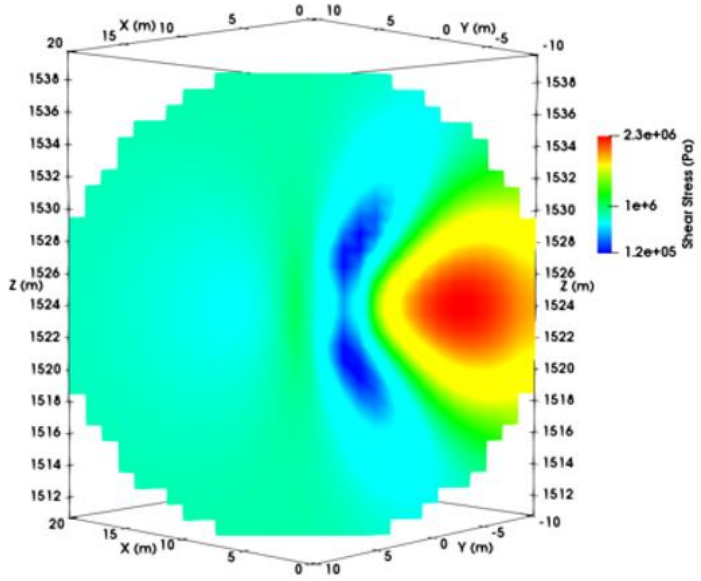

Figure 3.18: Shear stress acting on the plane of the natural fracture as the hydraulic fracture approaches.

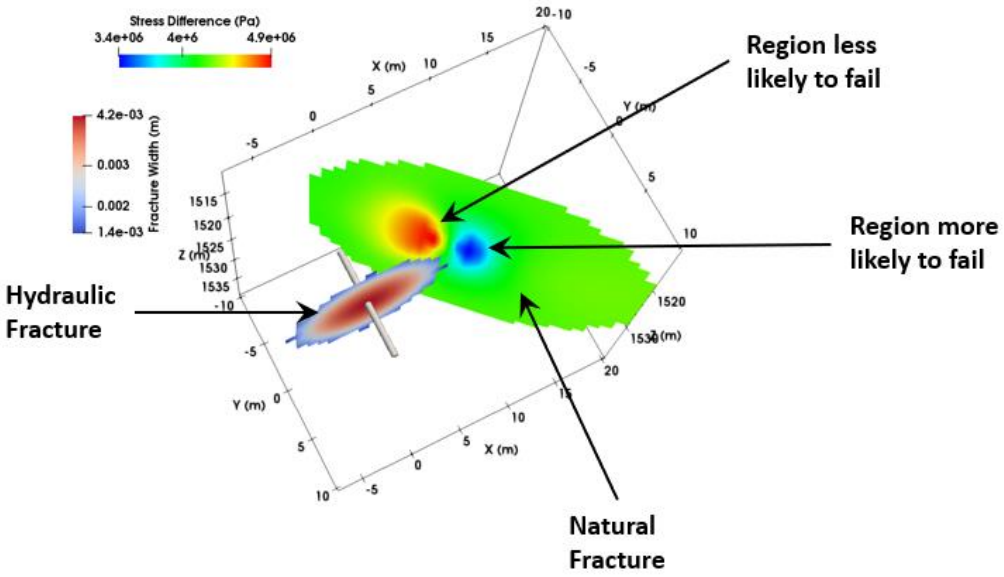

Figure 3.19: The figure shows the stress difference ($\mu\sigma_{normal} + c - |\sigma_{shear}|$) on the plane of the natural fracture. A lower stress difference represents a higher tendency of the natural fracture region to slip in shear.

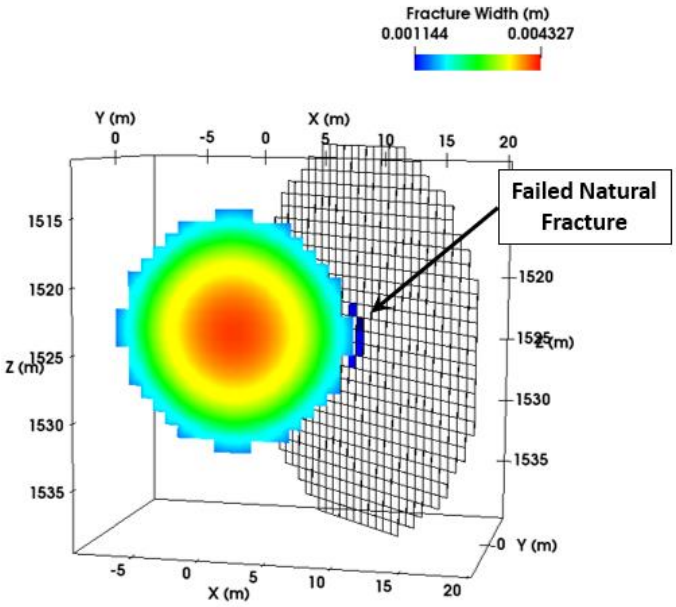

Figure 3.20: Figure shows the region of the natural fracture that fails before the hydraulic fracture intersects it (dark blue elements).

As the hydraulic fracture approaches the natural fracture, the magnitude of the stresses acting on the natural fracture starts to increase. This can lead to failure of the natural fracture even before its intersection with the hydraulic fracture. This was observed in the simulations, and the failed element along with the hydraulic fracture geometry is shown in Figure 3.20.

3.3.2 Hydraulic Fracture Crossing a Natural Fracture

In this case, the interaction of the hydraulic fracture with a natural fracture as the hydraulic fracture crosses the natural fracture is examined. A three-dimensional case with the same parameters as the previous case is setup. The approach angle of the hydraulic fracture is set at 90 degrees. Figure 3.21 shows the geometry of the case. In this case, the hydraulic fracture grows past the natural fracture, and the stress distribution on the natural

fracture is computed and recorded for different distances between the hydraulic fracture and the natural fracture.

Typically, the problem of hydraulic fracture-natural fracture interaction is studied for two-dimensional problems, and the intersection is treated as a point of contact. Although, in reality, the intersection between a three-dimensional hydraulic fracture and natural fracture can only be described by a line segment that changes in size as the hydraulic fracture crosses the natural fracture (see Figure 3.22). In the simulations conducted, as the hydraulic fracture (a disk) grows towards the natural fracture (a plane), the natural fracture experiences tensile stresses generated due to the point (fracture tip) on the fracture circumference that is closest to it. As the hydraulic fracture crosses the natural fracture, the natural fracture experiences stress due to two points (fracture tips) on the circumference of the hydraulic fracture that lie on the natural fracture. Hence, unlike in two-dimensional investigations, fracture crossing is not a discrete process, and the natural fracture continuously experiences the stresses generated from the hydraulic fracture tips.

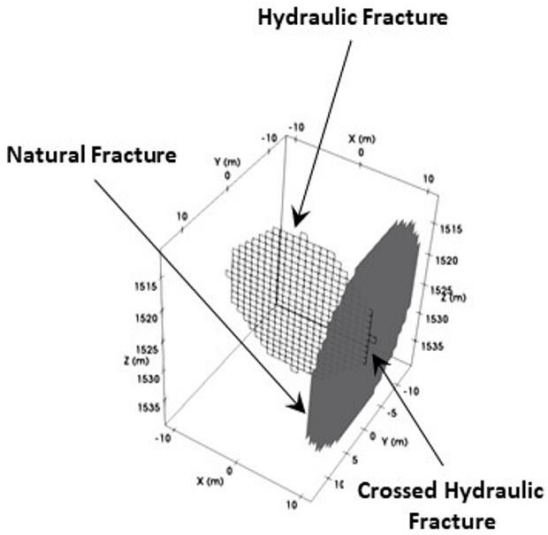

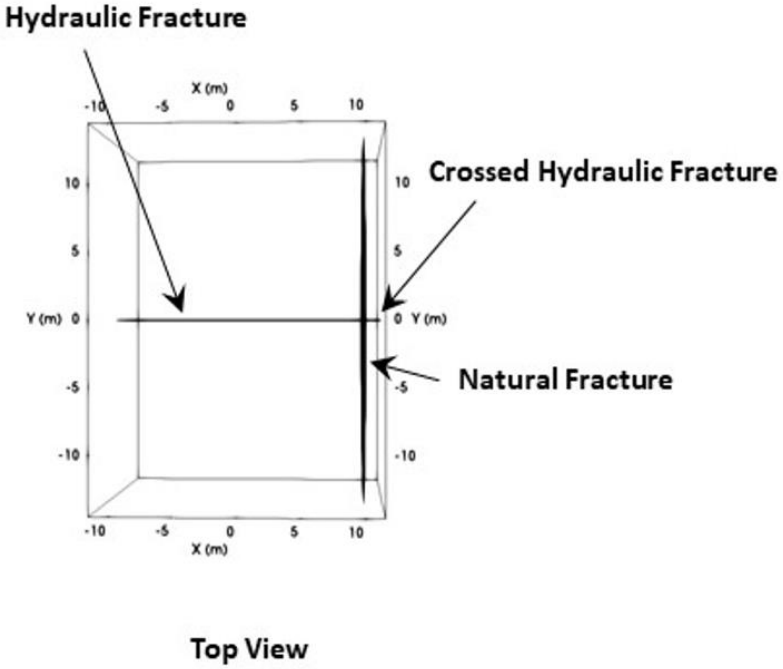

Figure 3.21: Geometry for the post-fracture intersection case.

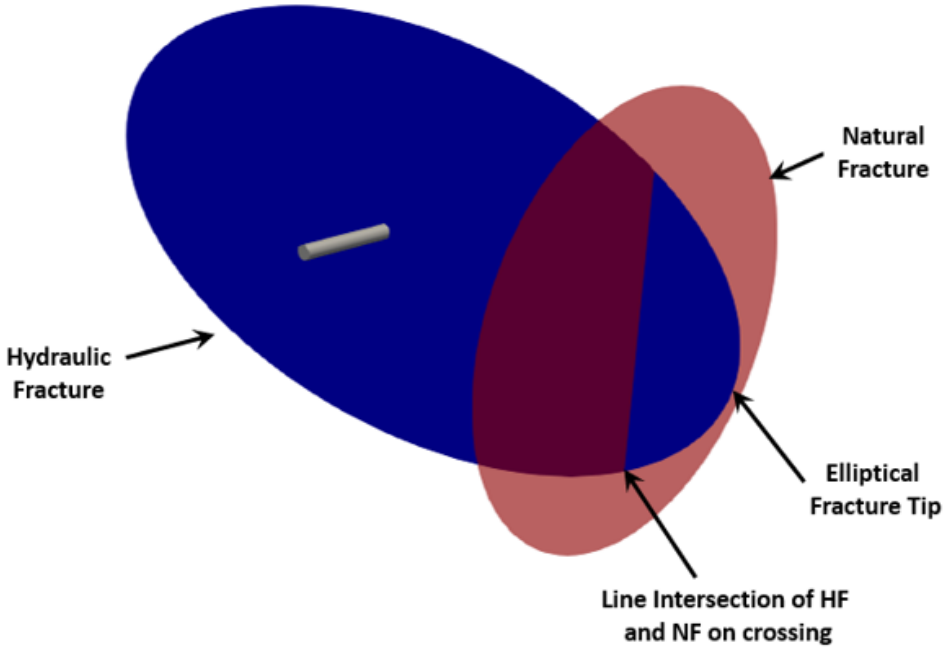

Figure 3.22: Three-dimensional intersection of a hydraulic fracture and a natural fracture in 3-dimensions.

The shear and normal stresses acting on the plane of the natural fracture as the hydraulic fracture crosses has been shown in Figure 3.23 and 3.24, respectively. The shear stresses are increased in the region near to the intersection of the fracture tip whereas the normal stress acting on the plane of the natural fracture is decreased. Both of these changes lead to an increased likelihood of the natural fracture to fail under shear. As the hydraulic fracture tips are always present on the natural fracture in case the hydraulic fracture crosses the natural fracture, the likelihood of the natural fracture failing and increasing the complexity of the fracture network increases significantly. It can be observed in Figure 3.24 that the model predicts two high-stress regions on the natural fracture as the hydraulic fracture crosses it. This behavior can result in simultaneous crossing and intersection of the hydraulic fracture with the natural fracture and increase the complexity of the created fracture network.

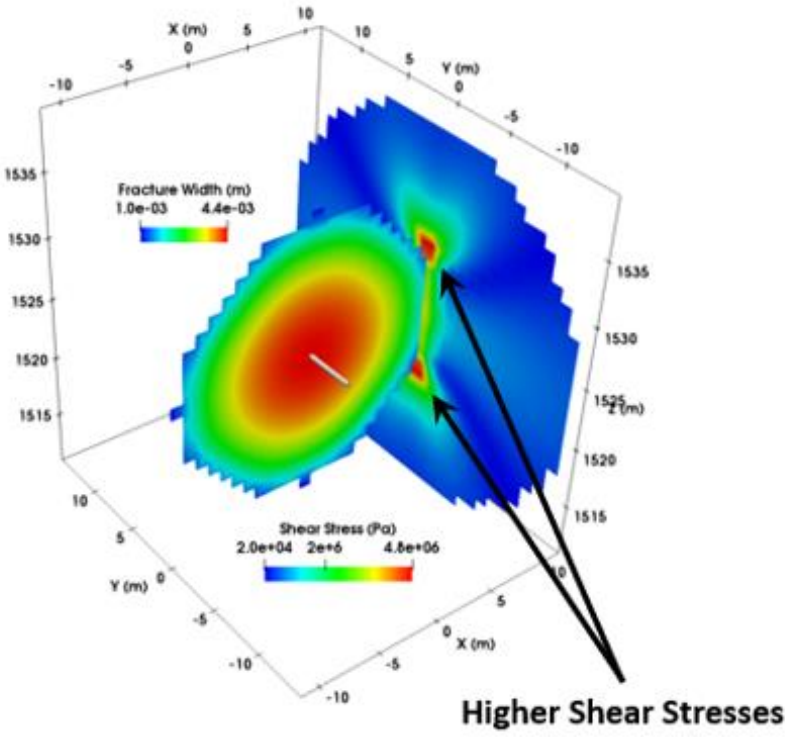

Figure 3.23: Figure shows the magnitude of shear stresses acting on the plane of the natural fracture.

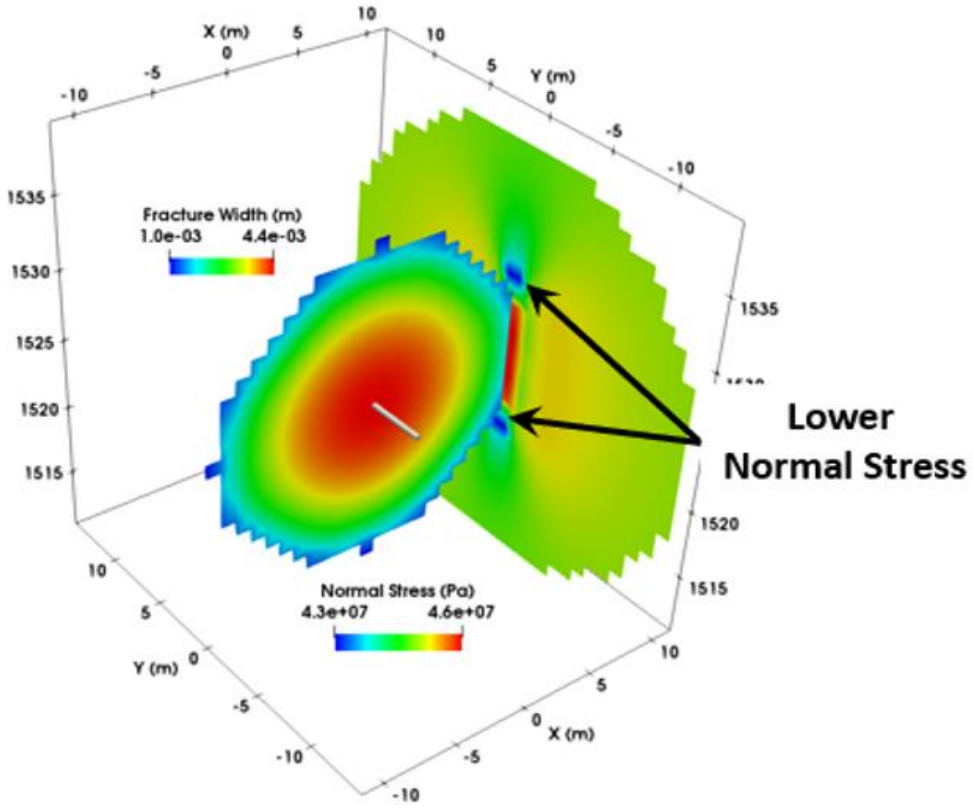

Figure 3.24: Figure shows the magnitude of the normal stresses acting on the plane of the natural fracture.

3.4 DISCUSSION

It is observed that natural fractures play an important role in determining the propagation direction of the hydraulic fractures. At high natural fracture density, the propagation direction of a hydraulic fracture is dominated by the orientation of natural fractures rather than the far-field stress magnitude and direction. The density of the natural fractures also affects the complexity of the final created fracture geometry.

In this chapter, we have analyzed the stresses around the natural fracture generated due to a three-dimensional hydraulic fracture as it approaches and then crosses the natural fracture in a field-scale scenario. The compressive and tensile stresses acting on the natural

fracture as the hydraulic fracture approaches have been presented and discussed. As the hydraulic fracture crosses the natural fracture, the stresses acting on the plane of the natural fracture due to the circumferential fracture tip of the radial hydraulic fracture are computed and shown to differ substantially from the 2-D cases. This investigation gives insight and presents the differences in stresses generated due to the shape of the hydraulic fracture and its possible effects.

It is shown that a natural fracture inclined at an angle to an approaching hydraulic fracture experiences compression in one region (due to the stress shadow of the growing hydraulic fracture) and tension in other regions (in front of the approaching hydraulic fracture tip). The generated stresses can fail the natural fracture partially. The failure of the natural fracture relaxes the stresses around it, which can modify the direction of propagation of the approaching hydraulic fracture. In addition, if the elliptical front of the hydraulic fracture crosses an intact planar natural fracture, the three-dimensional geometry results in a line of intersection (between natural fracture and hydraulic fracture). This can lead to failure of the natural fracture even after the elliptical front has partially crossed the natural fracture. Such an interaction can allow the hydraulic fracture to both cross the natural fracture and activate (or dilate) it. These effects cannot be captured by two-dimensional simulations. This work improves our understanding of the interaction between hydraulic fractures and natural fractures. The novel results provide new insights into the mechanisms responsible for the complexity that is often observed in hydraulic fractures.

3.5 CONCLUSION

We used the model presented in Chapter 3 to study the effect of natural fracture density, natural fracture orientation, and fracture height on the geometry of the fracture network. In addition, the interaction of a three-dimensional hydraulic fracture with a natural fracture

has been studied in detail using an extended model. The following conclusions can be drawn from these investigations:

- Natural fracture density can influence the complexity of the created fracture network. Higher natural fracture density increases the probability of the intersection of the growing fracture with natural fractures. This may redirect the growing fracture towards the natural fracture direction, creating fracture complexity.
- Two competing forces influence the overall dimension of the fracture network, far-field stresses and natural fractures orientation. The magnitude and the orientation of these guiding forces are important factors and should be accounted for in determining fracture and well spacing.
- The region near the intersection of the hydraulic fracture and the natural fracture experiences high stresses due to fracture opening. These stresses suppress the growth of the fractures and can limit the height of the fracture intersection.
- Stresses generated by a hydraulically connected fracture can suppress the growth of smaller fractures in its vicinity.
- It is observed that the natural fracture experiences both compressive and tensile stresses due to an approaching hydraulic fracture. This can result in partial failure of the natural fracture.
- The compressive stresses acting on the wing of the natural fracture closer to the hydraulic fracture will force the hydraulic fracture to grow along the wing away from the original hydraulic fracture in case of fracture intersection.
- The modified stresses near the growing hydraulic fracture can result in the failure of the natural fracture even before its intersection with the natural fracture.
- The failure of the natural fracture before its intersection with the hydraulic fracture can modify the stresses near the natural fracture and modify the approach angle as

the propagating hydraulic fracture approaches the natural fracture in a modified stress field.

- The intersection process of hydraulic fracture and natural fracture is a continuous (three-dimensional) process rather than a discrete one (as in the case of two-dimensional cases).

Chapter 4: Proppant Transport in Fracture Networks

4.1 INTRODUCTION

The success of hydraulic fracturing treatment requires the formation of proppant-filled conductive pathways connecting the created fracture area to the wellbore. The goal of the design engineer is to maximize the area of the pay zone connected to the wellbore with a propped channel. It is, therefore, imperative to understand the transport of proppant in fracture networks.

Simulators are often employed for determining the final distribution of proppant inside the fracture. Such simulators typically assume idealized single planar fracture propagation to keep the computational time required to solve the fracture growth problem tractable, although, several studies have shown that fractures can be complex due to their interaction with natural fractures and bedding planes (Warpinski and Teufel, 1987; Cipolla et al., 2008).

A few experimental attempts have been made to understand proppant transport in fracture networks. These studies are usually conducted with the assistance of Hele-Shaw like cells with fixed geometries (Sahai et al., 2014; Tong and Mohanty, 2016). Although these studies improve our understanding of proppant transport in fracture networks, they are unable to predict the complex behavior fractures exhibit during their growth or capture the effect of variation in fracture geometry, width, complexity, etc., which can significantly alter the distribution of proppant. For example, the opening of the fractures alters the stresses, which can influence the opening of other connected fractures in its vicinity. The region of intersection connecting a hydraulic fracture with an open and hydraulically connected natural fracture experiences stresses due to the opening of both the fractures. This can limit the growth of the fracture in the region near the connection and create

bottlenecks for the flow of proppant. This behavior can become much more complicated in three-dimensions, where an elliptical front of the growing hydraulic fracture intersects the natural fracture.

Typically, hydraulic fracturing is performed to enhance the production rate for low permeability formations. In such formations, due to the low leak-off rate, the fracture closure can take up to several days. During this period, the proppant can redistribute inside the fracture and may form a proppant bank at the bottom of the fracture (Warpinski et al., 2009). This can result in a large area of the fracture remaining unpropped. Although these unpropped regions can exhibit residual permeability (Wu et al., 2017), they can severely limit the production of hydrocarbons.

Proppant transport is a complicated multi-physics process. The proppant distribution is determined by the relative magnitude of the various physical parameters involved. To understand the behavior of proppant transport in complex fracture networks, the fully coupled three-dimensional hydraulic fracturing simulator presented in Chapter 2 has been used in this chapter. The chapter will discuss the impact of fracture complexity due to the interaction of growing hydraulic fractures with natural fractures and bed boundaries.

In the next section, we present an investigation of the effect of reservoir permeability on the settling behavior of proppant. This allows us to better understand the redistribution of proppant in fractures after the end of pumping and its impact on fracture conductivity.

4.2 Effect of the Permeability of Formation on Proppant Transport

In order to understand the effect of reservoir permeability (fluid leak-off rate) on proppant transport, four cases are simulated. The simulations are conducted for a single

radially growing vertical planar hydraulic fracture. A planar fracture is chosen for this study to ignore the effect of fracture complexity on the transport of proppant and only capture the effect of reservoir permeability. Table 4.1 shows the properties used for the simulation. The proppant is pumped along with the fracturing fluid to create the fracture, and simulation is continued after the end of pumping. The post-pumping simulation allows us to study the redistribution of proppant as the fracture closes. After the end of pumping, the simulation is run for sufficient time so that the proppant bank settles to its final configuration and doesn't change with time.

Table 4.1: Parameters used for simulation study of the effect of reservoir permeability on proppant settling.

Parameter	**Value**	**Units**
Young's Modulus	2	million psi
Poisson's Ratio	0.25	
Sh_{min}	3000	psi
Sh_{max}	3125	psi
Injection Rate	2	bbl / min
Fracturing Fluid Viscosity	1	cP
Pumping Time	20	minutes
Simulation Time	380	minutes
Maximum Proppant Concentration	0.1	
Reservoir Porosity	10	%
Reservoir Pressure	2000	psi

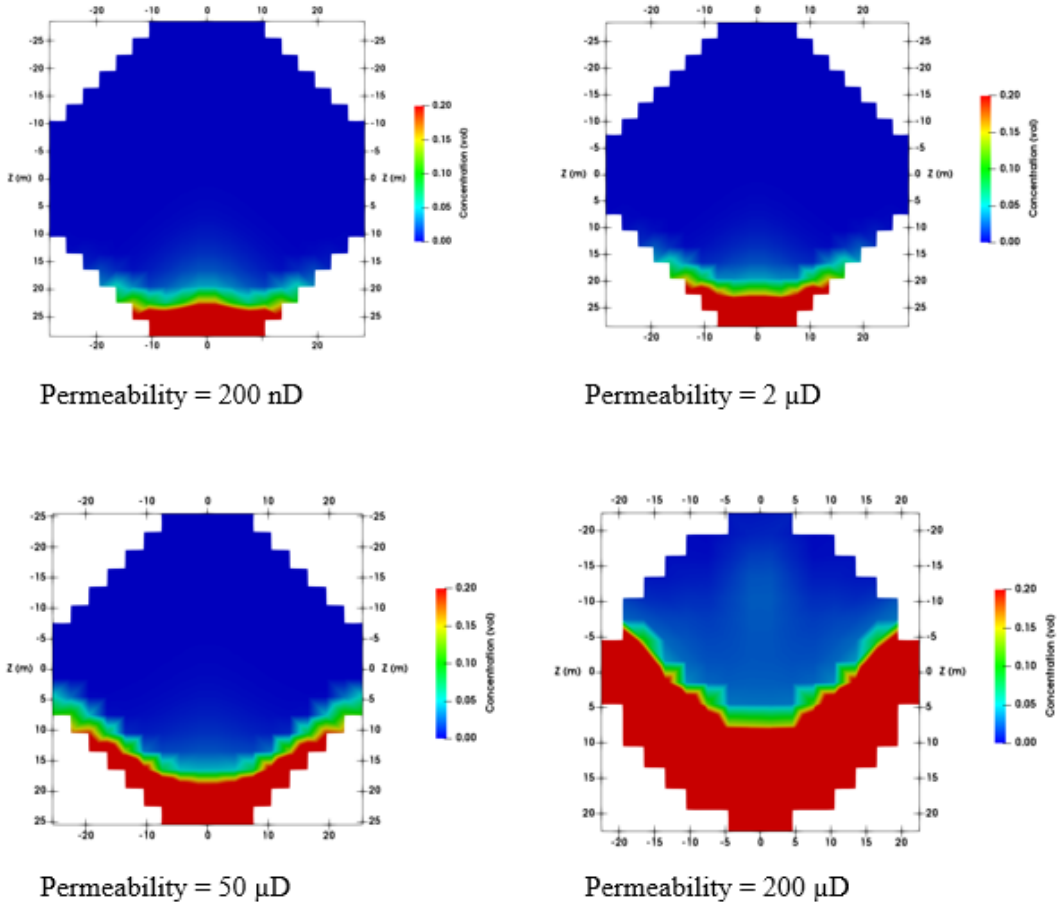

Figure 4.1: Proppant distribution in vertical planar fractures for four different permeabilities (200nD, 2µD, 50µD, 200µD). The color shows the volumetric concentration of proppant.

Four different cases are run with reservoir permeability of 200nD, 2µD, 50µD, and 200µD. The proppant size in the simulation is 100 mesh. The final distribution of the proppant for all the four cases is shown in Figure 4.1. It is observed that as the permeability increases, the created fracture area decreases (see Figure 4.2). This happens because as more fluid leaks-off into the formation, the volume of the fracturing fluid available to create the fracture decreases. Also, as the permeability of the formation increases, the percent area

of the fracture that is propped increases (see Figure 4.3). This happens because in low permeability formations, the fracture takes a much longer time to close compared to high permeability formations. As a result, in low permeability formations the proppant gets more time to settle before the fracture closes and holds the proppant in place.

In high permeability formations, the fracture closes on the proppant and traps it before the proppant can settle to the bottom of the fracture. Hence, in high permeability formations, the fracture has a higher percentage of the created fracture area that remains propped.

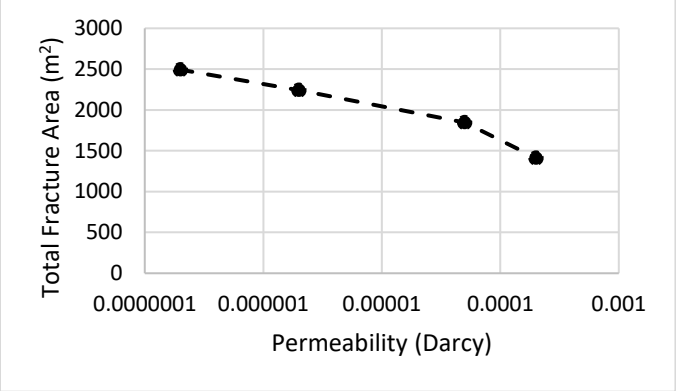

Figure 4.2: Area of the fracture created for the simulated cases with different permeability.

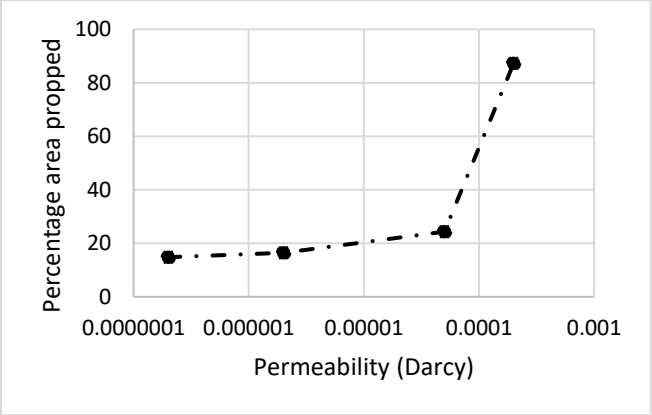

Figure 4.3: Percentage area of the fracture propped. The propped area is defined as the region containing a volumetric concentration of proppant greater than 0.001.

It can be seen from the results presented in this section that for typical low permeability shale reservoirs, the proppant particles are expected to settle to the bottom of the fracture and create a proppant bank.

4.3 Effect of Natural Fractures on Proppant Transport

We next investigate the effect of natural fractures on the transport of proppant. The properties of the natural fractures are varied, and the effect on the final configuration of the proppant is studied.

4.3.1 Effect of the Orientation of Natural Fractures

A case is set up to investigate the effect of natural fracture orientation on the transport of proppant. The case has a single hydraulic fracture originating from a horizontal wellbore. The hydraulic fracture is contained in the conducted simulations using high fracture strength (K_1^c) layers. This is done to limit the height growth of the hydraulic fracture in order to have a low stress shadow acting on the natural fracture. This allows the natural fracture to open completely on intersections. A natural fracture is placed at an angle to the hydraulic fracture. The orientation of the natural fracture with respect to hydraulic

fracture is varied to capture the effect of natural fracture orientation on the transport of proppant. Four cases are run with natural fracture orientation 45^o, 60^o, 75^o, and 90^o. The geometry of the case for 90^o orientation of the natural fracture is shown in Figure 4.4. The natural fracture is modeled as a closed plane of weakness with zero cohesion. This is done to ensure that the hydraulic fracture gets hydraulically connected to the natural fracture. Also, the minimum horizontal stress is kept equal to the maximum horizontal stress to avoid any bias in the transport of proppant due to the far-field stresses. The hydraulic fracture starts propagating from a horizontal wellbore and intersects with the natural fracture. Table 4.2 shows the parameters used in the simulations.

Table 4.2: Parameters used in the simulation study of the effect of natural fracture orientation on proppant transport.

Parameter	**Value**	**Units**
Young's Modulus	2	million psi
Poisson's Ratio	0.25	
Sh_{min}	3000	psi
Sh_{max}	3000	psi
Injection Rate	1	bbl / min
Pumping Time	20	minutes
Simulation Time	490	minutes
Maximum Proppant Concentration	0.1	
Proppant Size	40-60#	

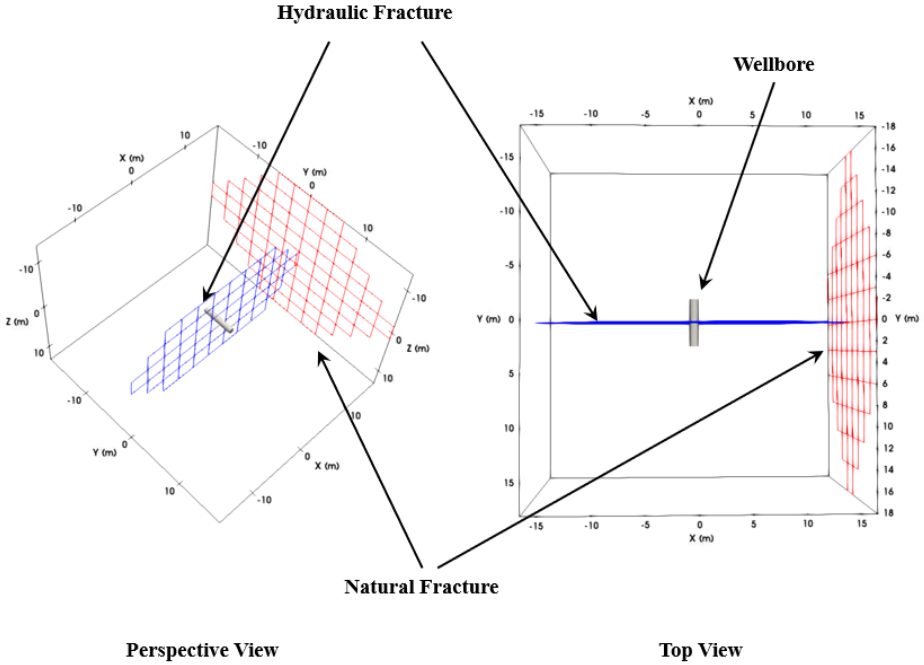

Figure 4.4: The geometry of the case used for investigating the effect of natural fracture orientation on the transport of proppant.

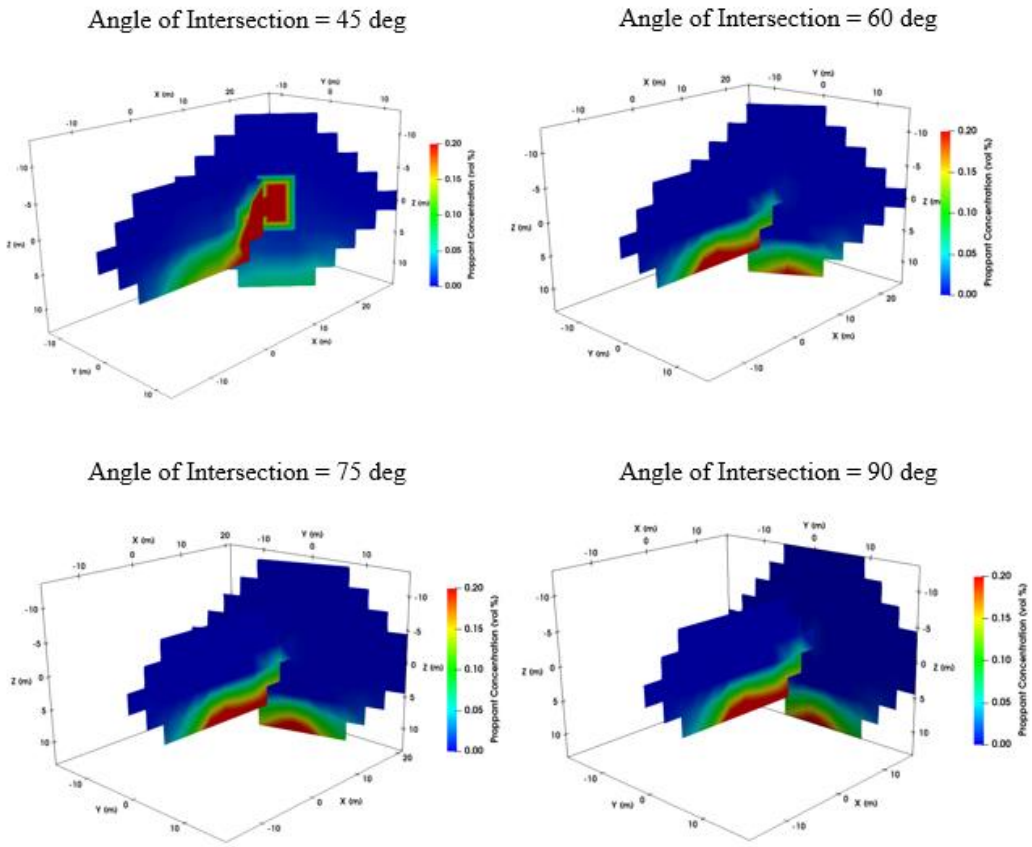

Figure 4.5: Proppant distribution in complex fracture networks for different angles of intersection.

Figure 4.5 shows the final distribution of proppant in the created fracture network for the four cases. The result is analyzed in terms of the mass of the proppant transported into the natural fracture. The mass of the proppant in the hydraulic fracture and the natural fracture are shown in Figure 4.6 and Figure 4.7, respectively. It is observed that the mass of the proppant in the natural fracture increases as the orientation of the natural fracture changes from 90^{o} to 75^{o} (Figure 4.8). This happens as one of the wings of the natural

fracture moves away from the hydraulic fracture while the other wing comes closer. This reduces the stress shadow on the hydraulic fracture due to the opening of the natural fracture and increases the width of the hydraulic fracture near the intersection region. As the angle decreases further, the stress from the wing of the natural fracture closer to the hydraulic fracture starts to exert a stress shadow strong enough to reduce the width of the intersection region. Overall, we see the maximum amount of proppant getting transported to the natural fracture when the orientation of the natural fracture is 75^{o}. Also, for 45^{o}, we observe the accumulation of proppant at the intersection region, which is not observed in other cases. This signifies the possible occurrence of a screen out of proppant at the intersection.

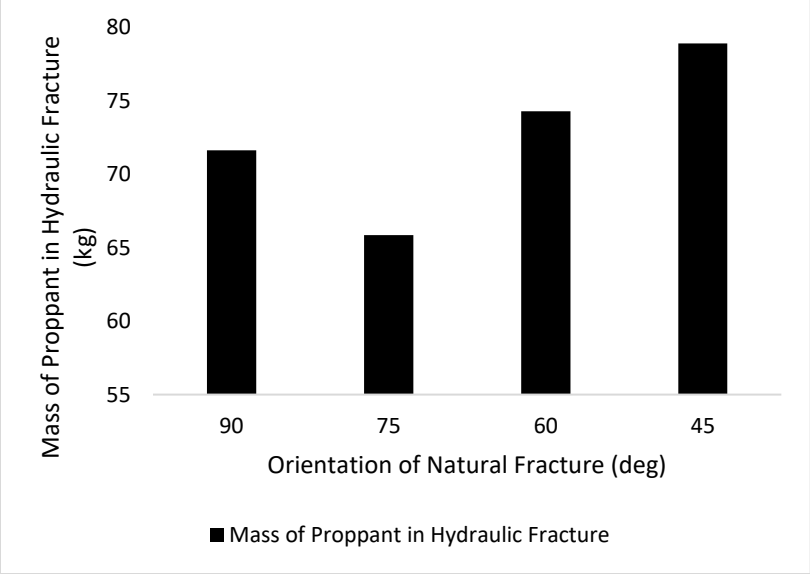

Figure 4.6: The figure shows the mass of the proppant in the hydraulic fracture after proppant settling.

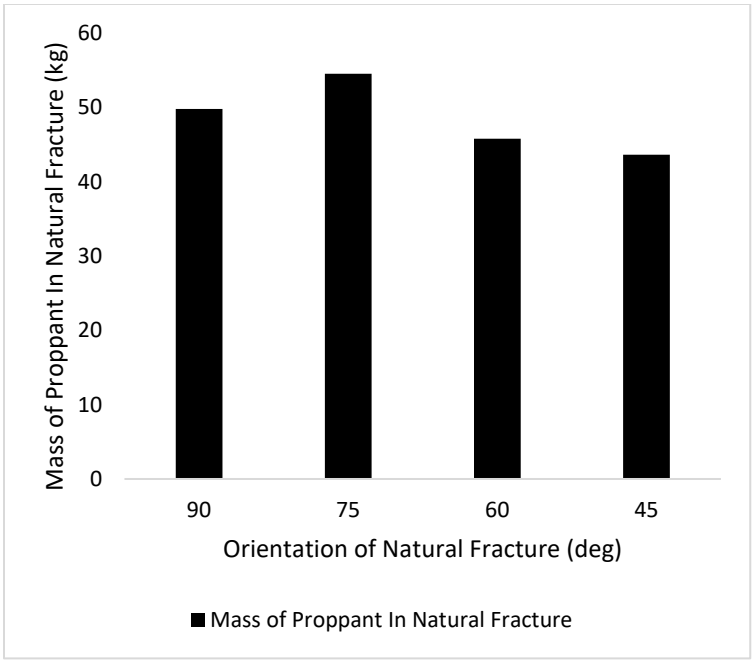

Figure 4.7: The figure shows the mass of the proppant in the natural fracture after proppant settling.

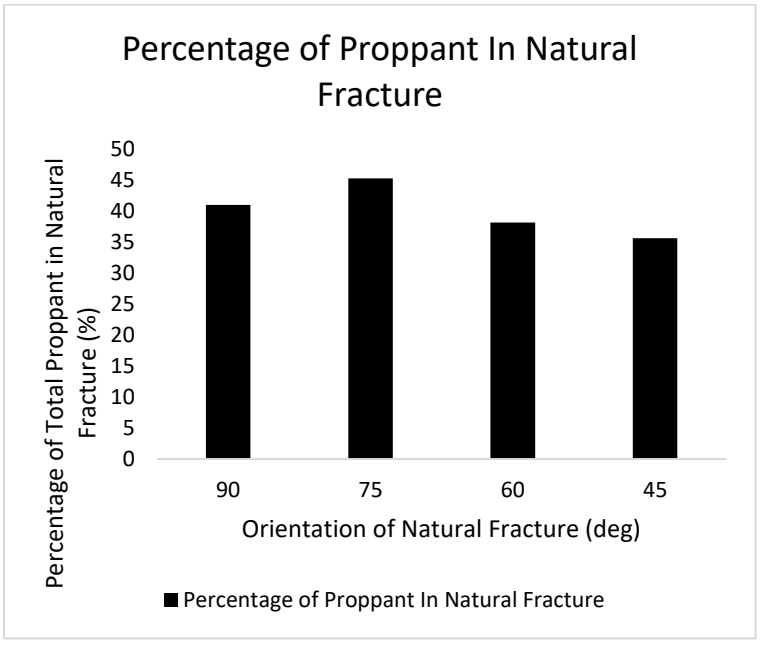

Figure 4.8: The figure shows the percentage mass of the proppant in the natural fracture after proppant settling.

4.3.2 Effect of Stress Contrast on Transport of Proppant in Natural Fractures

The effect of stress contrast (the difference between the value of maximum stress and minimum stress) on proppant transport in fracture networks is investigated using the model. A radially growing hydraulic fracture is allowed to intersect with a natural fracture at an orientation of 90^{o}. In these simulations, the hydraulic fracture opens against the minimum horizontal stress, and the natural fracture opens against the maximum horizontal stress. Figure 4.9 shows the geometry used for simulating the case. Four cases are simulated with different stress contrasts (0 psi, 50 psi, 100 psi, 125 psi), and the results are analyzed. The parameters used in the simulation are given in Table 4.3. Figure 4.10 shows the final distribution of proppant in the natural fracture for the four cases.

Table 4.3: Parameters used for simulation of the effect of stress contrast on proppant transport.

Parameter	**Value**	**Units**
Young's Modulus	2	million psi
Poisson's Ratio	0.25	
Sh_{min}	3000	psi
Injection Rate	5	bbl / min
Pumping Time	1	minutes
Simulation Time	80	minutes
Maximum Proppant Concentration	0.1	

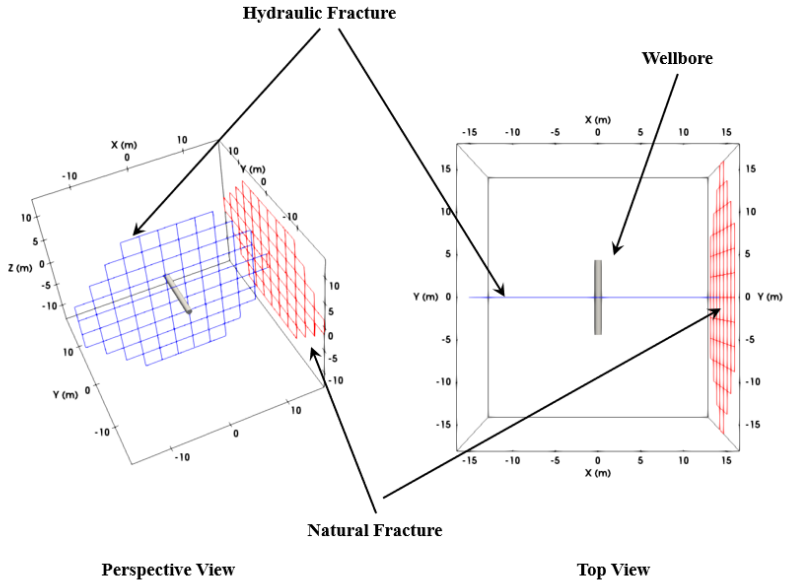

Figure 4.9: The geometry of the case used for investigating the effect stress contrast on the transport of proppant.

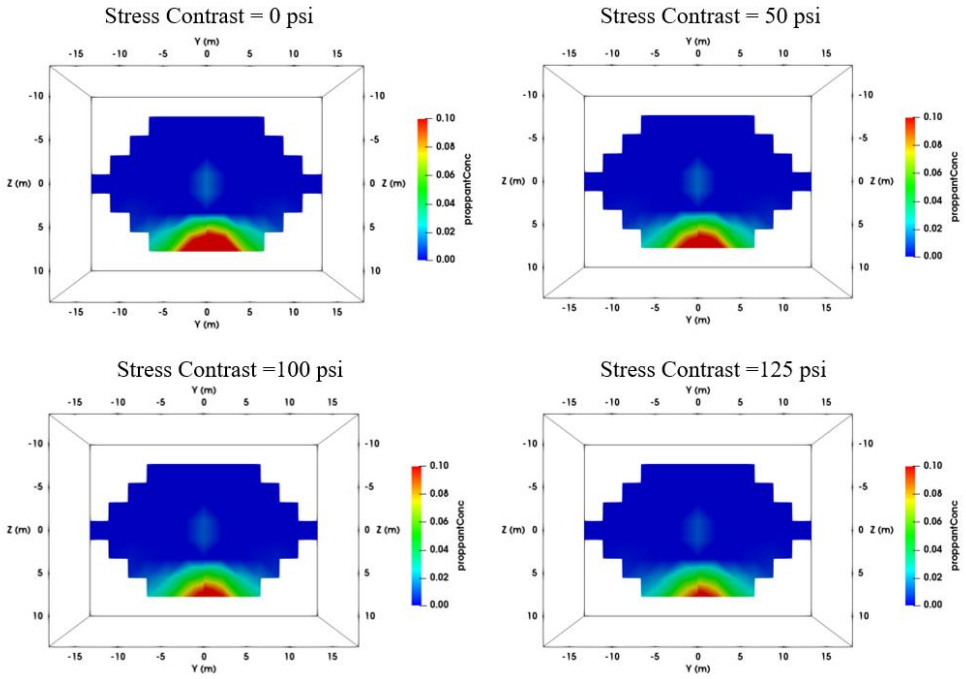

Figure 4.10: The distribution of proppant after fracture closure for different stress contrast.

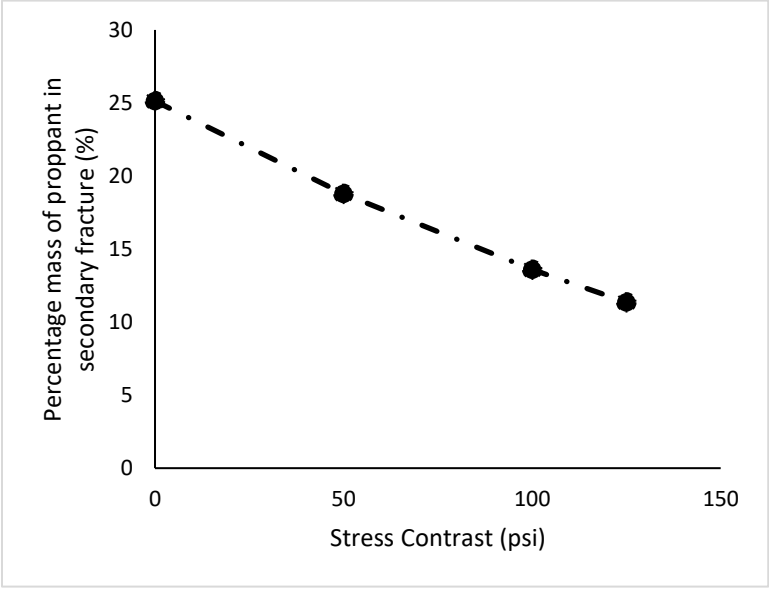

Figure 4.11: Percentage of proppant pumped in natural fracture for different stress contrast values.

It is observed that with an increase in stress contrast, the percentage of total proppant pumped going into the natural fracture decreases. This happens as the width of the natural fracture reduces due to higher stress acting on it (as the natural fracture is opening against the maximum stress). This reduced width increases the retardation factor of the proppant particles, and less proppant flows into the natural fracture.

4.3.3 Effect of Size of Proppant on Proppant Transport In Natural Fractures

A simulation case is set up as shown in Figure 4.12 to investigate the effect of proppant size on the transport of proppant in a fracture network created due to interaction with natural fractures. In this case, a hydraulic fracture propagates radially from a horizontal wellbore, and a natural fracture is placed along the Sh_{max} direction in the path of the growing hydraulic fracture in order to simulate fracture intersection. Proppant is injected along with the fracturing fluid. Two simulation cases are run using the model. In the first case, 40-70 mesh size of proppant is pumped with the fracturing fluid, and in the second case, a smaller proppant of 100 mesh size is pumped. In both cases, the intersection of the hydraulic fracture with the natural fracture is modeled, and the transport of proppant into the natural fracture is studied. The parameters used for the simulation of the cases are shown in Table 4.4.

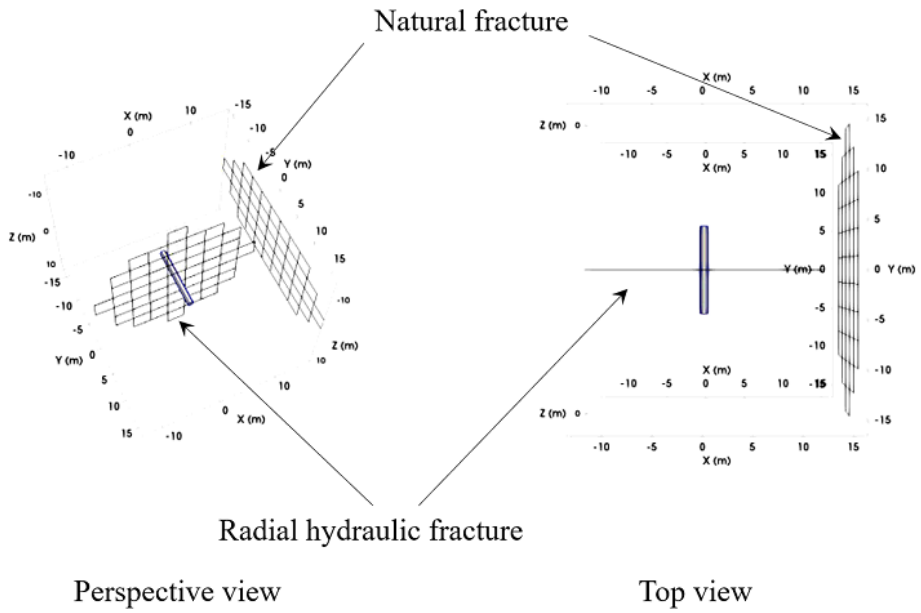

Figure 4.12: Geometry (perspective view and top view) of the case used for investigating the effect of proppant size on proppant transport.

After the intersection with the natural fracture, the proppant and fracturing fluid starts to flow in the natural fracture. In the case of the 40-70 mesh size proppant, it is observed that the proppant concentration starts to increase in front of the region of the intersection between hydraulic fracture and natural fracture (see Figure 4.13). For the 100 mesh size proppant, this increase in concentration is not observed (see Figure 4.14).

The region of intersection experiences higher stresses as the compressive stresses due to the opening of both hydraulic and natural fractures act on it. These higher stresses also hinder the growth of the fracture near the intersection region and create a bottleneck for the flow of slurry. This results in the width of the fracture in this region being small compared to the width of elements near other tips, where the compression due to opening of only one fracture (hydraulic or natural fracture) is experienced. This reduced width is comparable to the proppant diameter and results in a bottleneck for proppant flow. We

observe screenout occurring (high concentration of proppant particles blocking the flow of slurry) as the proppant starts accumulating in front of the intersection region. In the model, no explicit criterion is used to predict screenout, but it occurs as a result of the correlation used for retardation. The correlation accounts for the ratio of proppant diameter and width of the fracture on the velocity of proppant particles. This is not observed in the case where smaller proppant is used as the fracture width is still large enough to allow smaller proppants to flow through the intersection region without much retardation.

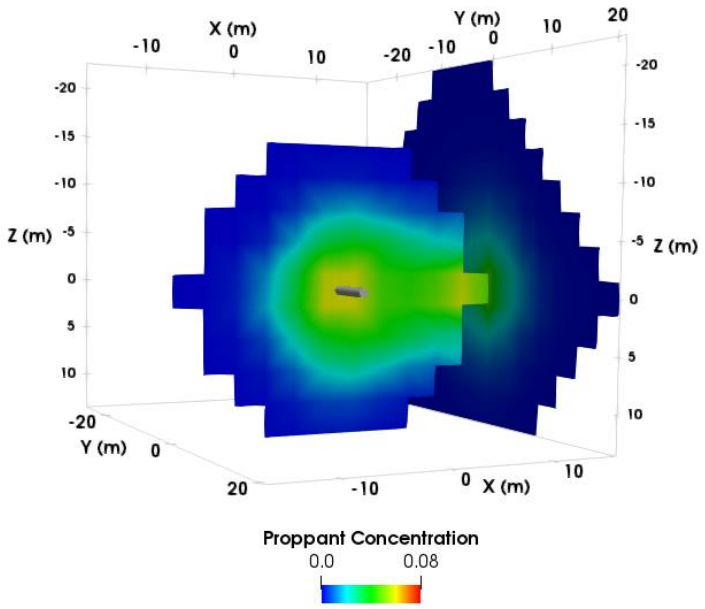

Figure 4.13: The figure shows the concentration of proppant particles in a fracture network with for proppant size of 100 mesh.

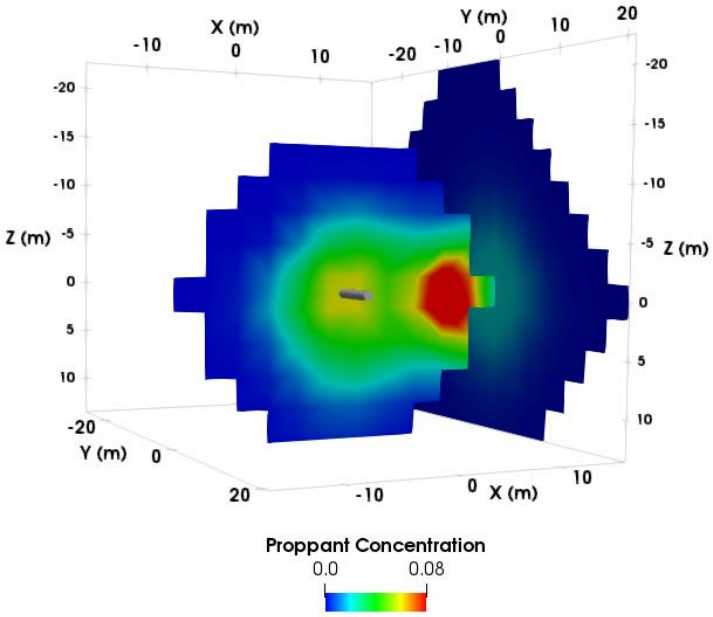

Figure 4.14: The figure shows the concentration of proppant particles in a fracture network with for proppant size of 40-70 mesh.

Table 4.4: Parameters used for investigation of the effect of proppant size on proppant transport

Parameter	**Value**	**Units**
Young's Modulus	2.15	million psi
Poisson's Ratio	0.25	
Sh_{min}	3000	Psi
Sv(vertical stress)	3060	Psi
Injection Rate	5	bbl / min
Pumping Time	400	Seconds
Maximum Proppant Concentration	0.1	

4.4 Proppant Transport in Complex Fracture Networks Created Due To Interaction with Natural Fractures

In order to understand the effect of multiple natural fracture intersections on the transport of proppant, a simulation case is set up (see Figure 4.15 and Figure 4.16). To simulate complex fracture network creation, a hydraulic fracture is allowed to grow radially from a horizontal well. Two natural fractures are placed in the simulation domain, and their interaction with the growing hydraulic fracture is investigated. The first natural fracture is perpendicular to the Sh_{max} direction and is at a distance of 5 m from the hydraulic fracture. It has been placed symmetrically so that at the time of the intersection the hydraulic fracture intersects the center of the natural fracture. The second natural fracture is parallel to the direction of the Sh_{max}. The distance between the hydraulic fracture and the second natural fracture is 5 m. It is placed asymmetrically to the first natural fracture to understand the behavior of proppant transport for an asymmetric intersection. Proppant transport is simulated during the fracture growth process to predict the distribution of proppant inside the fracture network.

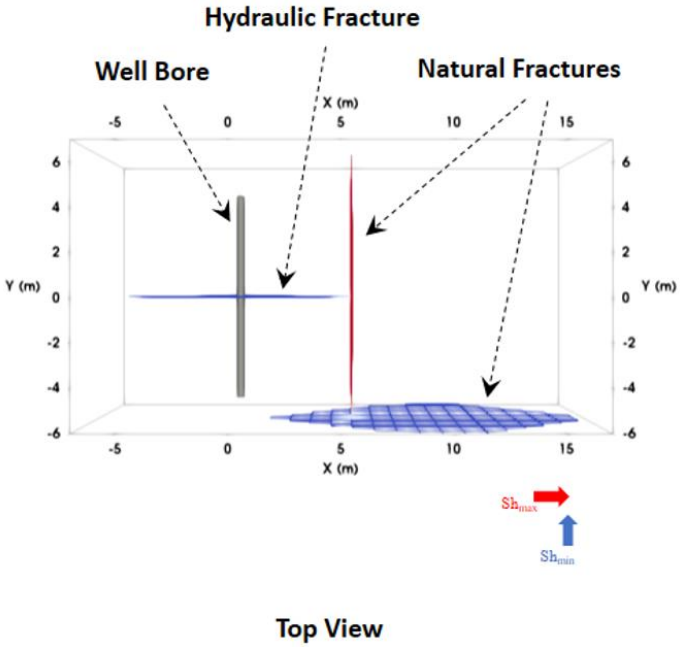

Figure 4.15: Top view of the fracture network simulated for investigating the effect of natural fracture intersection on the transport of proppant.

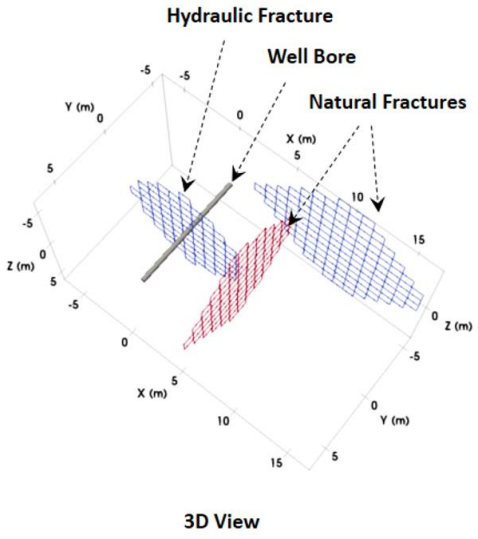

Figure 4.16: Perspective view of the fracture network simulated for investigating the effect of natural fracture intersection on the transport of proppant.

Table 4.5: Parameters used for simulation study of fracture network formation due to natural fracture.

Parameter	Value	Units
Young's Modulus	1	million psi
Poisson's Ratio	0.25	
Sh_{min}	3000	psi
Sh_{max}	3060	psi
Injection Rate	5	bbl / min
Pumping Time	60	seconds
Simulation Time	80	minutes
Maximum Proppant Concentration	0.1	

The fracturing fluid is pumped for 60 seconds, and the fracture is shut-in for 80 min. The shut-in is simulated to observe the redistribution of proppant as the fracture closes. As the fluid and proppant are pumped into the hydraulic fracture, the hydraulic fracture starts to propagate radially (see Figure 4.17). The hydraulic fracture tip closest to the natural fracture approaches the natural fracture and intersects it. As the natural fracture is modeled as a weak plane, the natural fracture provides little resistance to the growth of the hydraulic fracture. Hence, on the intersection with the natural fracture, the fracture network grows rapidly, and the connected area of the fracture network increases suddenly (see Figure 4.18). During this period, the slurry (proppant and fracturing fluid) flows into the natural fracture from the hydraulic fracture and opens it (see Figure 4.19). The movement of proppant is observed to take place at a rapid rate as the natural fracture provides little resistance to the growth of the hydraulic fracture. On further pumping, the

average width of the fracture network increases, and the intersected natural fracture starts to grow.

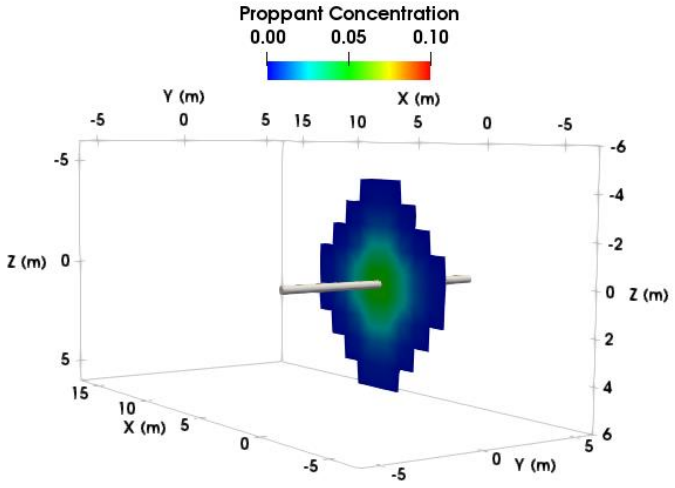

Figure 4.17: Radial growth of the hydraulic fracture. The distribution of proppant shows the proppant concentration to be low near the point of intersection.

The growing hydraulically connected natural fracture intersects with the second natural fracture. It is observed that the higher stresses generated due to the opening of the fractures reduce the width of the fracture elements near the intersection and retard the fracture's growth. This results in the formation of a thin channel for fluid and proppant transport between the connected fractures (Figure 4.19). This channel may grow if higher growth resistance is encountered at other fracture tips, and fracture growth in this region starts to provide the least resistance available for fracture growth. The parameters used in the simulation are shown in Table 4.5. At the end of the pumping stage, a uniform proppant distribution is observed in all the three fractures. The fracture farthest away from the wellbore is observed to have the lowest propped area relative to the created fracture area

because of proppant retardation. Subsequently, the post-pumping behavior of the fracture is simulated, and proppant settling is modeled as the fracture closes due to leak-off.

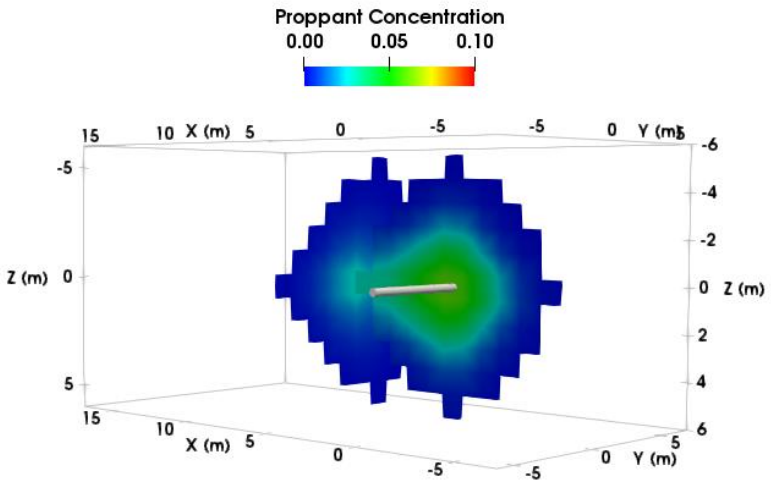

Figure 4.18: The distribution of proppant at the intersection with the first natural fracture. It can be observed that as fluid quickly moves into the newly intersected natural fracture, the proppant also moves into the natural fracture.

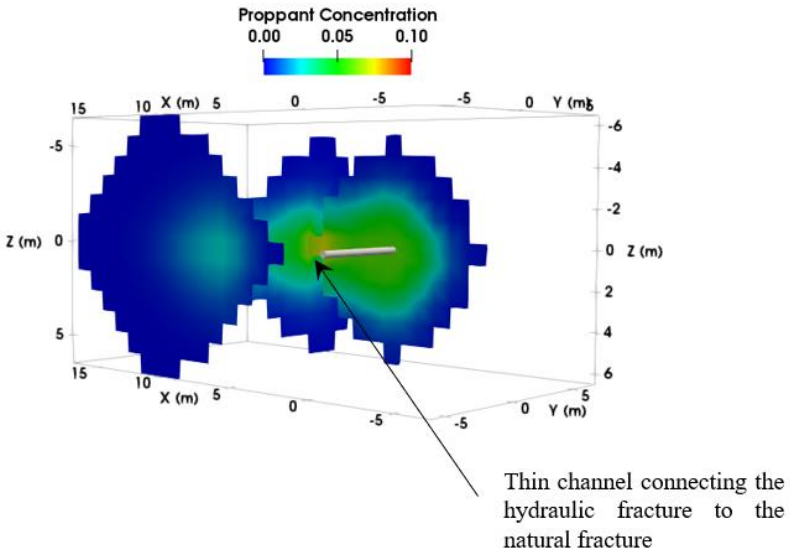

Figure 4.19: The distribution of proppant at the intersection with the second natural fracture at the end of pumping. It can be observed that the area of the natural fracture covered with proppant is lower compared to the first natural fracture.

It is observed that the proppant settles to the bottom of the fracture and forms proppant banks in all three fractures (Figure 4.20). The simulation is not continued once the change in the proppant distribution becomes numerically insignificant. The settling of proppant to the bottom of the three connected fractures results in the formation of three disconnected banks (Figure 4.21). These banks are disconnected from each other due to the geometry of the fracture network formed. This disconnected network of proppant banks in fractures can hinder the flow of hydrocarbons in the created fracture network.

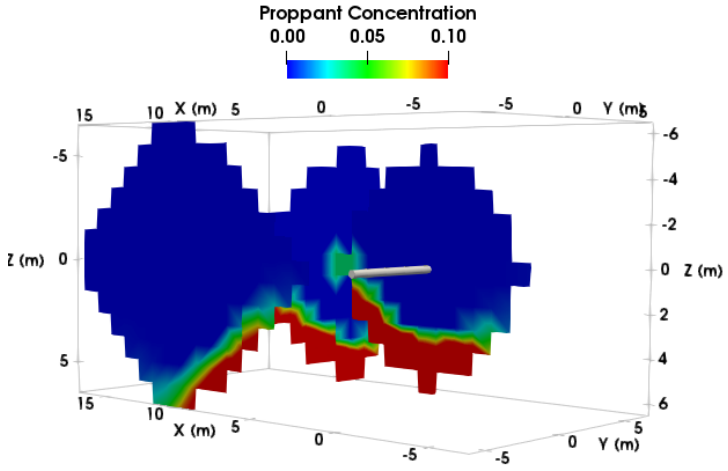

Figure 4.20: The distribution of proppant at the end of the simulation. It can be seen the proppant settles to the bottom of the fracture. This occurs as the rate of closure of the fracture is much slower compared to proppant settling.

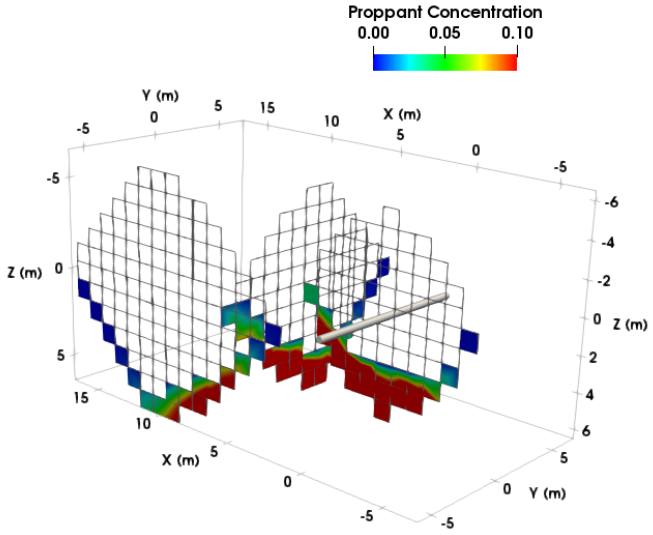

Figure 4.21: The colored region represents area of the fracture network containing proppant volumetric concentration higher than 10^{-6}. It is observed that three disconnected proppant banks are formed. Very low concentration regions (volumetric concentration less than 10^{-6}) are represented as empty grid cells.

4.5 Effect of Bedding Planes On the Transport of Proppant

Our model is next employed to understand the effect of bedding plane opening on the transport of proppant. Bedding planes can open when the vertical stress is comparable to the horizontal stress (thrust faulting or strike-slip regime). A case is set up to study the effect of bedding plane opening on proppant distribution. Figure 4.22 and Figure 4.23 show the top view and the side view of the final geometry of the created network. In this case, a radially growing hydraulic fracture intersects a horizontal or dipping weak bedding plane. The vertical stress value is kept 2% higher than the minimum horizontal stress. The parameters used in the simulation are shown in Table 4.6.

The bedding plane is modeled as a weak plane with a low critical stress intensity. As the hydraulic fracture intersects the bedding plane, the bedding plane opens and its width and conductivity increase. Fluid and proppant move from the vertical hydraulic fracture into the horizontal bedding plane if the bedding plane achieves a width greater than the proppant diameter. This is because the vertical stress that is acting against the horizontal bedding plane is comparable to the minimum horizontal stress and the fracturing fluid pressure inside the fracture is greater than the vertical stress. As the fluid pressure increases the width, the opening of the failed bedding plane starts to grow in size. This growing bedding plane comes into contact with the vertical natural fracture and intersects with it. Upon intersection, the vertical natural fracture is hydraulically connected with the created fracture network. The proppant and fluid from the horizontal fracture flow into the vertical natural fracture. The final distribution of the proppant and the fluid at the end of pumping in the three hydraulically connected fractures is shown in Figure 4.24. The vertical natural fracture grows upwards to avoid the higher stress region generated due to the opening of the initial hydraulic fracture. Following injection, post-pumping settling of proppant is simulated under shut-in (injection rate = 0) conditions, and the fracture is

allowed to close due to fluid leak-off. It is observed that the bedding plane remains propped during shut-in and the proppant inside the vertical fracture settles to form proppant banks.

In the simulation, the retardation of proppant due to the width of the fracture, the concentration of the proppant, and the diameter of the proppant are considered, and the retardation due to the horizontal nature of the bedding plane is not considered. In reality, we expect higher hindrance (retardation) to flow of proppant through the horizontal bedding plane.

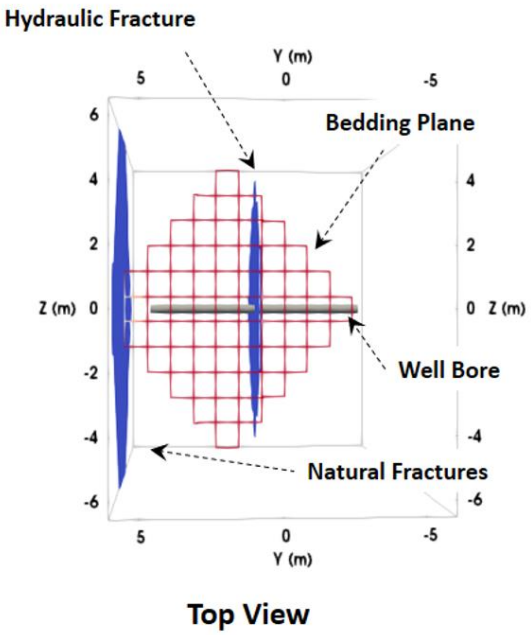

Figure 4.22: Top view of the fracture network simulated for investigating the effect of bedding plane opening on the transport of proppant.

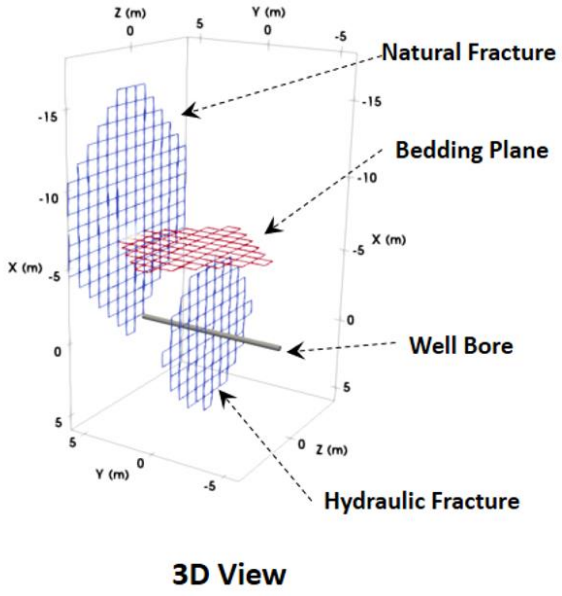

Figure 4.23: Perspective view of the fracture network simulated for investigating the effect of bedding plane opening on the transport of proppant.

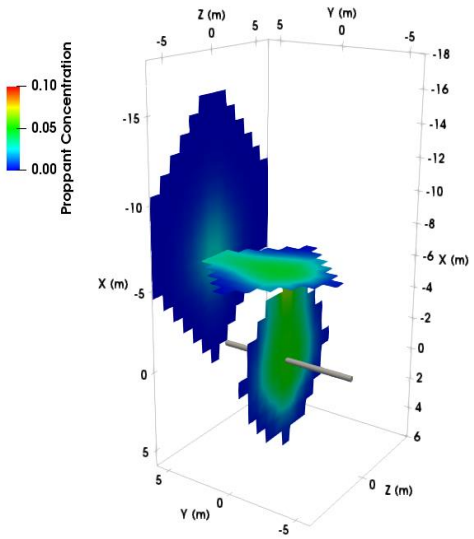

Figure 4.24: Distribution of proppant in the created fracture network at the end of pumping.

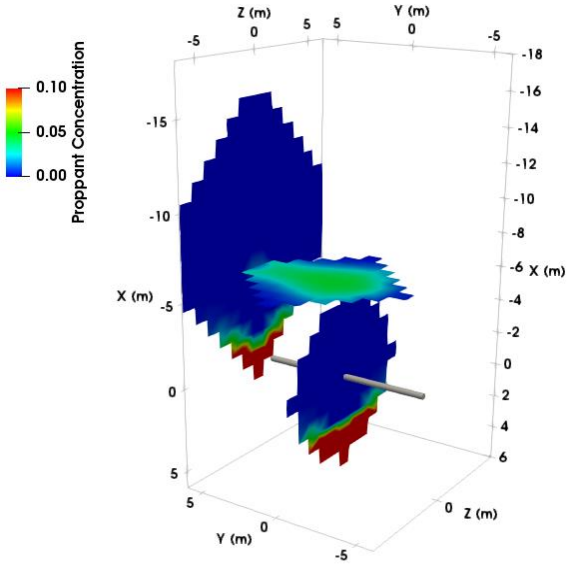

Figure 4.25: Distribution of proppant in the created fracture network after the proppant is completely settled in the network.

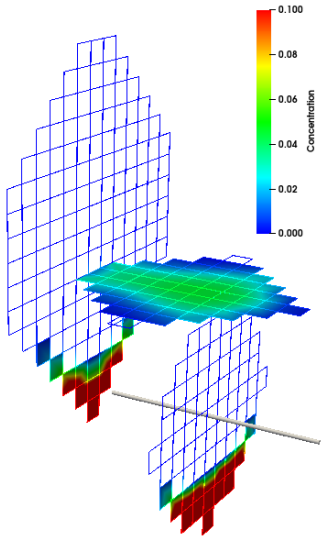

Figure 4.26: The figure shows the distribution of proppant in a complex fracture network generated by the interaction of the growing hydraulic fracture with a bedding plane. The colors show the volumetric concentration of proppant greater than 10^{-6}. Very low concentration regions (volumetric concentration less than 10^{-6}) are represented as empty grid cells.

Table 4.6: Parameters used for the simulation study of fracture network formation due to bedding planes.

Parameter	Value	Units
Young's Modulus	1	Mpsi
Poisson's Ratio	0.25	
Sh_{min}	3000	psi
Sv(vertical stress)	3060	psi
Injection Rate	5	bbl / min
Pumping Time	60	seconds
Simulation Time	80	minutes
Maximum Proppant Concentration	0.1	

4.5.1 Effect of Vertical Stress On Proppant Transport In Bedding Planes

Next, we investigate the effect of vertical stress on the transport of proppant through the bedding planes. The same geometry presented in the previous section is used for this study. Three cases with a stress contrast value of 60, 100, and 125 psi are simulated. The assumed cases represent situations of reverse faulting regime or strike-slip faulting regime as the vertical stress is comparable to the horizontal stresses. At high vertical stress conditions (in typical normal faulting regime), the bedding plane may not achieve significant width to allow proppant transport. The stress contrast in these cases is defined as the difference in the vertical stress and minimum horizontal stress. The distribution of proppant at the end of pumping in the three segments of the created fracture network (hydraulic fracture, bedding plane, and natural fracture) is analyzed. The parameters used

in the simulation are shown in Table 4.6. The final distribution of the proppant is shown in Figure 4.27.

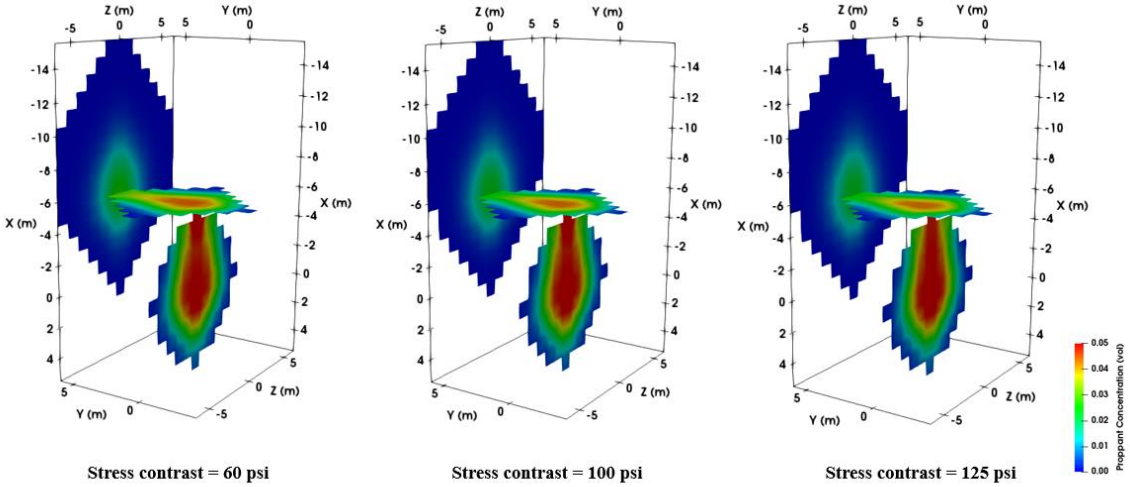

Figure 4.27: Proppant distribution at the end of pumping in the created fracture network for different stress contrast cases.

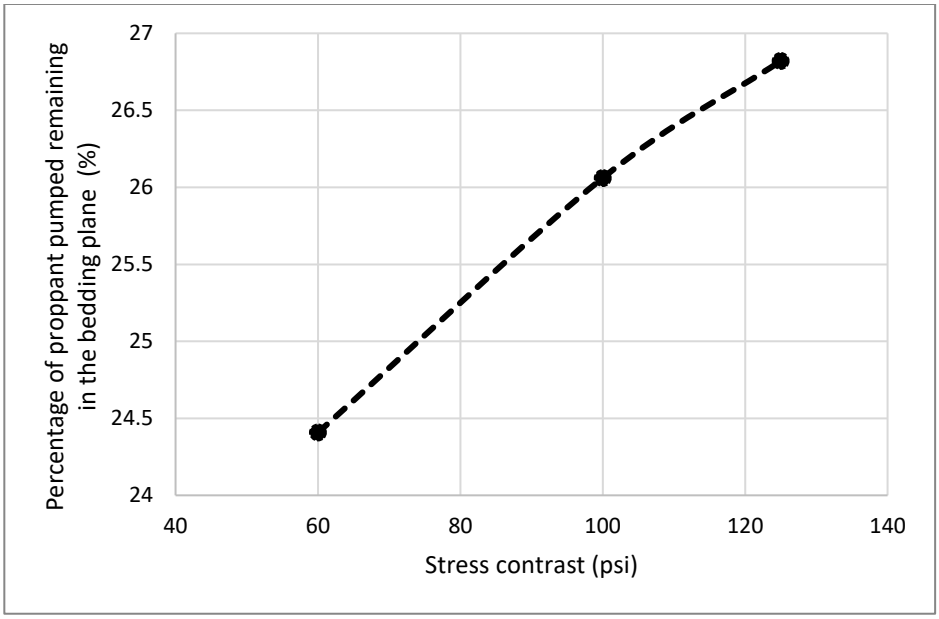

Figure 4.28: Percentage mass of proppant injected during pumping retained in the bedding plane.

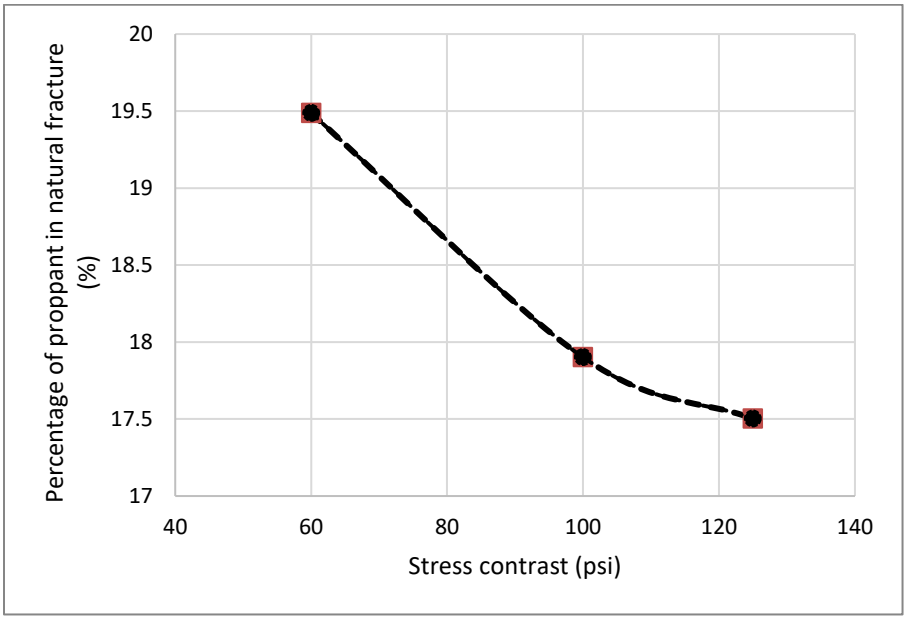

Figure 4.29: Percentage mass of proppant injected during pumping transported into the natural fracture.

The analysis of the proppant distribution in the created fracture network shows that as the stress contrast increases, the percentage of proppant retained in the bedding plane increases (see Figure 4.28). This happens because of the width attained by the natural fracture decreases as the vertical stress increases, which in turn increases the retardation to proppant flow in the bedding plane. In addition, as more proppant is retained in the bedding plane, it is observed that less proppant gets into the natural fracture (Figure 4.29).

4.5.2 Effect of Size of Proppant on Proppant Transport In Bedding Planes

A case is simulated to investigate the effect of proppant size on the transport of proppant through the bedding plane. Two different mesh sizes, 40-60# and 100#, of proppant are used in the investigation. The parameters used in the simulation are shown in Table 4.6. The following figure shows the distribution of proppant at the end of pumping.

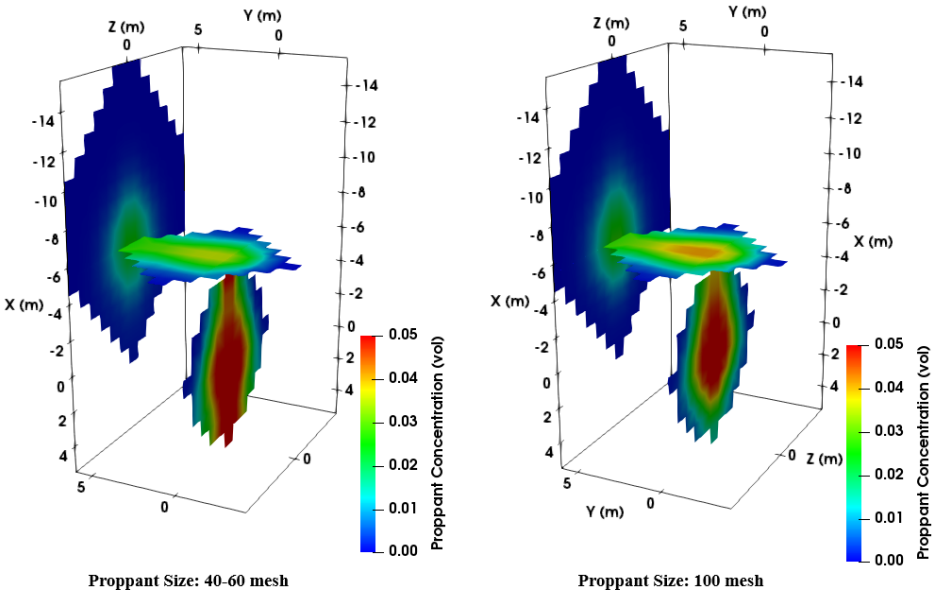

Figure 4.30: Distribution of proppant in the created fracture network at the end of pumping for 40-60# and 100# size proppant.

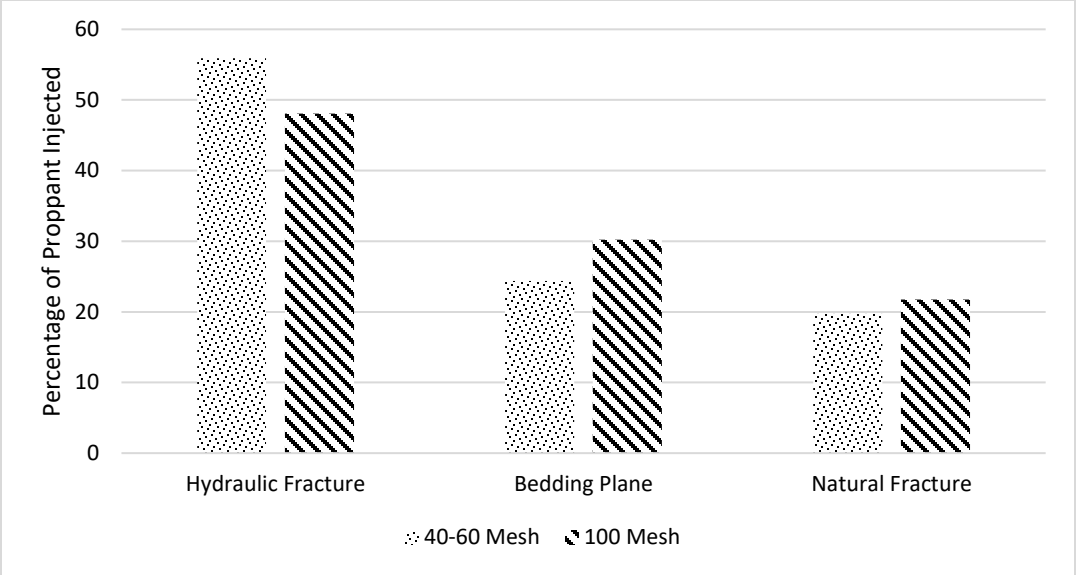

Figure 4.31: Percentage of injected proppant mass in the different sections of the created fracture network for the two simulated proppant sizes.

It is observed that for higher mesh size proppant (smaller proppant), more proppant travels into the natural fracture and the bedding plane compared to smaller mesh size (bigger proppant) proppant (Figure 4.31). In addition, it can be seen in Figure 4.30 that the bigger proppant starts to settle much faster, as expected.

4.6 DISCUSSION

During hydraulic fracturing, natural fractures and bedding planes can intersect with growing hydraulic fractures and can form complex fracture networks. This can result in the flow of fluid and proppant inside convoluted fracture pathways with variable fracture height. In this chapter, we investigated proppant transport in growing fracture networks using a fully three-dimensional fracture network model with the ability to simulate proppant transport. The model assumes that the proppant transport is affected by the width of the fracture, the diameter of the proppant particles, Reynold's number of the flowing slurry, and the concentration of the proppant particles.

In the cases that are simulated in this chapter for proppant transport in complex networks, due to the low permeability of the reservoir, the leak-off rate is very low, and the fracture doesn't close during the simulation period. This allows the proppant particles to settle to the bottom of the fracture and create proppant banks. In the case of planar fractures, it is expected that proppant settling may disconnect the conductive proppant bank from the wellbore, isolating the productive propped fracture from the wellbore. This problem is exaggerated, as observed, in the case of fracture networks, where every intersection point between fractures can potentially act as a bottleneck for the flow of produced hydrocarbons. The formation of disconnected proppant banks is observed.

The high stresses near the intersection of a hydraulic fracture and a natural fracture may reduce the fracture width and suppress the ability of the proppant to move into the natural fracture. The high stresses also hinder the growth of the fracture in the vicinity of the intersection region, creating a bottleneck for the flow of slurry during the injection. This region, due to its lower width, leads to higher retardation of the proppant particles. It is observed that the area of the propped region is smaller after each such bottleneck (intersection of one fracture with another not in the same plane). These regions, where the fracture area is smaller and the width of the created fracture is also smaller, is expected to also hinder the flow of hydrocarbons during production.

It was observed during the simulations that higher closure rate (as seen in high permeability formations) can significantly increase the propped area of the fracture. This can result in significant increase in hydrocarbon production. In order to achieve higher closure rate in low permeability formations, fracturing fluid can be flowed back to speed up the fracture closure process at the end of pumping. It is observed from the simulations that closure rate equivalent to 100 microD permeability can increase in propped area significantly. Although, fluid flow back may also lead to increase in production of proppant

particles. Hence, careful simulation study should be conducted in order to minimize the production of proppant during flowback and maximize the propped area.

The viscosity of the fracturing fluid can also have an impact on the overall transport of proppant in the created fracture networks. A high viscosity fracturing fluid creates wider fractures and typically will have low leak-off rates, hence fractures can take much longer time to close even for high permeability formations. Also, they decrease the settling rate of the proppant in the created fractures, hence the proppant takes more time to settle to the bottom of the fracture. In case of fracture intersection, due to the high viscosity of the fracturing fluid, it is expected that both the natural fracture and hydraulic fracture will attain larger width and can suppress the intersection region with much higher stresses compared to low viscosity fluid. This can result in further retardation of the proppant. Although, high viscosity can increase the proppant carrying capacity of the fracturing fluid. The model accounts for the non-Newtonian nature of the fracturing fluid and can capture the effect of fracturing fluid viscosity and concentration of proppant on proppant transport. In the future, the effect of fluid viscosity on transport of proppant can be explored and distribution of proppant in fracture networks can be investigated using the model.

4.7 CONCLUSION

- Low permeability formations experience very low leak-off rates. In such cases, the fracture may take several days to close on the proppant particles. This provides ample time for proppant settling. In such cases, we observed proppant bank formation at the bottom of the fracture in all the simulation cases after the shut-in period. This may lead to discontinuity in the propped regions inside the fracture and limit production.

- Natural fractures can intersect with hydraulic fractures and allow fluid and proppant to flow into them. During fracture intersection, the region of fracture intersection experiences high stresses and limits the width of the intersecting region. These intersections are clearly shown to act as a bottleneck for proppant transport and the flow of hydrocarbons.
- The natural fracture orientation can affect the transport of proppant in fracture networks. It is observed that there is an optimum intersection angle at which maximum proppant travels through the intersection region between a hydraulic and natural fracture.
- Higher stress contrast reduces the transport of proppant into the natural fracture that is oriented to open against maximum horizontal stress. This happens because such natural fractures achieve lower width in high-stress contrast environments.
- It may be beneficial to use smaller mesh proppant during hydraulic fracturing, to facilitate flow into natural fractures and increase the propped area. Smaller proppants are more likely to cross the width constricted region of fracture intersection into natural fractures. Larger proppants may experience higher retardation factors and form a proppant bank at the fracture intersection.
- In strike-slip stress conditions, weak bedding planes can slip and dilate to allow proppant transport. A bedding plane, if failed remains propped and can provide a continuous conductive channel between vertical fractures. The proppant banks in the vertical fractures may not remain connected due to proppant settling.
- Higher vertical stresses hinder the flow of proppant through bedding planes.

Chapter 5: Calibrating Hydraulic Fracture Model with Core Measurements from the Hydraulic Fracturing Test Site 1

5.1 INTRODUCTION

Natural fractures play an important role in the hydraulic fracturing process. The stresses generated by the growing hydraulic fracture can dilate or fail the insitu natural fractures. These dilated or failed natural fractures increase the effective permeability of the reservoir. Microseismic activity during hydraulic fracturing gives clear evidence of such failure events (Fisher et al., 2004; Warpinski et al., 2005; Cipolla et al., 2008). Also, the interaction of growing hydraulic fracture with the activated natural fractures or planes of weakness can result in the generation of complex fracture networks (Potluri et al., 2005; Olson and Wu, 2012; Wu et al., 2012; Wu and Olson, 2015b; McClure et al., 2016; Sesetty and Ghassemi, 2017; Shrivastava and Sharma, 2018a). The formation of fracture networks increases the surface area of contact of the created fracture (Gale et al., 2007) with the reservoir. In spite of the strong evidence of the generation of complex fractures during hydraulic fracturing, engineers often use models limited to bi-wing and planar fractures, and attempt to capture the effect of increased contact surface area and enhanced reservoir permeability using the concept of stimulated reservoir volume. The difference in the created fractures' morphology (complex fracture networks vs. planar bi-wing fractures), if not accounted for in the fracturing treatment design process can result in the inferior selection of fracture and well spacing. This understanding of created fracture morphology is also important to predict the time-dependent change in reservoir drainage area due to stress-dependent fracture permeability (Seth et al., 2018).

This chapter is based on "Formation of Complex Fracture Networks in the Wolfcamp Shale: Calibrating Model Predictions with Core Measurements from the Hydraulic Fracturing Test Site." Shrivastava, Kaustubh, Jongsoo Hwang, and Mukul Sharma. presented at *SPE Annual Technical Conference and Exhibition*. Society of Petroleum Engineers, 2018. In the published paper, Shrivastava developed the used hydraulic fracturing model, developed the synthetic coring technique, and documented the results.

A major hindrance in incorporating natural fractures into modern hydraulic fracturing simulators is the lack of information on the in-situ natural fracture system. Even with core-through experiments and careful examination of the sampled core, the one-dimensional nature of the core makes it difficult to identify the true length frequency distribution of the natural fractures.

In this chapter, we have used the core description from six horizontal cores drilled during the Hydraulic Fracture Test Site #1 (HFTS-1) project (Courtier et al., 2017; Gale et al., 2018; Kumar et al., 2018). The frequency of the natural fractures and hydraulic fractures observed in the cores is presented. The data from the analysis of the cores are used to generate a discrete network fracture (DFN) model. A synthetic coring technique is developed in order to match DFN model of the reservoir with data from the field in a stochastic manner. A population of natural fractures is generated using the developed synthetic coring technique. This generated population of natural fractures is then incorporated into the developed hydraulic fracturing simulator presented in Chapter 2, and a stage-scale hydraulic fracturing simulation is conducted using the DFN. From the fracture simulation result, a synthetic core is extracted, and the properties of the synthetic core (observed number of hydraulic fracture and natural fracture intersections) is presented and compared with HFTS core data.

In the next section of this chapter, we will describe the extracted core in the HFTS-1 project.

5.2 Field Core Data

We have visualized the core descriptions for six cores from the slant core well (SCW) (see Figure 5.1) from the Hydraulic Fracture Test Site (HFTS) industry consortium project (Courtier et al., 2017). This slant core well has 4 cores (Cores 1 to 4) located in the

Upper Wolfcamp formation, and 2 cores (Cores 5 and 6) in the Middle Wolfcamp formation. Cores 1 to 4 contain fractures mainly propagated from the adjacent Upper Wolfcamp well (AUWW), and Cores 5 and 6 contain fractures from the adjacent Middle Wolfcamp well (AMWW) (see Figure 5.1). The cores were described in detail by Gale et al. (2018) based on the type, number, location, orientation of fractures, morphology, features of fracture faces, etc. In this chapter, this description of the core has been used as a basis for generating a discrete fracture network for hydraulic fracturing simulation.

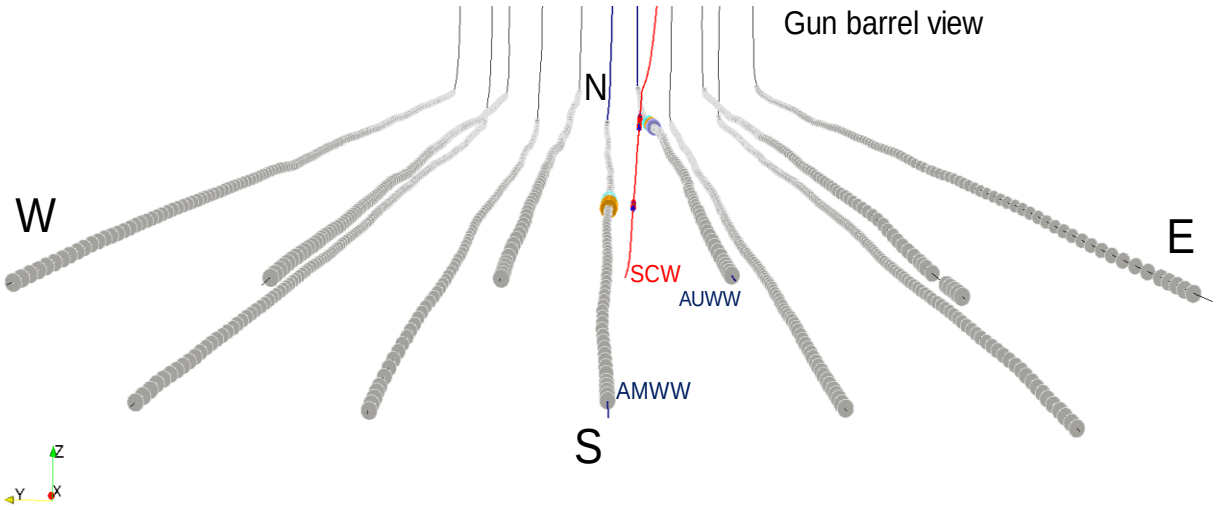

Figure 5.1: Gun barrel view of wells, cores, and perforation clusters in the Hydraulic Fracturing Test Site. Red line indicates the wellbore of the slant core well (SCW) where 6 cores were taken for the systematic core description.

5.3 Field Core Analysis

We used data from the core description to visualize fracture orientations, types of fractures (along with wellbores), and perforation clusters in field-scale, three-dimensional space. By visualizing the core descriptions, we intend to understand the primary origins of

fractures in terms of hydraulic, natural, and reactivated natural fractures. The density of individual types of fractures along the core depths and dominant orientations of each fracture type over the locations of cores relative to the wells/stages/clusters are important components for understanding the complex core description data obtained. This information helps in understanding the impact of the natural fracture network, stress interference, fracture reorientation during stimulation, and transport of fluid and proppant in the wellbore.

5.4 CORE VISUALIZATION AND ANALYSIS

In this section, we have used the fracture location (measured depth, MD), fracture dip angle, dip direction, and fracture origin to visualize the core description. In the presented visualizations, fractures induced by drilling, coring, or handling processes were not included and only intact natural fractures (N), reactivated natural fractures (NR), and hydraulically induced fractures (HF) are presented. The categorization process of the fractures in the core is described in Gale et. al (2018). To better understand the spatial location of fractures relative to their initiation points (perforation clusters), the well trajectories of the slant cored well (SCW in Figure 5.2) as well as those of the fracturing wells (AUWW and AMWW in Figure 5.2) were taken from the well survey data and are also shown. The adjacent perforation clusters are visualized as a large disk with different colors for each treatment stage. Three perforation clusters per stage were placed in the fractured wells. Each perforation cluster has a perforation density of 6 shots per ft with a cluster length of 2.5 ft. For cores 1 to 4, stages UWb and UWc of the well AUWW are the closest, and stages MWa and MWb of well AMWW were closest to cores 5 and 6 as shown in Figure 5.2.

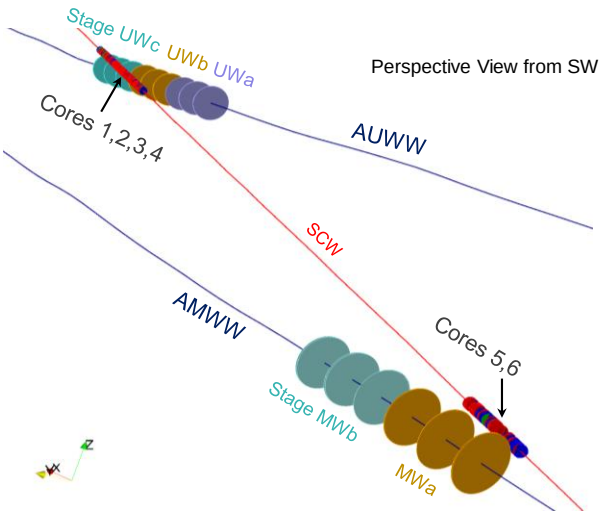

Figure 5.2: Perspective view of wells AMWW, AUWW and SCW (red line).

5.4.1 Description of Core Data – Cores 1 to 4

Cores 1 to 4 are located in the Upper Wolfcamp formation. The distance between the cores and adjacent AUWW wellbore is approximately 100 ft. Three perforation clusters from stage UWb and two toe-side perforation clusters from stage UWc of the AUWW well are closely located to cores 1 to 4 (see Figure 5.3). It can be assumed that fractures described in cores 1 to 4 are the fractures mainly originating from those clusters. In Figure 5.3 to Figure 5.5, the individual fractures are shown as disks with different colors. Red disks represent hydraulic fractures (HF), blue disks are intact natural fractures (N), and green disks are natural fractures reactivated during fracture treatment (NR). The orientation of the disks are as per the orientation data from the core description. Figure 5.4 shows fractures in a map view, and Figure 5.5 shows them in a side view from the west. The number of fractures in cores 1 to 4 are: HF = 298; N = 132 and, NR = 66 . When compared with the limited length (2.5 ft) of the perforation clusters and considering the distance from

the treatment well, it is evident that fractures have bifurcated and split repeatedly and created a very large number of fractures that ultimately make up the stimulated rock volume. In the visualized fracture orientations, the dip angle is very close to the vertical plane for all types of fractures. The direction of dip, however, shows different trends between hydraulic fractures and natural fractures (intact or reactivated). Hydraulic fractures are largely in the east-west direction, while the natural fractures are trending in NE-SW and WNW-ESE directions. The map view of fracture orientations from the core description are shown in Figure 5.4.

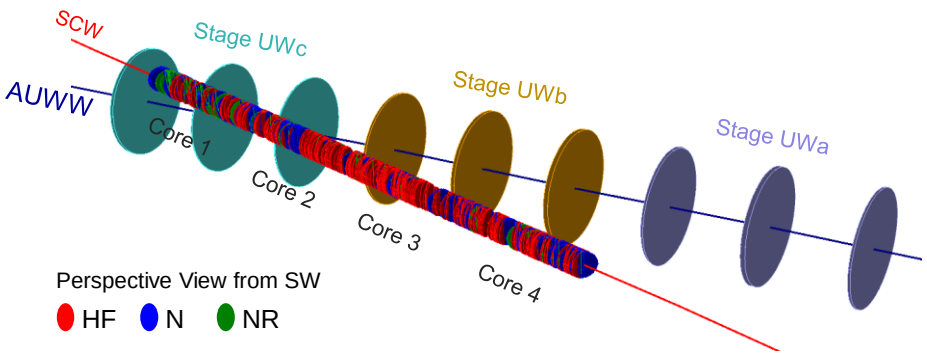

Figure 5.3: Perspective view of fractures in cores 1 to 4 from the southwest. Large circles are centered at locations of perforation clusters from stages UWb and UWc of well AUWW.

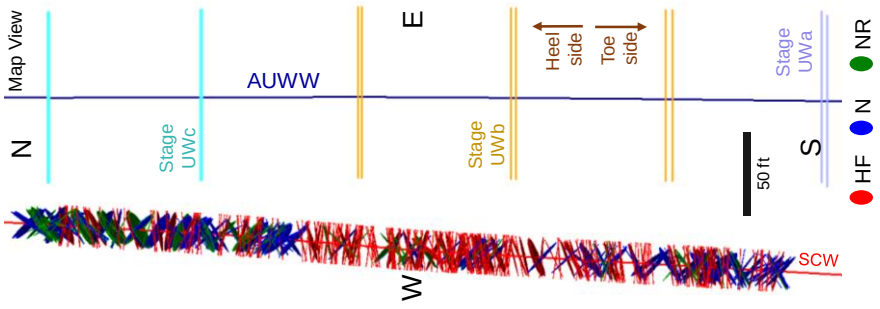

Figure 5.4: Map view of fractures in cores 1 to 4 with well AUWW.

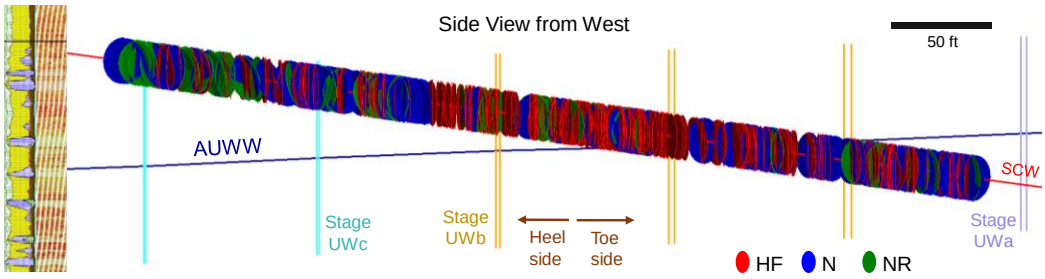

Figure 5.5: Side view of fractures in cores 1 to 4. The viewpoint is from the west direction. Lithology logs and borehole image logs are compared for reference purpose. Color codes for fracture types are HF: hydraulic fractures, N: intact natural fractures, and NR: reactivated natural fractures.

5.4.2 Presentation of Core Data – Cores 5 and 6

Cores 5 and 6 are extracted from the Middle Wolfcamp formation. The distance between the cores and adjacent Middle Wolfcamp well (AMWW) is approximately 125 ft, which is slightly farther than the distance between AUWW and cores 1 to 4. As shown in Figure 5.6, two heel-side perforation clusters from stage MWa of AMWW well are the closest to cores 5 and 6. It can be assumed that fractures observed in cores 5 and 6 are the fracture originating mainly from these clusters. In Figure 5.6 to Figure 5.8, the individual fractures are shown as disks with different colors. The color codes are the same as in the previous figures. Figure 5.7 shows fractures in a map view, and Figure 5.8 shows them in a side view from the west.

The number of fractures in cores 5 and 6 are: HF = 54, N = 26, and NR = 8. As in the previous cores, the large number of fractures observed in the core seems to indicate that a large number of additional fractures have been created by the growth of the main hydraulic fractures. Similar trends in the fracture orientations are observed in cores 5 and 6. The dip angle is again observed to be very close to the vertical plane for all types of

fractures. The direction of dip also shows similar trends. Hydraulic fractures are largely in the east-west direction, but natural fractures are oriented primarily along the WNW-ESE direction. Dip directions in NE-SW are less frequently observed in Middle Wolfcamp cores. The fracture orientations in the core description results are shown in Figure 5.6 to Figure 5.8.

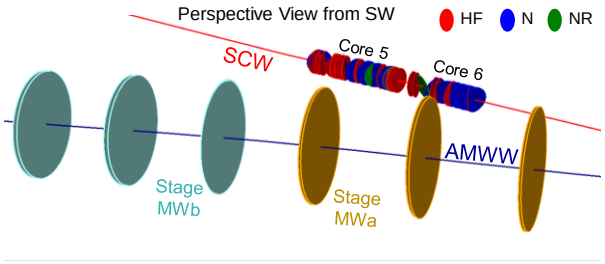

Figure 5.6: Perspective view of fractures in cores 1 to 4 from the southwest. Large disks are centered at locations of perforation cluster from stages MWa and MWb of well AMWW.

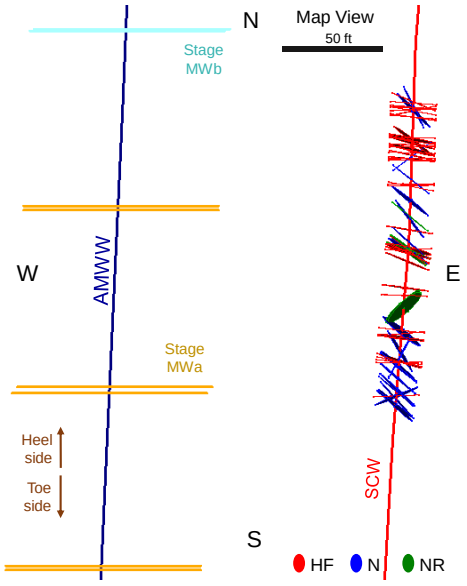

Figure 5.7: Map view of fractures in cores 1 to 4 with well AMWW.

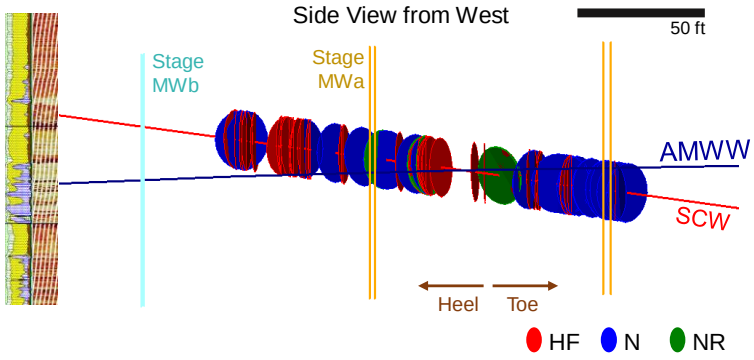

Figure 5.8: Side view of fractures in cores 1 to 4. The viewpoint is from the west. Lithology logs and borehole image logs are compared for reference purpose. Color codes for fracture types are HF: hydraulic fractures, N: (intact) natural fractures, NR: reactivated natural fractures.

5.5 Analysis of Core Data

From the compiled and visualized core description data, we conducted a statistical analysis to better understand how fracture propagation is impacted by the relative spatial locations of stages and clusters. In Figure 5.9(a), fractures are visualized separately for each type. All types of fractures are observed to be mainly in a vertical plane. Horizontal fractures are typically not observed. As a general trend, fractures in cores 1 to 4 are oriented in the E-W direction indicating direct propagation from the AUWW well with the creation of a large number of new fracture planes. These new fractures may be created by shear failure or activation of natural fractures or the bifurcation and splitting of hydraulic fractures during propagation. Natural fractures including both intact and reactivated fractures show two dominant orientations, the NE-SW and WNW-ESE directions.

5.5.1 Impact of Fluid/Proppant Transport Over Multiple Clusters in a Stage

The fracture density of different types of fractures over the length of cores 1 to 4 is shown in Figure 5.9(b). The number of all fractures per unit distance of 10 ft was

approximately 11.2. In these cores, the average fracture densities are 6.7, 3.0, and 1.5 fractures per 10 ft length of MD for hydraulic fractures (HF), intact natural fractures (N), and reactivated natural fractures (NR), respectively. In cores 5 and 6, average fracture densities are 3.5, 1.7, and 0.5 fractures per 10 ft length of MD for HF, N, and NR, respectively. The primary trend in the fracture density is that there are more hydraulic fractures near the heel-side cluster of stage UWb compared to toe-side clusters of either stage UWb or UWc (subsequent stage) as seen in Figure 5.9(c). This behavior of more fractures closer to heel-side clusters than toe-side clusters is a direct observation from a core description. There have been many indirect observations of this preferred fracture stimulation on the heel-side of a treatment stage (Ugueto C. et al., 2016; Wheaton et al., 2016; Haustveit et al., 2017). The primary reason for this heel-side domination is the preferred transport of fluid and proppant into the heel-side cluster. This has been verified by extensive numerical simulation, as well as field observations (Wu et al., 2017).

5.5.2 Impact of Inter-stage Stress Interference on Natural Fracture Reactivation

In Figure 5.9(d), the ratio of reactivated natural fractures (NR) to the total number of pre-existing natural fractures (N and NR) over the length of MD has been shown. The general trend is that the proportion of reactivated natural fractures increases from toe- to heel in a stage. The ratio increases from the toe-side of stage UWb to the heel-side of stage UWb in cores 1 to 4. In the subsequent stage UWc, the reactivation ratio becomes small at the toe-side and increases again toward the heel-side of the same stage. When Stage UWb is pumped and fractures are created, the magnitudes of stress increase in the area of subsequent Stage UWc. The stress change is primarily caused by the mechanical opening of the fractures in Stage UWb. The effect of the mechanical opening increases the

components of the stress tensor; however, the stress component in the north-south direction increases much more than the stress component in the east-west direction. As a result, the stress anisotropy decreases before fracturing stage UWc due to the stress shadow effect of Stage UWb. This decreased stress anisotropy on the toe-side of stage UWb may result in less natural fractures being reactivated (smaller reactivation ratio as seen in Figure 5.9d). As the magnitude of the stress shadow decreases towards the heel-side of Stage UWc, the reactivation ratio increases.

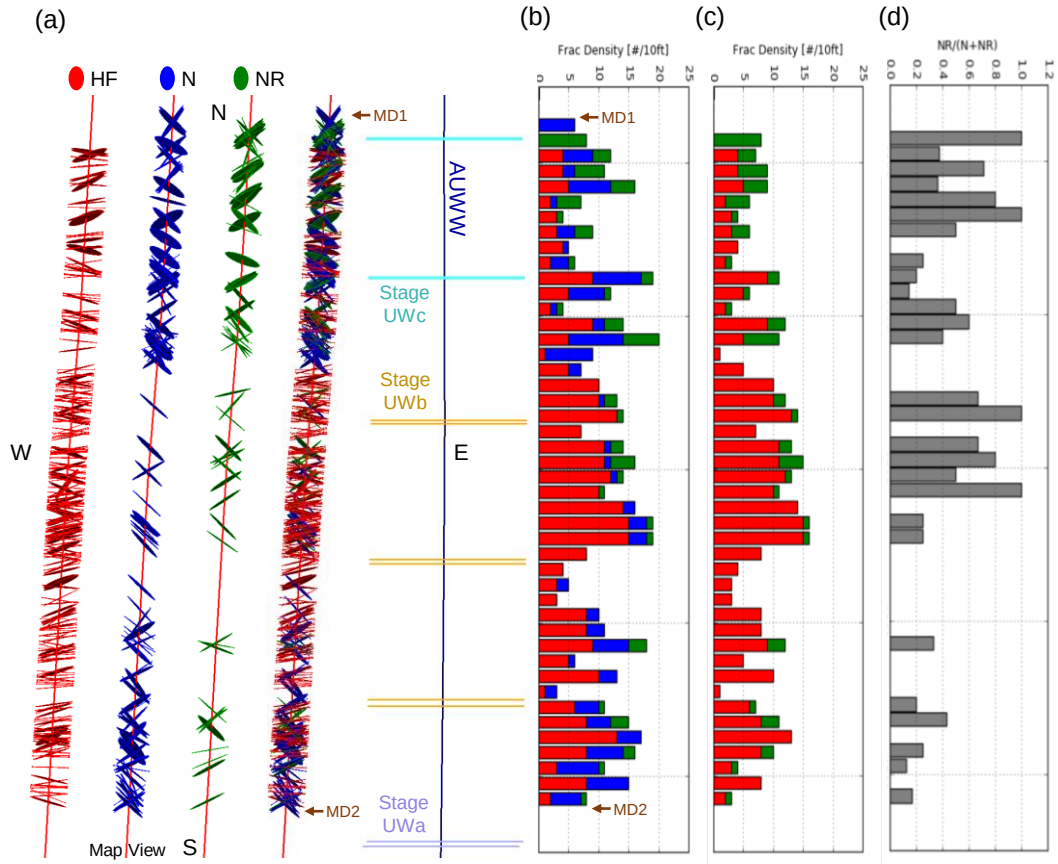

Figure 5.9: (a) Map view of fractures in cores 1 to 4. From left to right, fractures are shown individually for types of HF, N, and NR, and all types are shown together. Each group of fractures is shown separately, but the spatial location of fractures does not represent the actual subsurface location. (b) Fracture density by number of fractures per 10 ft. (c) Fracture density by number of fractures per 10 ft. Only HF and NR types are shown to represent the degree of stimulation. (d) The ratio of reactivated natural fractures per total number of initial natural fractures. The vertical axis of the plot is measured depth (MD) in feet.

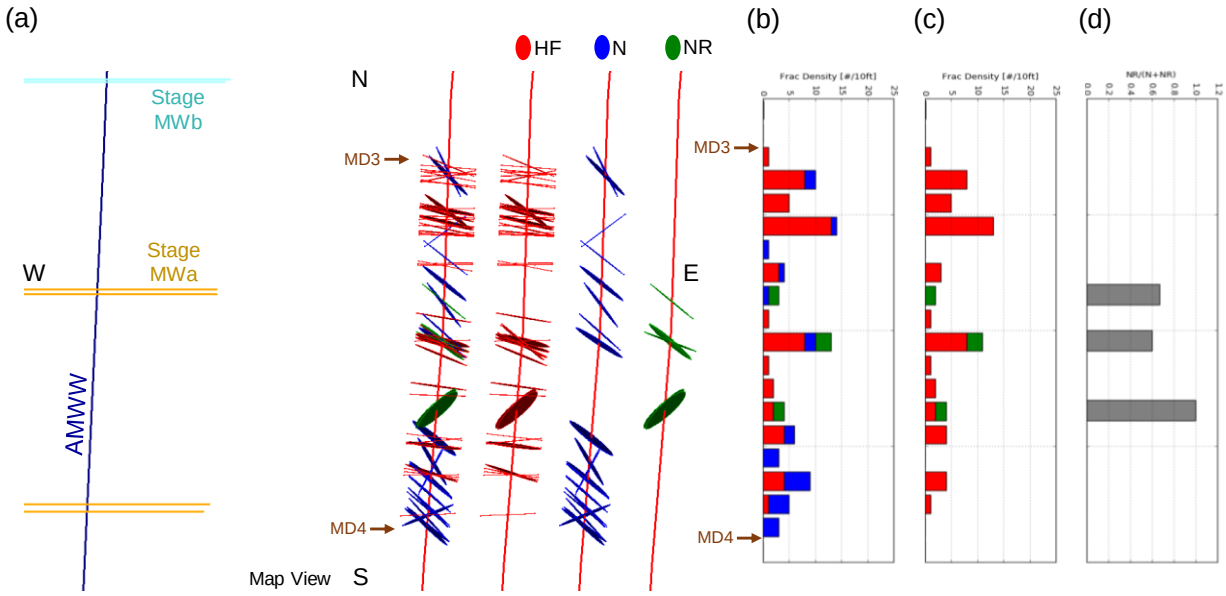

Figure 5.10: (a) Map view of fractures in cores 5 and 6. From left to right, all types of fractures are shown together, and fractures are shown individually for types of HF, N, and NR. Each group of fractures is shown separately, but the spatial location of fractures does not represent the actual subsurface location. (b) Fracture density, number of fractures per 10 ft. (c) Fracture density, number of fractures per 10 ft. Only HF and NR types are shown to represent the degree of stimulation. (d) The ratio of reactivated natural fractures per total number of initial natural fractures. The vertical axis of the plot is measured depth (MD) in feet.

5.6 Simulation Model Description

The data obtained during the HFTS study (described previously in the chapter) is used to calibrate the properties of a two-dimensional discrete fracture network. The one-dimensional nature of the core makes it difficult to determine the true length distribution of the natural fractures. Hence, in order to determine the length distribution for two-dimensional simulations from the one-dimensional HFTS core data, a statistical approach is employed. The simulator presented in Chapter 3 is extended to generate natural fractures for the simulation. The simulator is used to generate realizations of natural fracture

population with specified distributions for location, orientation, length, friction angle, cohesion, and K_1^c. The location is generated stochastically in the reservoir region as per the provided fracture density, whereas friction angle, cohesion, and K_1^c are generated as Gaussian distributions. The length distribution of natural fractures is generated using a power law as follows:

$$N = Ax^{-3} \tag{1}$$

where N is the frequency of the natural fractures, x is the length of the natural fractures, and A is a constant (Heffer and Bevan, 1990). The minimum size of the natural fractures assumed in the simulation is limited by the grid size chosen for the simulation. In this study, the grid size is 2m, and hence the minimum size of the natural fractures is assumed to be 2 meters. The orientation of natural fractures is generated using a probability density function based on the HFTS core data (see Figure 5.19).

5.7 SYNTHETIC CORING PROCEDURE

As the core data provides information only for the orientation and number of fractures intersected by the core, the length distribution and areal density of the simulated natural fracture network is computed using a synthetic coring process. The simulator is used to extract synthetic cores from the generated discrete fracture network by registering the intersection of the natural fracture with a specified coring trajectory (Figure 5.11).

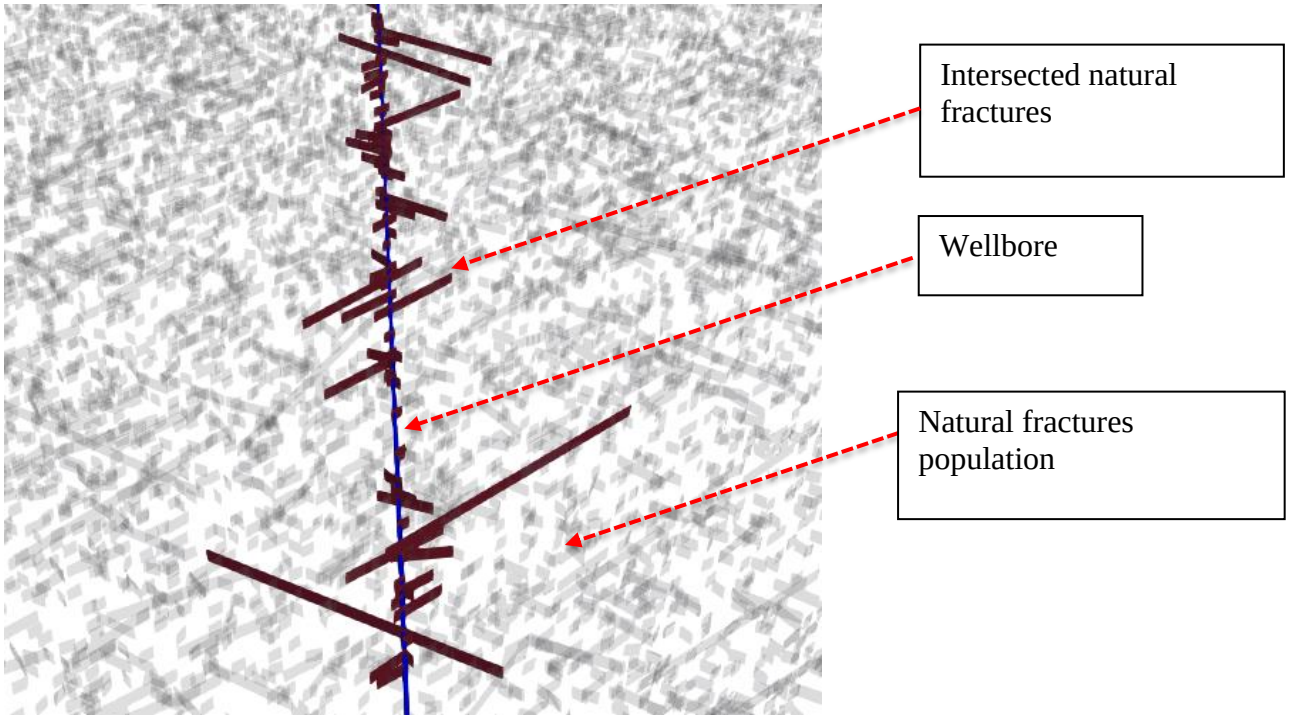

Figure 5.11 Synthetic core intersecting natural fractures

The intersected natural fractures are then analyzed to obtain the frequency distribution and their orientation. Nine synthetic cores, each of 100 meters in length (Figure 5.12), are extracted from the generated realizations. The observed natural fracture orientation distribution (see Figure 5.13) and the total number of natural fracture intersections is compared with the HFTS core. The length of the natural fractures is varied

by manipulating the coefficient (constant A in Eq. 1) in the power-law distribution. The areal density of the natural fractures in the reservoir and the length of the natural fractures are manipulated to match the number of natural fracture intersections with the HFTS data. As the process generates a different number of natural fracture intersections for each core, it is repeated ten times to get a total of 90 cores to get a statistical distribution of the number of fracture intersections (Figure 5.14). The objective of the exercise is to match the median of the distribution obtained from the simulated natural fracture network to the number of natural fractures obtained in the HFTS core. From this exercise, it is found that synthetic coring with a fracture areal density of 0.45 fractures/m^2 and an A of 37500 provides a good match with the HFTS core data. The exercise doesn't provide a unique solution to the problem, rather establishes a relationship between the natural fracture density and the constant A. Hence, multiple solutions of the pair of values can satisfy the data obtained from the field core. Although, each such pair represents a similar number of natural fracture intersections obtained for a synthetic core. On propagation of a hydraulic fracture in the created DFN, the probability that the growing hydraulic fracture will intersect with a natural fracture will remain the same for different pairs of the assumed values, as the synthetic coring ensures that the number of natural fracture planes encountered remain constant along a synthetic core. Therefore, it is not expected that the geometry of the growing hydraulic fracture will be significantly different, for a large enough population of natural fractures for different pairs of the assumed values of A and density of natural fractures. In our simulations, we chose a value of A and natural fracture density to obtain a range of the natural fracture length similar to the field data (from Gulf of Suez) given by Hefner and Bevan (1990). Although, the field data used is from a different formation, it still allows us to be in a reasonable range while selecting the parameters. From the

generated realizations of natural fractures, one realization is selected for simulating hydraulic fracture growth. Figure 5.15 shows the length distribution used in the simulation.

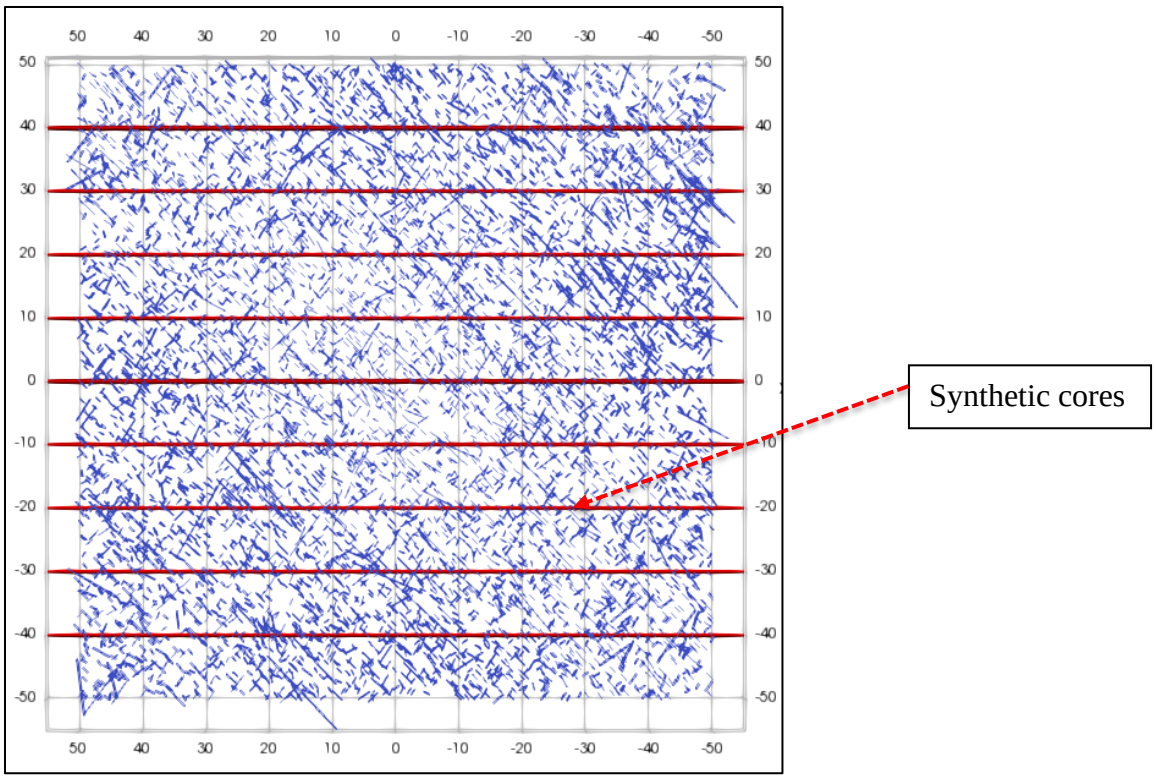

Figure 5.12: Location of the nine synthetic cores in the 100m X 100m two-dimensional reservoir. The length of each core is 100 m and the distance between them is 10m.

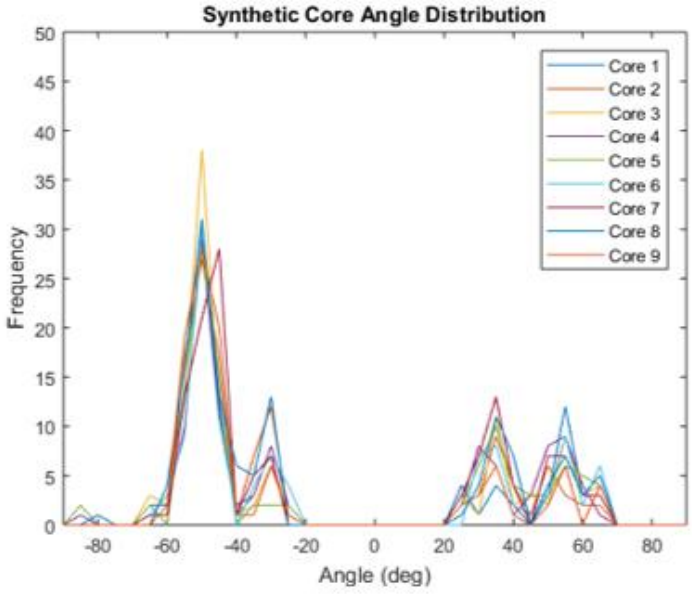

Figure 5.13: Orientation of natural fractures observed in the nine synthetic cores.

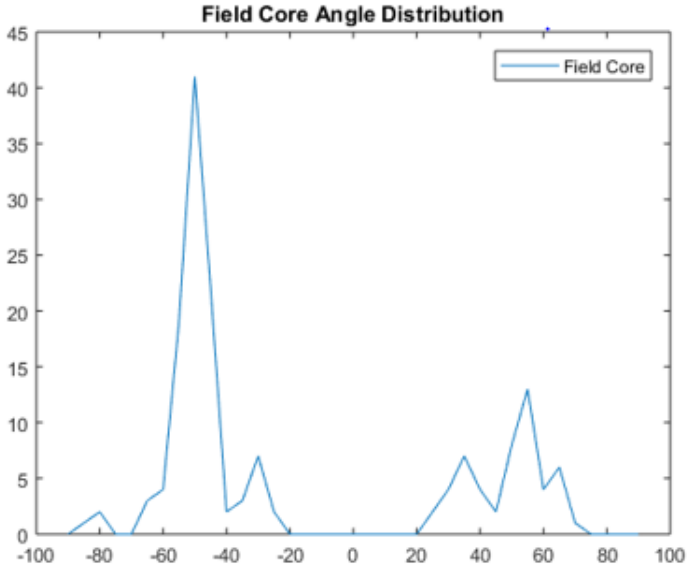

Figure 5.14: The orientation of the natural fractures observed in the HFTS slant core.

5.8 HYDRAULIC FRACTURING MODEL AND SIMULATION PARAMETERS

A hydraulic fracturing simulation is set up for the reservoir with the core-data-calibrated natural fracture network. The simulation of the hydraulic fracture network growth is performed using Multi-Frac-NF. The properties used in the simulation are shown in Table 5.1. The case of a single-stage hydraulic fracture with three clusters is simulated, with the fluid being equally divided into the three clusters.

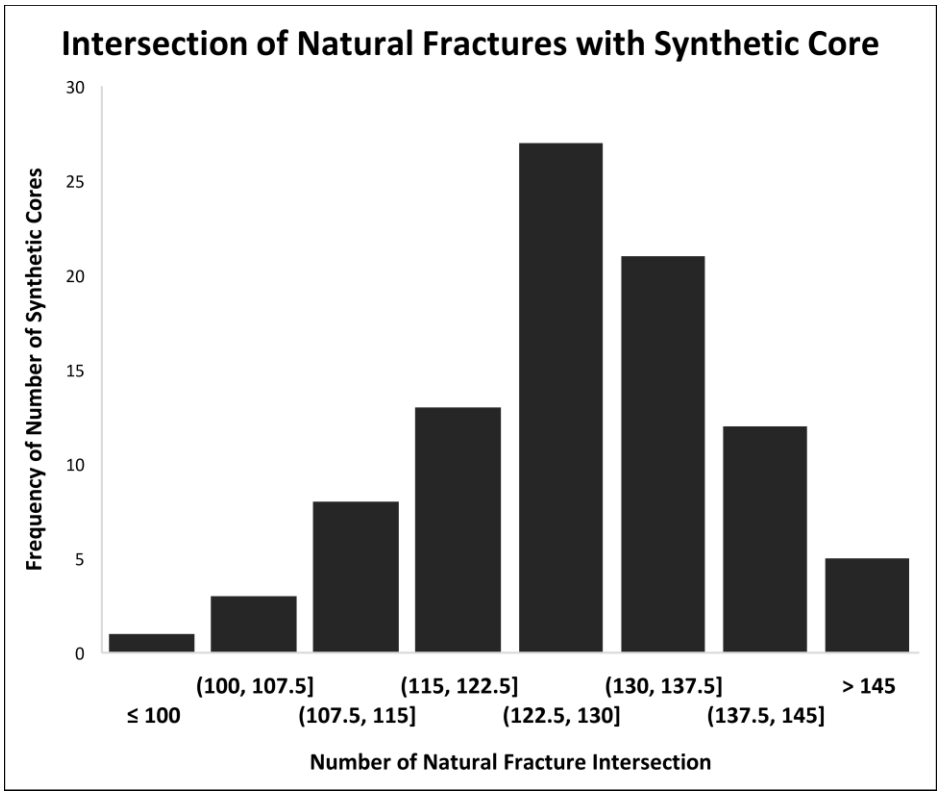

Figure 5.15: Frequency of synthetic cores versus the number of natural fracture intersection. The total number of synthetic cores extracted is 90 from a total of 10 realizations.

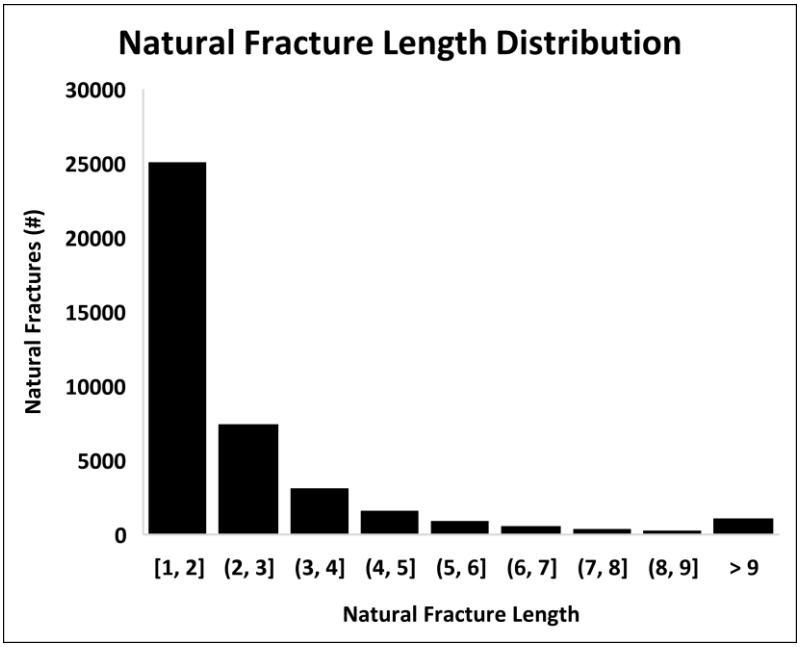

Figure 5.16: Natural fracture length distribution for the realization selected for the simulation study.

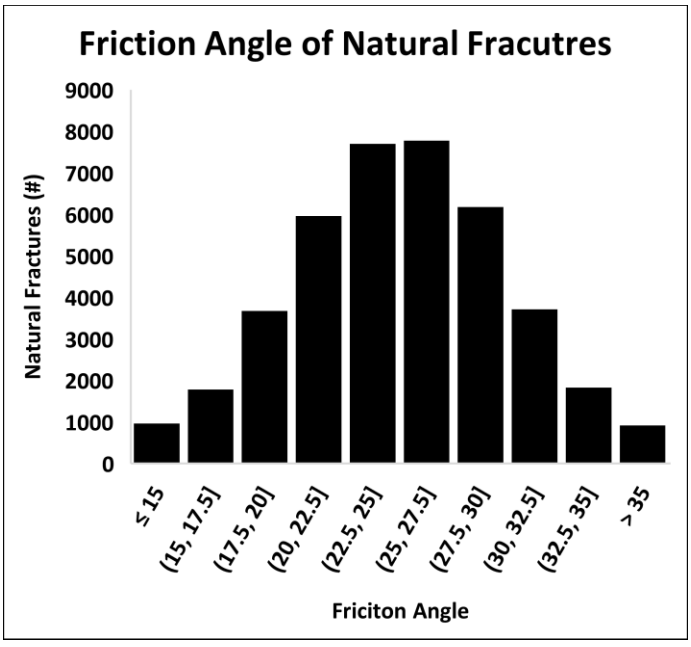

Figure 5.17: Distribution of friction angle used for the population of natural fractures in the simulation study.

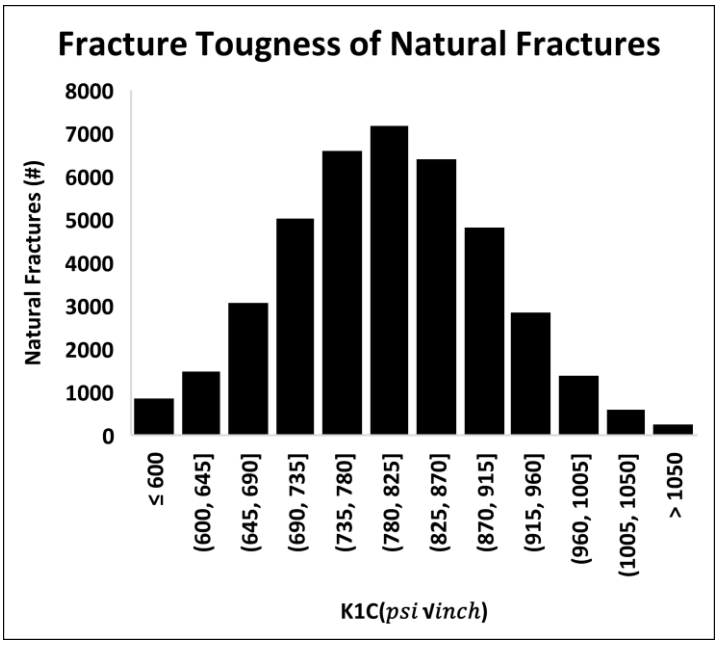

Figure 5.18: Distribution of fracture toughness of natural fracture population used in the simulation study.

The simulator is initialized with 40,500 natural fractures, and the domain of the simulation is 300m by 300m (natural fractures are populated in this area). The simulator allows intersection and merging of created fracture networks (originating from different perforations). The natural fractures and the hydraulic fracture are assumed to be vertical. It is assumed that only one fracture originates from each cluster.

Property	Value	Units
Minimum Horizontal Stress	5200	psi
Maximum Horizontal Stress	5720	psi
Youngs Modulus	2.4	Mpsi
Poisson's Ratio	0.25	
Reservoir Permeability	190	nD
Reservoir Porosity	6.3	%
Pore Pressure	3918	psi
Injection Rate	90	bbl/min
Injection Time	15	min
Frac-fluid viscosity	1	cP
Fracture height	50	m
Frac-fluid compressibility	$4.40x10^{-10}$	Pa^{-1}
Frac-fluid density	1000	kg/m^3
Reservoir-fluid viscosity	3	cP
Reservoir-fluid compressibility	$9.67x^{-10}$	Pa^{-1}

Table 5.1: Parameters used for hydraulic fracturing simulation.

Possible locations of microseismic events associated with shear failure events that occur during the hydraulic fracturing process are registered during the simulations as has been shown in section 2.2.7.2. As the simulation has a large number of natural fractures, the contribution of these slippage (microseismic) events on the geomechanics of the

reservoir is not accounted for in this study. This allows for each simulation to run in a tractable amount of time and utilize the model for stochastic analysis by running several simulations. After the fracturing process is complete, another synthetic core is extracted on the fractured reservoir at 100 feet from the cluster location parallel to the wellbore (see Figure 5.19). The number of intersections of hydraulic fractures and natural fractures are recorded during this synthetic coring process (to compare with the actual core taken)

5.9 SIMULATION RESULTS

Figure 5.19 shows the final fracture network shape obtained from the stage-scale hydraulic fracturing simulation. The cohesion of the natural fractures is varied to manipulate the morphology of the created fracture network. It is observed that at low values of cohesion, a large number of intersections of hydraulic fractures and natural fractures take place. This leads to the formation of highly branched fracture networks. Due to the large number of intersections, the hydraulic fracture growth direction is controlled by the dominant natural fracture direction. The hydraulic fracture orientation is almost always along the natural fractures. This is unlike what is observed in the HFTS core data. In comparison, in the case of high cohesion values, the tendency of the hydraulic fracture to intersect with the natural fractures decreases, leading to very few fracture branches and growth of the hydraulic fracture primarily along the Sh_{max} direction. In this work, we chose a moderate value of the cohesion given by a Gaussian distribution with a mean of 1.3 MPa and standard deviation of 0.2 MPa. The results indicate significant branching of the growing hydraulic fracture and the overall growth of the hydraulic fracture network along the Sh_{max} direction. The reorientation of the growing hydraulic fracture along the Sh_{max} direction can also be observed in the simulation. A synthetic core of a hundred-meter length is extracted from the simulation domain and analyzed (Figure 5.19) at a distance of 100 ft

(same as in the case of cores 1 to 4 described in the previous section). A total of 13 hydraulic fractures, 111 intact natural fractures and 10 reactivated natural fractures are observed in the synthetic core.

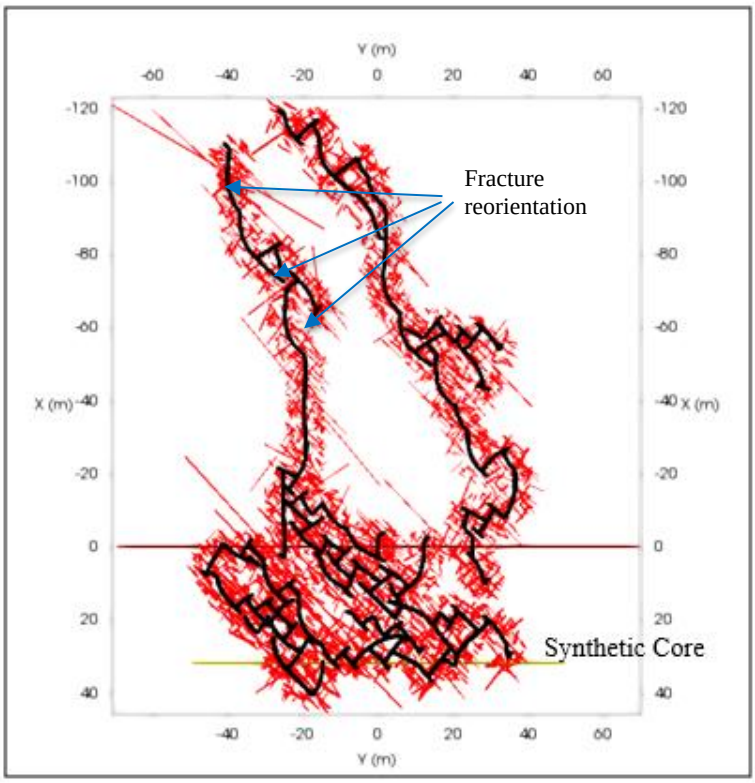

Figure 5.19: The final fracture shape along with the natural fractures simulated in the reservoir from the stage scale (three clusters) hydraulic fracturing simulations. It is assumed that each cluster leads to the formation of a single fracture. The location of synthetic core taken from the simulation is also shown.

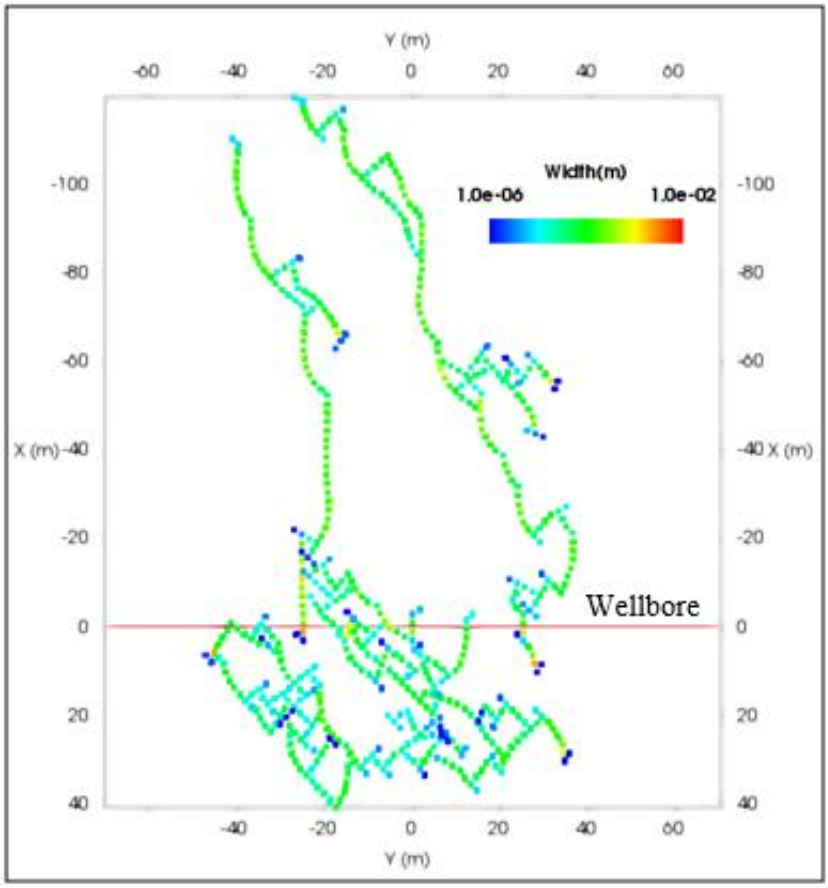

Figure 5.20: The width profile of the created fracture network (color bar shows a linear scale).

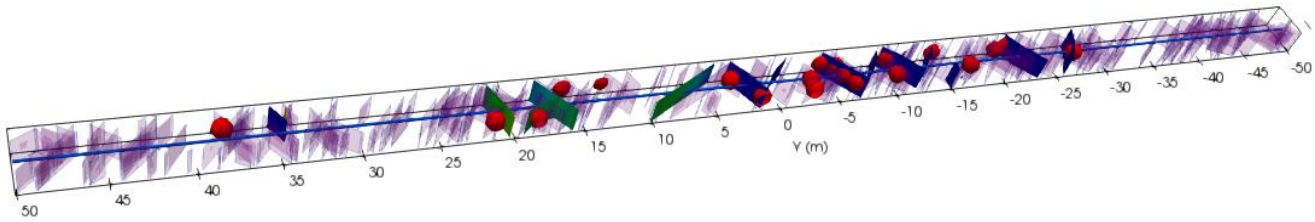

Figure 5.21: Synthetic core taken from the simulation results. Pink elements show natural fractures and the colored elements show the hydraulic fractures.

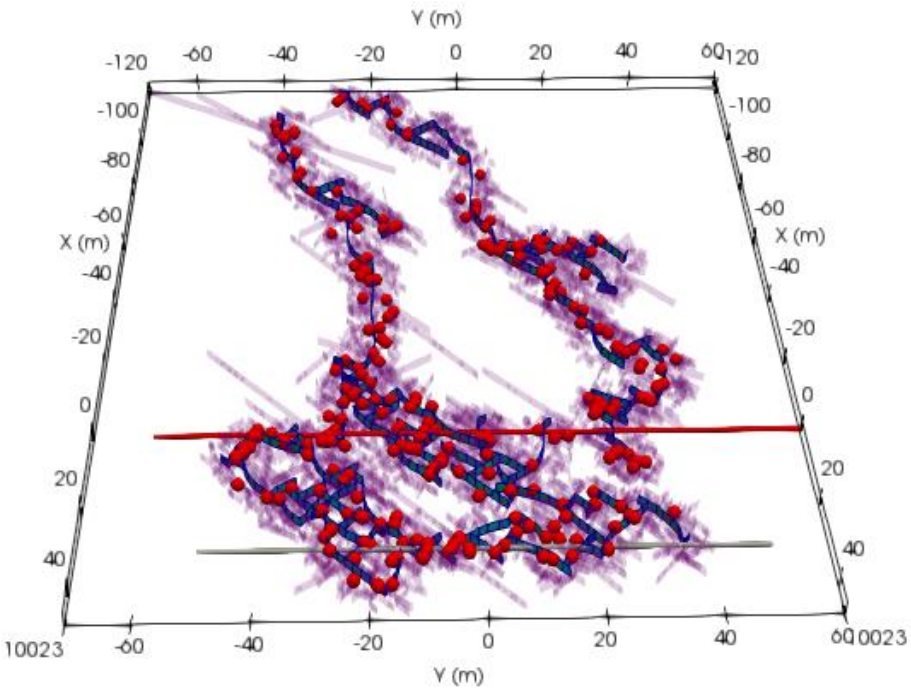

Figure 5.22: Perspective view of the microseismic cloud generated from the simulation during fracture growth.

5.10 DISCUSSION

The visualization of the detailed core description was very helpful in presenting and understanding the locations, orientations, and types of fractures in three-dimensional space relative to perforation clusters. Considering the limited lengths of each perforation cluster, the high fracture density indicates a substantial degree of natural fracture reactivation and fracture bifurcation as hydraulic fractures interact with bed boundaries and natural fractures during propagation. The unique and different directions of the hydraulic fractures versus the natural fractures show the relative number of reactivated vs. hydraulic fractures. Orientations of natural fractures can be grouped into two main directions of NE-SW and WNW-ESE, and hydraulic fractures are primarily trending in the E-W direction.

The method is presented that allows us to populate a reservoir domain with a population of natural fractures that is consistent with core observations. Subsequently, the method of synthetic coring of the two-dimensional population of natural fractures is shown to be a useful tool in confirming that the DFN model agrees with core data. Generating such DFN models and simulating the growth of hydraulic fractures in these models is essential for generalizing the learnings from rare and expensive field studies such as the Hydraulic Fracturing Test Site.

The hydraulic fracturing simulation results show that the orientation and total number of fractures in the simulation and the actual core are consistent. Furthermore, the orientation of simulated growing hydraulic fractures is primarily towards the far-field stress direction. This is consistent with observations from the core: more hydraulic fractures are oriented towards the far-field stress compared to the natural fractures. This is because we have chosen a suitable value for cohesion of the failure planes to ensure that the natural fractures have only a small influence on the direction of propagation of the hydraulic fracture network.

The two dominant orientations of the natural fractures observed in the field core are almost perpendicular to each other. This increases the probability of hydraulic fractures growing along natural fractures to intersect with other natural fractures. Although perpendicular intersections of a hydraulic fracture with a natural fracture increases the tendency of the hydraulic fracture to cross-over the natural fractures, this increased probability (of a growing hydraulic fracture to intersect natural fracture) could dominate and be a possible reason for the high fracture complexity in the Wolfcamp shale.

However, the number of hydraulic fractures observed in the simulations are less than the number of hydraulic fractures observed in the actual core. There are several possible reasons for this:

1. In the simulation, the smaller fractures (fractures smaller than 2m) are ignored as they are smaller than the grid size used in the simulation. As the frequency of natural fractures follows a power-law behavior, smaller size fractures are expected to be abundant in the formation. These fractures can intersect with the growing hydraulic fracture and can significantly contribute towards fluid leak-off and fracture surface area. Larger hydraulic fractures can suppress the growth of smaller fractures due to their large stress shadow (Shrivastava and Sharma, 2018a), so these fractures are less likely to grow compared to larger fractures. However, they will be registered as hydraulic fractures in the field core and will enhance the effective reservoir permeability.
2. It should be noted that the hydraulic fracturing is a three-dimensional phenomenon. The three-dimensional space permits hydraulic fractures to be staggered and allows them to interact with bedding planes, which cannot be observed in fixed-height three-dimensional simulations. This possibility of staggered hydraulic fractures coupled with the interaction of bedding planes could also contribute to the high fracture complexity, as is observed in the HFTS data. The simulator is limited by computational complexity of the solver that makes it difficult to run simulations with more number of natural fractures in three-dimension. The next chapter presents a novel algorithm to reduce the computational complexity of the problem.

Analysis of fracture density revealed that heel-side clusters in a treatment stage show more stimulation in terms of both hydraulic fractures and activated natural fractures. Higher stimulation in the heel-side cluster is likely to be a combined result of fluid and proppant distribution, and the inter-stage stress shadow. From the intact and reactivated natural fracture densities, it was also inferred that inter-stage stress shadowing will change

the stress anisotropy and this may lead to the observed trend of the increasing ratio of reactivated fractures to the total number of natural fractures from the heel to the toe.

In order to improve the prediction from model, future field experiments can collect additional data that can help reduce the uncertainty of the calibration process. One such dataset is the strain distribution as a function of time observed in nearby wells during fracturing. This can be collected using DAS-strain measurements and allow us to observe the strain generated due to propagating fracture on nearby wellbores. It can be useful in identifying the number of fractures propagating during the stimulation process that will further help us to calibrate the model. Also, future work can use the available microseismic data from the HFTS #1 project to compare with the shear failure map from the model. Moment tensor inversion analysis can be done on the simulation results to further constrain the problem.

In addition, better techniques to place natural fractures can be used to improve the prediction from the model. This will allow to place the natural fractures during the synthetic coring process in a more realistic pattern compared to the random distribution used in the current work.

5.11 CONCLUSIONS

In this chapter a direct comparison is made between the core-derived and numerically simulated hydraulic and natural fracture network in the Wolfcamp shale. Based on visualization and statistical analysis of the core data a new technique was developed for generating a fracture network in the reservoir domain. This discrete fracture network is consistent with the core data and was then used to propagate hydraulic fractures from clusters of perforations. By comparing the fracture network geometry from the simulations with the core data the following conclusions can be arrived at.

- A procedure of synthetic coring to establish natural fracture length and orientation distribution is presented. A value of 37500 for constant A in Eq 1 (assuming power-law natural fracture length distribution) and areal fracture density of 0.45 fractures per meter square gives a natural fracture population very similar in density and orientation to the HFTS core data in the discrete fracture network used in our simulations.
- The dip direction of natural fractures either intact or reactivated (NE-SW and WNW-ESE direction) is different from the orientation of the hydraulic fractures (E-W direction). This indicates some degree of reorientation of the hydraulic fracture as the hydraulic fractures propagate along or through the natural fractures. Similar behavior is also observed in the simulation results.
- The large number density and orientation of hydraulic fractures observed in the HFTS core indicates significant branching and bifurcation of hydraulic fractures over the course of the treatment. A similar behavior is observed in the hydraulic fracturing simulations.
- For cores 1 to 4, the number of all fractures was approximately 11.2 for every 10 ft of measured depth. The average fracture densities are 6.7, 3.0, and 1.5 fractures per 10 ft length of MD for hydraulic fractures (HF), intact natural fractures (N), and reactivated natural fractures (NR) respectively. In cores 5 and 6, average fracture densities are 3.5, 1.7 and 0.5 fractures per 10 ft length of MD for HF, N, and NR respectively. In the simulation study 1.3, 11.1, and 1.0 of HF, NF, and NR, respectively are observed for every 10 feet of core. Several possible reasons are provided in the paper for the smaller number of hydraulic fractures and the larger number of reactivated natural fractures seen in the simulations.

- As the minimum size of the fracture is limited by grid size (2 meters) in the simulation, the contribution of smaller fractures is neglected. As fracture frequency increase as the size decreases, these fractures can contribute significantly to the area of contact with the wellbore. This could be a possible reason for the difference in the density of hydraulic fractures observed between the field core and the simulation results.
- Heel-dominated hydraulic fracture growth is observed in the HFTS core data. This behavior is not observed in the simulation as the fluid is equally distributed in all the three perforations and no preference is given to clusters based on their location.
- Reactivation of natural fractures due to hydraulic fracturing is observed in the field core data and in the simulations.

5.12 ACKNOWLEDGMENTS

I would like to thank the entities involved in the Hydraulic Fracturing Test Site #1, Laredo Petroleum Inc., Gas Technology Institute (GTI), Core Laboratories, U.S. Department of Energy (DOE), National Energy Technology Laboratory (NETL), Devon, Discovery Natural Resources, Encana, Energen, ConocoPhillips, Shell, Halliburton, Chevron, TOTAL & Schlumberger. I would also like to acknowledge the funding and support from the member companies of the Hydraulic Fracturing and Sand Control Joint Industry Consortium at the University of Texas at Austin.

Chapter 6: Formulation of Extended Adaptive Integral Method for Displacement Discontinuity Method

In the previous chapter, the limitations of large scale multi-cluster three-dimensional cases with thousands of natural fractures are discussed. To understand the mechanisms of formations of complex fracture networks for field scenarios (three-dimensional simulations), it is imperative to simulate cases with thousands of natural fractures. One of the primary limitations of running such large cases comes from the needed computational requirements.

This chapter discusses a novel technique, Extended Adaptive Integral Method, that is developed here to speed up the solution of geomechanics equations and reduce the computational complexity of the solver in the simulator.

6.1 INTRODUCTION

Obtaining the solution of electromagnetic scattering/wave propagation from arbitrarily shaped electrical conducting structures is required for solving a wide variety of problems such as remote sensing, antenna performance, microwave circuit, etc. (Anastassiu et al., 1998; Bindiganavale et al., 1998; Ling et al., 1998; Zhang and Liu, 2002; Seo and Lee, 2005; Ewe et al., 2005; Yang and Yilmaz, 2011). To obtain the solution of scattering/wave propagation problems, several computational electromagnetic methods are available (Davidson, 2011). Typically for solving such problems, methods based on surface integral equation formulations are preferred. For such large scale problems surface integral equation formulations result in a smaller set of equations with fewer unknowns.

In the hydraulic fracturing simulator presented in the last chapter, the displacement discontinuity method was used for solving the stress field in the reservoir using a surface integral formulation (Crouch, 1976). We have explored the application of an efficient

computational method, Adaptive Integral Method, to solve the geomechanical system of equations.

The Adaptive Integral Method (AIM) is a fast iterative integral-equation solver used to solve large-scale electromagnetic scattering and radiation problems (Bleszynski et al., 1996; Phillips and White, 1997). As compared to the conventional method of moments (used for solving electromagnetic problems), the AIM solver provides significantly reduced storage and solution time (Bleszynski et al., 1996). This reduction is achieved through compression of the impedance matrix (equivalent to influence matrix in DDM), and splitting of the computational operation into near-field and far-field components (Bleszynski et al., 1996; Yang and Yilmaz, 2012). In this chapter, we have extended AIM for solving hydraulic fracturing problems using a displacement discontinuity method in three-dimensional space. The primary objective of this work is to speed up our hydraulic fracturing simulator for large scale problems.

6.2 ADAPTIVE INTEGRAL METHOD

In the models we have developed, the displacement discontinuity method is used for solving the geomechanics part of the problem (see section 2.2.1.1). In this method, the relationship between the displacement discontinuity of each fracture element and the stresses is described using the following equation:

$$\begin{bmatrix} A_{11} & . & A_{1,n-1} & A_{1,3n} \\ . & . & . & . \\ . & . & . & . \\ . & . & . & . \\ . & . & . & . \\ . & . & . & . \\ . & . & . & . \\ A_{3n-1,1} & . & . & A_{3n-1,3n} \\ A_{3n,1} & . & A_{3n,3n-1} & A_{3n,3n} \end{bmatrix} \begin{vmatrix} D_{x1} \\ . \\ D_{xn} \\ D_{y1} \\ . \\ D_{yn} \\ D_{z1} \\ . \\ D_{zn} \end{vmatrix} = \begin{vmatrix} \sigma_{x1} \\ . \\ \sigma_{xn} \\ \sigma_{y1} \\ . \\ \sigma_{yn} \\ \sigma_{z1} \\ . \\ \sigma_{zn} \end{vmatrix} \tag{6.1}$$

where the matrix A contains the coefficients of the influence matrix, σ is the resultant stress acting on the surface of elements; D_x, D_y, and D_z are the displacement discontinuities in the x, y, and z directions, and n is the total number of elements in the model. As every fracture element influences every other element in the simulation, the generated influence matrix is dense.

The obtained system of equations needs to be solved in each convergence loop iteration (see section 2.2.8.1) in the hydraulic fracturing simulation. This system of equations can be solved using a direct solver or an iterative solver. In case of direct solver, we find the inverse of the influence matrix (matrix A) and multiply it with the right-hand side vector. Usually, direct solvers use a variation of the LU decomposition method. In these methods the coefficient matrix A is represented as a product of an upper triangular and a lower triangular matrix. LU decomposition can be viewed as a form of the Gaussian elimination technique in the matrix form. In LU decomposition, the equation $AD = \sigma$ becomes $LUD = \sigma$, where L and U are the upper and lower triangular factors of matrix A, respectively. This modified system of equations can be solved using the forward or backward substitution method. The LU decomposition process has a computational complexity of $O(N^3)$, and the forward and backward substitution has a computational complexity of $O(N^2)$ where N is the size (number of rows or columns) of the square coefficient matrix (matrix A in equation 6.1). As these operations are performed in series, therefore the overall complexity of the direct method comes out to be $O(N^3)$. Hence doubling the size of the matrix requires about eight times more computational operations for direct solvers. Direct solvers lose efficiency for large-scale systems as computational operation can become excessive for large systems. In comparison, the iterative solvers solve the system of equations by only performing multiplication operations of A, and a few

vector operations. For example, in the First-Order Richardson Iteration method, the equation is written in the form $\alpha AD = \alpha\sigma$ by multiplying the system of equations by α on both sides. The equation is then simplified to the form $D + (\alpha A - I)D = \alpha\sigma$, where I is the identity matrix. From this we get $D^{k+1} = (I - \alpha A)D^k + \alpha\sigma$, where k is the iteration counter. This equation can be used iteratively to predict better and better approximation of the D vector till the problem converges below a tolerance. As the most time-consuming operation in iterative solvers involves multiplication of the A vector (which is a N x N dense matrix), hence iterative solvers follow $O(N^2)$ complexity.

Both types of solvers require $O(N^2)$ memory storage to store the matrix. As the system of equations created for solving for the pressure inside the fracture network is non-linear in nature, the geomechanical system of equations needs to be solved along with the pressure equation several times before a solution can be reached. Hence, for large problems with thousands of elements, obtaining a solution requires a significant number of computational operations. This is a major challenge in simulating large multi-stage and multi-well problems using hydraulic fracturing simulators based on the displacement discontinuity method.

In the model presented in this chapter, an extended AIM is used to reduce the computational complexity required to solve the dense system of equations that results from the displacement discontinuity method using iterative solvers. This method speeds up iterative solvers by compressing the dense influence matrix and treating the interaction between far-neighbors and near-neighbors using different methods.

In the next section, Krylov space methods, one of the most efficient iterative solvers are discussed, and the bottleneck that requires maximum computational operations in these solvers for a dense matrix is discussed.

6.2.1 Krylov Space Solvers

The efficient solution of linear systems of equations is a fundamental task in almost all computational problems. To efficiently solve a system of equations, iterative solvers are often employed as their computational complexity is less than direct solvers. An iterative method is a mathematical procedure that uses an initial guess to generate a sequence of improving approximate solutions. One of the most successful classes of iterative solvers for solving linear systems of equations are Krylov space methods. Examples of Krylov space methods are generalized minimal residual method (GMRES), biconjugate gradient method (BICG), and biconjugate gradient stabilized method (BiCGSTAB).

Krylov space methods for solving a system of equations works by forming a Krylov subspace of the coefficient matrix and the residual of the system of equations. The Krylov subspace is defined as follows:

$$K_r(A, b) = span\{b, Ab, A^2b, A^3b, \dots A^{r-1}b\} \tag{6.2}$$

where $K_r(A, b)$ is the Krylov subspace of order r generated by a coefficient matrix A of size NxN and a vector b of size Nx1.

In order to solve a system of equations given by the equation $Ax = B$ using the Krylov space method, a Krylov subspace $K_r(A, \boldsymbol{r})$ is formed where **r** is the residual of the problem (residual represents a measure of the error between the current iteration solution and the required result). The residual is defined differently for different Krylov space methods. The solution is obtained by minimizing the residual over the formed subspace. The most time-consuming step of these solvers is the matrix multiplication step during the creation of the Krylov subspace. This step involves N^2 multiplication operations for a dense square matrix of size N. Hence, the computational complexity of this step follow $O(N^2)$.

The Adaptive Integral Method reduces the computational complexity of the vector multiplication of the coefficient matrix and the residual vector step. The following section

explains the developed extended Adaptive Integral Method used for speeding up the hydraulic fracturing simulator in detail.

6.2.2 Extended Adaptive Integral Method

The Extended Adaptive Integral Method (AIM) is based on the principle that the influence of an element on another element sufficiently far away can be computed by using a set of weighted elements. In the case of DDM elements, influence is the stress acting on an element due to the opening of another element. In extended AIM, a three-dimensional auxiliary regular grid is created around the fracture elements. A set of weighted DDM elements for calculating the interaction between far elements are placed on the corner of the cells of the created auxiliary grid. This choice of having a regular grid for placing the weighted elements changes the nature of the created influence matrix, which is exploited for compressing the influence matrix and decreasing the computational complexity of the problem.

Each discretized fracture element in the simulation interacts with all other elements and influences the stresses acting on them. The influence of one element's displacement discontinuity on other elements is represented by the coefficients of the influence matrix. The element which is the source of the influence (due to its opening and shearing) is called a source element, and the element that observes the stresses acting on itself is called an observer element. In DDM, every element acts both as a source and as an observer.

In the simulator, it is assumed that the vertical stress is much higher than the horizontal stress, and hence, the fracture always propagates vertically. Therefore, the DDM elements are always placed with normal lying in the x-y plane. In order to generate a set of weighted elements, each fracture element is represented as a combination of two perpendicular elements oriented towards the global x and y directions. These equivalent

elements are assumed to be located at the original location of the fracture element (see Figure 6.1).

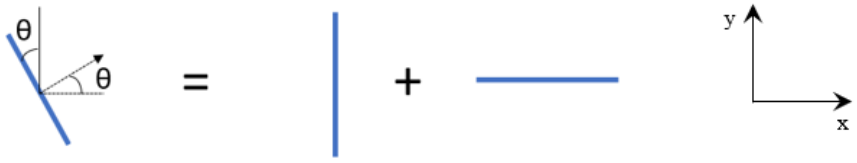

Figure 6.1: The figure shows an element oriented at an angle theta from the horizontal and its equivalent representation as two elements along the x and y-direction. The image lies in the x-y plane.

The displacement discontinuity associated with the equivalent elements is calculated by projecting the displacement discontinuity of the fracture element on the global x-direction and y-direction oriented equivalent elements. Equations 6.3 and 6.4 are used for calculating the projection on the global x-oriented and y-oriented elements.

$$D_{sl}^{x} = D_{sl}\cos(\theta) \tag{6.3a}$$

$$D_{sh}^{x} = \frac{D_{sh}}{2} \tag{6.3b}$$

$$D_{nn}^{x} = D_{nn}\cos(\theta) \tag{6.3c}$$

$$D_{sl}^{y} = D_{sl}\sin(\theta) \tag{6.4a}$$

$$D_{sh}^{y} = \frac{D_{sh}}{2} \tag{6.4b}$$

$$D_{nn}^{y} = D_{nn}\sin(\theta) \tag{6.4c}$$

where D_{sh}^{x}, D_{sl}^{x}, and D_{nn}^{x} represents the displacement discontinuity of the x-oriented grid element, D_{sh}^{y}, D_{sl}^{y}, and D_{nn}^{y} are the displacement discontinuity of the y-oriented grid

element, and D_{sh}, D_{sl}, and D_{nn} are the displacement discontinuity of the original fracture element along the height, length, and normal direction, respectively.

The uniform auxiliary grid for calculating the interaction between distant sources and observers encloses the volume of interest for the interpolation of DDM elements. The created grid contains $N = N_x N_y N_z$ corner nodes, where N_x, N_y, and N_z are the number of nodes in the global x, y, and z-direction, respectively, and the nodes are separated by Δx, Δy, and Δz lengths in the x, y, z directions, respectively. At each corner of the grid, two elements are placed. One element has its normal direction oriented along the global x-direction, whereas the other has its normal along the global y-direction (see Figure 6.2). For the elements on the auxiliary grid oriented along the x-direction, the projection of displacement discontinuity along the x-direction is interpolated, whereas, for the elements along the y-direction, the projection of displacement discontinuity along the y-direction is interpolated.

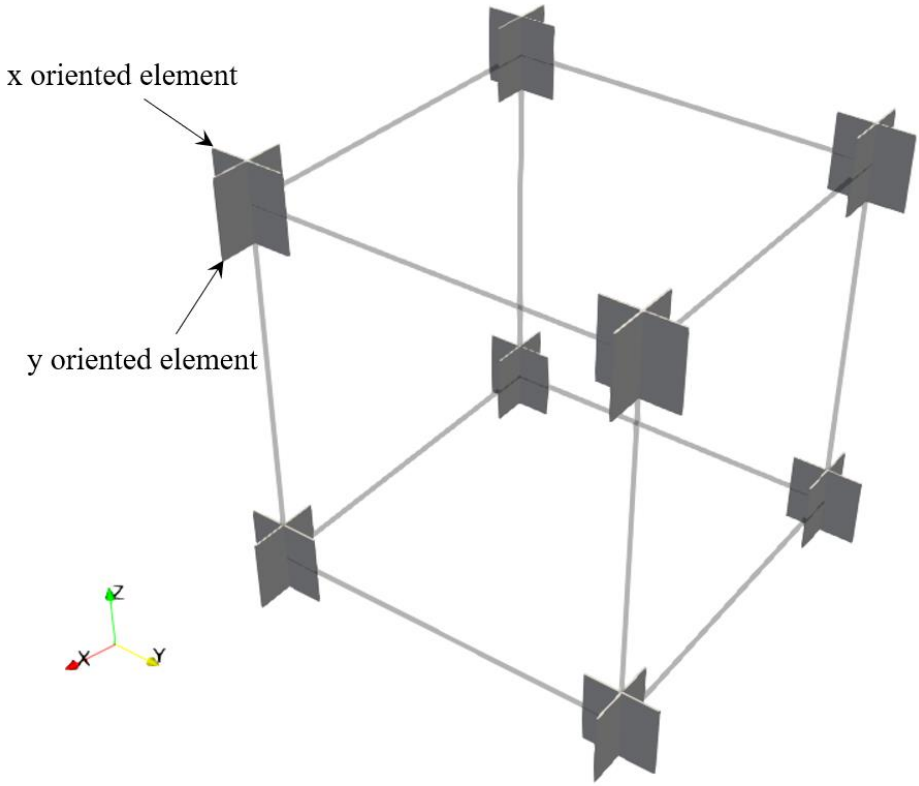

Figure 6.2: DDM elements at the corner of the created mesh. Each corner contains two elements: x-oriented elements with normal towards the x-direction, and y-oriented elements with normal towards the y-direction. The DDM simulation element inside the grid is interpolated on the corner elements.

After creating the auxiliary grid, the displacement discontinuity associated with each DDM element in the simulation is interpolated on the corner elements of the auxiliary grid (Figure 6.3). In the model, Lagrange interpolation of any odd order (first, third, fifth, seventh, etc.) can be used to interpolate the displacement discontinuity values on the auxiliary grid. An odd order of interpolation is used to keep the interpolation symmetric with respect to the grid containing the fracture element (each side of the grid that contains the fracture element has an equal number of interpolation grids).

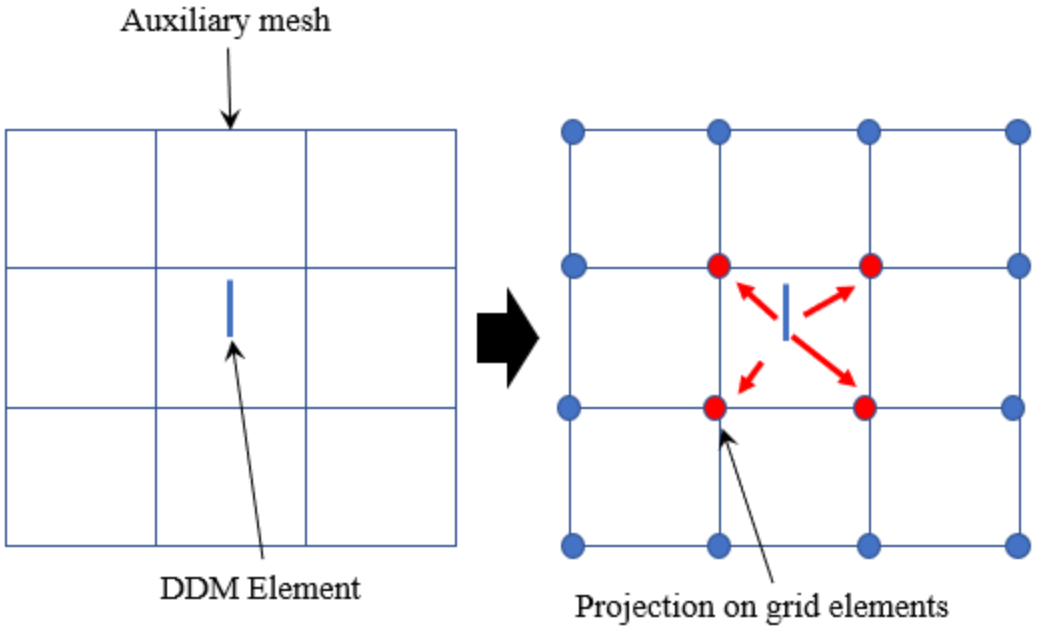

Figure 6.3: Figure shows the projection of the DDM element on the created auxiliary mesh for the x-oriented element. A similar process is followed for y-direction elements. The first-order Lagrangian interpolation is employed in the shown case.

For a first-order interpolation, only the grid containing the element is considered "near grid". For a third-order interpolation, the element is also interpolated on the corners of one neighboring grid in each direction, and hence, in a three-dimensional auxiliary grid, there are 64 grids corners on which the element's displacement discontinuity is interpolated. The elements inside the near grids are defined as near-neighbors, and elements outside these grids are defined as far-neighbors. Figures 6.4 and 6.5 show a representation of near and far-neighbors grid cells for first and third-order interpolation.

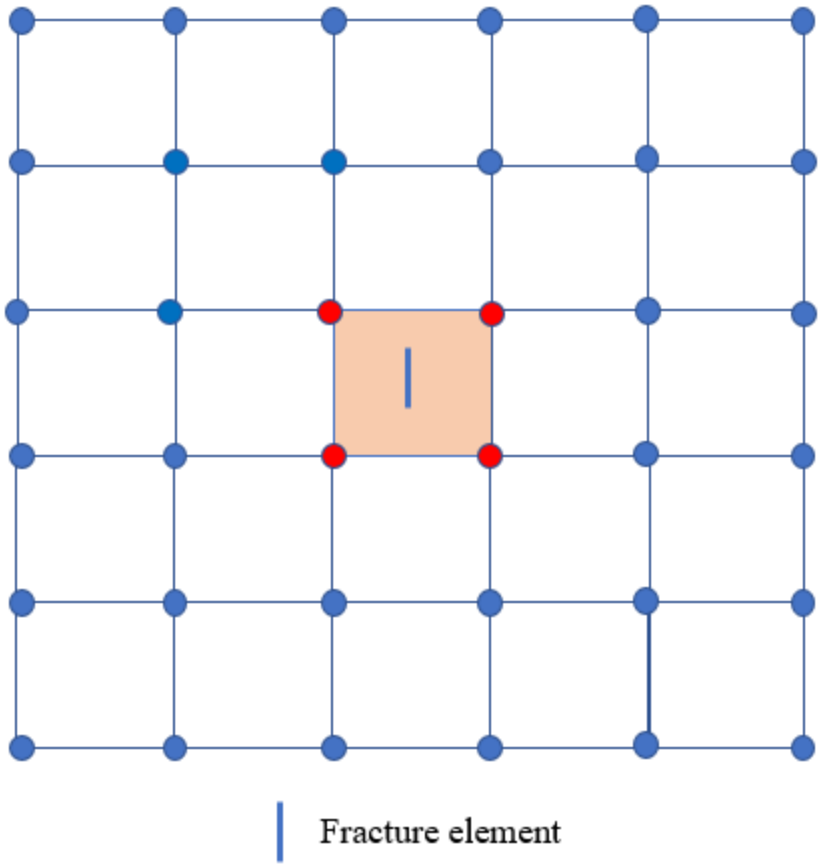

Figure 6.4: Figure showing grid corners used for interpolation for a first-order Lagrangian interpolation for a two-dimensional system as red circles. The blue element is the source fracture element whose effect on other elements is being calculated. For the first-order interpolation, only the elements in the colored grid cell are considered as near-neighbors.

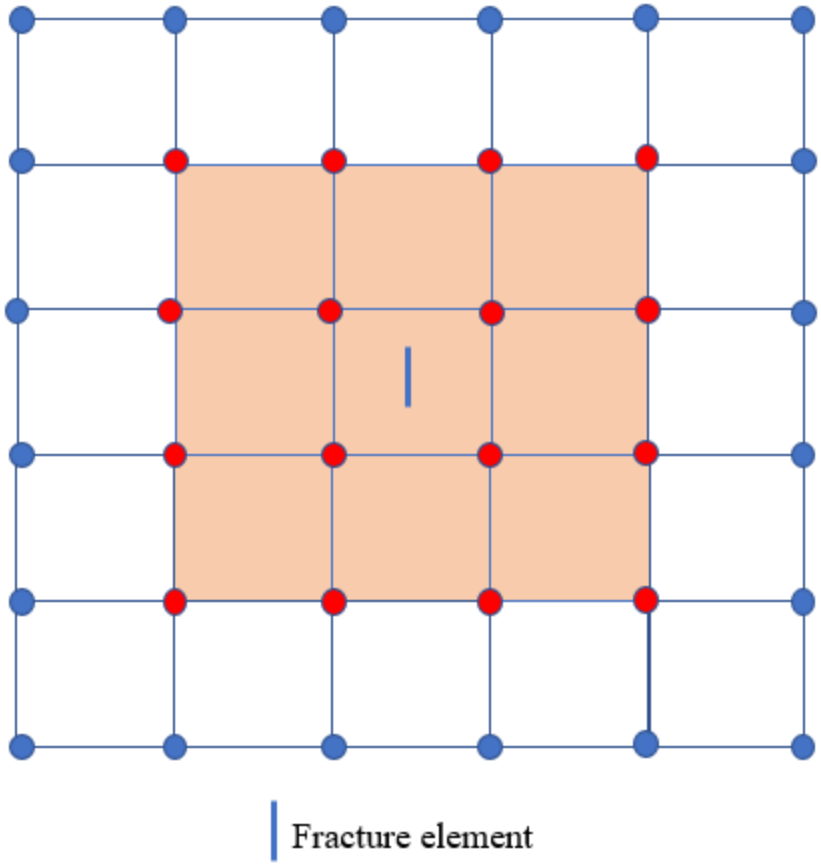

Figure 6.5: Figure showing grid corners used for interpolation for a third-order Lagrangian interpolation for a two-dimensional system as red circles. The blue element is the source fracture element whose effect on other elements is being calculated. For the third-order interpolation, grid cells next to the grid cell of the source element are also included in the interpolation.

As the equivalent sources and observers are placed on the corners of a regular auxiliary grid, the relative distance between the elements becomes a constant multiple of the grid size of the auxiliary mesh in each direction (Figure 6.6 shows the scenario for a one-dimensional case).

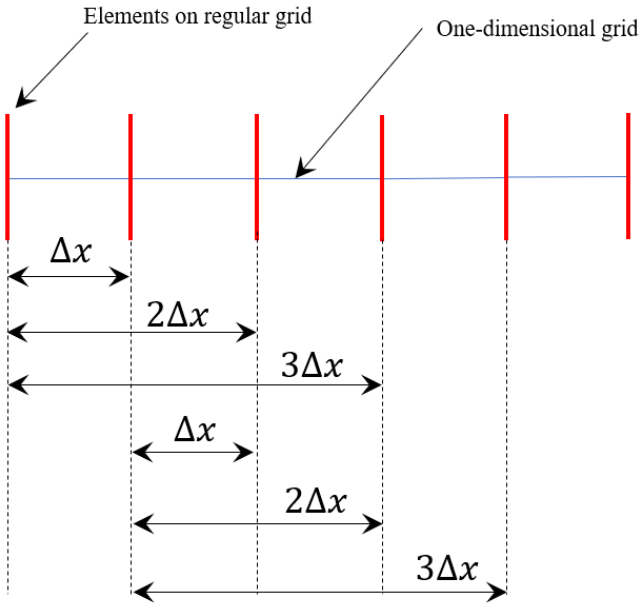

Figure 6.6: Due to the placement of elements on a regular grid, the relative distance between elements becomes a multiple of the grid size. The figure shows a one-dimensional grid (shown as a blue line) with DDM elements (shown in red) placed at the corner of the grid cells.

The influence coefficients calculated in the DDM are a function of the relative distance. Hence, such a configuration of elements on a regular grid results in a periodic behavior of the influence coefficients. On arranging these periodic influence coefficients to create the DDM influence matrix, the resultant matrix exhibits a regular pattern. Each descending diagonal of the created influence matrix moving from left to right has a constant value. This type of matrix is known as a Toeplitz matrix or a diagonal-constant matrix. Figure 6.7 shows the nature of the influence matrix obtained for elements placed on a regular grid for the case shown in Figure 6.6.

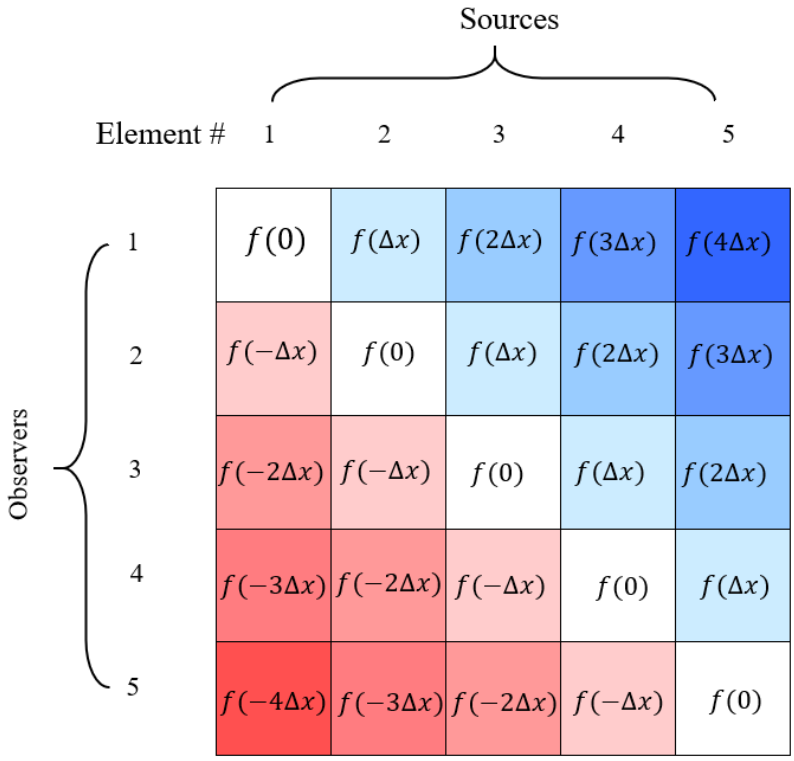

Figure 6.7: The figure shows the Toeplitz matrix formed as the elements are placed on a regular gird. The function f(x) gives the influence coefficients based on the relative distance of elements. For example, the influence coefficient at a location (1, 2) is a function of the relative distance between element number 2 and element number 1, which in this case is Δx (grid size of the auxiliary mesh). As the relative distance repeats in a regular pattern, the diagonals of the created influence matrix become constant. Similar color represents similar value in the figure.

Due to the regular nature of the grid, the number of unique influence coefficients in the created matrix reduces from N^2 to 2N (see Figure 6.8). Hence, the information required to represent the influence matrix gets compressed if a regular grid is used. This compressed information can be visualized as a wave (see Figure 6.9), representing the behavior of the influence of a source element as the observer moves from one end to another end of the created regular auxiliary mesh. Similarly, for a three-dimensional

auxiliary grid, the wave representing the compressed influence matrix is three-dimensional in nature and can be represented as a three-dimensional matrix.

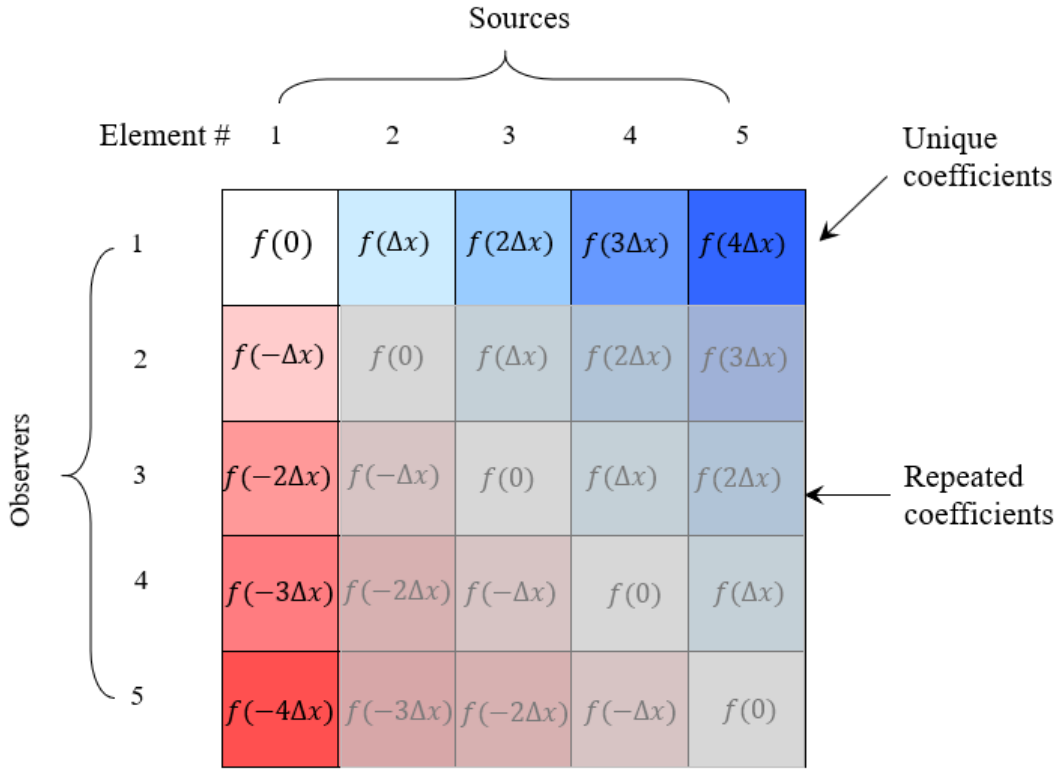

Figure 6.8: The figure shows the unique coefficients in the created influence matrix of the auxiliary grid. The elements of the first row and first column are sufficient to represent the entire influence matrix.

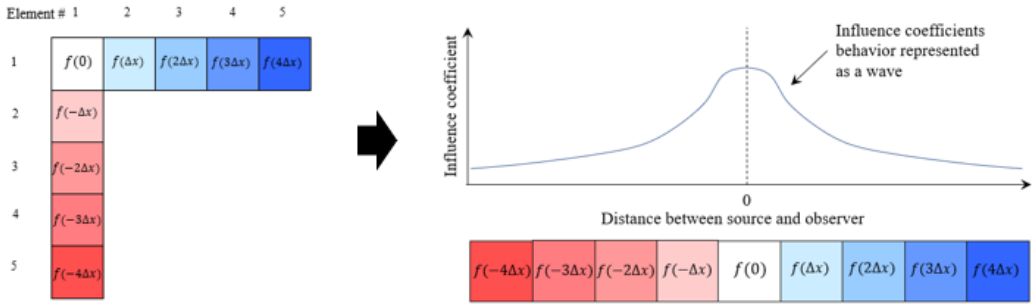

Figure 6.9: Representation of the influence matrix of a one-dimensional auxiliary grid as a one-dimensional vector. The one-dimensional matrix can be represented as a wave. The wave represents the variation of the influence coefficients as the observer moves from one farthest corner of the created auxiliary grid to the other.

The AIM method exploits the property associated with the multiplication operation of the created Toeplitz matrix. If one of the matrix in a multiplication operation is Toeplitz in nature, then the multiplication operation can be constructed as a convolution operation. Hence for a Toeplitz matrix **A,** its multiplication with a vector **b** can be written as follows:

$$\boldsymbol{y} = \boldsymbol{Ab} = \boldsymbol{A} * \boldsymbol{b} \tag{6.5}$$

where * is the convolution operation.

The nature of the created matrix converts the multiplication operation in the iterative Krylov space algorithm involving the influence matrix into a convolution operation. After converting the multiplication operation into a convolution operation, the problem is transferred in the frequency domain, as shown below:

$$FFT(\boldsymbol{y}) = FFT(\boldsymbol{Ab}) = FFT(\boldsymbol{A} * \boldsymbol{b}) \tag{6.6}$$

where FFT is the fast Fourier transform operation.

Now, according to the Convolution Theorem, the Fourier transform of the convolution of two signals (inputs) is the pointwise product (term by term multiplication) of the Fourier transform of each signal.

Hence, the equation can be written as follows:

$$FFT(\boldsymbol{y}) = FFT(\boldsymbol{Ab}) = FFT(\boldsymbol{A} * \boldsymbol{b}) = FFT(\boldsymbol{A}).FFT(\boldsymbol{b}) \tag{6.7}$$

where the term on the RHS is the pointwise product or term by term multiplication.

In order to get the final result of the multiplication process, the inverse FFT is taken of the product of the term by term multiplication. Hence, Equation 6.7 can be written as:

$$y = FFT^{-1}\big(FFT(\boldsymbol{A}).FFT(\boldsymbol{b})\big) \tag{6.8}$$

The pointwise product or term by term multiplication has a complexity of O(N) as N points in the space domain (at the corner of the auxiliary mesh) are to be multiplied. In addition, the FFT operation and inverse FFT operation both have a computational complexity of O(NlogN). As the FFT operation, the term by term multiplication, and inverse FFT operation are done in series, the overall computational complexity is governed by the slowest step, i.e. the FFT/inverse FFT operation. This results in a reduction of the complexity of the multiplication operation from $O(N^2)$ for multiplication in the space domain (direct multiplication) to O(NlogN) for multiplication in the frequency domain (by AIM).

The above explanation is for a one-dimensional problem with a single Green's function representing the interaction between elements. In DDM, the three local displacement discontinuities are related to three local stresses (normal, shear in the horizontal direction, and shear in the vertical direction) through nine equivalent Green's functions. The relationship between displacement discontinuity and stress is given by the equation shown below:

$$\sigma_{sL}^{i} = \sum_{i=1}^{i=N} A_{sL\to sL}^{ij} D_{sL}^{j} + \sum_{i=1}^{i=N} A_{sH\to sL}^{ij} D_{sH}^{j} + \sum_{i=1}^{i=N} A_{nn\to sL}^{ij} D_{nn}^{j} \tag{6.9a}$$

$$\sigma_{sH}^{i} = \sum_{i=1}^{i=N} A_{sL\to sH}^{ij} D_{sL}^{j} + \sum_{i=1}^{i=N} A_{sH\to sH}^{ij} D_{sH}^{j} + \sum_{i=1}^{i=N} A_{nn\to sH}^{ij} D_{nn}^{j} \qquad (6.9b)$$

$$\sigma_{nn}^{i} = \sum_{i=1}^{i=N} A_{sL\to nn}^{ij} D_{sL}^{j} + \sum_{i=1}^{i=N} A_{sH\to nn}^{ij} D_{sH}^{j} + \sum_{i=1}^{i=N} A_{nn\to nn}^{ij} D_{nn}^{j} \qquad (6.9c)$$

where $\sigma_{sL}^{i}, \sigma_{sH}^{i}, \sigma_{nn}^{i}$ are stresses acting on the i^{th} fracture element surface, $D_{sL}^{j}, D_{sH}^{j}, D_{nn}^{j}$ are the displacement discontinuities associated with the j^{th} element, N is the total number of elements in the domain, and A are the influence coefficients. The subscripts sH, sL represents shear displacement discontinuity in the height and length direction of the element and the subscript nn represents displacement discontinuity in the normal direction of the element. These influence coefficients are calculated from the Green's function solution representing the effect of displacement discontinuity of the sources on the stresses acting on observers. The details about the calculation of these coefficients are explained in Chapter 2. In addition, a fracture element, when acting as a source, is represented as a combination of a set of two perpendicular elements; and a fracture element acting as an observer is also represented as a combination of two perpendicular elements on the corners of the created auxiliary mesh. Hence, the interaction between a source and an observer is described by four types of interactions between the corner elements of the auxiliary mesh. These interactions are between x-oriented elements as the source and x-oriented elements as the observer, x-oriented elements as the source and y-oriented elements as the observer, y-oriented elements as the source and x-oriented elements as the observer, and y-oriented elements as the source and y-oriented elements as the observer. The following figure depicts these interactions.

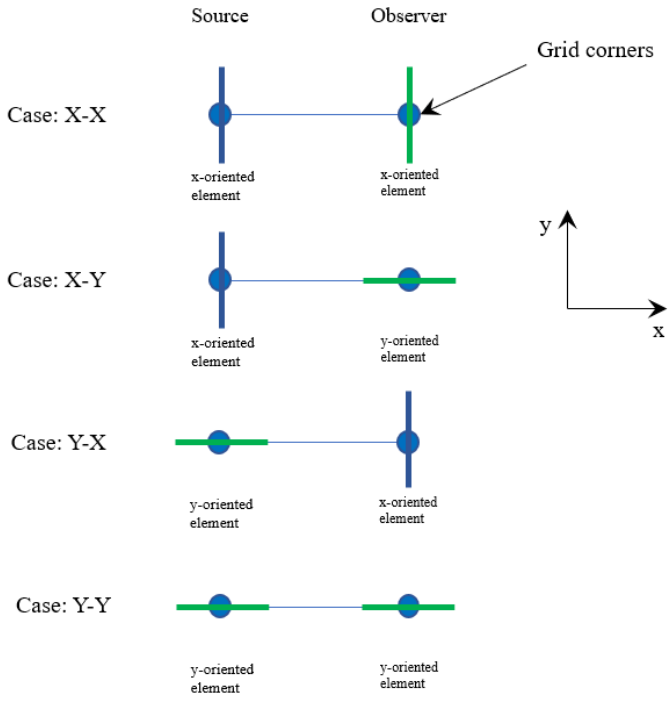

Figure 6.10: Four interaction scenarios between the grid elements are possible. The figure shows the four interaction scenarios as case X-X, case X-Y, case Y-X, and case Y-Y. The first direction in the case represents the orientation of the source and the second represents the direction of the observer.

In order to represent the contribution of far-neighbor interactions in the multiplication operation of the iterative solver using weighted elements correctly, the influence of source element on observers through the created auxiliary mesh should account for all the four types of interactions (interaction between elements represent their contribution in the matrix multiplication process of the iterative solvers). To capture all the four types of interaction for the nine different Green's functions, the interaction between the grid elements has to be calculated 36 times for each iteration of the iterative solver.

In this process of calculation of interaction through the auxiliary mesh, the far-neighbors and near-neighbors are not treated separately (the interaction between far

neighbors and near neighbors are included in the total interaction calculated through the auxiliary grid). Hence, in addition to the far-neighbor interaction, the near-neighbor interactions are also included in the result. The near-neighbor interaction result has a high error as the weighted elements cannot represent the near-neighbor interaction correctly. Hence, in order to capture the interaction of only far-neighbors, a correction term representing the interaction of near-neighbor is subtracted from the matrix product. This is done for each pair of neighbors considered as near-neighbors. This is achieved by directly using the influence matrix for the auxiliary mesh (influence matrix of the elements placed on the auxiliary mesh in the space domain). The influence matrix for calculating this correction term only contains the influence coefficients between near grid cell corner elements (corner elements on which the interpolation takes place), as only the near neighbor interaction through the auxiliary grid has to be subtracted. Therefore, the influence matrix for correction is a square matrix of size $3(O+1)^3$, where O is the order of interpolation. Due to the small size of the matrix, the correction step does not impede the performance of the AIM method. Although, if there are a significant number of near-neighbor corrections, the overall algorithm can be limited by these correction operations.

After calculating the contribution between far-neighbor interaction in the multiplication product and correcting for the near-neighbor interaction through an auxiliary grid, the correct near-neighbor interaction is added. To calculate the near-neighbor interaction's correct contribution, the fracture element's influence matrix is used (as described in Chapter 2) and multiplied with the displacement discontinuity vector. Although, as only the interaction between each pair of near-neighbor is calculated, the created influence matrix has only 36 entries rather than the $9N^2$ elements for the full influence matrix of all the elements in the system, where N is the number of elements in the system. As the computational complexity of multiplying a matrix with a vector follows

$O(N^2)$, the computational operations required to calculate the near neighbor interaction is significantly less (almost negligible) compared to the multiplication of the full influence matrix. Although, in cases having a significant number of near-neighbor elements (several elements sharing a grid), computational operations associated with the near neighbor interaction can start dominating the behavior of the overall problem.

The contribution from both the operations described (far-neighbor through the auxiliary mesh and near-neighbor by direct multiplication) above is added, and the total contribution of the interactions of fracture elements is calculated.

The following section describes the implementation of the Extended Adaptive Integral Method for DDM in a numerical simulator.

6.3 IMPLEMENTATION OF THE EXTENDED ADAPTIVE INTEGRAL METHOD

In AIM, the matrix multiplication done in the iterative solvers for finding the solution of the system of equation is split into two parts, i.e., the contribution to the matrix multiplication due to near-neighbor interaction and the contribution to the matrix multiplication due to far-neighbor interaction. The matrix multiplication is written mathematically as follows:

$$AD = A^{near}D + A^{far}D \tag{6.10}$$

where A is the influence matrix of fracture elements, D is the displacement discontinuity vector, A^{near} represents the contribution to the product due to the interaction of near-neighbors, and A^{far} represents the contribution to the product due to the interaction of far-neighbors. The contribution A^{near} is calculated by using a full DDM matrix for each pair of neighbors. The contribution to the matrix product due to interaction between far-neighbors is further simplified and consists of the following three operations: 1) interpolation of the displacement discontinuity from the fracture elements on the auxiliary

grid elements; 2) propagation of interaction through the grid (calculation of interaction between grid elements); 3) anterpolation (opposite of interpolation) of the displacement discontinuity from the auxiliary grid elements back on the fracture element. These three operations are represented mathematically in a matrix form as follows:

$$A^{far} = \lambda G \lambda^T \tag{6.11}$$

where λ^T is a matrix which operates on the D (displacement discontinuity vector) vector and interpolates the fracture element's displacement discontinuity on the auxiliary grid, G (the created Toeplitz matrix) is the matrix that calculates the interaction through the grid, and λ is the transpose operation of λ^T. This operation anterpolates the displacement discontinuity from the auxiliary grid on the DDM elements.

Hence, equation 6.11 can be written as

$$AD = A^{near} D + \lambda G \lambda^T D \tag{6.12}$$

In order to calculate the λ and λ^T matrices, the interpolation terms are arranged in a matrix form such that each displacement discontinuity gives $(N+1)^3$ interpolated values associated with the grid corners where N is the order of interpolation. The following figure shows the equation used for interpolation of elements on the corner grids using first-order Lagrange interpolation in the x-direction.

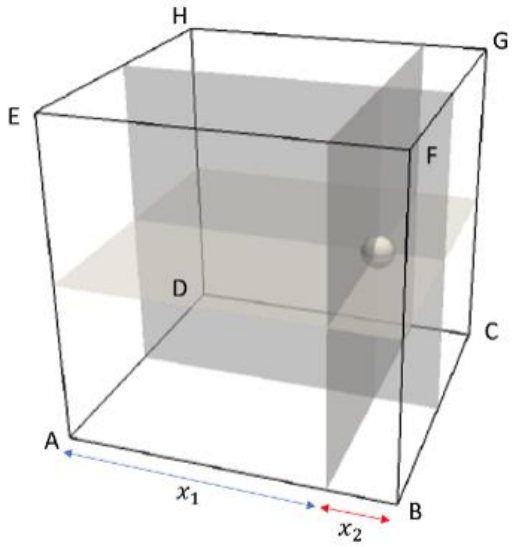

$$A_{interpolation} = \frac{x_1}{x_1 + x_2}$$
$$B_{interpolation} = \frac{x_2}{x_1 + x_2}$$
$$C_{interpolation} = \frac{x_2}{x_1 + x_2}$$
$$D_{interpolation} = \frac{x_1}{x_1 + x_2}$$
$$E_{interpolation} = \frac{x_1}{x_1 + x_2}$$
$$F_{interpolation} = \frac{x_2}{x_1 + x_2}$$
$$G_{interpolation} = \frac{x_2}{x_1 + x_2}$$
$$H_{interpolation} = \frac{x_1}{x_1 + x_2}$$

Figure 6.11: Figure shows the first order Lagrange interpolation. $X_{interpolation}$ shows the value of the interpolation coefficient for the corner X.

The interpolation coefficients are calculated using the Lagrange interpolation polynomial formula. The following formula gives interpolation coefficients for a k[th] order interpolation:

$$P_j(x) = y_j \prod_{\substack{k=1 \\ k \neq j}}^{n} \frac{x - x_k}{x_j - x_k} \tag{6.13}$$

where j represents the interpolation points, k represent the corner points, y_j is the value at the corners and P_j is the interpolated value.

In order to correct the error generated due to the inclusion of the interaction of the near-neighbors in the A^{far} matrix, a correction matrix is generated by considering the interaction of near-neighbors through the auxiliary grid. This correction matrix is then

subtracted to get the correct value of matrix multiplication. After including the correction term, equation 6.13 can be written as:

$$AD = A^{near}D - A_{near}^{grid}D + \lambda G \lambda^T D \tag{6.14}$$

The matrices A^{near}, A_{near}^{grid}, λ, G, and λ^T are required to be calculated only when new elements are added to the network; hence, for each iteration of the solver, only the D matrix is changed. The FFT of the G matrix is also calculated only once for a specified grid (only to be calculated once if the dimensions of the auxiliary grid do not change). This reduces the required computational operations for each iteration, even though at the start of the simulation creation and storage of these matrices may require significant computational operations.

The next section presents results obtained by the application of AIM for the displacement discontinuity method.

6.4 RESULTS

In this section, two different aspects of the implementation are tested: 1) the accuracy of the Extended Adaptive Integral Method, 2) the improvement in the speed of the solver using the AIM, and the results are presented.

6.4.1 Accuracy of the Extended Adaptive Integral Method

In this section, we investigate the error observed in the results obtained from the Extended Adaptive Integral Method relative to the results obtained by direct multiplication.

6.4.1.1 Effect of Order of Interpolation

To investigate the effect of the order of interpolation on the error observed in the implemented AIM formulation, a case is set up with 25 fractures (DDM elements). The following table shows the properties used for conducting the simulation.

Table 6.1: Parameters used for simulation

Property	Value
Young's modulus	2.4 million psi
Poisson's ratio	0.26
Sh_{min}	5381 psi
Sh_{max}	5381 psi
Element length (x)	0.5 m
Element length (y)	0.5 m
Auxiliary grid cell height	1 m
Auxiliary grid cell length	4 m
Auxiliary grid cell width	1 m
Auxiliary grid length	50 m
Auxiliary grid height	1 m
Auxiliary grid width	1 m

The fractures are distributed randomly in space (25 individual fracture elements), and the Extended Adaptive Integral Method is used to calculate the influences. All the elements are oriented at an angle of 45 degrees from the global x-axis. This orientation is chosen to have a projection on both x- and y-oriented grid elements and verify the calculation associated with the X-X, X-Y, Y-X, and Y-Y interactions. Figure 6.12 shows the distribution of the elements in the simulation domain. The elements are distributed in the space in an auxiliary grid containing 48 corners and a total of 96 elements on the grid corners (x and y-oriented). The number of fracture elements, in this case, is limited to 25 to keep the results tractable and easy to interpret.

Four cases are run with a different order of interpolation. The locations of the elements in all the four cases are kept the same. Figure 6.13 shows the results obtained for the product of the coefficient matrix and residual vector for an iteration. The results include the effect of both far and near elements. Figure 6.14 shows the mean error for the results for different orders of interpolation. It can be observed that for the first order of interpolation, although the results obtained through AIM are close to the results obtained from direct multiplication, the cumulative error is significantly high (close to 100%). It can be seen that most of the vector product results (or the acting stresses) obtained from AIM are very close to the values obtained from direct multiplication, although for high magnitude points, the error is high. The high magnitude points represent near-neighbor interaction, as elements influence (exhibit stresses) other nearby elements strongly. As for the first-order interpolation, the near-neighbors are defined only in one grid cell, hence nearby fracture elements in the neighboring grid cells are also treated as far-neighbors. This leads to the calculation of the influence of nearby elements in the neighboring grid cells through the auxiliary grid without any correction, resulting in high error. The error decreases as the order of interpolation is increased. For third-order interpolation, one grid cell on either side of the element's grid cell is considered for interpolation, and all the elements in them are considered as near-neighbor. We observe that for third-order interpolation, the model predicts low error. As the influence of coefficients decreases sharply with distance, after third-order interpolation, the calculation of the error doesn't change much.

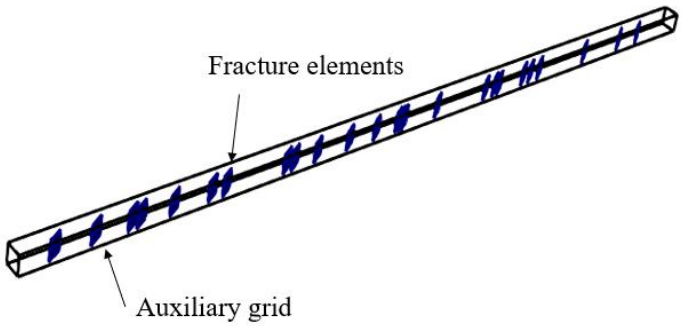

Figure 6.12: Distribution of elements in the created auxiliary grid for the case.

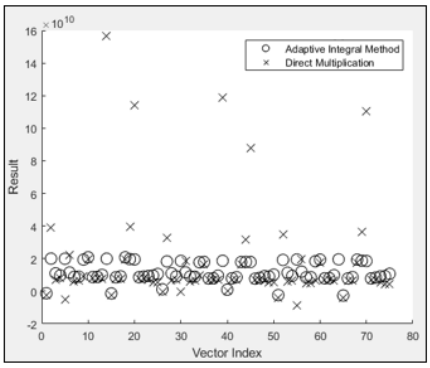

First-order interpolation

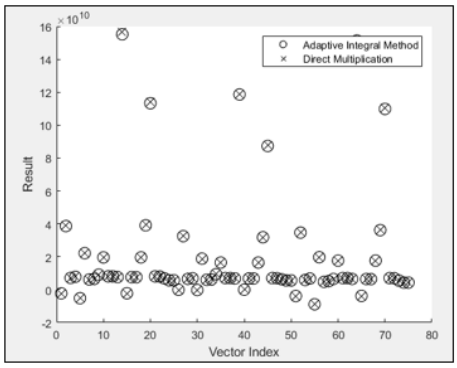

Third-order interpolation

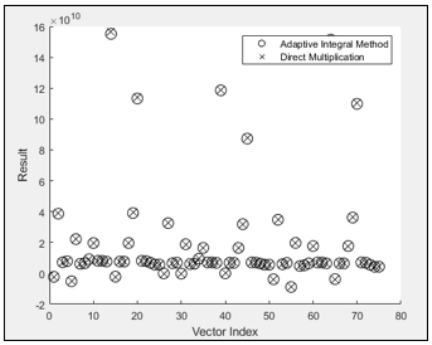

Fifth-order interpolation

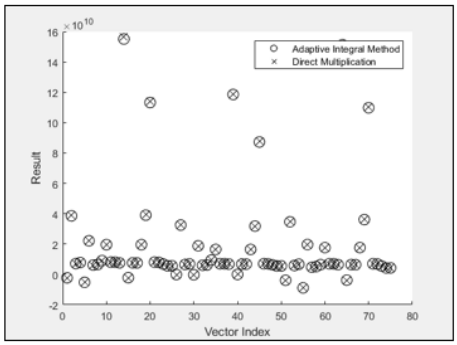

Seventh-order interpolation

Figure 6.13: Comparison between the multiplication result of the influence matrix with the residual vector for the Extended Adaptive Integral Method and direct multiplication for different orders of interpolation.

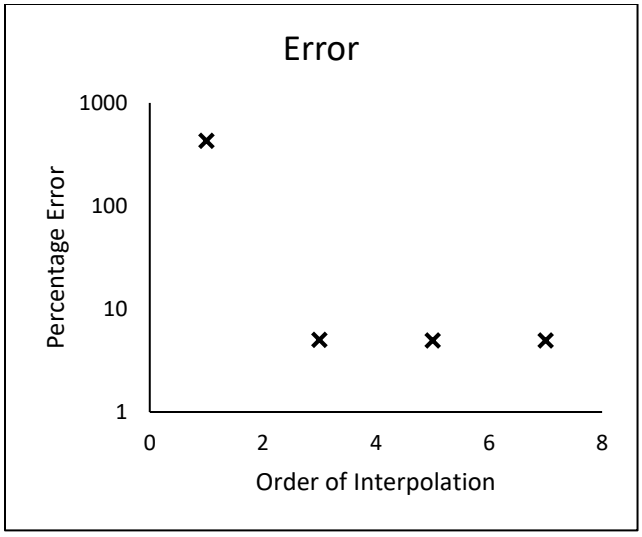

Figure 6.14: Mean percentage error for the obtained result of influence matrix multiplication with the residual vector for different orders of interpolations.

6.4.1.2 Effect of Distance Between Fracture Elements on Error

Another case is simulated to observe the effect of the change in the distance between the elements on the obtained error. Two fracture elements are placed in the auxiliary grid, and the distance between the elements is varied. The simulation parameters are similar to the previous case and are shown in Table 6.1. Third-order interpolation is used for this case. Figure 6.15 shows the percentage error observed between the results obtained from AIM and the result obtained from the direct multiplication step for the coefficient matrix and the residual vector.

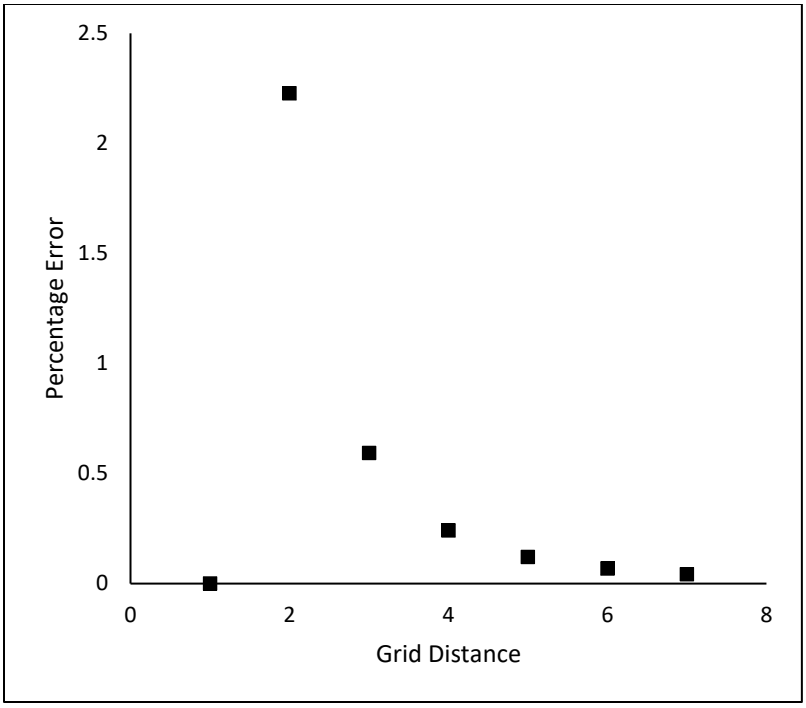

Figure 6.15: Percentage error for the results obtained from influence matrix multiplication with the residual vector for two elements case as a function of the distance between the two elements. The grid distance represents the distance between the two elements in terms of grid length. The elements are always placed at the center of grids.

As the distance between the two elements decreases, we observe an increase in the percentage error in the result. This happens because the representation of fracture elements on a weighted regular grid element becomes more and more imperfect as the distance between fracture elements decreases. Although, as the element distance decreases further, and the element enters the neighboring grid cell, the simulator starts to treat the elements as near-neighbor and calculates the interaction directly. This leads to the disappearance of the error. In this case, third-order interpolation is used; hence, three grids are used for interpolation (one on each side of the grid of fracture elements) Therefore, when the element enters the neighbor grid (grid distance is one), the error disappears.

6.4.1.3 Effect of Grid Size on Error

A case is set up to investigate the effect of grid size on the error observed. The simulation has two elements located at a distance of 29 m. The dimension of the auxiliary grid is 1m X 1m X 30m. The fracture elements are placed at the center of the auxiliary grid in the x and y direction (elements are at a distance of 0.5m from the x- and y-axis). The size of the auxiliary grid is chosen such that multiple grid cell sizes (1m, 2m, 3m, 5m, 6m, and 10m) all can be chosen for the same dimensions of the auxiliary grid. Figure 6.16 shows the geometry of the grid for 10m grid size. The parameters used in the simulation are shown in Table 6.2.

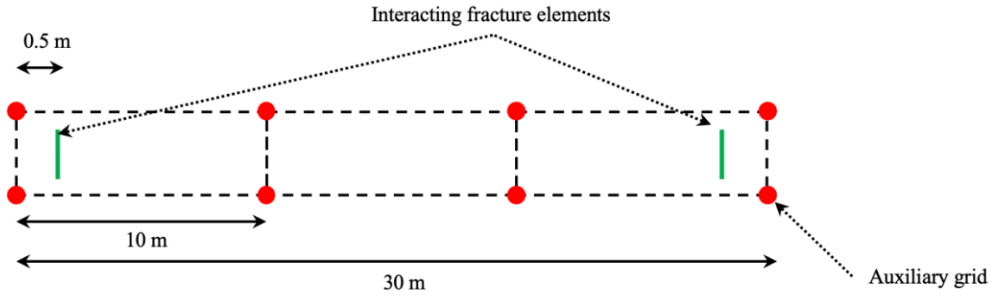

Figure 6.16: Two-dimensional view of the geometry of the auxiliary grid and the location of the fracture elements for the investigation of the effect of grid size on error

Table 6.2: The table shows the properties used for investigation of the effect of grid sizes on the error.

Property	Value	
Young's modulus	2.4	million psi
Poisson's ratio	0.26	
Sh_{min}	5381	psi
Sh_{max}	5381	psi
Element length (x)	0.5	m
Element length (y)	0.5	m

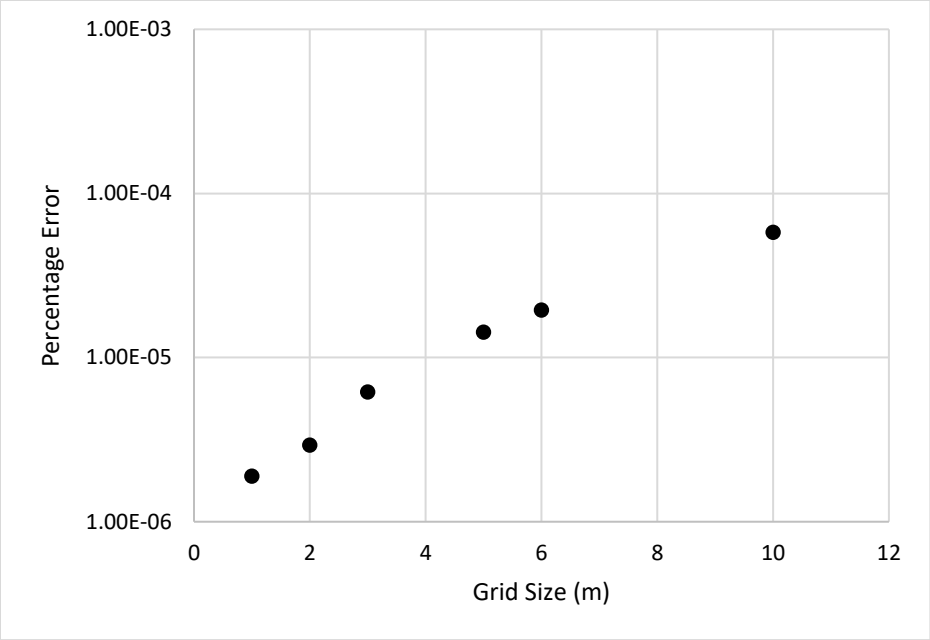

Figure 6.17: Percentage error in the solution observed for different sizes of the grid cells in the auxiliary grid.

Figure 6.17 shows the error observed for different grid cell sizes chosen for the auxiliary grid for the simulated case. It is observed that the error reduces as the size of the grid cell decreases. On reduction of the grid cell size, the DDM elements on the auxiliary grid start coming closer to the fracture elements, whereas the distance between the fracture elements remains the same. This leads to a better representation of the fracture element through the auxiliary grid for far interaction as the error in the location of equivalent elements introduced due to interpolation decreases. In other words, the auxiliary elements start to come closer to the location of the fracture element itself which improves fracture element's representation on the grid and reduces the error.

6.4.1.4 Effect of Location of Element in the Grid Cell on Error

A case is set up to investigate the effect of the location of the fracture element in the auxiliary grid cell on the obtained error. In order to conduct this study, a case similar to previous section is set up with two elements at a distance of 29m. The size of the auxiliary grid is 1m X 1m X 30m, and the grid cell size is chosen to be 1m X 1m X 1m. The parameters used in the simulation are given Table 6.2. In this study, the y coordinate of only one of the elements is varied (moving element) and the other coordinates are kept fixed. The location of the other element is not changed (fixed element). The y coordinate is chosen as it allows us to capture only the contribution to the error arising by the change in location and ignore the contribution to the error due to reduction in the distance between the fracture elements. Nine cases are simulated with different y-location of the moving element and the errors are recorded. Figure 6.18 shows the locus of the center of the moving element.

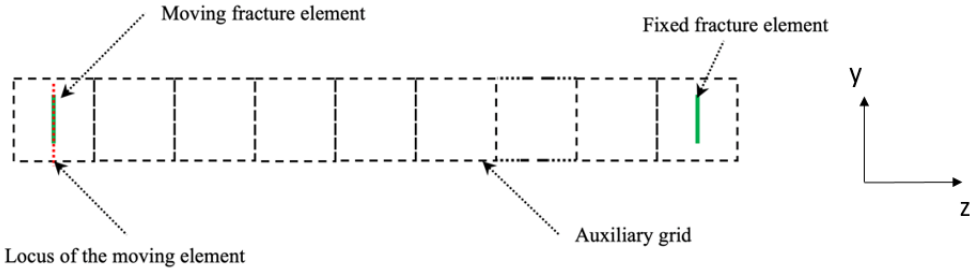

Figure 6.18: The figure shows the locus of the moving element in the simulation.

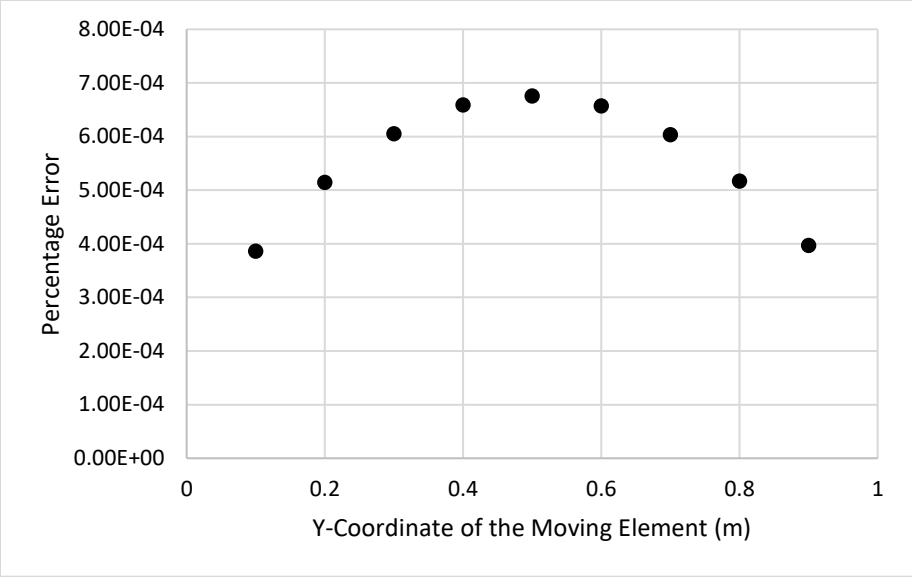

Figure 6.19: The percentage error observed in the solution as a function of the location (y-coordinate) of the moving element.

It is observed that as the element moves towards the center of the grid cell from near the face of the grid cell, the error increases, and as the element moves from the grid center to the grid face on the opposite side, the error decreases. This happens because when the moving element is placed on one of the faces, its influence is represented by the auxiliary grid elements situated on that face. This reduces the overall error as the error for this case primarily results from interpolation in the two directions (in this case x and z-direction) and the error due to interpolation in the third direction reduces (y-direction). As the element moves closer to the center of the grid cell, it is represented equally by all the eight corner elements, and hence errors arising due to interpolation in all the three directions contribute to the overall error.

An extreme case of this behavior will occur if the fracture element is placed on the corner of the auxiliary grid cell itself. In this scenario, only one element of the auxiliary

mesh will be sufficient to represent the entire contribution for the fracture element, and the contribution to error due to interpolation will become zero.

6.4.1.5 Effect of the Relative Size of the Auxiliary Grid Corner Elements to Size of Grid on Error

A case is set up to investigate the effect of relative size of fracture elements to the auxiliary grid cell size on the observed error. The dimension of the auxiliary grid in the simulation is 1m X 1m X 30m, and the size of the grid cell is 1m X 1m X 1m. The parameters used for this investigation are shown in Table 6.3. The size of the fracture element and the grid corner elements are kept equal in the simulation for all the cases. The size of the grid corner elements is reduced, and the effect on the observed error is studied.

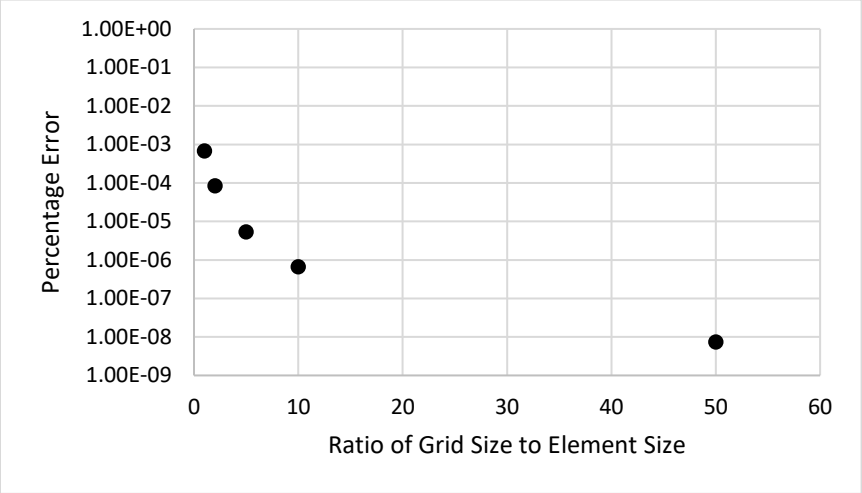

Figure 6.20: The percentage error observed in the solution as a function of the location (y-coordinate) of the moving element.

Table 6.3: Table shows the properties used for investigation of the ratio of element size to grid cell size on the error.

Property	Value	
Young's modulus	2.4	million psi
Poisson's ratio	0.26	
Sh_{min}	5381	psi
Sh_{max}	5381	psi

Figure 6.20 shows the error observed for different ratios of grid size to auxiliary element size. Auxiliary element size is varied from 1 m to 0.02 m. Elements of size greater than 1 m are not chosen in the simulation as longer elements will overlap for a 1 m grid cell and the interaction coefficients will become infinite.

It is observed that as the corner elements become smaller relative to the grid size, the error decreases. This happens because the elements are presented as rectangular elements rather than points at the grid corners. As the element size is reduced, the auxiliary corner elements start acting more like a point at the corner of the grid cell. This improves their representation as points on the auxiliary grid cell and reduces the error.

6.4.2 Computational Efficiency of the Extended Adaptive Integral Method

A case is set up to investigate the computational efficiency and complexity of the extended AIM. The properties used for the simulation are shown in Table 6.4.

Table 6.4: Parameters used for speed comparison

Property	Value	
Young's Modulus	2.4	million psi
Poissons Ratio	0.26	
Sh_{min}	5381	Psi
Sh_{max}	5381	Psi
Element Length (x)	0.5	M
Element Length (y)	0.5	M
Grid cell Height	1	M
Grid cell Length	4	M
Grid cell Width	1	M
Auxiliary Grid Length	7000	M
Auxiliary Grid Height	1	M
Auxiliary Grid Width	1	M

Fractures in the simulations are distributed randomly in the created auxiliary grid of 7000 m length. There are 7000 cells of 1m length each in the created auxiliary mesh. In total, the simulation has 28,004 corner points with a total of 56,008 DDM elements (x-oriented and y-oriented) placed at the corner of the cells. If the influences between 56,008 fracture elements are calculated explicitly by constructing an influence matrix using DDM, the size of the matrix will be 168,024x168,024 with 28.3 billion influence coefficients. In AIM we only calculate the influence coefficients between a single element with all the corner points of the auxiliary mesh to create a 3D wave for four different types of calculation (X-X interaction, X-Y interaction, Y-X interaction, and Y-Y interaction). Hence, in total, we need to calculate only 112,016 influence coefficients for calculating the far-neighbor interaction, significantly less by comparison. This is an example of the compression of the influence matrix that reduces the storage and computational requirement significantly with the AIM method is used.

Five cases with a different number of DDM elements (500, 800, 1000, 2000, and 3000 elements) are run to investigate computational time. Figure 6.21 shows a comparison of simulation time using direct multiplication and using the Extended Adaptive Integral Method. It can be observed that, for a small number of elements, the AIM method shows close to O(NLogN) computational scaling. Although, as the number of elements increases, more and more elements start to become near-neighbors and the computational complexity is dominated by the calculation of the near-neighbor correction term.

As the number of elements increases to 3000, the calculation of the near-neighbor correction term starts to dominate. In addition, the simulator is developed using Matlab, an interpreted language, hence for such extremely large simulations, the overhead time associated with calling functions becomes significant. Therefore, we observe that the complexity of the algorithm changes from O(NLogN) to greater than $O(N^2)$ for large simulations.

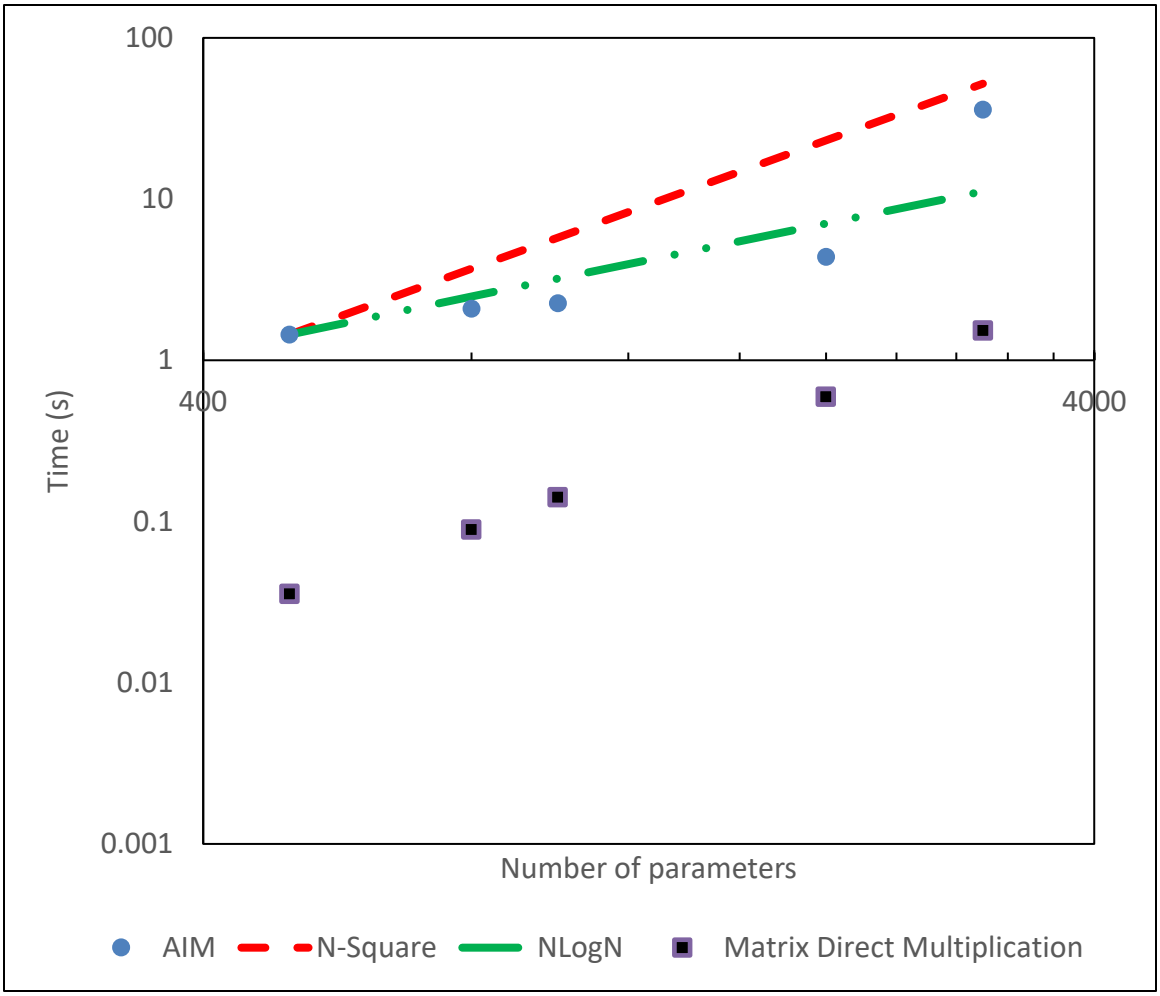

Figure 6.21: Comparison between simulation time required when using the direct multiplication and Extended Adaptive Integral methods. The figure also shows the $O(N^2)$ and O(NLogN) behavior for comparison. The simulations were run on a desktop computer with a quad-core Intel processor (i7-6700k) and 16 gigabytes of RAM.

6.5 CONCLUSION

- Adaptive Integral Method is extended for solving geomechanics problems using the displacement discontinuity method and the formulation of this new method is presented.

- The method shows larger errors for first-order interpolation and the errors are observed to decrease as the order of interpolation increases. This is because, for low order of interpolation, the influence between close-by elements (elements in the next-neighbor grid cells) are also calculated through the auxiliary grid, causing large errors.
- As the auxiliary grid cell size is reduced, the observed error in the result obtained through AIM decreases. This is because the smaller grid cells provide a better equivalent representation of the fracture elements.
- Smaller error is observed when the fracture element is closer to the face of the grid cell than when the fracture element is at the center of the grid cell. This happens because a smaller number of grid corners represent the fracture element in case it is closer to the grid face, which in turn reduces the error due to interpolation.
- As the element size on the auxiliary grid is reduced, the error decreases. This happens because smaller auxiliary elements provide a better representation of the fracture element as points on the corner of the grid cell compared to larger auxiliary elements.
- The behavior of the computational complexity of the implemented AIM based solver is observed to be O(NlogN) when the number of elements is less than the number of grid cells, but it becomes $O(N^2)$ as the elements becomes comparable to the number of grid cells. This is because, with higher element density, the behavior of the near-neighbor correction term dominates the computational complexity of the AIM solver. Near-neighbor correction is done using direct multiplication which follows $O(N^2)$ computational complexity. Hence, the overall computational complexity of the problem changes from O(NLogN) to O(N2).

Chapter 7: Conclusions and Future Work

This chapter summarizes the research presented in this dissertation. New directions for extending these research topics are proposed.

7.1 Summary and Conclusion

A hydraulic fracturing model that accounts for the interaction of propagating hydraulic fractures with natural fractures has been developed. The model simulates fracture growth in a computationally efficient manner. The main conclusions developed in the dissertation are summarized in the following sections.

7.1.1 Development of the Model (Chapter 2)

In the second chapter, the details of the DDM model are presented. The hydraulic fracturing model couples the Displacement Discontinuity Method and Finite Difference Method for simulating the propagation of the hydraulic fracture network in the presence of natural fractures. The Displacement Discontinuity Method is used to solve the geomechanics of the problem, and the Finite Difference Method is used to solve for the fluid mechanics of the slurry flow inside the fracture network. The interaction of natural fractures and hydraulic fractures, leak-off of fracturing fluid in the reservoir, and the proppant transport equations used in the simulator are also discussed. The model uses the same mesh for solving the geomechanics problem and for solving the fluid mechanics problem for the fracture network. The fracture propagates based on the stress intensity at the fracture tips, and the direction of propagation is determined using the maximum circumferential stress criterion. Multiple fracture tips can grow simultaneously in the new simulator (Multi-Frac-NF).

A novel solution algorithm to solve the coupled fluid-solid interaction problem is presented. The predictor step algorithm, referred to as the Local Linearization method, linearizes the fluid flow to compute an initial guess which can then be used in the iterative solution scheme. This speeds up the computations significantly. Model verification and validation cases are also presented to ensure that the numerical algorithms have been properly implemented.

7.1.2 Effect of Natural Fractures on Hydraulic Fracture Generation (Chapter 3)

The new model is used to investigate the effect of natural fracture density, orientation, and fracture height on the created fracture network. The following observations are made:

- The complexity of the hydraulic fracture network increases as the density of the natural fracture increases.
- The dominant natural fracture direction and the orientation of the far-field stress determine the overall growth direction of the hydraulic fracture network. These should be accounted for determining well spacing.
- The reservoir in the vicinity of the interaction of the hydraulic and natural fractures experiences higher stresses due to the opening of both the natural fracture and hydraulic fracture. This can suppress the growth of the fracture in the region near the intersection of the hydraulic fracture and natural fracture.
- Stresses generated by a hydraulically connected fracture can suppress the growth of smaller fractures in its vicinity.
- As the hydraulic fracture approaches a natural fracture, it experiences both compressive and tensile stresses, which can lead to partial failure of the natural

fracture. This can result in the failure of the natural fracture even before the intersection happens.

- The intersection process of the hydraulic fracture and natural fracture is shown to be a continuous process rather than a discrete process.

7.1.3 Transport of Proppant in Fracture Networks (Chapter 4)

- As natural fractures intersect with the hydraulic fracture, fluid and proppant flow into natural fractures. As the region of intersection experiences high stresses (as it experiences stresses from both the open hydraulic fracture and connected open natural fracture), the region of intersection can have a smaller width and restrict the flow of proppant through them.
- It is observed that in low permeability formations, the fractures take much longer to close compared to the settling of proppant. Hence, multiple disconnected banks can form in the created fracture network.
- In a low vertical stress environment, bedding planes can slip, and the proppant can enter the bedding planes if the width achieved by the bedding plane is larger than the proppant particles.
- Using higher mesh proppant during hydraulic fracturing can be beneficial, as smaller proppants are more likely to cross the region of intersection between hydraulic and natural fractures.

7.1.4 Calibrating Hydraulic Fracture Models using Field Data: Synthetic Coring Technique (Chapter 5)

In Chapter 5, a comparison between a synthetic core from the Hydraulic Fracture Test Site #1 and the simulation results is presented.

- A procedure of coring simulation (Synthetic coring technique) is developed, and by comparing the density of hydraulic, natural, and reactivated natural fractures in synthetic core with field results, a discrete fracture network is generated in two-dimensions that resembles the natural fracture distribution in the Wolfcamp formation.
- A large number of hydraulic fractures in the HFTS core indicates significant branching and bifurcation of the growing hydraulic fractures. Similar behavior is observed in the simulation results when the initial natural fracture density and orientation is matched with the core data.
- For cores 1 to 4, the number of all fractures was approximately 11.2 for every 10 ft of measured depth. The average fracture densities are 6.7, 3.0, and 1.5 fractures per 10 ft length of MD for hydraulic fractures (HF), intact natural fractures (N), and reactivated natural fractures (NR) respectively. In cores 5 and 6, average fracture densities are 3.5, 1.7, and 0.5 fractures per 10 ft length of MD for HF, N, and NR, respectively. In the simulation study 1.3, 11.1, and 1.0 HF, NF, and NR, respectively are observed for every 10 feet of core.
- The minimum size of the natural fractures in the simulation is limited by grid size (2 meters) in the simulation, and hence, the contribution of smaller fractures is neglected. Smaller fractures are expected to be abundant in the reservoir (natural fracture frequency increases as the size of the natural fractures decreases). This could be a possible reason for the difference in the density of hydraulic fractures observed between the field core and the simulation results.
- Heel-dominated hydraulic fracture growth is observed in the HFTS core data. This behavior is not observed in the simulation as the fluid is equally distributed in all three perforations, and no preference is given to clusters based on their location.

- Reactivation of natural fractures due to hydraulic fracturing is observed in the field core data and in the simulations.

7.1.5 Reducing Computational Complexity: Extended Adaptive Integral Method (Chapter 6)

- A new Extended Adaptive Integral Method is discussed and extended to solving geomechanics problems using the Displacement Discontinuity Method. The formulation of the Extended Adaptive Integral Method is presented.
- The error is observed to be a function of the order of interpolation. For the first-order interpolation, a large error is observed. As the order of interpolation increases, the error decreases.
- As the auxiliary grid cell size is reduced, the observed error in the result obtained through AIM decreases.
- Smaller error is observed when the fracture element is closer to the face of the grid cell than when the fracture element is at the center of the grid cell.
- The behavior of the computational complexity of the implemented Extended AIM-based solver is observed to be O(NlogN) when the number of elements is less than the number of grid cells, but it becomes $O(N^2)$ as the number of elements becomes comparable to the number of grid cells in the simulation.

7.2 FUTURE RESEARCH

1. In this work, we have presented simulations investigating the effect of natural fracture properties on the created fracture network. However, all the simulations are conducted using a single realization of the natural fractures. An investigation can be conducted for multiple realizations of natural fractures to obtain the uncertainty in the results. This kind of Monte-Carlo simulation will be helpful for

providing clear trends to engineers designing hydraulic fracturing treatments in naturally fractured reservoirs.

2. In this work, the grid size used for DDM is constant. This can result in the creation of a lot of discretized elements, even in the regions where it may not be necessary. In the hydraulic fracturing problem, the pressure inside the fracture doesn't change significantly over most of the area of the fracture, hence large sections of the hydraulic fractures can be represented with single elements. Adaptive meshing is a technique commonly used in other solution methods (FEM/FVM/Peridynamics) that can significantly reduce the number of grids and have a substantial impact on the speed of the simulation. In addition, adaptive meshing will also improve the stability of the simulator. Therefore, adaptive meshing in DDM should be explored as it has tremendous benefits. Implementation of adaptive meshing can affect the fracture growth behavior (fracture turning) and the effect of using multiple element size on the growing fracture should be also be explored.
3. Implementation of a contact model for capturing the physics of the fracture surface coming in contact can increase the stability of the solver and capture the closure of complex fracture networks.
4. The proppant transport correlations used in the model do not account for the momentum change of proppant due to changes in the direction of proppant flow. CFD-DEM simulations can be run to capture the effect of change of direction of proppant flow to improve the correlations.
5. The proppant transport model can be extended to model transport of multiple sizes of proppants/tracers in complex fracture networks. In order to simulate multiple sizes of proppants, better correlations can be developed using CFD-DEM modeling

that can allow to capture the effect of multi-size proppant particles on to the retardation factor and settling velocity of proppant particles.

6. The Extended Adaptive Integral Method formulation can be implemented using a low-level (C++/Fortran) language for running larger-scale simulations. The current version using MATLAB is memory limited.

References

Adachi, J., Siebrits, E., Peirce, A., Desroches, J., 2007. Computer simulation of hydraulic fractures. Int. J. Rock Mech. Min. Sci. 44, 739–757. https://doi.org/10.1016/j.ijrmms.2006.11.006

Agrawal, S., Shrivastava, K., Sharma, M.M., 2019. Effect of shear slippage on the interaction of hydraulic fractures with natural fractures, in: Society of Petroleum Engineers - SPE Hydraulic Fracturing Technology Conference and Exhibition 2019, HFTC 2019. Society of Petroleum Engineers. https://doi.org/10.2118/194361-ms

Al Tammar, M.J., 2018. Experimental studies in hydraulic fracture growth: fundamental insights and validation experiments for geomechanical models. https://doi.org/10.26153/TSW/1391

Anastassiu, H.T., Smelyanskiy, M., Bindiganavale, S., Volakis, J.L., 1998. Scattering from relatively flat surfaces using the adaptive integral method. Radio Sci. 33, 7–16. https://doi.org/10.1029/97RS02104

Ativani, S.H., Lee, T.S., Lee, J.K., 1990. Three-Dimensional Modeling of Hydraulic Fractures in Layered Media: Part I-Finite Element Formulations. J. Energy Resour. Technol. Trans. ASME 112, 1–9. https://doi.org/10.1115/1.2905706

Atkinson, B.K., 2015. Fracture Mechanics of Rock.

Bahorich, B., Olson, J.E., Holder, J., 2012. Examining the Effect of Cemented Natural Fractures on Hydraulic Fracture Propagation in Hydrostone Block Experiments, in: SPE Annual Technical Conference and Exhibition. Society of Petroleum Engineers. https://doi.org/10.2118/160197-MS

Barree, R.D., 1983. A Practical Numerical Simulator for Three-Dimensional Fracture Propagation in Heterogeneous Media, in: SPE Reservoir Simulation Symposium. Society of Petroleum Engineers. https://doi.org/10.2118/12273-MS

Bindiganavale, S.S., Volakis, J.L., Anastassiu, H., 1998. Scattering from Planar Structures Containing Small Features Using the Adaptive Integral Method (AIM), Ieee Transactions On Antennas And Propagation.

Bleszynski, E., Bleszynski, M., Jaroszewicz, T., 1996. AIM: Adaptive integral method for solving large-scale electromagnetic scattering and radiation problems. Radio Sci. 31, 1225–1251. https://doi.org/10.1029/96RS02504

Bochkarev, A., Budennyy, S., Nikitin, R., Mitrushkin, D., 2016. Pseudo-3D hydraulic fracture model with complex mechanism of proppant transport and tip screen out. 15th Eur. Conf. Math. Oil Recover. ECMOR 2016. https://doi.org/10.3997/2214-4609.201601775

Boone, T.J., Ingraffea, A.R., 1990. A numerical procedure for simulation of hydraulically-driven fracture propagation in poroelastic media. Int. J. Numer. Anal. Methods Geomech. 14, 27–47. https://doi.org/10.1002/nag.1610140103

Chen, Z., Bunger, A.P., Zhang, X., Jeffrey, R.G., 2009. Cohesive zone finite element-based modeling of hydraulic fractures. Acta Mech. Solida Sin. 22, 443–452. https://doi.org/10.1016/S0894-9166(09)60295-0

Chuprakov, D., Melchaeva, O., Prioul, R., 2013. Hydraulic Fracture Propagation Across a Weak Discontinuity Controlled by Fluid Injection. https://doi.org/10.5772/55941

Chuprakov, D.A., Akulich, A. V., Siebrits, E., Thiercelin, M., 2011. Hydraulic-Fracture Propagation in a Naturally Fractured Reservoir. SPE Prod. Oper. 26, 88–97. https://doi.org/10.2118/128715-PA

Cipolla, C.L., Warpinski, N.R., Mayerhofer, M.J., 2008. Hydraulic Fracture Complexity: Diagnosis, Remediation, And Exploration. Presented at the SPE Asia Pacific Oil and Gas Conference and Exhibition, Society of Petroleum Engineers. https://doi.org/10.2118/115771-MS

Cleary, M.P., Kavvadas, M., Lam, K.Y., 1983. Development of a Fully Three-Dimensional Simulator for Analysis and Design of Hydraulic Fracturing.

Courtier, J., Chandler, K., Gray, D., Martin, S., Thomas, R., Wicker, J., Ciezobka, J., 2017. Best Practices in Designing and Executing a Comprehensive Hydraulic Fracturing Test Site in the Permian Basin. Presented at Unconventional Resources Technology Conference (URTeC), Austin, Texas, 24-26 July. URTeC-2697483-MS. https://doi.org/10.15530/URTeC-2017-2697483.

Crawford, A. M., & Curran, J. H. (1982, June). Higher-order functional variation displacement discontinuity elements. In International Journal of Rock Mechanics and Mining Sciences & Geomechanics Abstracts (Vol. 19, No. 3, pp. 143-148). Pergamon.

Crouch, S.L., 1976. Solution of plane elasticity problems by the displacement discontinuity method. I. Infinite body solution. Int. J. Numer. Methods Eng. 10, 301–343. https://doi.org/10.1002/nme.1620100206

Crouch, S.L., Starfield, A.M., 1983. Boundary element methods in solid mechanics, S. L. Crouch and A. M. Starfield.

Dahi-Taleghani, A., Olson, J.E., 2011. Numerical Modeling of Multistranded-Hydraulic-Fracture Propagation: Accounting for the Interaction Between Induced and Natural Fractures. SPE J. 16, 575–581. https://doi.org/10.2118/124884-PA

Dahi Taleghani, A., & Olson, J. E. (2013). How natural fractures could affect hydraulic-fracture geometry. SPE journal, 19(01), 161-171.

Damjanac, B., Cundall, P., 2016. Application of distinct element methods to simulation of hydraulic fracturing in naturally fractured reservoirs. Comput. Geotech. 71, 283–294. https://doi.org/10.1016/j.compgeo.2015.06.007

Davidson, D.B., 2011. Computational Electromagnetics for RF and Microwave Engineering.

Dong, C. Y., & De Pater, C. J. (2001). Numerical implementation of displacement discontinuity method and its application in hydraulic fracturing. Computer methods in applied mechanics and engineering, 191(8-10), 745-760.

Dunphy, R., Campagna, D., 2011. Fractures, Elastic Moduli & Stress : Geological Controls on Hydraulic Fracture Geometry in the Horn River Basin, CSPG CSEG CWLS Convention.

Economides, M.J., Nolte, K.G., 2000. Reservoir stimulation. Wiley.

Erdogan, F., Sih, G.C., 1963. On the Crack Extension in Plates Under Plane Loading and Transverse Shear 9.

Ewe, W. Bin, Li, L.W., Wu, Q., Leong, M.S., 2005. Analysis of reflector and horn antennas using adaptive integral method, in: IEICE Transactions on Communications. Institute of Electronics, Information and Communication, Engineers, IEICE, pp. 2327–2332. https://doi.org/10.1093/ietcom/e88-b.6.2327

Fisher, M.K., Heinze, J.R., Harris, C.D., Davidson, B.M., Wright, C. a., Dunn, K.P., 2004. Optimizing Horizontal Completion Techniques in the Barnett Shale Using Microseismic Fracture Mapping. Presented at SPE Annual Technical Conference and Exhibition, Houston, Texas. 26-29 September. SPE-90051-MS. https://doi.org/10.2118/90051-MS

Fisher, M.K.., Wright, C.A.., Davidson, B.M.., Goodwin, A.K.., Fielder, E.O.., Buckler, W.S.., Steinsberger, N.P.., 2005. Integrating fracture-mapping technologies to improve stimulations in the Barnett shale. SPE Prod. Facil. 20, 85–93. https://doi.org/10.2118/77441-pa

Fung, R.L., Vijayakumar, S., Cormack, D.E., 1987. Calculation of vertical fracture containment in layered formations. SPE Form. Eval. 2, 518–522. https://doi.org/10.2118/14707-PA

Gadde, P.B., Liu, Y., Norman, J., Bonnecaze, R., Sharma, M.M., 2004. Modeling Proppant Settling in Water-Fracs.

Gale, J.F.W., Elliott, S.J., Laubach, S.E., 2018. Hydraulic Fractures in Core From Stimulated Reservoirs : Core Fracture Description of HFTS Slant Core, Midland Basin , West Texas. Presented at Unconventional Resources Technology Conference (URTeC), Houston, Texas, 23-25 July. URTeC - 2902624. doi: https://doi.org/10.15530/urtec-2018-2902624

Gale, J.F.W., Laubach, S.E., Olson, J.E., Eichhubl, P., Fall, A., 2017. Natural fractures in shale: A review and new observations. Am. Assoc. Pet. Geol. Bull. 101, 2165–2216. https://doi.org/10.1306/08121413151

Gale, J.F.W., Reed, R.M., Holder, J., 2007. Natural fractures in the Barnett Shale and their importance for hydraulic fracture treatments. Am. Assoc. Pet. Geol. Bull. 91, 603–622. https://doi.org/10.1306/11010606061

Gordeliy, E., Peirce, A., 2013. Coupling schemes for modeling hydraulic fracture propagation using the XFEM. Comput. Methods Appl. Mech. Eng. 253, 305–322. https://doi.org/10.1016/j.cma.2012.08.017

Gu, H., Siebrits, E., Sabourov, A., 2008. Hydraulic-fracture modeling with bedding plane interfacial slip, in: Society of Petroleum Engineers - SPE Eastern Regional/AAPG Eastern Section Joint Meeting 2008. pp. 216–223. https://doi.org/10.2118/117445-ms

Gu, H., Weng, X., 2010. Criterion for Fractures Crossing Frictional Interfaces at Non-orthogonal Angles. 44th US Rock Mech. Symp. 5th U.S.-Canada Rock Mech. Symp. 27-30 June, Salt Lake City 1–6.

Hackett, P. (1959). An elastic analysis of rock movements caused by mining. Trans. Instn Min. Engrs, 118(7), 421-433.

Haustveit, K., Dahlgren, K., Greenwood, H., Peryam, T., Kennedy, B., Dawson, M., 2017. New Age Fracture Mapping Diagnostic Tools-A STACK Case Study. Presented at SPE Hydraulic Fracturing Technology Conference and Exhibition, The Woodlands, Texas, USA . 24–26 January. SPE - 184862-MS. https://doi.org/10.2118/184862-MS

Heffer, K.J., Bevan, T.G., 1990. Scaling Relationships in Natural Fractures: Data, Theory, and Application. Presented at European Petroleum Conference, The Hague, Netherlands. 21-24 October. SPE -20981-MS. https://doi.org/10.2118/20981-MS

Howard, G.C., Fast, C.R., 1957. Optimum Fluid Characteristics for Fracture Extension. American Petroleum Institute.

Howard, G.C., Fast, C.R., 1970. Hydraulic Fracturing, Mono. Ser., 2, Society of Petroleum Engineers, Richardson, Texas, 1970.

Jeffrey, R.G., Settari, A., 1995. A Comparison of Hydraulic Fracture Field Experiments, Including Mineback Geometry Data, with Numerical Fracture Model Simulations, in: SPE Annual Technical Conference and Exhibition. Society of Petroleum Engineers. https://doi.org/10.2118/30508-MS

Khristianovic, S.A., Zheltov, Y.P., 1955. FORMATION OF VERTICAL FRACTURES BY MEANS OF HIGHLY VISCOUS LIQUID.

Kresse, O., Weng, X., 2013. Hydraulic Fracturing in Formations with Permeable Natural Fractures. Intech 24. https://doi.org/10.5772/56446

Kumar, A., Seth, P., Shrivastava, K., Manchanda, R., Sharma, M.M., 2018. Well Interference Diagnosis through Integrated Analysis of Tracer and Pressure Interference Tests. Presented at Unconventional Resources Technology Conference (URTeC), Houston, Texas, 23-25 July. URTeC - 2901827. https://doi.org/10.15530/urtec-2018-2901827

Lander, R.H., Laubach, S.E., 2014. Insights into rates of fracture growth and sealing from a model for quartz cementation in fractured sandstones. Bull. Geol. Soc. Am. 127, 516–538. https://doi.org/10.1130/B31092.1

Lee, D., Cardiff, P., Bryant, E.C., Manchanda, R., Wang, H., Sharma, M.M., 2015. A Fully 3-Dimensional Model for Hydraulic Fracture Growth in Unconsolidated Sands with Plasticity and Coupled Leak-off. SPE Annu. Tech. Conf. Exhib. https://doi.org/10.2118/174818-MS

Lee, H. P., Olson, J. E., Holder, J., Gale, J. F., & Myers, R. D. (2015). The interaction of propagating opening mode fractures with preexisting discontinuities in shale. Journal of Geophysical Research: Solid Earth, 120(1), 169-181.

Ling, F., Wang, C.F., Jin, J.M., 1998. Application of Adaptive Integral Method To Scattering and Radiation Analysis of Arbitrarily Shaped Planar Structures. J. Electromagn. Waves Appl. 12, 1021–1037. https://doi.org/10.1163/156939398X01268

Manchanda, R., Zheng, S., Gala, D., Sharma, M.M., 2019. Simulating the Life of Hydraulically Fractured Wells Using a Fully-Coupled Poroelastic Fracture-Reservoir Simulator. https://doi.org/10.15530/urtec-2019-490

Maxwell, S.C., Urbancic, T.I., Steinsberger, N., Energy, D., Zinno, R., 2002. SPE 77440 Microseismic Imaging of Hydraulic Fracture Complexity in the Barnett Shale.

McClure, M.W., Babazadeh, M., Shiozawa, S., Huang, J., 2016. Fully Coupled Hydromechanical Simulation of Hydraulic Fracturing in 3D Discrete-Fracture Networks. SPE J. 21, 1302–1320. https://doi.org/10.2118/173354-PA

Mcclure, M.W., Kang, C.A., 2017. SPE-182593-MS A Three-Dimensional Reservoir, Wellbore, and Hydraulic Fracturing Simulator that is Compositional and Thermal, Tracks Proppant and Water Solute Transport, Includes Non-Darcy and Non-Newtonian Flow, and Handles Fracture Closure. Soc. Pet. Eng. https://doi.org/10.2118/182593-MS

Montgomery, C.T., Smith, M.B., 2010. Hydraulic fracturing: History of an enduring technology.

Nordgren, R.P., 1972. Propagation of a Vertical Hydraulic Fracture. Soc. Pet. Eng. J. 12. https://doi.org/10.2118/3009-PA

Olson, J.E., Bahorich, B., Holder, J., 2012. Examining hydraulic fracture-natural fracture interaction in hydrostone block experiments. SPE 152618, 6–8. https://doi.org/10.2118/152618-MS

Olson, J.E., Wu, K., 2012. Sequential versus Simultaneous Multi-zone Fracturing in Horizontal Wells : Insights from a Non-planar , Multi-frac Numerical Model. Presented at SPE Hydraulic Fracturing Technology Conference, The Woodlands, Texas. 6-8 February. SPE-152602-MS. https://doi.org/10.2118/152602-MS

Olson, Jon Edward. Fracture mechanics analysis of joints and veins. Dissertation. Stanford University, 1991.

Oterkus, S., Madenci, E., Oterkus, E., 2017. Fully coupled poroelastic peridynamic formulation for fluid-filled fractures. Eng. Geol. 225, 19–28. https://doi.org/10.1016/j.enggeo.2017.02.001

Ouchi, H., Foster, J.T., Sharma, M.M., 2017. Effect of reservoir heterogeneity on the vertical migration of hydraulic fractures. J. Pet. Sci. Eng. 151, 384–408. https://doi.org/10.1016/j.petrol.2016.12.034Perkins, T.K., Kern, L.R., 1961. Widths of Hydraulic Fractures. J. Pet. Technol. 13. https://doi.org/10.2118/89-PA

Ouchi, H., Katiyar, A., Foster, J., Sharma, M.M., 2015. A Peridynamics Model for the Propagation of Hydraulic Fractures in Heterogeneous, Naturally Fractured Reservoirs, in: SPE Hydraulic Fracturing Technology Conference. Society of Petroleum Engineers. https://doi.org/10.2118/173361-MS

Perkins, T. K., & Kern, L. R. (1961). Widths of hydraulic fractures. Journal of Petroleum Technology, 13(09), 937-949.

Phillips, J.R., White, J.K., 1997. A precorrected-FFT method for electrostatic analysis of complicated 3-D structures. IEEE Trans. Comput. Des. Integr. CIRCUITS Syst. 16, 1059–1072.

Potluri, N.K., Zhu, D., Hill, A.D., 2005. The Effect of Natural Fractures on Hydraulic Fracture Propagation, Presented at SPE European Formation Damage Conference, Sheveningen, The Netherlands. 25-27 May. SPE-94568-MS. https://doi.org/10.2118/94568-MS

Rahman, M.M., Rahman, S.S., 2013. Studies of hydraulic fracture-propagation behavior in presence of natural fractures: Fully coupled fractured-reservoir modeling in poroelastic environments. Int. J. Geomech. 13, 809–826. https://doi.org/10.1061/(ASCE)GM.1943-5622.0000274

Raterman, K.T., Farrell, H.E., Mora, O.S., Janssen, A.L., Gomez, G.A., Busetti, S., McEwen, J., Davidson, M., Friehauf, K., Rutherford, J., Reid, R., Jin, G., Roy, B., Warren, M., 2017. Sampling a Stimulated Rock Volume: An Eagle Ford Example. Presented at Unconventional Resources Technology Conference (URTeC), Austin, Texas. 24-26 July. URTeC-2670034-MS. https://doi.org/10.15530/URTEC-2017-2670034.

Renshaw, C.E., Pollard, D.D., 1995. An experimentally verified criterion for propagation across unbounded frictional interfaces in brittle, linear elastic materials. Int. J. Rock Mech. Min. Sci. Geomech. Abstr. 32, 237–249. https://doi.org/10.1016/0148-9062(94)00037-4

Sahai, R., Miskimins, J.L., Olson, K.E., 2014. Laboratory Results of Proppant Transport in Complex Fracture Systems. Presented at the SPE Hydraulic Fracturing Technology Conference, Society of Petroleum Engineers. https://doi.org/10.2118/168579-MS

Schechter, R.S., 1992. Oil Well Stimulation. Hart's E P.

Seo, S.M., Lee, J.F., 2005. A fast IE-FFT algorithm for solving PEC scattering problems, in: IEEE Transactions on Magnetics. pp. 1476–1479. https://doi.org/10.1109/TMAG.2005.844564

Sesetty, V., Ghassemi, A., 2017. Complex Fracture Network Model for Stimulation of Unconventional Reservoirs. Presented at 51st U.S. Rock Mechanics/Geomechanics Symposium, San Francisco, California, USA. 25-28 June. ARMA-2017-0762.

Seth, P., Kumar, A., Manchanda, R., Shrivastava, K., Sharma, M., 2018. Hydraulic Fracture Closure in a Poroelastic Medium and its Implications on Productivity, in: Hydraulic Fracture Closure in a Poroelastic Medium and Its Implications on Productivity. Presented at 52nd American Rock Mechanics Association, Seattle. ARMA-18-695.

Settari, A., Cleary, M.P., 1986. Development and testing of a pseudo-three-dimensional model of hydraulic fracture geometry. SPE Prod. Eng. 1, 449–466. https://doi.org/10.2118/10505-PA

Shah, S. N. (1993). Rheological characterization of hydraulic fracturing slurries. SPE Production & Facilities, 8(02), 123-130.

Sheibani, F., Olson, J.E., 2013. Impact of Fracture Height on Mixed Mode Fracture Propagation: Insights from 3D Displacement Discontinuity Modeling. American Rock Mechanics Association.

Shi, F., Wang, X., Liu, C., Liu, H., Wu, H., 2017. An XFEM-based method with reduction technique for modeling hydraulic fracture propagation in formations containing frictional natural fractures. Engineering Fracture Mechanics 173, 64–90. https://doi.org/10.1016/j.engfracmech.2017.01.025

Shou, K.-J., 1993. A higher order three-dimensional displacement discontinuity method with applications to bonded half-space problems. The University of Minnesota.

Shrivastava, K., Agrawal, S., Kumar, A., Sharma, M.M., 2018. 3-D Interactions of Hydraulic Fractures with Natural Fractures, in: SPE International Hydraulic Fracturing Technology Conference and Exhibition. Society of Petroleum Engineers. https://doi.org/10.2118/191447-18IHFT-MS

Shrivastava, K., Hwang, J., Sharma, M.M., 2018. Formation of Complex Fracture Networks in the Wolfcamp Shale: Calibrating Model Predictions with Core Measurements from the Hydraulic Fracturing Test Site, in: Formation of Complex Fracture Networks in the Wolfcamp Shale: Calibrating Model Predictions with Core Measurements from the Hydraulic Fracturing Test Site. SPE Annual Technical Conference and Exhibition, Dallas, Texas, USA.

Shrivastava, K., Sharma, M.M., 2018a. Mechanisms for the Formation of Complex Fracture Networks in Naturally Fractured Rocks, in: SPE Hydraulic Fracturing Technology Conference and Exhibition. Society of Petroleum Engineers. https://doi.org/10.2118/189864-MS

Shrivastava, K., Sharma, M.M., 2018b. Proppant Transport in Complex Fracture Networks, in: SPE Hydraulic Fracturing Technology Conference and Exhibition. The Woodlands, Texas, USA. 23-25 January. SPE-189895-MS. https://doi.org/10.2118/189895-MS

Simonson, E.R., Abou-Sayed, A.S., Clifton, R.J., 1978. Containment of Massive Hydraulic Fractures. Soc Pet Eng AIME J 18, 27–32. https://doi.org/10.2118/6089-pa

Taleghani, A.D., Olson, J.E., 2009. Analysis of Multi-stranded Hydraulic Fracture Propagation: An Improved Model for the Interaction Between Induced and Natural Fractures. Society of Petroleum Engineers (SPE). https://doi.org/10.2118/124884-ms

Taleghani, A.D., Olson, J.E., 2014. How Natural Fractures Could Affect Hydraulic-Fracture Geometry.

Tong, S., Mohanty, K.K., 2016. Proppant transport study in fractures with intersections. Fuel 181, 463–477. https://doi.org/10.1016/j.fuel.2016.04.144

U.S. Energy Information Administration, 2013. Technically Recoverable Shale Oil and Shale Gas Resources: An Assessment of 137 Shale Formations in 41 Countries Outside the United States.

Ugueto C., G.A., Huckabee, P.T., Molenaar, M.M., Wyker, B., Somanchi, K., 2016. Perforation Cluster Efficiency of Cemented Plug and Perf Limited Entry Completions; Insights from Fiber Optics Diagnostics, Presented at SPE Hydraulic Fracturing Technology Conference, The Woodlands, Texas, USA. 9-11 February. https://doi.org/10.2118/179124-MS

Wang, W., Olson, J. E., Prodanović, M., & Schultz, R. A. (2018). Interaction between cemented natural fractures and hydraulic fractures assessed by experiments and numerical simulations. Journal of Petroleum Science and Engineering, 167, 506-516.Warpinski, N., 2009. Microseismic Monitoring: Inside and Out. J. Pet. Technol. 61, 80–85. https://doi.org/10.2118/118537-MS

Wang, W., Olson, J.E., Prodanović, M., 2013. Natural and Hydraulic Fracture Interaction Study Based on Semi-Circular Bending Experiments, in: Unconventional

Resources Technology Conference, Denver, Colorado, 12-14 August 2013. Society of Exploration Geophysicists, American Association of Petroleum Geologists, Society of Petroleum Engineers, pp. 1645–1652. https://doi.org/10.1190/urtec2013-168

Warpinski, N., Kramm, R.C., Heinze, J.R., Waltman, C.K., 2005. Comparison of Single- and Dual-Array Microseismic Mapping Techniques in the Barnett Shale. Presented at SPE Annual Technical Conference and Exhibition, Dallas, Texas. 9-12 October. SPE-95568-MS. https://doi.org/10.2118/95568-MS

Warpinski, N.R., Mayerhofer, M.J., Vincent, M.C., Cipolla, C.L., Lolon, E.P., 2009. Stimulating Unconventional Reservoirs: Maximizing Network Growth While Optimizing Fracture Conductivity. J. Can. Pet. Technol. 48, 39–51. https://doi.org/10.2118/114173-PA

Warpinski, N.R., Teufel, L.W., 1987. Influence of Geologic Discontinuities on Hydraulic Fracture Propagation (includes associated papers 17011 and 17074). J. Pet. Technol. 39, 209–220. https://doi.org/10.2118/13224-PA

Weng, X., Kresse, O., Cohen, C.-E., Wu, R., Gu, H., 2011. Modeling of Hydraulic-Fracture-Network Propagation in a Naturally Fractured Formation. SPE Prod. Operations. 26, 368–380. https://doi.org/10.2118/140253-PA

Wheaton, B., Haustveit, K., Deeg, W., Miskimins, J., Barree, R., 2016. A Case Study of Completion Effectiveness in the Eagle Ford Shale Using DAS/DTS Observations and Hydraulic Fracture Modeling. Presented at SPE Hydraulic Fracturing Technology Conference, The Woodlands, Texas, USA. 9-11 February. SPE-179149-MS . https://doi.org/10.2118/179149-MS

Wu, C.-H., Yi, S.S., Sharma, M.M., 2017. Proppant Distribution Among Multiple Perforation Clusters in a Horizontal Wellbore. Presented at SPE Hydraulic Fracturing Technology Conference and Exhibition, The Woodlands, Texas, USA. 24–26 January. SPE-184861-MS. https://doi.org/10.2118/184861-MS

Wu, K., 2014. Numerical Modeling of Complex Hydraulic Fracture Development in Unconventional Reservoirs. UT Austin.

Wu, K., Olson, J.E., 2014. Mechanics Analysis of Interaction Between Hydraulic and Natural Fractures in Shale Reservoirs. Unconventional Resources Technology Conference. https://doi.org/10.15530/URTEC-2014-1922946

Wu, K., Olson, J.E., 2015a. Simultaneous Multifracture Treatments : Fully Coupled Fluid Flow and Fracture Mechanics for Horizontal Wells. SPE Journal. 20-02,337-346.

Wu, K., Olson, J.E., 2015b. Numerical Investigation of Complex Hydraulic Fracture Development in Naturally Fracture Reservoirs. Soc. Pet. Eng. 3–5. https://doi.org/10.2118/173326-MSWu, K., Olson, J.E., 2016. Numerical investigation of complex hydraulic-fracture development in naturally fractured reservoirs. SPE Prod. Operations, 31, 300–309. https://doi.org/10.2118/173326-PA

Wu, R., Kresse, O., Weng, X., Cohen, C., Gu, H., 2012. SPE 152052 Modeling of Interaction of Hydraulic Fractures in Complex Fracture Networks. Presented at SPE Hydraulic Fracturing Technology Conference, The Woodlands, Texas, USA. 6-8 February. SPE-152052-MS. https://doi.org/10.2118/152052-MS

Xu, T., Ranjith, P.G., Au, A.S.K., Wasantha, P.L.P., Yang, T.H., Tang, C.A., Liu, H.L., Chen, C.F., 2015. Numerical and experimental investigation of hydraulic fracturing in Kaolin clay. J. Pet. Sci. Eng. 134, 223–236. https://doi.org/10.1016/j.petrol.2015.08.003

Xu, W., Zhao, J., Rahman, S.S., Li, Y., Yuan, Y., 2019. A Comprehensive Model of a Hydraulic Fracture Interacting with a Natural Fracture: Analytical and Numerical Solution. Rock Mech. Rock Eng. 52, 1095–1113. https://doi.org/10.1007/s00603-018-1608-9

Yang, K., Yilmaz, A.E., 2011. Comparison of precorrected FFT/adaptive integral method matching schemes. Microw. Opt. Technol. Lett. 53, 1368–1372. https://doi.org/10.1002/mop.26006

Yang, K., Yilmaz, A.E., 2012. A three-dimensional adaptive integral method for scattering from structures embedded in layered media. IEEE Trans. Geosci. Remote Sens. 50, 1130–1139. https://doi.org/10.1109/TGRS.2011.2166765

Yao, Y., 2012. Linear elastic and cohesive fracture analysis to model hydraulic fracture in brittle and ductile rocks. Rock Mech. Rock Eng. 45, 375–387. https://doi.org/10.1007/s00603-011-0211-0

Yew, C.H., Weng, X., 2014. Mechanics of Hydraulic Fracturing. Gulf Professional Publishing.

Yoon, J.S., Zang, A., Stephansson, O., 2014. Numerical investigation on optimized stimulation of intact and naturally fractured deep geothermal reservoirs using hydro-mechanical coupled discrete particles joints model. Geothermics 52, 165–184. https://doi.org/10.1016/j.geothermics.2014.01.009

Yoon, J.S., Zang, A., Stephansson, O., Hofmann, H., Zimmermann, G., 2017. Discrete Element Modelling of Hydraulic Fracture Propagation and Dynamic Interaction with Natural Fractures in Hard Rock, in: Procedia Engineering. Elsevier Ltd, pp. 1023–1031. https://doi.org/10.1016/j.proeng.2017.05.275

Yoon, J. S., Zang, A., Stephansson, O., & Zimmermann, G. (2016). Modelling of fluid-injection-induced fault reactivation using a 2D discrete element based hydro-mechanical coupled dynamic simulator. Energy Procedia, 97, 454-461.

Yoon, J.S., Zimmermann, G., Zang, A., 2015. Numerical Investigation on Stress Shadowing in Fluid Injection-Induced Fracture Propagation in Naturally Fractured Geothermal Reservoirs. Rock Mech. Rock Eng. 48, 1439–1454. https://doi.org/10.1007/s00603-014-0695-5

Zhang, X., Jeffrey, R.G., 2006. The role of friction and secondary flaws on deflection and re-initiation of hydraulic fractures at orthogonal pre-existing fractures. Geophys. J. Int. 166, 1454–1465. https://doi.org/10.1111/j.1365-246X.2006.03062.x

Zhang, X., Jeffrey, R.G., 2008. Reinitiation or termination of fluid-driven fractures at frictional bedding interfaces. J. Geophys. Res. Solid Earth 113. https://doi.org/10.1029/2007JB005327

Zhang, X., Jeffrey, R.G., Thiercelin, M., 2007. Deflection and propagation of fluid-driven fractures at frictional bedding interfaces: A numerical investigation. J. Struct. Geol. 29, 396–410. https://doi.org/10.1016/j.jsg.2006.09.013

Zhang, Z.Q., Liu, Q.H., 2002. A Volume Adaptive Integral Method (VAIM) for 3-D inhomogeneous objects. IEEE Antennas Wirel. Propag. Lett. 1, 102–105. https://doi.org/10.1109/LAWP.2002.805126